

MEASUREMENT OF THE Σ^+ PRODUCTION AND THE
p- Σ^+ CORRELATION FUNCTION IN PROTON-PROTON
COLLISIONS WITH ALICE AT THE LHC

Dissertation
zur Erlangung des Doktorgrades
der Naturwissenschaften

vorgelegt beim Fachbereich Physik
der Johann Wolfgang Goethe-Universität
Frankfurt am Main

von
Benedict Heybeck
aus Frankfurt am Main

Frankfurt 2025
D30

Vom Fachbereich Physik
der Johann Wolfgang Goethe-Universität
als Dissertation angenommen.

Dekan: Prof. Dr. Marc Wagner

Gutachter: Prof. Dr. Harald Appelshäuser
PD Dr. Benjamin Dönigus
Prof. Dr. Johanna Stachel

Datum der Disputation: 29.10.2025

Abstract

In the past decades, progress in the development of particle accelerators and detectors enabled scientists to study the production, interactions, and collective phenomena of many particle species in great detail. Ranging from light mesons to nuclei, even rare or short-lived probes could be measured over a broad range of collision energies. Nonetheless, data on one row of the baryon octet, the Σ baryons, is scarce. In previous measurements, mostly the excited states of Σ baryons were measured [1]. Some results also exist on the Σ^0 (e.g. Ref. [2, 3]). The charged ground-state Σ baryons are, however, mostly unexplored. The only measurements of the Σ^+ production in high-energy collisions so far were performed by the DELPHI, OPAL, and L3 collaborations, which were all situated at the LEP collider at CERN and measured the Σ^+ in hadronic decays of the Z^0 boson [4–6]. The reason for the scarce data situation is that the charged ground-state Σ baryons are extraordinarily challenging to measure, which will be discussed in detail in this thesis. The aforementioned measurements have been compared to different Monte Carlo event generators and showed sizeable deviations in the yield and shape of the obtained momentum spectra [1, 2, 4–6]. It is well known that common event generators generally underpredict the production of strangeness [7, 8], which also reflects in an underprediction of Σ baryons in these models. In this regard, the measurement of Σ^+ cannot only provide a valuable cross check of the yields and spectral shape but also serve as an input to improve those models.

Moreover, a good knowledge about the production cross sections of Σ baryons is of importance for the measurements of protons and Λ s, as the Σ s feed down into the measured yields of these particles via their weak decays [9].

The observed enhancement of the production of strangeness in hadronic collisions with increasing multiplicity was historically seen as a signature of the quark-gluon plasma [10]. Currently, only one single strange ground-state baryon, the Λ , is measured multiplicity differentially [10] and also in this regard, the

measurement of Σ baryons can help to complete the picture.

Apart from the measurement of the production cross section, the reconstruction of the Σ^+ baryons opens up the possibility to study their interactions with other hadrons via the femtoscopy method [11]. The interaction between nucleons and hyperons as well as the interaction between hyperons is generally not well known. This is related to the fact that neither targets nor beams can be created from hyperons, inhibiting scattering experiments. Knowledge about the aforementioned interactions is crucial for the equation of state of dense astrophysical objects like neutron stars, since the Pauli principle implies that the presence of hyperons might be energetically favorable at densities well above the nuclear saturation density [12–14]. Among the interactions including hyperons, the N – Λ interaction is rather well known from femtoscopic measurements [15, 16] and the analysis of hypernuclei [17]. These results have already created tension with astronomical observations, known as the “hyperon puzzle”. On the other hand, it has recently emerged that non-negligible three-body contributions might be responsible for the discrepancy and may even inhibit Λ baryons from appearing in neutron stars [18, 19]. This, however, does not rule out other hyperons like Σ or Ξ baryons from emerging, depending on their respective interactions with the surrounding neutron star matter. These interactions are, however, even less known and thus the extension of the femtoscopic studies to the Σ sector can provide valuable information. In this regard, the N – Σ ($I = 3/2$) channel gives access to the partially Pauli-forbidden decuplet, which can neither be accessed by the N – N nor by the N – Λ interaction [20]. Specifically, the p – Σ^+ interaction studied in this thesis stands out, as it is closely related to the unmeasurable n – Σ^- interaction, which is most important for neutron stars [12–14]. Furthermore, given sufficient data, this channel allows to test the $SU(3)$ flavor symmetry breaking in the 27-plet interaction [20, 21]. Moreover, knowledge about the p – Σ^0 correlation function is an important input for the measurement of the p – Λ correlation function, as both systems are not fully separable experimentally [15].

Previous femtoscopic studies focused on the p – Σ^0 system [22, 23]. This seems natural, as the Σ^0 is relatively easy to access experimentally. However, specific challenges arise which hinder the extraction of the relevant information in this system. This will be addressed in detail in this thesis. It will also be discussed why the p – Σ^+ system is in fact more promising, both experimentally and the-

oretically, and which challenges there are.

The difficulty of reconstructing the Σ^+ baryon in high-energy collision experiments reflects itself in the lack of previous measurements and will take a prominent part in this thesis. Besides the results obtained from the available data, the methods which have been developed in the scope of this thesis will be useful for the measurement of other particle pairs and the data to come.

Zusammenfassung

Durch den Fortschritt in der Entwicklung von Teilchenbeschleunigern und Detektoren ist es in den vergangenen Jahrzehnten gelungen, die Produktion, Wechselwirkungen und kollektive Effekte von vielen Teilchen in großem Detail zu studieren. Von leichten Mesonen bis hin zu Kernen konnten sogar seltene oder kurzlebige Teilchen über eine große Bandbreite von Kollisionsenergien gemessen werden. Daten zu einer Reihe des Baryonen-Oktetts, die Σ -Baryonen, sind jedoch nur spärlich vorhanden. In früheren Messungen wurden hauptsächlich die angeregten Zustände der Σ -Baryonen gemessen [1]. Zudem lassen sich einige Ergebnisse über das Σ^0 finden (z.B. Ref. [2, 3]). Die geladenen Σ -Baryonen im Grundzustand sind jedoch weitestgehend unerforscht. Die einzigen Messungen der Σ^+ -Produktion in hochenergetischen Kollisionen wurden von den DELPHI, OPAL und L3 Kollaborationen gemessen, welche alle am LEP-Speicherring am CERN angesiedelt waren und welche Σ^+ in hadronischen Zerfällen des Z^0 -Bosons gemessen haben [4–6]. Der Grund für die spärliche Datenlage ist, dass die geladenen Σ -Baryonen im Grundzustand ausgesprochen schwer zu messen sind. Dies wird in dieser Arbeit im Detail diskutiert. Die zuvor angesprochenen Messungen wurden mit verschiedenen Monte-Carlo-Ereignisgeneratoren verglichen und zeigten erhebliche Abweichungen in der Menge der produzierten Teilchen und der Impulsspektren [1, 2, 4–6]. Bekanntermaßen unterschätzen gängige Ereignisgeneratoren die Produktion von Strangeness [7, 8], was sich auch in einer zu geringen Produktion von Σ -Baryonen in diesen Modellen zeigt. In diesem Zusammenhang kann die Messung von Σ^+ nicht nur der Überprüfung bisheriger Modelle dienen, sondern auch als Input, um diese Modelle zu verbessern.

Gute Kenntnis über die Produktionsquerschnitte von Σ -Baryonen sind zudem auch für die Messung von Protonen und Λ s wichtig, da Σ s schwach in diese Teilchen zerfallen können [9].

Der beobachtete Anstieg der Produktion von Strangeness in hadronischen Kol-

lisionen mit steigender Multiplizität wurde historisch als Signatur des Quark-Gluon-Plasmas gesehen [10]. Gegenwärtig wurde nur ein einfach seltsames Baryon im Grundzustand, das Λ , in Abhängigkeit der Multiplizität gemessen [10] und auch in diesem Zusammenhang kann die Messung von Σ -Baryonen helfen, das Verständnis der Produktion von Strangeness zu verbessern.

Abgesehen von der Messung der Produktionsquerschnitte eröffnet die Rekonstruktion der Σ^+ -Baryonen die Möglichkeit, ihre Wechselwirkung mit anderen Hadronen mittels der femtokopischen Methode zu untersuchen [11]. Die Wechselwirkung zwischen Nukleonen und Hyperonen, sowie die Wechselwirkung zwischen Hyperonen ist generell nicht gut bekannt. Grund dafür ist, dass weder Targets noch Strahlen aus Hyperonen erzeugt werden können, wodurch Streu-Experimente erschwert werden. Die Kenntnis dieser Wechselwirkungen ist für die Zustandsgleichung dichter astrophysikalischer Objekte wie Neutronensterne von entscheidender Bedeutung, da das Pauli-Prinzip impliziert, dass die Entstehung von Hyperonen bei Dichten weit oberhalb der Kernsättigungsdichte energetisch günstig sein könnte [12–14]. Unter den Wechselwirkungen mit Hyperonen ist die N - Λ -Wechselwirkung vergleichsweise gut durch femtoskopische Messungen [15, 16] und die Analyse von Hyperkernen [17] bekannt. Diese Ergebnisse haben bereits Spannungen mit astronomischen Beobachtungen, bekannt als “Hyperonen Puzzle”, hervorgerufen. In jüngster Zeit hat sich jedoch herausgestellt, dass nicht vernachlässigbare Dreikörperbeiträge der Wechselwirkung für die Diskrepanz verantwortlich sein könnten und diese möglicherweise sogar das Auftreten von Λ -Baryonen in Neutronensternen verhindern können [18, 19]. Das schließt jedoch nicht aus, dass andere Hyperonen wie Σ - oder Ξ -Baryonen abhängig von ihren jeweiligen Wechselwirkungen mit der umgebenden Neutronenstern-Materie auftreten. Diese Wechselwirkungen sind jedoch noch weniger bekannt und daher kann die Ausweitung der femtoskopischen Studien auf Σ -Baryonen wertvolle Informationen liefern. In diesem Zusammenhang gibt der N - Σ ($I = 3/2$)-Kanal Zugang zum teilweise Pauli-verbotenen Dekuplett, welches weder durch die N - N - noch durch N - Λ -Wechselwirkung erschlossen werden kann [20]. Im Speziellen sticht die p - Σ^+ -Wechselwirkung, welche in dieser Arbeit untersucht wird, hervor, da sie nah mit der n - Σ^- -Wechselwirkung verwandt ist, die von zentraler Bedeutung für Neutronensterne ist [12–14]. Darüber hinaus lässt sich in diesem Kanal, genügend Daten vorausgesetzt, die Brechung der $SU(3)$ -Flavor-Symmetrie in der 27-plet-Wechselwirkung überprüfen [20, 21].

Weiterhin ist die Kenntnis über die p - Σ^0 -Korrelationsfunktion ein entscheidender Input für die Messung der p - Λ -Korrelationsfunktion, da sich diese Systeme experimentell nicht vollständig trennen lassen [15].

Frühere femtoskopische Studien fokussierten sich auf das p - Σ^0 -System [22, 23]. Das erscheint sinnvoll, da das Σ^0 vergleichsweise einfach zu rekonstruieren ist. Es treten jedoch bestimmte Hürden auf, welche in diesem System die Extraktion der relevanten Informationen erschweren. Dies wird in dieser Arbeit im Detail besprochen. Es wird außerdem besprochen, warum das p - Σ^+ -System tatsächlich vielversprechender ist, sowohl experimentell als auch theoretisch, und welche Herausforderungen es gibt.

Die Schwierigkeit, das Σ^+ -Baryon in Hochenergie-Kollisionsexperimenten zu rekonstruieren, spiegelt sich in der geringen Zahl an früheren Messungen wider und wird einen erheblichen Teil dieser Arbeit einnehmen. Neben den Ergebnissen, welche mit den verfügbaren Daten erhalten wurden, sind die Methoden, welche im Rahmen dieser Arbeit entwickelt wurden, hilfreich für die Messung anderer Teilchen-Paare und die zukünftigen Daten.

Contents

Abstract	3
Zusammenfassung	6
Contents	9
List of Figures	11
List of Tables	15
List of Abbreviations	16
1 Introduction	18
1.1 Standard model of particle physics	18
1.1.1 Quantum chromodynamics	20
1.1.2 Quark-gluon plasma	22
1.2 Particle production	25
1.2.1 Statistical hadronization model	25
1.2.2 Monte Carlo generators	30
1.3 Particle interactions	34
1.3.1 Theoretical treatment	34
1.3.2 Experimental studies	39
1.3.3 Neutron stars	46
1.4 Femtoscopy	51
1.4.1 Experimental correlation function	52
1.4.2 Theoretical approach	55
2 The ALICE experiment	71
2.1 The Large Hadron Collider	71
2.2 The ALICE detector	74
2.2.1 Inner Tracking System	75
2.2.2 Time Projection Chamber	76
2.2.3 Time-Of-Flight detector	78

2.2.4	Calorimeters	80
2.2.5	V0 detectors	80
2.3	Data processing	81
2.3.1	Tracking	82
2.3.2	Online secondary reconstruction	83
3	Software tools	86
3.1	Kalman filter	87
3.2	Machine learning	88
3.2.1	Boosted decision trees	91
4	Measurement of the Σ^+ production	96
4.1	Σ^+ reconstruction	97
4.1.1	Proton selection	98
4.1.2	π^0 measurement	99
4.1.3	Σ^+ selection	106
4.2	Reconstruction efficiency	107
4.2.1	Custom Monte Carlo simulation	109
4.2.2	Efficiency results	110
4.3	Invariant-mass spectra	115
4.3.1	Background description	116
4.3.2	Peak extraction	118
4.3.3	Cross checks	122
4.3.4	Systematic uncertainties	125
4.4	Integrated yields	130
4.5	Thermal model comparison	133
4.6	MC comparisons	134
5	Measurement of the p–Σ^+ correlation function	137
5.1	Σ^+ sample	138
5.1.1	Missing-mass reconstruction	139
5.1.2	Resolution improvement	141
5.1.3	Σ^+ selection	144
5.1.4	Purity determination	152
5.1.5	Reconstruction efficiency and cross check	154

5.1.6	Alternative reconstruction methods	157
5.2	Proton sample	158
5.3	λ parameter determination	165
5.4	Experimental correlation function	174
5.4.1	Uncorrelated sample	175
5.4.2	Alternative method	176
5.4.3	k^* resolution	180
5.4.4	Systematic uncertainties	181
5.5	Theoretical correlation function	184
5.5.1	Source size	184
5.5.2	Comparison with theoretical calculations	188
5.5.3	Source size dependence of the correlation function	191
5.5.4	Decomposition of the correlation function	192
5.5.5	Generic potential fits	194
	Summary	208
	List of Literature	211

List of Figures

1.1	Standard model of particle physics	19
1.2	Strong coupling constant	21
1.3	Phase diagram of QCD matter	23
1.4	Strangeness production vs. multiplicity	24
1.5	Cross sections of p - Σ^+ scattering from KEK E251, E289 & E40 .	44
1.6	Mass-radius relation of neutron stars	46
1.7	m_T scaling of r_{core}	57
1.8	Comparison of the Coulomb treatments in correlation functions .	64
1.9	Comparison of the Lednický-Lyuboshits approach and the usage of full wave functions	68
2.1	Experimental facilities at CERN	71
2.2	LHC interaction points	73
2.3	ALICE detector	74
2.4	Inner Tracking System	75
2.5	Time Projection Chamber	77
2.6	Particle identification in the TPC	78
2.7	Particle identification by the time-of-flight	79
4.1	Armenteros-Podolanski plot	103
4.2	Bad cell fractions	105
4.3	Invariant-mass distribution of Σ^+ showing the effect of the energy correction	107
4.4	Reconstructed MC Σ^+ spectrum	111
4.5	Σ^+ reconstruction efficiency	112
4.6	Photon conversion and reconstruction efficiency	113
4.7	Reconstruction efficiency of Σ^+ and $\bar{\Sigma}^-$	114
4.8	Invariant-mass distribution of Σ^+ with the PCM-PCM method .	115
4.9	Invariant-mass distribution of Σ^+ with the PCM-Calo method .	116

4.10	Invariant-mass ratio in same and mixed events	119
4.11	Invariant-mass distribution of Σ^+ with mixed-event distribution with the PCM-PCM method	120
4.12	Invariant-mass distribution of Σ^+ with mixed-event distribution with the PCM-Calo method	121
4.13	Invariant-mass distribution with subtracted background	122
4.14	Invariant-mass distribution with subtracted background with MC distribution	123
4.15	Raw p_T spectra of Σ^+	124
4.16	Comparison of default and strict cluster selection	125
4.17	Comparison of PCM-PCM and PCM-Calo spectra	126
4.18	Systematic uncertainty contributions	128
4.19	Σ^+ p_T spectra with fits	131
4.20	Σ^+ p_T spectra with fit variations	132
4.21	Comparison of the Σ^+ p_T spectrum with event generators	136
5.1	Invariant-mass distribution of Σ^+ reconstructed with the single- γ method	141
5.2	Secondary vertex resolution	143
5.3	Momentum resolution improvement	143
5.4	Σ^+ feature correlations	145
5.5	Σ^+ ROC-AUC curves	146
5.6	Σ^+ features for BDT 1	148
5.7	Σ^+ features for BDT 2	149
5.8	Σ^+ BDT score distributions	150
5.9	Σ^+ feature importance	150
5.10	Σ^+ η vs. φ distribution	151
5.11	Σ^+ invariant-mass distribution with template fits	153
5.12	Σ^+ purity	154
5.13	Σ^+ reconstruction efficiency with single- γ method	155
5.14	Σ^+ single- γ spectra cross check	156
5.15	Proton feature correlations	160
5.16	Proton ROC-AUC curves	161
5.17	Proton feature distributions	162
5.18	Proton BDT score distributions	163

5.19	Proton feature importance	163
5.20	Proton and Σ^+ raw p_T distributions	164
5.21	Proton Σ^+ η vs. φ distribution	164
5.22	Efficiency comparison	168
5.23	Extrapolated proton p_T spectra	170
5.24	Effective proton spectra	171
5.25	Proton purity and primary fractions	171
5.26	k^* vs. p_T matrices	172
5.27	λ parameters	173
5.28	Comparison of new uncorrelated sample method	179
5.29	Normalization of the correlation function	180
5.30	k^* resolution	181
5.31	Systematic uncertainty contributions	183
5.32	m_T distribution	185
5.33	Source distributions	187
5.34	Theoretical correlation functions	189
5.35	Strong wave functions	190
5.36	Correlation function for both sources	191
5.37	Decomposition of the correlation function	193
5.38	Correlation functions from Gaussian potentials	197
5.39	χ^2 vs. V_0	198
5.40	V_0 vs. a_0	200
5.41	Distribution of fits from the bootstrapping procedure	201
5.42	$\Delta\chi^2$ vs. p-value	202
5.43	Exclusion plots	203
5.44	Projections of χ^2	204
5.45	Gaussian potential fits	206

List of Tables

1.1	Baryon–baryon multiplet table	35
1.2	Model scattering parameters of $p\text{--}\Sigma^+$	38
4.1	Selections of Σ^+ with variations	129
4.2	Integrated yields of Σ^+	132
4.3	Yields of Λ	133
5.1	S-wave scattering lengths of the $p\text{--}\Sigma^+$ interaction, evaluated using Gaussian and Reid-like potentials	205

List of Abbreviations

QFT	Q uantum F ield T heory
QCD	Q uantum C hromod Y namics
QGP	Q uark G luon P lasma
SHM	S tatistical H adronisation M odel
HRG	H adron R esonance G as
CSM	C anonical S tatistical M odel
MC	M onte C arlo
PDF	P arton D istribution F unction
CR	C olor R econnection
PDG	P article D ata G roup
SU(N)	S pecial U nitary group with all $N \times N$ unitary matrices with determinant 1
irrep	i rreducible r epresentation
NSC	N ijmegen S oft C ore
ESC	E xtended S oft C ore
EFT	E ffective F ield T heory
LEC	L ow- E nergy C onstant
N(2)LO	N ext to (next to) L eading O der
SMS	S emi-local M omentum S pace
HBT	H anbury- B rown and T wiss
FSI	F inal S tate I nteraction
LL	L ednický- L yuboshits
ERE	E ffective R ange E xpansion
LHC	L arge H adron C ollider
CERN	C onseil E uropéen pour la R echerche N ucléaire
LEP	L arge E lectron P ositron collider

ALICE	A Large Ion Collider Experiment
ITS	Inner Tracking System
SPD	Silicon Pixel Detector
TPC	Time Projection Chamber
PID	Particle Identification
TOF	Time Of Flight
PHOS	Photon Spectrometer
EMCal	Electromagnetic Calorimeter
DCal	Di-jet Calorimeter
MB	Minimum Bias
HM	High Multiplicity
DCA	Distance of Closest Approach
ESD	Event Summary Data
AOD	Analysis Oriented Data
PCA	Point of Closest Approach
(C)PA	(Cosine of the) Pointing Angle
ML	Machine Learning
BDT	Boosted Decision Tree
ROC	Receiver Operating Characteristic
AUC	Area Under the Curve
TPE	Tree-structured Parzen Estimator
Shap	Shapley additive explanation
PCM	Photon Conversion Method
MIP	Minimum Ionizing Particle
OADB	Offline Analysis Database
GEANT	Geometry And Tracking

1 Introduction

1.1 Standard model of particle physics

Since ancient times, scientists and philosophers have been trying to uncover the nature of matter. Early on, the idea matured that all matter is composed of finite, indivisible parts. However, those concepts remained intellectual games until the beginning of the 20th century, when Rutherford discovered that matter is composed of highly compact nuclei, themselves being composed of positively charged nucleons, the protons, and neutral nucleons, the neutrons [24]. This picture was refined by Bohr who proposed that the nuclei are orbited by electrons with discrete energy levels, resulting in a model of the atom close to the one we have today [25]. Not much later, in the 1950s, the invention of new experimental techniques has led to the discovery of a whole “zoo”¹ of particles and thus established the field of particle physics [9]. It quickly became clear that those particles could not all be elementary, but have an underlying structure. This was resolved in 1964 when Gell-Mann [27] and Zweig [28] independently proposed 3 fermionic elementary particles, the quarks, organized in a $SU(3)$ symmetry. Only three years earlier, the symmetry was already introduced by Gell-Mann and named the “Eightfold Way” [29]. These quarks were the up and down quarks from which the nucleons are composed of and whose names originated from the existing isospin formalism [30]. The third was the strange quark whose name is related to the “strange” observation that hadrons containing these quarks lived more than 10 orders of magnitude longer than other decaying hadrons, indicating that these carry new quantum numbers. Building on these early findings, the standard model of particle physics describes all known elementary particles and their interactions [31]. The particles of the standard model are depicted in Fig. 1.1.

¹The term “zoo” was reportedly first used in this regard by Oppenheimer in 1956 at the 6th Annual Conference on High Energy Nuclear Physics in Rochester [26].

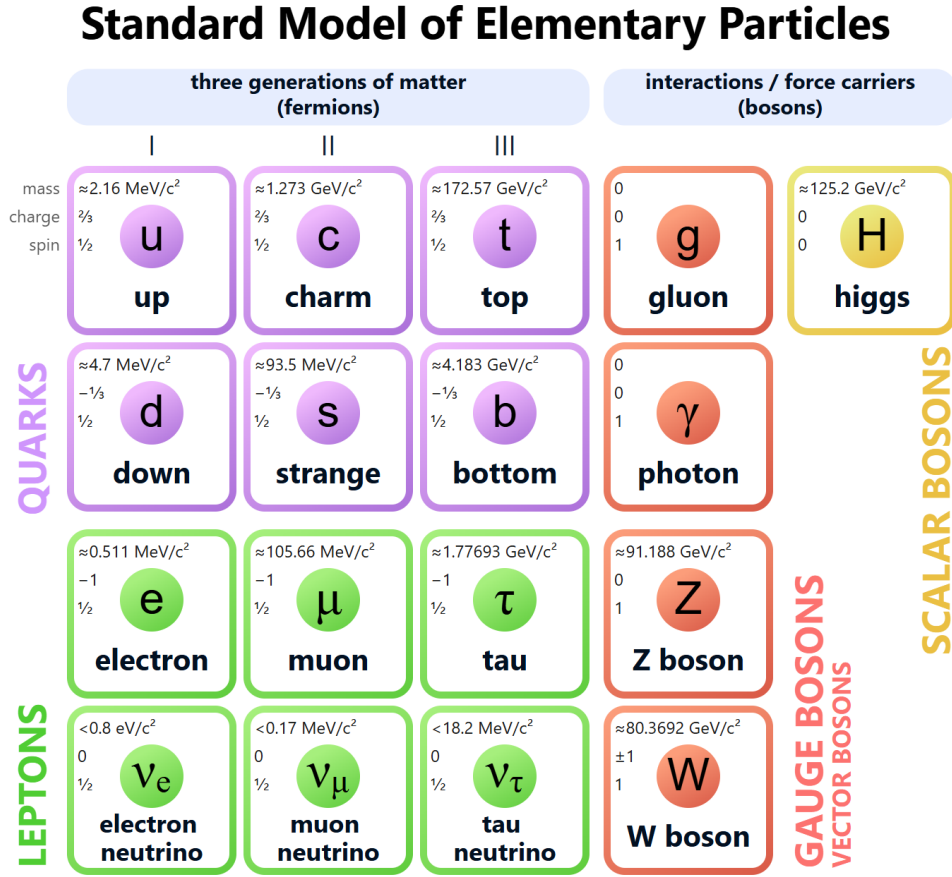


Figure 1.1: The elementary particles of the standard model of particle physics. Figure from Ref. [32].

The standard model [31] comprises six quarks with the so-called “flavors” up (u), down (d), charm (c), strange (s), top (t), and bottom (b), arranged in three generations. All quarks are fermions, i.e. carry a spin of $\hbar/2$. The u , c , and t quarks carry an electric charge of $+2/3e$, while the other quarks carry $-1/3e$. All quarks have a baryon number of $1/3$. Each generation also contains a charged and a neutral fermionic lepton. The charged leptons are the electron (e^-), the muon (μ^-), and the tauon (τ^-), the neutral leptons are the corresponding neutrinos (ν_e , ν_μ , ν_τ). All of the above particles also have anti-particles with opposite quantum numbers.

Alongside, the standard model contains four kinds of gauge bosons which serve as force carriers within the quantum field theory (QFT) [33], giving rise to the three fundamental forces, the electromagnetic, the weak, and the strong force. Only the gravitational force - even though possibly mediated by the hypothet-

ical gravitation - is not part of the standard model, as it is - according to general opinion - a result of the curvature of space-time, which is described by the theory of general relativity [34].

The gauge bosons are the photon for the electromagnetic interaction, the W and Z bosons for the weak interaction, and the gluons for the strong interaction. All gauge bosons are vector bosons carrying a spin of \hbar .

In addition, the standard model recognizes the scalar (spinless) Higgs-boson as the quantum excitation of the Higgs field, which gives all particles their rest mass through the Higgs mechanism [35].

1.1.1 Quantum chromodynamics

The introduction of the quark model brought order into the system of particles, but has also raised the question why the quarks themselves were not observed. Another important aspect was how a nucleon containing 3 fermionic quarks could satisfy the Pauli exclusion principle, which requires the total wave function of a set of fermions to be antisymmetric under the exchange of two particles. This could be resolved by the introduction of an additional degree of freedom, a triplet of “colors”. This concept was first postulated by Han and Nambu in 1965 [36] and later refined by Bardeen, Fritzsch, and Gell-Mann [37]. These colors act at the same time as the charge of the strong interaction. Quarks carry one of the colors red (r), green (g), or blue (b), while anti-quarks carry the corresponding anti-colors. While these colors are completely unrelated to the colors in an optical sense, the similarity to the color theory eases the human perception; a set of quarks can become color-neutral (“white”) either by combining 3 (anti-)quarks forming a (anti-)baryon or by combining a quark and an anti-quark forming a meson.

The strong interaction differs from the other fundamental interactions in a very important aspect, which is that the mediators, the gluons, themselves carry the charge of the interaction. The gluons carry a combination of a color and an anti-color. Thus, they do not only mediate the strong interaction, but also participate in it. This has the crucial consequence that the field lines between color charges are pulled together as a result of the gluon self-interaction, resulting in a dense flux tube called string. The string can be pictured as a rubber band under tension. The string tension is often reported with a value of around

1 GeV/fm [38]. When quarks are pulled apart, the energy stored in the string increases until it is sufficiently large that a quark–anti-quark pair, emerging from the vacuum, can become on-shell, resulting in a breaking of the string and a restoration of color-neutrality at both ends. This easily explains the impossibility to remove a single quark from a hadron and observe color-charged particles directly, which is called confinement.

The quantum field theory which theoretically describes the strong interaction is quantum chromodynamics (QCD) [39, 40]. It is a Yang-Mills theory, i.e. it is based on the $SU(3)$ gauge symmetry group, which is non-abelian, meaning that the multiplication of group elements is generally not commutative [41]. As a consequence, the QCD Lagrangian contains terms that are responsible for the gluon self-interaction. The strong coupling constant α_s , which defines the strength of the strong interaction, is, as the consequence of the gluon self-interaction, far from constant, but strongly depends on the momentum transfer [39, 40]. This so-called running coupling is depicted in Fig. 1.2.

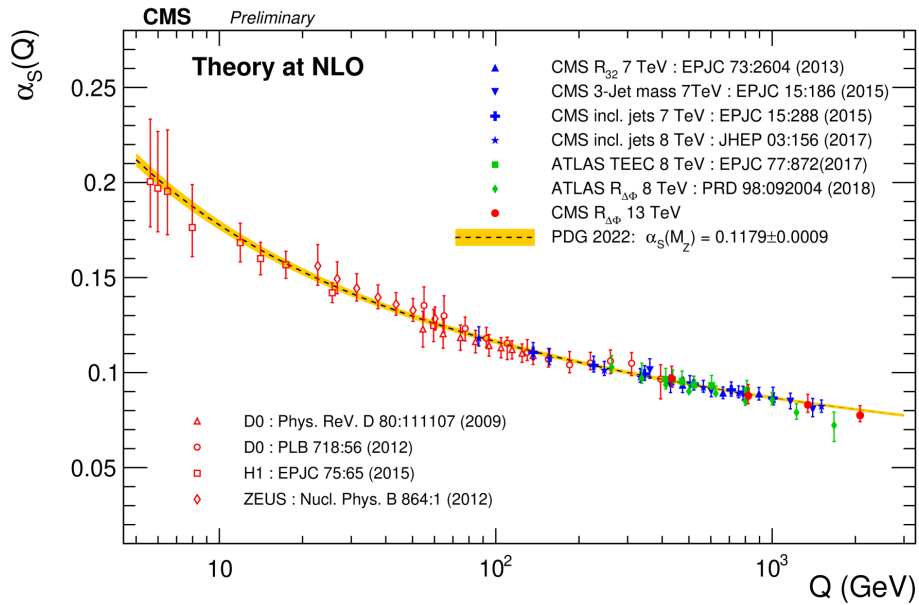


Figure 1.2: Strong coupling constant α_s as a function of the momentum transfer Q . At small energies the coupling constant diverges, while it vanishes at high energies [39, 40]. Figure from Ref. [42].

In the low-energy regime, α_s is large, which leads to the confinement. At small distances or, correspondingly, large energies, α_s , in turn, vanishes, resulting in the so-called asymptotic freedom [39, 40] at which quarks can move as if they

would be free. This is the exactly opposite behavior than in the other fundamental interactions where particles are asymptotically free at large distances. Like most field theories, QCD cannot be solved in an exact way, but requires appropriate approximations to be dealt with [39]. Generally, this is aggravated by the large coupling constant. At large energies where α_s is small, QCD can be treated using perturbation theory [43]. The solutions are expanded in a perturbation series in powers of the coupling constant. The terms of this series can be visualized in terms of Feynman diagrams [44]. Since the coupling constant enters at every vertex, the series rapidly converges if $\alpha_s \ll 1$ and thus, can be truncated at some point. At low energies, however, the series diverges and the perturbative approach breaks down. In this regime, effective field theories [45, 46] have been found useful which limit the degrees of freedom to the relevant ones by averaging over the substructure of the underlying theory, resulting in an approximate but simpler model at the desired length scale. With the availability of large-scale computers, it has also become possible to approximate solutions numerically using lattice QCD [47]. There, the space time is discretized by placing the quarks on a finite lattice, which ultimately makes the required path integrals solvable analytically; at the price of very high computational cost. While lattice QCD has now entered the era of precision, it still lacks applicability at low temperatures and high densities due to the emergence of a numerical sign problem [48].

1.1.2 Quark-gluon plasma

The running coupling implies that, given sufficiently large temperature or pressure, a quark-gluon plasma (QGP) can be created, which is a state in which the quarks and gluons are deconfined [49–51]. Such conditions can be prepared in the laboratory by colliding (heavy) ions at relativistic velocities, which allows to study the created medium experimentally [52, 53]. The phase diagram of QCD matter is typically expressed in terms of the baryo-chemical potential² μ_B and the temperature T [54, 55]. It is sketched in Fig. 1.3.

Most features of the QCD phase diagram are conjectured [55]. Lattice simulations can be used to study the region of high temperature and vanishing

²The baryo-chemical potential is the energy needed to add one additional baryon to the system and is a measure for the baryon to anti-baryon ratio, i.e. the net-baryon content. At LHC energies μ_B is close to zero.

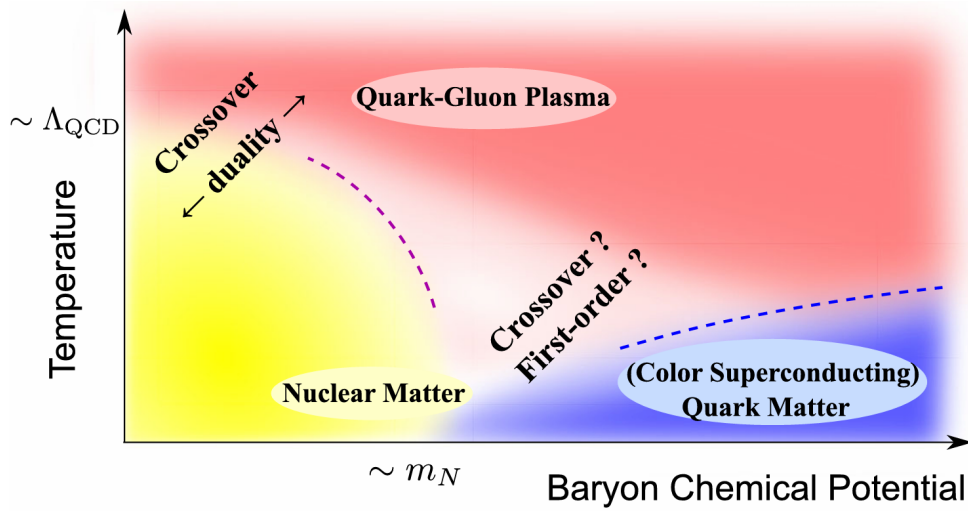


Figure 1.3: Conjectured phase diagram of QCD matter as a function of the baryo-chemical potential μ_B and the temperature T . At high energies, as found at the LHC, the high T , low μ_B part of the phase diagram is probed. The diagram also shows a conjectured critical endpoint as well as a color-superconducting phase, neither of which has yet been established. Figure from Ref. [56].

baryo-chemical potential [57]. It is found that the entropy increases rapidly, yet smoothly, with temperature around a critical temperature, which is related to the emerging degrees of freedom. The critical temperature is extracted from the peak of the chiral susceptibility and is found to be 156.5 MeV, known to a precision below 1% [58]. The smooth behavior implies a cross-over transition at small baryo-chemical potentials. In contrast, a first order phase transition is expected at high μ_B . Yet this implies the existence of a critical endpoint. Up to now, the position of such a point is not established [54, 55]. Lattice simulations cannot extend to the region of real and non-zero μ_B due to a numerical sign-problem and solely rely on extrapolations to access this region. Therefore it is necessary to explore the QCD phase diagram experimentally. Depending on the beam energy, different regions of the phase diagram are probed. Within beam energy scans (BES), the collision energy is varied in the search of critical phenomena [59]. These can express in increased fluctuations, for instance in the net-baryon number. In the absence of critical fluctuations, the net-baryon number is normally distributed. As Gaussian distributions only have two non-zero moments, higher order cumulants of the net-baryon number are a hint of criticality [60, 61].

However, the magnitude of such cumulants and whether they are detectable in the final state at all are still open questions. Since the QGP can only be observed indirectly, no definite proof of its creation is at hand. However, evidence is provided by several observations, hinting towards deconfinement. These include for instance an extremely large stopping power of highly energetic partons, known as jet quenching [65] or a hydrodynamical behavior [66] of the medium. Interestingly, such observations cannot only be made in heavy-ion collisions, but also in small systems like proton-proton (pp) collisions. This could mean that either a QGP could also be formed in such systems or that the observables are not unique features of the QGP. An example for such a misconception is the enhancement of the production of strange hadrons with increasing multiplicity, which was earlier proposed as a signature of deconfinement [67]. Conceptually, the lower in-medium mass of the strange quark would lead to an increased thermal production. However, the enhancement of strangeness is now seen as a lifting of the canonical suppression with increasing multiplicity and, in fact, a smooth transition across multiple collision systems is observed as seen in Fig. 1.4. Another important signature of deconfinement is the grouping of baryons and mesons in the v_2 flow component, which can be explained by quark coalescence [68, 69]. The splitting

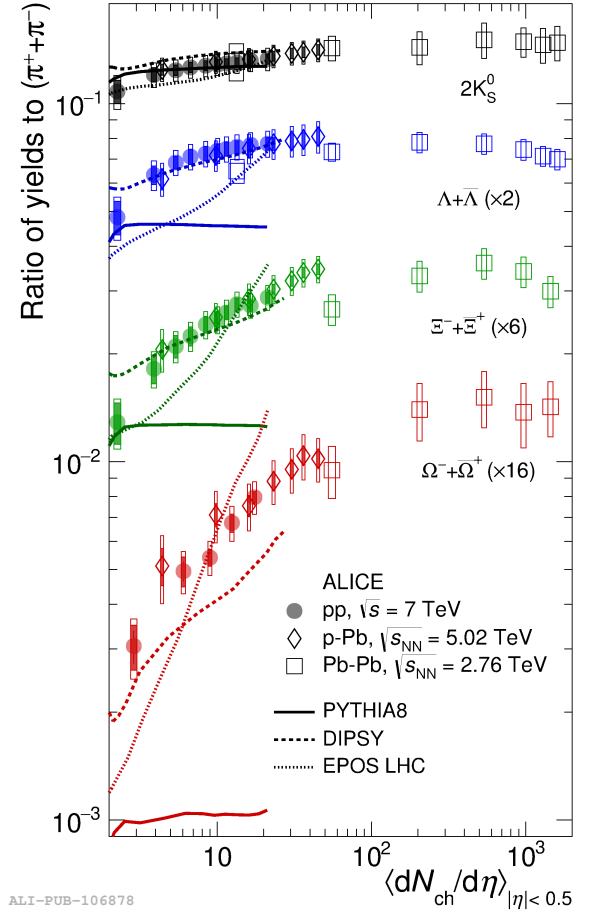


Figure 1.4: Ratio of the integrated yields of various strange hadrons to pions as a function of the multiplicity. Several model predictions are also shown. PYTHIA 8 [62] (solid lines) fails to describe the data, predicting almost no multiplicity dependence. EPOS LHC [63] captures the trend of the data, but overestimates the slope. In contrast, DIPSY [64] describes the data very well, only compromising on the triple strange Ω baryons. Figure from Ref. [10].

emerges at high multiplicities also in pp collisions, indicating that small bubbles of deconfined matter might also be present in high-multiplicity elementary collisions [70].

1.2 Particle production

In order to obtain information about the created medium and the processes from which the particles are produced, the experimentally accessible momentum spectra have to be related to the quantities of interest through theoretical calculations. Particle momentum spectra and their comparison in various collision systems can thereby provide valuable insight to the medium properties and the dynamical evolution of heavy-ion collisions [71].

From the theoretical point of view, the description of hadronic collisions is challenging for the reasons discussed in the previous sections. Quarks and gluons are color-charged objects, and thus a hadronic collision is governed by the strong interaction and resident in the QCD. Both the high- and the low-energy regimes contribute to the particle production during the evolution of the collision. Therefore, a complete calculation of the ongoing processes from the incoming projectiles to the outgoing hadrons remains impossible. However, statistical and phenomenological methods are at hand which are capable of describing the production of particles successfully. These will be described in the following.

1.2.1 Statistical hadronization model

Before introducing the statistical approach to hadronization, one has to recall the basic concepts of thermodynamics and statistical physics [72]. One may consider a system of N particles, each having certain degrees of freedom. The laws of mechanics or quantum mechanics allow to derive the equations of motion of each individual particle. However, in reality one is often faced with systems containing an amount of particles in the order of the Avogadro constant, i.e. $N_A \approx 10^{23}$ particles. In these cases, it is neither possible nor fruitful to consider each particle individually. If the particles are able to interact with each other, they will undergo random scattering processes, blurring their initial information. Given sufficient time, the system will reach a thermodynamic

equilibrium which is characterized by a maximized entropy [72]. In equilibrium, the system may be fully described by global quantities, such as temperature, which effectively average over the microscopic degrees of freedom.

The properties of a system in thermodynamic equilibrium can be expressed in terms of a partition function, which is a function of certain state variables, e.g. the temperature T . Other thermodynamic quantities can be expressed as derivatives of the partition function. The partition function is calculated with respect to a certain statistical ensemble, each of which might be appropriate for the system under study. Often, three distinct ensembles are considered. The micro canonical ensemble corresponds to an isolated system in which the volume, the number of particles, and the energy are conserved exactly. The canonical ensemble corresponds to a closed system where again the volume and the number of particles is conserved, but the system is in contact and in equilibrium with a surrounding heat bath, and thus the energy can change. Finally, the grand-canonical ensemble corresponds to an open system where in addition to the energy also the number of particles can change. In this case, each particle species is given a chemical potential μ_i , which corresponds to the energy needed to add one additional particle to the system [73].

The probability to find the system in a certain microstate with the energy E is proportional to the Boltzmann factor $\exp\left(-\frac{E}{k_B T}\right)$ where k_B is the Boltzmann constant, which relates the temperature T and the energy E [72]. In the statistical picture, the partition function can easily be understood as the normalization constant of the Boltzmann distribution. Naturally, the sum over the probabilities of all possible microstates must equal unity.

The idea to describe the particle production in hadronic collisions using statistical methods grew very early and dates back to Hagedorn who tried to model the data from the Proton Synchrotron at CERN in the early 1960s [74]. In the statistical hadronization model (SHM), the matter is described as an ideal gas of hadrons and resonances (HRG), which is assumed to be in thermal and chemical equilibrium [75]. Thermal models have been found to be very successful in describing such data [76–78].

The success of a thermal treatment of hadronic collisions might seem surprising, considering the fundamental assumption discussed earlier. In a macroscopic system, the number of particles is virtually infinite. On the contrary, the number of particles might be in the order of a few thousand in a central heavy-ion

collision like lead-lead (Pb–Pb), while in a proton-proton collision this number might be as small as 10 or less per unit in rapidity [79]. In such a small system, one may doubt if the system is able to reach thermal equilibrium or if one can even speak about a temperature. However, apparently at least partial equilibrium can be reached, which reflects in the fact that the thermal description produces useful results [80].

The aforementioned statistical hadronization model treats the system as a grand-canonical ensemble where the charges are only conserved on average. This might not be appropriate if the number of particles carrying a certain conserved charge is small, which gives rise to the canonical statistical hadronization model (CSM) [80, 81]. In the CSM, the quantum numbers of interest, i.e. electrical charge, baryon number, and strangeness are conserved exactly within a certain correlation volume V_c . It is well possible to treat only selected charges canonically and preserve the grand-canonical treatment for the others.

The exact conservation of charges drives the so-called canonical suppression in small systems, which lowers the yields of particles carrying those charges. In the minimal version of the CSM which was applied to LHC data, referred to as vanilla CSM, it is assumed that both chemical and thermal equilibrium are reached and that the temperature at the chemical freeze-out is 155 MeV independent of the multiplicity [80]. The description of particle ratios by the vanilla CSM as a function of the multiplicity is only reasonable, but it completely fails in the ϕ/π ratio where it predicts the opposite trend as observed in data [80]. It is worth to note that the ϕ meson is a particularly sensitive probe; since it is neutral in all three charges and feed-down from charged particles is absent, it is not affected by canonical effects. The observed discrepancy can be cured by two modifications to the aforementioned model. Firstly, a multiplicity dependence of the temperature is introduced. It is found that smaller systems have a higher temperature at freeze-out, which is related to the shorter lifetime of small systems. Secondly, the so-called strangeness (under-)saturation factor γ_s is introduced, which incorporates the possible incomplete equilibration of strangeness at the chemical freeze-out. The model employing these modifications is therefore referred to as the γ_s CSM model [80].

The strangeness saturation factor is also multiplicity dependent. It affects strange quarks and anti-quarks in a likewise fashion and is thus capable of explaining the observed suppression of the ϕ meson at low multiplicities. The

multiplicity dependence of the temperature and γ_s is obtained by fitting to data, i.e. pp, p-Pb, and Pb-Pb collisions.

The results of the γ_s CSM model will be compared to the data measured in this thesis in section 4.5.

Transverse momentum spectra

The models discussed before can provide integrated yields of particles, given the medium properties. Often, one is also interested in their distribution in phase space. This is of particular relevance, as it contains both thermal and bulk properties of the expanding medium. In particular, the comparison of transverse-momentum (p_T) spectra in several collision systems can provide insight to collective effects. Furthermore, particles can often only be measured in certain regions of the phase space and appropriate extrapolations are required to obtain the integrated yields. Such relations can be derived using again a statistical approach. As discussed, the probability of finding a particle in a state with the energy E is given by the Boltzmann factor. The energy of a particle depends on its momentum p and its rest mass m . Conveniently, the transverse mass $m_T = \sqrt{m^2 + p_T^2}$ can be introduced, which allows to write the energy as $E = m_T \cosh(y)$, where y is the rapidity. With this, one finds for the p_T differential yield [82, 83]

$$\frac{dN}{dp_T} \propto p_T m_T \int_{y_{\min}}^{y_{\max}} dy \cosh(y) \times \left[\exp \left(\frac{m_T \cosh(y) - \mu}{T} \right) + S \right]^{-1} \quad (1.1)$$

where T is the temperature and μ is the chemical potential. The factor S is 0 for the Maxwell-Boltzmann, 1 for the Fermi-Dirac and -1 for the Bose-Einstein statistics [82]. The Maxwell-Boltzmann statistics is appropriate at sufficiently large temperatures. At lower temperatures, the Fermi-Dirac or Bose-Einstein statistics may be used, depending on the spin of the involved hadrons. At LHC energies, the baryo-chemical potential μ_B is close to zero. Integrating over the rapidity, one obtains the modified Bessel function K_1 . One may also note that $\cosh(y) \approx 1$ for $y \ll 1$, which gives rise to a simple m_T scaling in the vicinity of mid-rapidity ($y = 0$). At very high momenta, the m_T scaling converges to a p_T scaling, since $m_T \approx p_T$ for $p_T \gg m$.

The aforementioned equations hold true for a stationary thermal source without

resonances. In the experiments, sizeable disagreement from such a scenario has been found, which has led to the development of more sophisticated models. Generally, when a system transitions from a deconfined to a confined state, two distinct so-called freeze-outs occur. The first one is the chemical freeze-out at which all inelastic reactions cease and the chemical composition is fixed. One may note that decays can still occur after this point and alter the particle composition. The second is the kinetic freeze-out at which also the elastic interactions cease and the particles' momenta are fixed. Evidently, these two freeze-outs can occur at different times. This allows the system to continue a hydrodynamical evolution after the chemical freeze-out, which is imprinted on the spectra as radial flow. The Boltzmann-Gibbs Blast-Wave (BGBW) model [84, 85] mimics this behavior by assuming a thermal source in local thermal equilibrium, flowing outwards with a radius-dependent velocity profile $\beta(r)$. Particularly in small systems like pp collisions, another modification is required. For this, one has to recall that the number of particles in a hadronic collision is much smaller than the Avogadro number and that long-range correlations are present, which leads to a non-extensivity of the entropy. A generalization of the entropy was brought forward by Tsallis in 1988, which introduces an additional free parameter q to the standard Boltzmann-Gibbs entropy to account for the amount of non-extensivity [86]. The parameter is related to the temperature variance of the system. The corresponding entropy is the Tsallis-entropy S_q , which is given by $S_q = -k \sum_i p_i^q \ln_q(p_i)$. It converges to the well known Boltzmann-Gibbs entropy for $q = 1$. Using this entropy, the so-called Lévy-Tsallis distribution can be derived, which is well suited to describe the transverse momentum spectra in pp collisions as demonstrated in Ref. [87–90]. One finds [91, 92]

$$\frac{dN}{dp_T} \propto p_T m_T \int_{y_{\min}}^{y_{\max}} dy \cosh(y) \times \left[1 + (q-1) \frac{m_T \cosh(y) - \mu}{T} \right]^{q/(q-1)} \quad (1.2)$$

which converges³ to Eq. (1.1) for $q = 1$.

A combination with the blast wave approach is also present which is known as the Tsallis Blast-Wave (TBW) model [93].

³One may note that $\lim_{q \rightarrow 1} (1 + (q-1) \cdot x)^{q/(1-q)} = e^{-x}$.

1.2.2 Monte Carlo generators

While thermal model calculations are very successful, the statistical nature of these models only allows to make statements about the average production of particles. The same holds for their distribution in the phase space.

To study hadronic collisions on an event-by-event basis, so-called event generators have been developed which generate collisions fully differentially in all relevant quantities. Since the processes are random in nature, event generators employ Monte Carlo (MC) methods [94] based on pseudo-random numbers to sample the underlying processes. As already elaborated, the processes which are resident in the QCD cannot be solved analytically and thus, event generators rely on effective or phenomenological models and the separation of perturbative and non-perturbative scales.

Common generators employing these principles are PYTHIA [62, 95] and EPOS [63, 96–99], which will be compared to data in section 4.6. One may note that these models are very sophisticated and a complete introduction is therefore far beyond the scope of this thesis. Nonetheless, a brief yet comprehensive overview shall be given in this section, mostly based on the extensive elaboration of the PYTHIA collaboration given in Ref. [62].

Roughly, one can divide the collision of high-energy particles into two domains, a perturbative and a non-perturbative. While the perturbative part can be calculated rigorously from first principles, the non-perturbative one relies on phenomenological approximations, which require numerous input parameters that need to be tuned to data [62].

The two domains are connected by the concept of factorization, which builds on separating the non-perturbative physics of the incident nucleons from the perturbative physics of the parton scattering at the so-called factorization scale, which corresponds to the spatial resolution at which the nucleons are probed, determined by the momentum transfer [62]. Then, the cross section of the nucleon–nucleon (N–N) scattering is given by a convolution of the parton distribution functions (PDFs) of the nucleons and the cross sections of the elementary parton–parton scatterings.

The PDFs thereby correspond to the longitudinal momentum distributions of the partons within the nucleons [100]. At low energies, essentially the three valence quarks are visible, while at high energy the true quantum-mechanical

nature of the nucleons becomes apparent by the emergence of numerous virtual sea quarks. It may also be noted that the PDFs cannot be computed theoretically, but must be determined experimentally [39, 40].

The differential cross section of the hard scattering of two partons into a final state is proportional to the square of the corresponding matrix element. Since the momentum transfer is large, α_s is small and thus, the matrix element can be calculated perturbatively as discussed in section 1.1.1.

A finite number of processes is implemented to determine the partonic cross section. PYTHIA 8 for instance considers $2 \rightarrow 2$ and $2 \rightarrow 3$ processes of light quarks and gluons, the $2 \rightarrow 2$ production of heavy quarks as well as electroweak processes like the production of prompt or virtual photons, the production of weak gauge bosons and parton-photon or photon-photon collisions. Additionally, also top quarks and Higgs bosons may be produced [62].

The physical truth is in fact more complex as the produced hadrons will themselves radiate partons and photons in a cascade-like topology called shower. Nonetheless, event generators are still capable of reproducing many physical processes very well. As the particles become increasingly soft, a complete perturbative description is often not possible. Instead, numerous implementations exist to simulate the ongoing processes by introducing probabilities of particle emissions. The resulting amount of outgoing partons is numerous and can be of the order of 100 in a single proton-proton collision [62]. At the cut-off scale, the partons are finally subject to hadronization.

Hadronization is the formation of color-neutral hadrons from deconfined partons. This is the natural consequence of the evolution of a system which expands and cools down and thereby transitions from the regime of asymptotic freedom back to the regime of confinement. As discussed, there is no exact theoretical description for the process of hadronization. However, phenomenological models are employed successfully, typically based on string or cluster hadronization [101, 102]. Both PYTHIA and EPOS event generators use the Lund model [101], which is based on string fragmentation and will be discussed in the following.

In the Lund model, each color dipole is treated as a string. As the quarks move apart, energy is transferred to the string, increasing its tension. Hadrons are produced by the consecutive breaking of the strings as touched in section 1.1.1. The strings break until the energy is consumed and the remaining string frag-

ments are identified as hadrons. The breaking of the strings occurs by the emergence of virtual quark–anti-quark pairs. Due to the conservation of energy, massive quarks are thereby produced off-shell and need to absorb energy from the string to become on-shell. The quark pair produced at a common vertex therefore needs to tunnel a distance given by the mass divided by the string tension. The tunneling probability leads to a suppression of strange quarks and the non-occurrence of heavy-quark string breaks [62].

The pure quark–anti-quark string break produces ground-state mesons only. In fact, the majority of produced particles in ultrarelativistic hadronic collisions are mesons. However, a satisfactory description requires a method of baryonization, i.e. the creation of baryons, which is not obvious in the string-breaking picture. Therefore, double string breaks are allowed, which produce a diquark–anti-diquark pair simultaneously, allowing the formation of baryons. Due to the double mass, this process is also suppressed by the tunneling probability.

Since the diquark mechanism leads to highly correlated baryon–anti-baryon pairs, further string breaks and thus meson production is allowed in between the diquark pairs, which is referred to as the popcorn mechanism [103]. In PYTHIA, currently only one intermediate meson is allowed [62].

One may note that in all previously discussed processes, the concept of color has not yet been touched. In fact, the assignment and flow of colors is typically treated in a simplified way by considering the limit of infinite colors, the so-called leading color (LC) approximation [62]. This means that a color singlet created in a hard scattering is unique and can be traced through the full evolution of the system, i.e. every color dipole created in the initial state results in a string fragment. This means that quark–anti-quark pairs, which do not belong to the same color singlet, so-called LC-unconnected pairs, are unable to form a meson even if they were close in phase space. This is, however, unphysical as quarks can change color by the exchange of gluons. In the LC picture this is handled by the so-called color reconnection (CR) mechanism, which models this behavior [62]. Experimentally, the effect of the color reconnection can be seen for instance in the production yield of J/ψ , which can only be described by PYTHIA when color reconnection is enabled [104].

Most of the produced hadrons are unstable and decay into other particles. The decays are also simulated using the known lifetimes and decay channels listed

by the particle data group (PDG) [9]. The non-trivial phase space distribution of the daughters is thereby handled by specialized tools [105].

The final output is simply a list of particles containing their identity, position, momentum, as well as their production history. This can be used directly or be fed into other algorithms to simulate the interactions of the produced particles with matter or detectors. This will be elaborated in section 4.2.

1.3 Particle interactions

The previous sections introduced the quarks and gluons as the carriers of the color charge and QCD as the fundamental theory of the strong interaction between them. This section shall now focus on the interactions among baryons. In particular, the p - Σ^+ system will be discussed as this is the system under study in this thesis.

In the following, the theoretical as well as the experimental perspective of the study of the interactions between baryons will be briefly reviewed. Subsequently, the implications for neutron stars will be discussed and the method of femtoscopy will be introduced.

1.3.1 Theoretical treatment

From the viewpoint of the strong force, all quarks are equal, implying an exact flavor symmetry. However, since the quarks have different masses, the symmetry is broken. For the three lightest quarks, however, the symmetry is approximately fulfilled, which is mathematically formulated in terms of the special unitary (SU) group. The $J^P = 1/2^+$ baryons can be organized in an octet, which is a representation of the underlying SU(3) group [29]. Since the theory is not exact, the eight baryons have similar, but different masses [9].

Similarly, group theory is used to construct pairs of baryons to study their interactions. If one expresses the baryon octet in a matrix representation, all combinations of two of those octets can be constructed by their Kronecker product [106]. The resulting combinations can be decomposed into six multiplets, which are so-called irreducible representations (irreps). One finds [106, 107]

$$8 \otimes 8 = 27 \oplus 10 \oplus \overline{10} \oplus 8_a \oplus 8_s \oplus 1. \quad (1.3)$$

The 27-plet, the singlet and one of the octets are symmetric, while the others are antisymmetric. The symmetry properties restrict the allowed partial waves due to the Pauli principle, which requires the total wave function to be antisymmetric. One can consider the irreps as base vectors of a six-dimensional abstract vector space, such that any two-particle wave function (of baryons from the octet) can be written in terms of a linear combination of the wave functions of the given multiplets [107]. Depending on the quantum numbers of

the pair, certain multiplets contribute to their interaction.

The decomposition into the multiplets is practical as it allows to relate the interactions between the octet baryons to one another within the limits of the SU(3) flavor symmetry. A good example is the $p\text{--}\Sigma^+$ system, which is a pure isospin $I = 3/2$ state. Using the above mentioned space-spin symmetry properties, this implies that in the S-wave, the triplet state is only represented by the 10-plet and the singlet by the 27-plet [20]. The latter, the 27-plet, is related to the well known N–N interaction, which also resides in the 27-plet for $I = 1$. The arrangement of the aforementioned multiplets is listed in Tab. 1.1 for systems with strangeness content 0 and -1.

If the SU(3) flavor symmetry was exact, both interactions of the 27-plet would be identical. Even though there is sizeable symmetry breaking [21], one can still make use of the relation to constrain the less-known N– Σ interaction, as explained in section 1.3.2. If sufficient data is available, a comparison of the 27-plet contributions from the N–N and N– Σ systems can shed light on the exact strength of the symmetry breaking.

channel			spin-parity	
baryon pair	strangeness	isospin	singlet-even/triplet-odd	triplet-even/singlet-odd
N–N	0	0	-	$(\overline{10})$
N–N	0	1	(27)	-
N– Λ	1	1/2	$\frac{1}{\sqrt{10}}[(8_s) + 3(27)]$	$\frac{1}{\sqrt{2}}[-(8_a) + (\overline{10})]$
N– Σ	1	1/2	$\frac{1}{\sqrt{10}}[3(8_s) - (27)]$	$\frac{1}{\sqrt{2}}[(8_a) + (\overline{10})]$
N– Σ	1	3/2	(27)	(10)

Table 1.1: Association of the multiplets (Eq. (1.3)) to the baryon–baryon channels with strangeness content 0 and -1. The multiplets are written in brackets to distinguish them from the prefactors. The normalization factors arise from the fact that the multiplets are base vectors and are thus added quadratically. Singlet channels have spin $s = 0$ and triplet channels $s = 1$. The parity is given by $(-1)^L$ with L being the angular momentum. It is 1 for even and -1 for odd values of L . Relations taken from Ref. [20].

The interactions between baryons are fundamentally described by the theory of QCD. Their properties can, however, not be derived from QCD directly due to the challenges discussed in section 1.1.1, but it can be approached with the methods discussed there. The two general approaches either rely on numerical

simulations performed on a discrete lattice [47], or on effective theories [45, 46], which can be solved perturbatively.

Lattice simulations are a valuable tool, but still struggle with physical quark masses, as this is computationally costly. However, unphysical quark masses are an issue, particularly in the nucleon sector [108]. This has led to a certain mismatch between theory and experiment where heavy systems like $\Xi - \Xi$ can be accessed through the lattice, but not experimentally, and vice versa for light systems. However, with ongoing advances in the computational performance, lattice simulations will at some point be capable to describe also the N–N sector with good precision.

Apart from this, effective theories reduce the degrees of freedom in order to allow perturbative calculations. This can be accomplished by introducing massive mediators as degrees of freedom. It is worth to note that this concept was already introduced in 1935 by Hideki Yukawa [109], decades before the quark model was established [29]. From the range of the interaction among nucleons, he concluded that the mediator particles had to be roughly 200 times heavier than the electron. Only later this particle was understood as the pion. Consequently, the interaction between nucleons can be interpreted as the exchange of a quark–anti-quark pair from the sea-quarks.

Meanwhile, very sophisticated models have been developed with numerous parameters, including several different mesons. The different approaches differ mainly in the treatment of the short-range part of the interaction. In the so-called meson-exchange models, this is described by the exchange of heavy mesons. This concept is adopted by various models from Jülich and Nijmegen, e.g. Jülich04 [110] and the Nijmegen soft-core models (NSC), e.g. NSC97f [111]. Furthermore, the Nijmegen extended soft-core models (ESC) [112], e.g.

ESC16 [113], additionally employ the exchange of gluonic mediators, so-called pomerons, to introduce repulsion.

On the other hand, the so-called constituent quark models (e.g. FSS [114] and its successor fss2 [115, 116]) handle the short-range part of the interaction by explicitly taking into account the colors of the quarks and their anti-symmetrization. This is a major difference, as the other effective models completely neglect the quark degrees of freedom, considering only the composite hadrons. Due to the Pauli principle, a rather strong repulsion naturally emerges in the triplet channel of the N– Σ ($I = 3/2$) system [115, 116], which is strongest among the

models considered in this thesis (see Tab. 1.2).

Finally, chiral effective field theory (χ EFT) approaches the perturbative expansion systematically by a power counting scheme [117, 118], which allows to evaluate the calculation at the desired order and thus precision [119, 120]. There, the short-range interaction is included by contact terms, containing so-called low-energy constants (LECs), which need to be fitted to data. Results of this approach are available up to next-to-next-to-leading order (N^2 LO) [121]. In this thesis, the calculations at NLO will be used to compare with, notably NLO19 [122], as it was also compared to the latest scattering data (see Fig. 1.5). A chiral calculation, which simulates the behavior of the constituent quark model fss2 and reproduces its scattering parameters quite closely, is also available under the name NLO(sim) [123]. Concerning the chiral effective field theory calculations, one may note that in the original version of NLO19, a very slow convergence of the correlation function to unity was observed. Even above 300 MeV/ c in k^* , a region where the normalization of the data is typically performed, the theoretical correlation function differed considerably from unity. A careful investigation found that the slow convergence was caused by a non-local momentum cut-off that was used in the meson exchange. In this regard, “non-local” means that the potential in the momentum space does not only depend on the relative momentum of the particles in the initial and the final state, but also on the individual momenta. Translated into the position space by a Fourier transform, the potential does then not only depend on the distance between the particles. In the chiral expansion this is the case for the contact terms. A more recent calculation which uses a semi-local momentum space (SMS) regularization [121, 124] does not exhibit this behavior and converges as expected. To allow for a comparison, the model parameters were tuned to reproduce the scattering parameters of NLO19⁴ [125]. This version of the calculation will be referred to as “SMS NLO (NLO19)” in the following, while for the original model “NLO19” will be used. For NLO(sim), the SMS version will be referred to as “SMS NLO(sim)”.

It must be noted that meanwhile also results from the lattice are available in the Y-N sector. While these results look promising, the used pion masses

⁴It must be noted that the SMS NLO model [121, 124] is an independent fit to the available data and was only retuned to reproduce the S-wave scattering parameters of NLO19 [122]. The behavior at higher momenta also depends on the higher partial waves, which differ significantly. For a comparison see Ref. [121].

are still unphysical and there are still sizeable uncertainties, resulting in a discrepancy of the obtained phase shifts and potential depths compared to other models [126, 127].

While all of the above approaches generally describe the N–N and Y–N interactions reasonably well, there are of course differences, mainly related to the different treatment of the short-range interactions. One may also note that all models have free parameters that need to be fitted to data. Thus, later models could already profit from the growing body of experimental data. Tab. 1.2 is a non-exhaustive list of model calculations, comprising the scattering parameters of the p – Σ^+ interaction as well as the year the model was published, which can be compared to those of the p – Σ^+ scattering experiments, particularly E251 [128], E289 [129] and E40 [20], which will be discussed in section 1.3.2.

Model	Nagels73	NSC97f	fss2	Jülich04	ESC16	NLO19	NLO(sim)
Ref.	[130]	[111, 131]	[115, 116]	[110]	[113, 123]	[122]	[123]
Year	1973	1997	2001	2004	2016	2019	2021
a_s (fm)	-2.42	-4.35	-2.28	-3.60	-4.30	-3.62	-2.39
r_s (fm)	3.41	3.16	4.68	3.24	3.25	3.50	4.61
a_t (fm)	0.71	-0.25	0.83	0.31	0.57	0.47	0.80
r_t (fm)	-0.78	28.9	-1.52	-12.20	-3.11	-5.77	-1.25

Table 1.2: Scattering parameters of the p – Σ^+ interaction from selected models, sorted by the year of the first publication. It must be noted that in some models the values were updated later, in which case the latest values are given in the table. For fss2, the given values are from 2007. For NSC97f and Jülich04 the effective ranges were reevaluated with updated particle masses and published in a different reference [122]. In the table the updated values are given. Uncertainties are only given for the singlet of Nagels73 and are quoted as 0.3 fm for both the scattering length and the effective range.

Looking at the singlet, one may note that all models predict an attractive interaction in this channel. As discussed, this channel is related to the N–N and the N– Λ interactions via the 27-plet and is thus much better constrained than the triplet. Still, one can see that even the singlet scattering lengths show quite some divergence, ranging from -2.28 fm (fss2) to -4.35 fm (NSC97f), thus differing by almost a factor of 2. Here, one has to keep in mind that the relation through the irreps is only valid assuming a perfectly fulfilled SU(3) flavor symmetry, which is, however, not the case, as there is a sizeable symmetry breaking

also in the S-wave of $p\text{-}\Sigma^+$ [21]. Moreover, fitting the model parameters to the scattering cross sections constrains singlet and triplet at the same time. In case of the singlet scattering length being around -4 fm, the cross sections are essentially saturated [123], leaving little room for the triplet contribution, which then takes values around 0.5 fm or less. In contrast, if one has more repulsion in the triplet, the singlet scattering length is significantly smaller, being around -2 fm. Most strikingly, the NSC97f model predicts, in contrast to all other models, attraction also in the triplet channel. This scenario is generally disfavored by experimental observations, which will be discussed in the following section. One may also note that the shallowness of the interaction leads to the artefact of very large effective ranges, making the underlying effective range expansion [132] less useful. This will be detailed in section 1.4.2.

1.3.2 Experimental studies

Experimentally, the interactions among baryons can be studied either by spectroscopy of bound states or by scattering experiments, both of which will be discussed in the following.

While nucleons are readily available, hyperons have to be produced within the experiment first. The short lifetimes of the hyperons complicate the measurements. Generally, hyperons can either be produced in the hadronization of hadronic collisions as already discussed or alternatively in so-called strangeness exchange reactions. In such reactions, a secondary kaon beam is impinged on a solid target, eventually producing a hyperon and an outgoing pion⁵ [133]. The produced hyperon can then either scatter off, or be captured by, a surrounding nucleus, which can then be studied.

Bound states

Nuclei are bound states of nucleons, while hypernuclei additionally contain one or more hyperons. Spectroscopy of (hyper)nuclei can provide valuable information about the interactions among the constituents. It must be noted that the only established di-baryon is the well known deuteron, which, however, does not have excited states due to its low binding energy [134]. Therefore, all nuclei are many-body systems, incorporating both two- and many-body interactions,

⁵Alternatively a pion beam can be used, producing a hyperon and an outgoing kaon [128].

which need to be considered. The importance of this aspect will be discussed further in section 1.3.3 in the light of the neutron star hyperon puzzle.

The body of Λ hypernuclei data is incredibly rich [17], ranging from the hypertriton [135], an extremely loosely bound state of a proton, a neutron, and a Λ , to $^{208}_{\Lambda}\text{Pb}$, a lead nucleus containing a Λ . From this data, the N - Λ single particle potential can be extracted, which amounts to around -30 MeV [136, 137]. In the Σ sector, the situation is totally different due to the possibility of conversions of Σ to Λ hyperons within the nuclei. Therefore, hypernuclei with Σ hyperons are, if existent, only quasi-bound states, resulting in additional experimental challenges in identifying them [138].

To the present day, only one Σ hypernucleus, $^4_{\Sigma}\text{He}$, is found. This state was already reported in 1989 [139]. In this experiment, K^- produced in a primary target were stopped in a liquid ^4He target and the outgoing pions were measured. A bump is visible in the pion spectrum roughly 3 MeV below the Σ^+ threshold. The bump only appears in the (K^-, π^-) reaction and is absent in the (K^-, π^+) reaction. This was interpreted as an isospin dependence of the N - Σ potential [139]. The (K^-, π^-) reaction produces both 1/2 and 3/2 isospin states, while (K^-, π^+) only populates 3/2. This suggests that the observed state had an isospin of 1/2. These results were challenged since the stopped kaon reaction has several background contributions in the region of the bump, making it difficult to draw definite conclusions. This was clarified in 1998 by the E905 experiment at BNL [140]. There, the same reaction channels were used, but instead of stopped kaons, the in-flight reaction was used with a kaon momentum of 600 MeV/ c , which is much simpler, both experimentally and theoretically. The same isospin dependence was observed, with a clear peak below the threshold in the (K^-, π^-) channel, indicating a binding energy of roughly 4 MeV [140]. These findings are consistent with an earlier theoretical prediction [141]. It was suggested that the N - Σ potential had an isoscalar, i.e. isospin-independent contribution, which was repulsive, and an isovector contribution, which was attractive in the isospin 1/2 channel and repulsive in the 3/2 channel. The isovector contribution is suppressed by the mass number, such that the repulsive isoscalar contribution dominates in larger, isospin saturated systems. This could explain why heavier Σ hypernuclei are experimentally not observed [142]. In fact, the spectral shape was probed in the (π^-, K^+) reaction on heavier targets, revealing the repulsive nature of the interaction between Σ

baryons and nuclei [143].

Negatively charged hadrons can be electromagnetically bound to nuclei, forming so-called hadronic atoms. This is also possible for the Σ^- , providing an additional opportunity to study the interaction of Σ baryons with nucleons [144, 145]. When captured in a high atomic orbit, the Σ^- will transition to lower orbits under the emission of X-rays, which can be measured. The lower energy levels are modified by the strong interaction due to the considerable overlap of the orbits with the nucleus. One may, however, note that mainly the low-density surface of the nuclei is probed and a model-dependent extrapolation is required to obtain the values at nuclear saturation density [146]. Results from heavy Σ^- atoms like Pb point towards a repulsive N- Σ potential [147, 148], in line with the aforementioned findings from hypernuclei.

Scattering

The scattering of particles is a very direct method of investigating the interaction between the scattered particles. Conceptually, scattering differs from the study of nuclei by probing the two-body interaction in vacuum, while in nuclei many-body interactions are present and particles are probed at the nuclear saturation density. By polarizing the incident particles, the spin dependence of the interaction can be studied. Experimentally, the accessible quantity is the cross section, differentially in the scattering angle and the energy or momentum.

Theoretically, the scattering can be approached by decomposing the scattering amplitude with respect to the angular momentum in a partial-wave analysis, allowing to relate the measured differential cross sections to the phase shifts. From the data, the scattering parameters can eventually be computed, yielding precise information about the interaction.

To perform scattering, it is typically necessary to prepare a beam and a target of the particles under study. For nucleons as constituents of normal matter, this is easily possible. Thus, a large body of data is available of N-N scattering, comprising several thousand data points⁶, both polarized and unpolarized, contributing to a profound knowledge of the N-N interaction. In terms of the SU(3) flavor symmetry, however, the N-N interaction only allows to access the

⁶For an overview one can refer to several publicly available data bases, for instance NN-Online [149] or SAID [150]. The latter currently lists roughly 37000 data points of elastic N-N scattering.

27-plet as well as one of the decuplets ($\overline{10}$) (compare Eq. (1.3)). Thus, it is unavoidable to extend the experimental studies to the strangeness sector to complete the picture.

In the hyperon sector, the experimental situation is much more challenging. Since hyperons have rather short lifetimes with decay lengths ($c\tau$) no larger than 7.9 cm (Λ) [9], it is impossible to build a target or even a beam out of those particles. Nonetheless, hyperon–nucleon (Y – N) scattering is feasible and several experiments have been performed [20, 128, 129, 151–155]. These experiments rely on the in-flight production of the hyperon in a strangeness exchange reaction using either a kaon or pion beam and a proton target. The produced hyperons eventually scatter within the production target, decay, and their decay products are subsequently measured.

The results on the p – Σ^+ scattering will be discussed in the following in greater detail, as it is the system under study in this thesis. The challenges for p – Σ^+ scattering measurements are large, and thus, the available data is scarce and has sizeable uncertainty [20, 128, 129, 154, 155], which underlines the importance of further measurements.

The first measurement of the p – Σ^+ cross section was performed very early at the CERN Proton Synchrotron in 1971 [154, 155]. In this experiment, the Saclay Hydrogen Bubble Chamber was exposed to a K^- beam, which was stopped inside of the chamber. The experiment was not dedicated for the scattering analysis, but it was intended to study rare decay channels of the produced hyperons. A reanalysis of the images, however, found 283 elastic scatterings of Σ^+ and even 1521 elastic scatterings of Σ^- , which allowed to report the first experimental N – Σ scattering cross sections [154, 155]. The kinematic range of available Σ momenta was very narrow. This is due the fact that the kaons were very low in momentum, such that the production of the Σ baryons essentially occurred at rest. In this case, momentum conservation implies a momentum of the Σ of 180 MeV/ c [154, 155]. Towards lower momenta the particle trajectories become increasingly short, imposing a limit of roughly 100 MeV/ c to be measurable. Since the statistics decreased towards low momenta, the first measured bin starts at 140 MeV/ c in the p – Σ^+ channel, resulting in a total of 4 bins for this channel. Even though the uncertainties are sizeable towards low momenta, they are still compatible or even superior to later measurements and additionally the kinematic region is unique, which explains why this data

is still used for model comparisons today [122].

In the 1990s two closely related experiments were conducted at the KEK facility, namely E251 [128] and E289 [129] where E251 was the pilot experiment for E289. In contrast to the bubble chamber experiment, these experiments were dedicated to study Y - N scattering. E251 only analyzed the p - Σ^+ channel, while E289 also considered the p - Σ^- and p - Λ channels. The setup differed significantly from the bubble chamber experiment. First of all, the hyperons were produced in the associate production using a pion beam. The outgoing kaon was measured in a dedicated spectrometer. From the momenta of the pion and the kaon, the momentum of the Σ could be calculated accurately. Furthermore, an active target consisting of scintillating fibers was used, which served as the production target, scattering target, and detection system at the same time. The active target allowed to image the scattering processes in a similar fashion as a bubble chamber. The major drawback was that the scintillating material contained carbon atoms in addition to hydrogen atoms, which naturally posed a major source of background. The accessible momentum region of the Σ^+ was 300 to 600 MeV/ c in E251 and 350 to 750 MeV/ c in E289.

Despite the promising and dedicated setup, the accumulated statistics in the p - Σ^+ channel was disappointingly low, with only 11 identified scatterings recorded by E251 and 31 by E289. Consequently, only 2(4) data points of the angle differential cross section could be measured by E251(E289) and the uncertainties are huge, making it almost impossible to draw any quantitative conclusions from this data [128, 129].

The situation did not change until recently, with the E40 experiment [20] at J-PARC. The E40 experiment was dedicated for Σ - p , investigating the Σ^+ - p and Σ^- - p channels. The experimental setup comprised several concepts of the previous experiments. Again, a pion beam was used and the outgoing kaon was measured in a dedicated spectrometer arm, allowing the computation of the properties of the produced Σ . In contrast, however, a liquid hydrogen target was used, which is free of carbon contamination. To measure the outgoing particles, the target was enveloped by several detectors, which allowed to track and identify both the scattered protons and the decay daughters of the Σ . The scatterings could thereby be identified by a kinematic consistency check. The overall kinematics is complicated and will not be discussed in detail here. How-

ever, it is worth to note that even though the scattering cannot be imaged directly, the system allowed to suppress background events by more than 90%, while preserving a selection efficiency above 50%. This way, it was possible to collect roughly 2400 $\Sigma^+ - p$ scatterings within a Σ^+ momentum region of 440 to 800 MeV/c, embodying the by far largest data set on this reaction [20]. The differential cross section could be measured in three momentum slices, providing a total of 41 data points with small uncertainties. It should be pointed out that the momentum range overlaps with the previous experiments, allowing a direct comparison. The data of E40, E289 and E251 is shown in Fig. 1.5 together with model predictions.

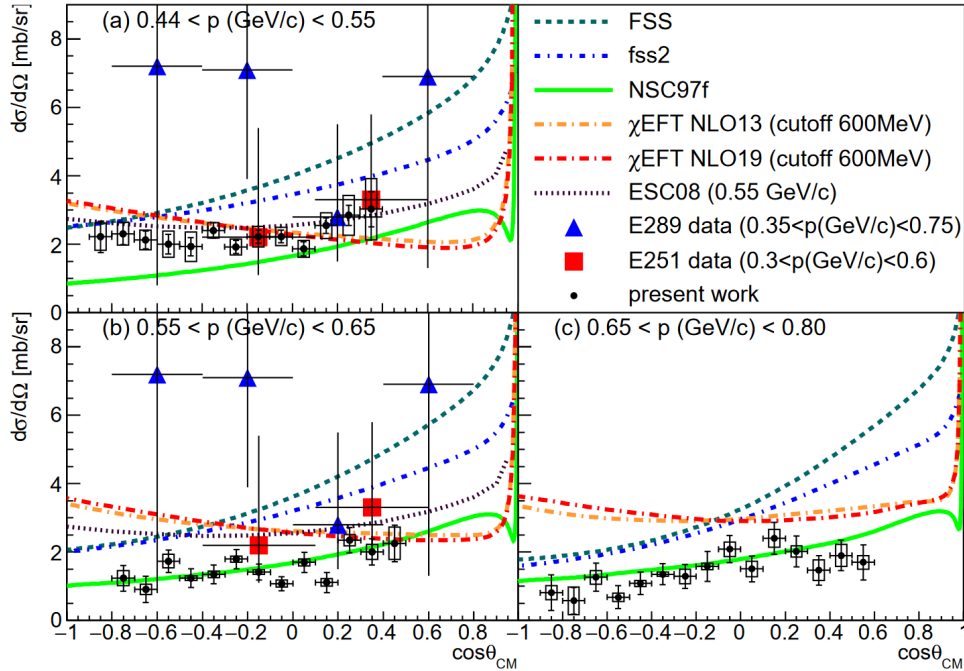


Figure 1.5: Cross sections of $p - \Sigma^+$ scattering measured by the E40 [20] (black markers), E251 [128] (red markers) and E289 [129] (blue markers) experiments. Clearly, the E40 data is most constraining due to the smaller uncertainties. The observed cross sections are much smaller than predicted by most models, particularly FSS [114] and fss2 [115, 116]. In general, NSC97f [111, 131] describes the cross sections best, which will be discussed later in this section. Figure from Ref. [20].

It can be seen that the data points of E40 and E251 are in good agreement. The data from E289, however, shows sizeable disagreement in all but one of the four data points, even though they are still compatible within the given uncertainties. The data has been compared to several models using different

approaches, the quark models FSS [114] and fss2 [115, 116], the soft-core models ESC08 [112] and NSC97f [111, 131], as well as the χ EFT models NLO13 [120] and NLO19 [122]. It can be concluded that none of the models describes the data satisfactorily well over the full considered momentum range. The two χ EFT models are very similar and overpredict the cross sections, while also missing the shape. This is related to the LECs as experimental inputs to these models being insufficiently well constrained. The quark models predict a strong repulsion due to the quark Pauli blocking, leading to an increased cross section, which is in better agreement with the E289 data, but strongly disfavored by the precise E40 data. The ESC08 model captures the data best in the lowest momentum bin, but starts to deviate significantly in the second. In contrast, the NSC97f model describes the data well in the upper two momentum bins, deviating only in the lowest.

A phase shift analysis was carried out with the E40 data, considering the first three orders in the partial-wave decomposition [20]. In order to reduce the number of free parameters, the phase shifts of the 27-plet were constrained to p-p scattering. Since the values are expected to be modified in the p- Σ^+ case, a constraint to two models, namely ESC16 and NSC97f, was used as a variation. However, it was pointed out that these models were tuned to the p-p scattering data as well, implying that these values might also not be fully correct. From the decuplet, the D-wave contributions were fixed to the models, as there is apparently rather good agreement on these parameters. Since these values are rather small, they were also fixed to 0 as a variation. Thus, the phase shifts of the S- and P-waves of the decuplet, δ_{3S_1} and δ_{1P_1} , corresponding to the short-range part of the p- Σ^+ interaction, remained as the only two fit parameters. The values of δ_{1P_1} are very sensitive to the made variations and the uncertainties are large, while the differences between the models are rather small, such that no conclusion could be drawn from this parameter. However, generally a positive value is favoured, corresponding to attraction.

In the case of δ_{3S_1} , the uncertainties are much smaller and the values are essentially insensitive to the variations. Nonetheless, there is still an ambiguity concerning the sign, which might be positive or negative, even though only one model, NSC97f, predicts the sign to be positive. The data has been found to be in agreement with NSC97f as well as ESC16, thus either supporting a moderate attraction (NSC97f) or moderate repulsion (ESC16), while disfavoring

the strong repulsion predicted by the fss2 quark model, which is in line with the comparison to the differential cross section [20]. Interestingly, the NSC97f model describes both observables very well, even though this is the only model predicting an attractive interaction in the triplet channel of the N - Σ interaction, which is disfavored by the other experimental data. From the scattering experiments, however, no conclusion can be drawn yet which would point towards either one of the soft-core models, in particular NSC97f cannot be ruled out.

The results of the E40 experiment, which have been published during the course of this thesis, constitute the most precise data on the p - Σ^+ scattering so far and are thus interesting to compare to the femtoscopic data obtained in this thesis, which will be discussed in chapter 5.

1.3.3 Neutron stars

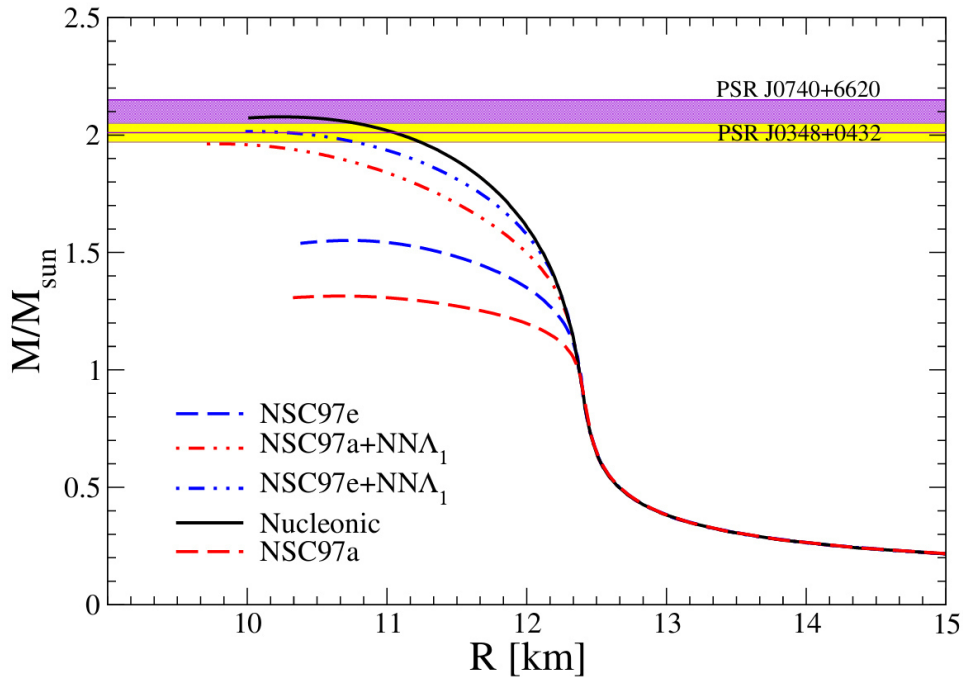


Figure 1.6: Theoretical calculations of the mass-radius relation of neutron star matter plotted with observed neutron star masses. Purely nucleonic matter is shown in black. In the presence of Λ hyperons, heavy neutron stars above 2 solar masses can only be supported when including three-body forces (dashed-dotted lines). Figure from Ref. [156].

To gain a profound knowledge about the properties of matter under extreme conditions, hadronic collisions are a key tool. However, one may also look into space. Heavy stars, and particularly their remnants, are sites where those extreme conditions naturally occur. Neutron star cores might for instance be the only place in the universe where deconfined or possibly color-superconducting matter naturally occurs [157, 158]. Also, neutron star mergers show striking similarities with heavy-ion collisions in terms of temperatures and densities, despite their completely different scales [159]. The measurement of neutron star masses and radii puts tight constraints on the equation of state of the neutron star matter and the observation of gravitational waves from merger events can also provide valuable insights [160]. Therefore, astrophysics and nuclear physics complement each other.

First of all, one may consider how a neutron star is formed [161]. It is well known that stars produce energy by nuclear fusion of hydrogen to helium in their core. Since this process requires the conversion of protons to neutrons via the weak interaction, this process is slow and takes most of the lifetime of the star. The produced helium aggregates in the core and the fusion of the hydrogen relocates to the shell around the core. Once the helium core is heavy enough, it contracts and thereby heats up and if the star is heavy enough, the helium starts fusing into carbon and oxygen forming a carbon-oxygen (CO) core. Eventually, further fusion stages are reached until finally iron and nickel is produced. At this point, the fusion ceases as no further energy can be generated.

During the nuclear fusion, the star is stabilized by the radiation pressure pushing against the contracting gravitational force. Once the fusion in the core has come to a halt, the core is only stabilized by the degenerate electron gas. The maximum mass, which can resist its gravitational self-attraction only by the degeneracy pressure of the electrons, is known as the Chandrasekhar limit and amounts to roughly 1.4 solar masses [162]. When this is exceeded, the core collapses, releasing enormous amounts of gravitational energy, resulting in a sudden, tremendous increase of the stars luminosity. Such an event is called core-collapse supernova. The shell of the star falls towards the collapsed core, leading to further compression. In the core, the protons and electrons form neutrons, producing large amounts of neutrinos, which carry away most of the gravitational energy. Incoming matter is reflected by the core and accelerated

by the neutrinos and is finally emitted into outer space. The collapsed core is eventually stabilized by the degenerate neutron gas if its mass remains below the Tolman–Oppenheimer–Volkoff (TOV) limit [163, 164]. The remnant is then a neutron star. Above the threshold, the core collapses into a black hole, making neutron stars the densest known objects without an event horizon.

Despite the name, neutron stars are not only composed of neutrons. The current knowledge about their composition and structure is mainly based on theoretical calculations, but X-ray spectroscopy and seismology are and will be used to infer information directly [165, 166]. The outer shells are rather well established. It is believed that neutron stars possess a crust composed of ions and electrons alongside neutrons, which extends over a few kilometers. Below is a Fermi liquid, mainly composed of neutrons and a few percent protons [14, 167]. The composition of the core, which exceeds the nuclear saturation density, is uncertain.

Since neutrons are fermions, they must obey the Pauli exclusion principle, which requires the neutrons at such high densities to occupy increasingly high energy levels. This gives rise to the degeneracy pressure, stabilizing the neutron star. The original calculation of the TOV limit yielded a maximum mass of only around 0.7 solar masses. Later calculations also include the repulsive contribution of the strong force between nucleons at small distances, which gives values of 2-3 solar masses [168], sufficient to support the heaviest neutron stars observed so far [169].

Due to the high occupation of energy levels, a few percent protons remain present, even though charge conservation then requires the presence of additional fermions, the electrons. The degeneracy pressure of the electrons is relaxed by the emergence of muons as carriers of the negative charges [12–14]. At even higher densities, the increasing degeneracy pressure implies that at some point, the emergence of strangeness as an additional degree of freedom becomes energetically favorable. The Λ hyperons are less than 19% heavier than the neutron [9], neutral and, most importantly, distinguishable from the neutrons and can thus occupy lower energy levels. Going further, Σ hyperons as well as Ξ hyperons might also occur. Their fraction as a function of the density depends on their respective mass and their interactions with each other and the surrounding nucleonic matter, which are not well known. Generally, however, calculations show that the presence of hyperons softens the equation of state

insomuch that neutron stars above 2 solar masses could not be supported [12] (see Fig. 1.6, black vs. dashed lines). However, such neutron stars are observed in nature (e.g. Ref. [169]), which is known as the “hyperon puzzle”. Several approaches exist to resolve this puzzle.

One is that the core of heavy neutron stars might transition into a color-superconducting quark-gluon plasma where the degrees of freedom are not anymore the nucleons, but the quarks. It might be that the deconfined phase is only present in the inner core, which would be called a hybrid star, or that it extends over the full radius, which would be called a quark star. Even though there are candidates for such objects, no definite proof of their existence is present [157, 170].

Another solution that has gained attention in the recent years is the consideration of three-body forces or, more generally, many-body forces in the calculation of the equation of state [18, 19]. The (genuine) three-body force is a force among three participating hadrons, which exceeds the trivial combination of the three two-body interactions. It has been found that the inclusion of such forces is crucial for the proper description of neutron star matter, particularly in the hyperon sector. The existence of such forces can in fact already be seen when comparing the binding potential of Λ hyperons extracted by extrapolating the binding energies of hypernuclei with the potential obtained from femtoscopy (see section 1.4) of protons and Λ s. In the hypernuclei case, a potential depth of around -30 MeV is found [136, 137], while in femtoscopy around -36 MeV is measured at nuclear saturation density [16]. This obvious discrepancy can be explained by the fact that hypernuclei are many-body systems and thus probe both two- and three-body interactions, while femtoscopy only measures the two-body contribution. This implies that the N - N - Λ interaction is repulsive and counteracts the attractive two-body interactions. In the meantime, the femtoscopic technique has been extended to the three-body sector and, given sufficient statistics, will be able to probe three-body interactions between various hadrons precisely [171]. On the theory side, the inclusion of repulsive three-body interactions can stiffen the equation of state enough to support the observed neutron star masses [18] (see Fig. 1.6, dash-dotted lines). Potentially, the density dependence of the Λ chemical potential μ_Λ is modified such that it does not anymore cross the chemical potential of the nucleons, in which case it would never be energetically favorable to produce Λ s, inhibiting their appear-

ance [19].

Heavier hyperons might still be present in neutron stars, foremost the Σ^- baryon [12–14]. As it is negatively charged, it would not only replace a neutron, but also ease the Fermi pressure of the leptons. Depending on its interaction, this could potentially lead to an even earlier appearance of Σ^- than Λ . However, considering the results presented in section 1.3.2, the N – Σ interaction is expected to be repulsive, in which case Σ baryons are unlikely to occur. While the n – Σ^- system is almost impossible to access experimentally, the p – Σ^+ system studied in this thesis can also clarify the situation, as it can yield information about the n – Σ^- channel through the isospin symmetry.

Concerning the Λ baryons, it has furthermore been brought forward that the coupling between the N – Λ and the N – Σ sector carefully needs to be considered for the overall Y – N interaction [172]. Attraction might be induced by this coupling, while the coupling could be suppressed at high densities, also pointing towards an overall repulsive interaction between nucleons and hyperons at large densities [119].

In conclusion, the hyperon “puzzle” can be fully attributed to the incomplete knowledge about the relevant interactions. Potentially, hyperons do not even appear due to repulsive interactions with the surrounding medium, such that the fundamental problem does not even arise. In this case, the neutron star would remain purely nucleonic, supporting the observed masses. This alone does, however, not rule out that a quark-gluon plasma might be present in the neutron star core. For a profound understanding, a joint effort of astronomy, high-energy experiments, and theory is required. Femtoscopy can be used to pin down the interactions between nucleons and various hyperons as well as the interactions among hyperons, both in the two- and three-body sector, to complete the picture.

1.4 Femtoscopy

Scattering of particles is a very valuable source of information on their interactions, however, concluding the discussion of the previous sections, it is challenging for short-lived particles such as hyperons. For even heavier systems, such as hyperon–hyperon, charmed particles, or in the three-body sector, scattering is most difficult or even unfeasible and at the same time bound systems are typically not available. Luckily, another method exists which can be used to study the interaction among particles, femtoscopy [11]. In the recent years, femtoscopy stood out as a key-tool to study the interactions among hadrons [173] and will also be used in this thesis to study the interaction between protons and Σ^+ hyperons. In this section, a brief historical introduction will be given and the theoretical and experimental concepts will be discussed.

The history of femtoscopy dates back to the 1950s, when Robert Hanbury-Brown and Richard Q. Twiss discovered the Hanbury Brown and Twiss (HBT) effect [174] and used it to determine the apparent size of stars that could not be resolved by telescopes [175].

The HBT effect describes correlated fluctuations of the intensities of particles, gauged by two independent and spatially separated detectors. In the case of a star, the emitted photons are observed by two telescopes. The measured quantity is the correlation function $C(\vec{d})$ at the detector distance \vec{d} , given by the ratio of the averaged (correlated) product of the intensities $\langle I_1 I_2 \rangle$ and the averaged individual intensities $\langle I_1 \rangle$ and $\langle I_2 \rangle$. In the absence of a correlation, the correlation function naturally equals unity [176, 177]. When the detector distance is varied within a characteristic scale given by the ratio of the wavelength of the photons and the apparent angle of the star, a correlation signal is observed.

The correlation can be fully attributed to the wave nature of the photons. One may consider a monochromatic thermal source, emitting spherical electromagnetic waves. The spherical waves can be described by the amplitude, the wave vector \vec{k} and a random phase. In this case, the individual intensities measured at one of the telescopes only depend on the amplitudes, while the random phases average out. In the product $\langle I_1 I_2 \rangle$, however, the averaging over the random phases takes place after the multiplication, giving rise to an additional

term, which does not vanish. If one now assumes that the individual sources are distributed according to a density distribution $\rho(\vec{r})$ and that the distance between the source and the detectors is much larger than the size of the star, it can be shown that the correlation function is given by the Fourier transform of the density distribution of the source, thus [176, 177]

$$C(\vec{d}) = 1 + \left| \int \rho(\vec{r}) e^{ik\vec{d}\vec{r}} d^3r \right|^2. \quad (1.4)$$

Not much later in the 1960s, the paradigm of the HBT correlations was applied by Goldhaber et al. [178] to study the effect of the Bose–Einstein statistics on pion correlations. From the 1970s onward, the concept was then used for the same purpose as the original HBT measurement, yet at a completely different length scale, to study the size of the particle emitting source. This was done by investigating correlations among pions in $p\text{--}\bar{p}$ collisions. Owing to the typical scale of hadron physics, this framework was later named femtoscopy. For several decades, femtoscopy was used primarily to study the source properties. However, since the correlation function relates the source distribution with the pair wave function, as will be shown, femtoscopy can also be used to study the interaction between the particle pairs, given that the source distribution is known beforehand. This concept was used by the STAR experiment in the 2000s to study the $p\text{--}\bar{\Lambda}$ and $\bar{p}\text{--}\Lambda$ interactions [179]. In the 2010s, they employed the method to study the interaction among Λ baryons [180] as well, which is interesting due to a potential bound state, the H-dibaryon [181]. However, experimental challenges obstructed a definite conclusion. This changed only recently, particularly due to the extensive work by the ALICE collaboration, allowing to fix the source distribution for any system under study [182, 183].

In the following, the experimental and theoretical approaches will be introduced, particularly putting weight on the arising caveats.

1.4.1 Experimental correlation function

Following the HBT paradigm, the quantity of interest in femtoscopy is the correlation function, given by the ratio of the correlated and uncorrelated two-particle intensity distributions. Boosting into the rest frame of the particle pair, the intensity distributions come down to a simple number distribution of pairs as a function of the relative momentum. Conventionally, the correlation

function is expressed in terms of k^* , defined as half of the relative momentum between the particle pair in their rest frame⁷ q^* . A small value of k^* can be visualized as particles moving almost collinearly at a similar velocity, allowing them to interact with each other. The experimental correlation function is thus computed as [11]

$$C(k^*) = \frac{N_{\text{corr.}}(k^*)}{N_{\text{uncorr.}}(k^*)} \quad (1.5)$$

where $N_{\text{corr.}}$ and $N_{\text{uncorr.}}$ are the distributions of particle pairs as a function of k^* in a correlated and an uncorrelated sample, respectively. It must be noted that $N_{\text{corr.}}$ and $N_{\text{uncorr.}}$ are generally not equally large. The ratio between the two samples highly depends on how $N_{\text{uncorr.}}$ is constructed. Typically, some kind of normalization is needed, which will be discussed in detail within this thesis, particularly in section 5.4.1.

Despite the minimal complexity of Eq. (1.5), many experimental caveats are present, which have to be treated carefully. First of all, the construction of the uncorrelated sample is itself not trivial. Generally, one seeks to break the correlation of interest, the interaction, but preserve all others, such that the correlation function equals unity at larger k^* . The k^* distribution of the pairs is driven by the single-particle momentum distributions, folded by the angular distribution, which in turn is constrained by the acceptance of the detector system. An angular dependence of the efficiency might be present and is potentially also momentum dependent. Regularly, these effects are considered by using the mixed-event technique, constructing the pairs from particles originating from different events [11, 15]. Naturally, such particles could not interact with each other and the detector acceptance is properly reproduced. Since the momentum spectra are a function of the multiplicity, only events which have a similar multiplicity can be mixed. This mixed-event technique works well for large collision systems like Pb–Pb collisions, but struggles for small ones like pp [11, 15]. This is related to the fact that pp collisions are dominated by a few hard parton scatterings, giving rise to preferential directions. In low-multiplicity collisions, pure momentum conservation also imposes a correlation between the particles' momenta [15, 184]. Since the mixed event averages over many events, such correlations are not preserved and the momentum conservation is violated.

⁷In the following, the asterisk always denotes that the value is considered in the pair rest frame.

Consequently, the correlation function contains these contributions, giving rise to a so-called non-femtoscopic background, which will be further discussed in section 5.4.1. Often, only the first few hundred MeV/ c of the correlation functions are shown, effectively hiding the deviations from unity at larger k^* [15]. Still, this potentially makes it challenging to extract the femtoscopic signal, while at least introducing uncertainty. Therefore, as part of this thesis, an alternative approach for the construction of the uncorrelated sample is proposed, which will be discussed in section 5.4.1.

Moreover, the sample of particles always contains a finite amount of contamination from misidentification or feed-down, which might have a (residual) femtoscopic correlation with the respective other particle. If the purity is only modest, a very good knowledge about these contributions is crucial to disentangle the measured correlation function and extract the contribution of interest. This will be discussed further in section 5.3.

The correlation function can be studied in all kinds of collision systems. In this thesis, pp collisions are used which have been triggered on high multiplicity, which will be explained later. Such collisions have been used extensively in ALICE to study the correlation functions of various particle pairs. Due to the small source size of these collisions and the thus small average inter-particle distances, the correlation signal is much more pronounced compared to heavy-ion collisions. Furthermore, pp collisions are also easier in terms of purity and particularly knock-out, together improving the significance of the signal. At the same time, triggering on high multiplicity significantly enhances the statistics of pairs per event, which might only be exceeded by a dedicated pair trigger. In particular, strange hadrons are produced with a higher abundance at high multiplicities [10], which also aids the study of the p - Σ^+ system discussed here. Nonetheless, the properties of the small source imply a complication as discussed. Furthermore, source sizes of around 1 fm also complicate the theoretical treatment of the correlation function, which will be elaborated in the following section.

1.4.2 Theoretical approach

In order to draw conclusions from a measured correlation function, it needs to be related to the two-particle wave function $\Psi(\vec{k}^*, \vec{r}^*)$, which contains the information about the interaction between the particles. This relation is given by the Koonin-Pratt equation, which reads [11, 185]

$$C(k^*) = \int S(r^*) \left| \Psi(\vec{k}^*, \vec{r}^*) \right|^2 d^3 r^* \quad (1.6)$$

where $S(r^*)$ is the source distribution, which corresponds to the probability that the pair of particles is created at a separation of r^* . The integral in Eq. (1.6) evaluates unity in the absence of a final-state interaction (FSI)⁸.

Extensive work related the source distribution has been done beforehand [182, 183], which will be discussed in the following section. The treatment of the wave function and the inclusion of the Coulomb interaction will be discussed later in this chapter.

In the case of identical particles, the Fermi-Dirac or Bose-Einstein statistics needs to be considered, respectively. Moreover, as already touched in section 1.3.3, coupled channels might be present if other particle pairs exist, which have the same quantum numbers and similar masses [186]. However, the latter two contributions will not be detailed further, as they are irrelevant for the system studied in this thesis.

Source distribution

The particle emitting source is in reality a very complicated entity, which does not only depend on the radius, but also on the momenta of the particles. Furthermore, it is not homogeneous and different for every event. Particularly in small systems like pp collisions, it cannot be assumed that the source is isotropic. In this case, the angular distribution between the distance vector \vec{r}^* and the momentum vector \vec{k}^* is not flat anymore, which is, however, a common assumption in the theoretical treatment of the correlation function [187].

It was already pointed out earlier that the k^* dependence could possibly factorize and thus be integrated out of the Koonin-Pratt equation [188]. This term would then give rise to the non-femtoscopic background. Quantifying the

⁸For non-identical particles without coupled channels.

non-femtoscopic background is challenging theoretically and is mostly treated experimentally by means of a phenomenological fit, which will be discussed.

The remaining r^* dependence of the source distribution is typically modelled by a Gaussian distribution centered at 0 with a standard deviation of r_0 , thus [182]

$$S(r^*) = (4\pi r_0^2)^{-3/2} \exp\left(-\frac{1}{4} \frac{r^{*2}}{r_0^2}\right). \quad (1.7)$$

However, this implies that the source is a static object of fixed size, which is not the case. It has been found that the size r_0 of the source scales with the transverse mass m_T of the pair [182], which is given by⁹ [11, 182]

$$m_T = \sqrt{\left(\frac{|\vec{p}_{T,1} + \vec{p}_{T,2}|}{2}\right)^2 + \left(\frac{m_1 + m_2}{2}\right)^2}. \quad (1.8)$$

Going even further, the Gaussian source can be complemented by a corona model, which accounts for the strong decays of short-lived resonances feeding into the measured particles. This is of course unique for every particle species and effectively enlarges the source size. When the corona is considered, the m_T scaling of the remaining Gaussian core collapses onto a single line, common to all investigated systems, as depicted in Fig. 1.7. In fact, the observed scaling behavior holds for meson–meson, meson–baryon and baryon–baryon systems in the same way [183]. The common scaling and its m_T dependence are not trivial. Generally, one may note the following considerations. Within the particle emitting source, gradients of the collective velocity are present, both in the beam direction and transverse to it. In order to form a pair with a vanishing relative velocity, the difference in the collective velocities of the two particles needs to be balanced by their thermal velocities, where the latter is proportional to $1/\sqrt{m_T}$ [11, 189]. A pair with a large m_T effectively moves slower, which restricts the so-called region of homogeneity to a smaller size. Below a certain value of m_T , the region of homogeneity expands over the full geometric expansion of the hadronization surface, leading to a saturation in the m_T scaling [183]. Both features can be seen in Fig. 1.7. While the shown parametrization is only phenomenological, it allows to extract the core radius for any system under study, thus also for the p – Σ^+ system. The contribution of resonance decays is evaluated using a simulation procedure, which will be discussed in section 5.5.1.

⁹One may note the different definition of m_T in section 1.2.1.

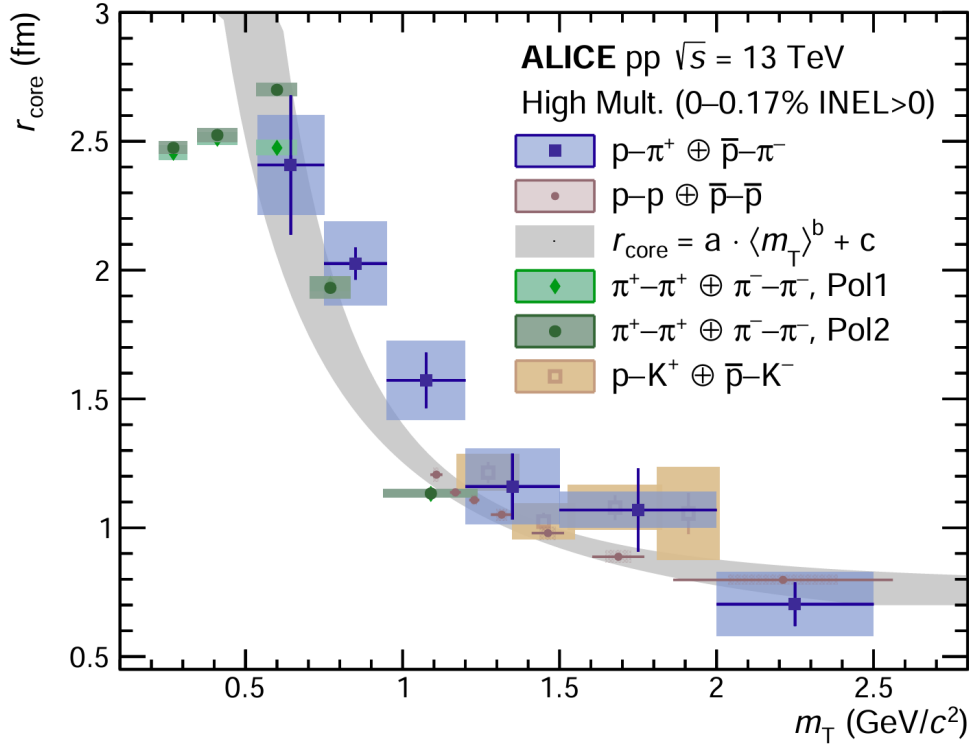


Figure 1.7: Scaling of the core radius r_0 of the particle emitting source with m_T in pp collisions at $\sqrt{s} = 13$ TeV. Above around $0.5 \text{ GeV}/c^2$ in $\langle m_T \rangle$, r_{core} exhibits a $1/\langle m_T \rangle$ dependence and flattens out to a constant size at high values of $\langle m_T \rangle$. Below $0.5 \text{ GeV}/c^2$ a saturation of r_{core} is observed, which can be interpreted as the maximum expansion of the fireball created in the collision. Figure from Ref. [191].

When using the Lednický-Lyuboshits [190] approach (see next section), it is more convenient to use a Gaussian source, as the exponential tails of the resonance source do not deliver an analytical solution of the Koonin-Pratt equation. This can be done by using an effective Gaussian fitted to the full resonance source. If necessary, the description of the source distribution can be improved by the usage of a weighted sum of multiple Gaussians. Nonetheless, one may note that the long tails caused by long-lived resonances are not necessary for a proper calculation of the correlation function and rather cause undesired artefacts.

Since the range of the strong interaction is approximately 1 fm, no effects of the interaction are expected at distances of $\mathcal{O}(10 \text{ fm})$, and consequently a Gaussian source is typically sufficient as long as the first few fm are well described [183]. For the $p-\Sigma^+$ system, this can be seen in Fig. 5.36 on page 191.

It is worth to note that the distance at which the wave function is probed is

determined by the source distribution. Studying the same particle pair in collision systems of different sizes can thus yield additional information about the radial dependence of the wave function.

Besides the remarkable achievements with respect to the source distribution, the description is clearly not complete. A 3-dimensional decomposition of the source could improve the situation and will possibly be available with more statistics.

As a remark, one may note that if the same particle pair is measured in multiple collision systems or at multiple centralities with different source sizes, one might be able to extract the scattering parameters by means of a simultaneous fit, leaving the radius as a free parameter.

Lednický-Lyuboshits approach

The second ingredient in Eq. (1.6) is the wave function $\Psi(\vec{k}^*, \vec{r}^*)$. In order to determine it, the Schrödinger equation must be solved for a given potential. There is no analytical solution for this problem, but numerical tools exist to perform the calculation [192]. On the other hand, for practical purposes, often an approximate analytical solution is used. The corresponding formalism is called Lednický-Lyuboshits¹⁰ (LL) approach [190]. Here, the wave function is considered in the approximate asymptotic form, consisting of a superposition of the incoming plane wave and the scattered spherical wave, where the latter is weighted by the scattering amplitude $f(k^*)$. The wave function then takes the form [190, 194]

$$\Psi(k^*, r^*) = e^{-ik^*r^*} + f(k^*) \frac{e^{ik^*r^*}}{r^*}. \quad (1.9)$$

The scattering amplitude thus gives the probability for a scattering into a certain final state. It is consequently related to the differential cross section via $d\sigma/d\Omega = |f(\theta)|^2$ [194, 195]. For spherically symmetric potentials, it is often practical to expand the scattering amplitude with respect to the angular momentum number L . At low energies, it can then be sufficient to consider only the lowest order, the S-wave, which eases the calculation [194, 195]. For the incoming wave, the plane wave expansion allows to write the plane wave as a

¹⁰One should also take note of the pioneering work of Lednický and Podgoretsky, available in Russian language only [193].

superposition of spherical waves and express them in terms of Legendre polynomials $P_L(\hat{k}\hat{r})$, where \hat{k} and \hat{r} are unit vectors in the direction of k^* or r^* , respectively.

After a few transformations and the identification of the terms in the ansatz made in Eq. (1.9), the scattering amplitude can be written as [194]

$$f(\hat{k}\hat{r}) = \sum_{L=0}^{\infty} (2L+1) f_L(k) P_L(\hat{k}\hat{r}) \quad (1.10)$$

with

$$f_L = \frac{e^{2i\delta_L} - 1}{2ik^*} = (k^* \cot(\delta_L) - ik^*)^{-1} \quad (1.11)$$

where δ_L is the phase shift between the incoming and the outgoing wave. The latter term $-ik^*$ comes from the unitary condition and ensures that the number of particles in the scattering process is conserved. If only the S-wave is considered, Eq. (1.10) trivially becomes $f(\hat{k}\hat{r}) = f_0$. In this case, the term $k^* \cot(\delta_L)$ can be expanded in a Taylor series around $k^* = 0$, a procedure called effective range expansion (ERE) [132, 190, 194]

$$k^* \cot(\delta_0) \approx -\frac{1}{a_0} + \frac{d_0}{2} k^{*2} + \mathcal{O}(k^{*4}). \quad (1.12)$$

The quantity a_0 is the so-called scattering length and d_0 is the effective range. The sign of a_0 is convention. In the convention used in this thesis, the scattering length is negative if the interaction is attractive but not binding¹¹. The name “effective range” can be misleading, as one needs to keep in mind that d_0 is first and foremost only the second coefficient of the Taylor expansion. It indeed gives approximately, or in case of a square-well potential exactly, the range of the interaction for potentials, which are short-ranged and have a scattering length that is larger than the range of the interaction [132, 196]. For vanishing values of a_0 , however, the first term of Eq. (1.12) diverges, which implies that the other terms of the expansion will grow large too in order to preserve finite scattering cross sections. The effective range can in this case become orders of magnitude larger than the actual range of the interaction. Those values are not particularly meaningful, but rather indicate that the effective range expansion

¹¹In femtoscopy sometimes the opposite convention is used.

breaks down. Most likely, the higher order terms are non-negligible in this case as well. As they enter with even higher powers of k^* , the region of validity is then limited to very small values of k^* .

With the wave function in Eq. (1.9), the effective range expansion, and the Gaussian source, the correlation function can be computed analytically and conveniently only depends on the scattering length, the effective range, and the source radius. One finds [190]

$$C_{LL}(k^*) = 1 + \frac{|f(k^*)|^2}{2r_0^2} F_0(d_0) + \frac{2\Re f(k^*)}{\sqrt{\pi}r_0} F_1(2k^*r_0) - \frac{\Im f(k^*)}{r_0} F_2(2k^*r_0) \quad (1.13)$$

where $\Re f(k^*)$ and $\Im f(k^*)$ correspond to the real and the imaginary part of the scattering amplitude, respectively. The functions $F_1(x)$ and $F_2(x)$ are given by

$$F_1(z) = \frac{\sqrt{\pi}}{2} z^{-1} e^{-z^2} \operatorname{erfi}(z) \quad (1.14)$$

and

$$F_2(z) = z^{-1} (1 - e^{-z^2}) \quad (1.15)$$

where $\operatorname{erfi}(z)$ is the imaginary error function, defined as $\operatorname{erfi}(z) = \frac{2}{\sqrt{\pi}} \int_0^z e^{x^2} dx$. The asymptotic approximation made in the Lednický-Lyuboshits approach is technically only valid at larger distances from the scattering center, at least larger than the effective range of the interaction. This is, however, not the case in pp collisions with source sizes of about 1 fm. Furthermore, even in larger sources the Gaussian distribution is inevitably peaked at 0 and the second term of Eq. (1.9) diverges at $r^* = 0$. This is cured only by the three-dimensional integration over the source, which introduces an additional factor of r^{*2} through the Jacobian determinant. Integrated over φ and θ one can write the source as

$$S(r^*) = \frac{r^{*2}}{2\sqrt{\pi}r_0^3} \exp\left(-\frac{r^{*2}}{4r_0^2}\right) \quad (1.16)$$

which has to be integrated in one dimension over r^* . Apparently, the function vanishes towards $r^* = 0$ and so does the volume of the integral. The maximum is shifted outwards to $2r_0$. Consequently, the wave function is probed at much larger distances as one would naively expect from a Gaussian distribution.

Nonetheless, the particle separations in small systems are still small, which can be cured to some extent by the term F_0 , defined as [190]

$$F_0 = 1 - \frac{d_0}{2\sqrt{\pi}r_0} \quad (1.17)$$

which tries to correct the deviation from the full wave function at small distances and is therefore called small source correction [190]. It has been demonstrated that this works well for the p- Λ system in pp collisions [15]. Depending on the experimental and model uncertainties, the uncertainty coming from the LL approach may be acceptable. One must, however, be aware that this does not hold for any system and there is no guarantee that Eq. (1.13) provides useful results.

Generally, there is no rule to determine if the approach is applicable without comparing to full calculations, however, the limit of validity can already be seen from the small source correction term F_0 . In the limit of an infinitely large source (or vanishing effective range), the term amounts to unity. As it is intended to be a small correction, the fraction $d_0/(2\sqrt{\pi}r_0)$ should also be small, at least smaller than unity. If one assumes a source size of 1 fm for a pp collision, this results in a maximum effective range of around 3.5 fm. This may not be fulfilled, particularly in the triplet channel of the N- Σ interaction due to the small scattering length. In such cases, larger deviations from the true solution must be expected. For very large effective ranges, the term F_0 can even cause negative values of the correlation function, which is clearly unphysical, as the correlation function is a ratio of intensities and thus positive definite.

One may at this point recall that the effective range is the second coefficient of a Taylor series. If it is extraordinary large, the series will, if truncated after the second term, potentially diverge from the real solution so quickly that it is sometimes counter-intuitively a better approximation to keep only the first term and drop the effective range completely. This is, however, only a rule of thumb and it is not guaranteed that it will produce reasonable results. For instance, for the considered models of the p- Σ^+ interaction (see Tab. 1.2), this works well down to a source size of around 1.2 fm, even for the NSC97f model, which has an effective range of 28.9 fm in the triplet channel. For a comparison see Fig. 1.9 on page 68.

Coulomb interaction in the Lednický-Lyuboshits approach

In the case of charged particles, the Coulomb interaction influences the correlation function substantially. It does not only effect the scattering amplitude, but also the shape of both the incoming and the scattered wave. It can be shown that Eq. (1.9) then takes the non-trivial form [187, 194, 197]

$$\Psi(k^*, r^*) = e^{i\sigma_c} \sqrt{A_c(\eta)} \left(e^{-ik^*r^*} F(-i\eta, 1, i\epsilon) + f_c(k^*) \frac{\tilde{G}(k^*r^*, \eta)}{r^*} \right) \quad (1.18)$$

where σ_c is the Coulomb phase shift. The strength of the Coulomb interaction is contained in the two-particle Bohr radius a , which is given by

$$a = \frac{m_e}{\mu q_1 q_2} \cdot a_0 \quad (1.19)$$

where m_e is the electron mass, q_i are the charges of the particles, and a_0 is the ordinary Bohr radius.

The first term of Eq. (1.18) - $e^{i\sigma_c}$ - always evaluates unity when calculating the modulus squared of the wave function. Also, it is negligible if a is large compared to $(k^*)^{-1}$. This is typically the case, as a is more than 50 fm for a pair of two singly charged baryons. The second term $A_c(\eta)$ is the so-called Gamow or Coulomb penetration factor and is given by [194, 198]

$$A_c(\eta) = \frac{2\pi\eta}{e^{2\pi\eta} - 1} \quad (1.20)$$

with $\eta = (k^*a)^{-1}$. F and G are functions that can be expressed in terms of so-called confluent hypergeometric functions which occur in the solution of the Coulomb wave equations [199]. While this will be detailed later, it may be noted at this point that they do not have a closed-form representation, which inhibits an analytical solution of the Koonin-Pratt equation like Eq. (1.13). Therefore, the modification of the shape of the waves induced by the Coulomb interaction is regularly dropped and only the terms in front of the brackets are considered. This is the so-called Gamow approximation [188, 197]. With the Gamow approximation, the Gamow factor can be integrated out of the Koonin-Pratt equation, such that the Coulomb correction is limited to multiplying the correlation function with the Gamow factor. In this case, however, larger deviations

to the full calculations must be expected, such that one should abstain from using this approximation. Alternatively, suitable approximations of the confluent hypergeometric functions may be used. The expansion of F reads [187, 197]

$$F = 1 + \frac{r^*}{a} \cdot (1 + \cos(\theta^*)) + \mathcal{O}\left(\left(\frac{r^*}{a}\right)^2\right) \quad (1.21)$$

and can thus be approximated by unity as r^*/a is small. Similarly, \tilde{G} can be approximated by purely analytic functions [187, 197]

$$\tilde{G} \approx \cos(k^* r^*) + i A_c(\eta) \sin(k^* r^*). \quad (1.22)$$

One may note that in this approximation, \tilde{G} is very similar to the case without Coulomb and only the imaginary part is modified by the Gamow factor.

The scattering amplitude f is also modified in the presence of the Coulomb interaction. The Coulomb-modified scattering amplitude is denoted as f_c . It can be expanded in the same manner as Eq. (1.12), namely [187, 197]

$$f_c(k^*) \approx \left(-\frac{1}{a_0} + \frac{d_0}{2} k^{*2} + \frac{2}{a} h(\eta) - i k^* A_c(\eta)\right)^{-1} \quad (1.23)$$

where a_0 and d_0 in this case denote the Coulomb-modified scattering length and effective range, respectively, and a is the two-particle Bohr radius defined in Eq. (1.19). The function h can be approximated for $\eta \ll 1$ by [187, 197]

$$h(\eta) \approx 1.2\eta^2 - \ln(|\eta|) - \gamma \quad (1.24)$$

where $\gamma = 0.5772$ is the Euler-Mascheroni constant. With these approximations, one can converge back to an analytical solution [188, 192, 197]

$$\begin{aligned} C_{LL}(k^*) = A_c & \left(1 + \frac{|f_c|^2}{2r_0^2} \left[F_0 + \frac{(A_c - 1)^2}{2} (1 - e^{-4(r_0 k^*)^2}) \right] \right. \\ & \left. + \frac{2\Re f_c}{\sqrt{\pi} r_0} F_1 - \Im f_c \left[\frac{F_2}{r_0} + 2(A_c - 1) k^* \cos(r_0 k^*) e^{-(r_0 k^*)^2} \right] \right). \end{aligned} \quad (1.25)$$

This equation is more precise than the previous Gamow approximation, while still being analytical. However, one must be aware that the Gamow factor employed here is a crude approximation by itself. It assumes that the particles

are emitted from a point-like neutral source [198, 200]. Hence, no information about the source distribution and particularly the size of the source enter its calculation. Naturally, the Gamow factor overestimates the influence of the Coulomb interaction for any source of finite size. The correlation functions calculated with the point-like assumption of the Gamow factor and the correct results are shown in Fig. 1.8 for multiple source sizes typically encountered in hadronic collisions.

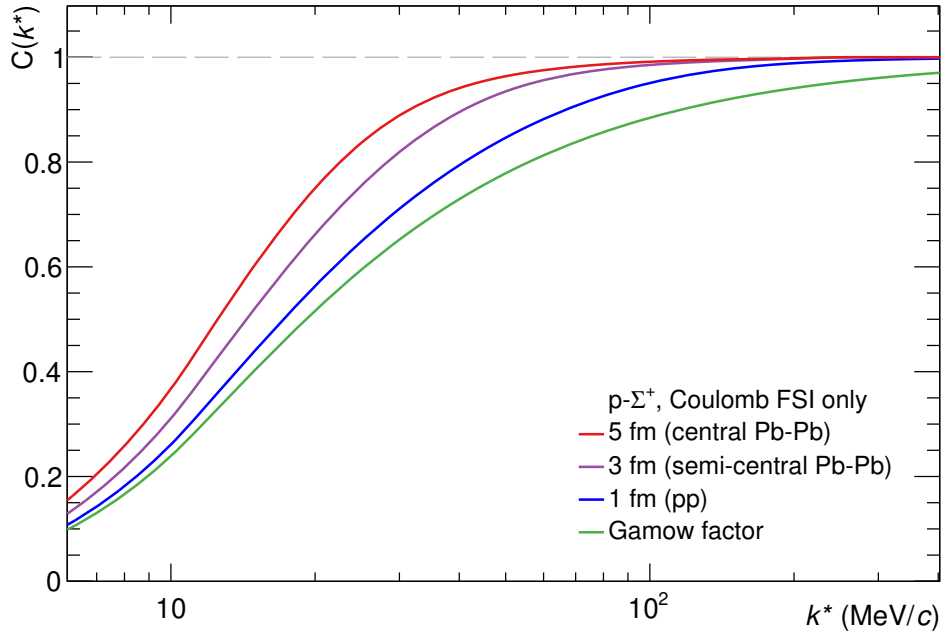


Figure 1.8: Comparison of the correlation functions calculated by integrating the Coulomb wave functions (Eq. (1.28)) over a Gaussian source for various radii typically encountered in hadronic collisions and the Gamow factor. The proper solutions approach the Gamow approximation towards low radii, but show sizeable deviations even for pp collisions.

In the limiting case of an infinitely small source size, the correlation function calculated using the Coulomb wave functions equals the result using the Gamow factor. However, even in pp collisions, where the source size is around 1 fm, the deviations are sizeable. Thus, it is recommendable to replace the Gamow factor by the proper Coulomb wave function integrated over the source¹². The Coulomb wave functions are the solutions of the Schrödinger equation in a

¹²One may note that here only the term $A_c \times 1$ - the incoming plane wave - should be replaced by the integral over the Coulomb wave function, as described in paragraph 1.4.2 on page 66.

Coulomb potential. The solutions can be expressed in terms of the aforementioned confluent hypergeometric functions. While their derivation is not trivial, the solutions are readily available in scientific libraries, for instance GSL [201]. For the calculation of the correlation function, it is most practical to use the partial-wave expansion of the Coulomb wave functions. Here, only the so-called regular solution $F_L(\eta, \rho)$ is required. The Coulomb wave function then reads [202]

$$\Psi^C(k^*, r^*) = \sum_{L=0}^{\infty} (2L+1) i^L e^{i\sigma_L} \frac{F_L(\eta, \rho)}{\rho} P_L(\cos(\theta)) \quad (1.26)$$

where $\rho = k^* r^*$ and σ_L is again the Coulomb phase shift. Thereby one can take advantage of the orthogonality of the Legendre polynomials, which cancels the mixed terms of the sum when integrating θ over the solid angle, such that [194, 203]

$$\int_0^\pi d\theta \sin \theta P_m(\cos \theta) P_n(\cos \theta) = \frac{2}{2m+1} \delta_{mn} \quad (1.27)$$

with δ_{mn} being the Kronecker delta. Furthermore, the term $i^L e^{i\sigma_L}$ always evaluates unity when calculating the modulus squared of the Coulomb wave function. Thus, it can be written in a simple representation as

$$|\Psi^C(k^*, r^*)|^2 = \sum_{L=0}^{\infty} (2L+1) \left(\frac{F_L(\eta, \rho)}{\rho} \right)^2 \quad (1.28)$$

which just needs to be integrated over the given source distribution. One may note that the series over L converges quite quickly, so it can be truncated at some point. For larger source radii, more terms are needed. However, one needs to consider that, depending on η and ρ , libraries may break down at certain values of L . Thus, a careful consideration of the maximum value of L is vital. Empirically, 40 terms is a reasonable starting point when using the GSL [201] library.

Full wave functions

As already discussed, the equations presented in the previous sections have to be taken with a grain of salt, as the requirements of the made approximations are formally not fulfilled for all interactions, particularly in small systems.

Considering the lengthy nature of Eq. (1.25) and the necessity of the proper Coulomb treatment, the only remaining advantage of the Lednický-Lyuboshits approach is that it only requires the two scattering parameters, the scattering length and the effective range, which can either be taken from the literature or extracted from the data by means of a fit, for a comparison to model calculations [15, 190]. Nonetheless, the correlation function should in any case be cross checked with a proper calculation, which thus needs to be computed anyway. Also, the statement 'the approach worked for a certain interaction, so it should work for all others' does not hold, as the properties of the interactions might differ substantially, even across models. Therefore, it is clear that for a solid model comparison, the correlation function must be based on the full wave function obtained by solving the Schrödinger equation for a given potential. In general, the wave function in the absence of the Coulomb interaction can be written as [190, 204, 205]

$$\Psi(\vec{k}^*, \vec{r}^*) = e^{i\vec{k}^* \cdot \vec{r}^*} + \Psi_0^S(k^*, r^*) - j_0(k^*, r^*). \quad (1.29)$$

Here, only the S-wave is considered, denoted by the index 0.

The first term is the incoming plane wave. This term always evaluates unity upon integrating over the solid angle. The second term is the modification by the strong interaction. The last term is the spherical Bessel function, which constitutes the non-interacting wave function.

In the presence of the Coulomb interaction, the terms are modified. Firstly, the plane wave is replaced by the full Coulomb wave function given in Eq. (1.26). One may note that it does generally not evaluate unity in this case. The strong wave function is now computed considering the additional Coulomb potential. Finally, the Bessel function in the S-wave is replaced by the corresponding regular Coulomb wave function F_0 divided by ρ . The wave function can thus be written as [204, 206]

$$\Psi(\vec{k}^*, \vec{r}^*) = \Psi^C(\vec{k}^*, \vec{r}^*) + \Psi_0^{SC}(k^*, r^*) - \frac{F_0(\eta, \rho)}{\rho} \quad (1.30)$$

One may note that the last term of the modulus squared of Eq. (1.30) equals the first term of the sum in Eq. (1.28), such that one can simply sum from

$L = 1$ to ∞ . The modulus squared of the full wave function then reads

$$|\Psi(k^*, r^*)|^2 = |\Psi_0^{SC}(k^*, r^*)|^2 + \sum_{L=1}^{\infty} (2L+1) \left(\frac{F_L(\eta, \rho)}{\rho} \right)^2. \quad (1.31)$$

Given that the wave function $\Psi_0^{SC}(k^*, r^*)$ is available, one can obtain the correlation function by integrating Eq. (1.31) over the source distribution.

Fig. 1.9 shows a comparison of correlation functions calculated using either the full wave functions or the approximations introduced early, exemplarily for two specific models. The strong wave functions in the presence of the Coulomb interaction $\Psi^{SC}(k^*, r^*)$ were provided by J. Haidenbauer [125] and the Coulomb wave functions were taken from the GSL library [201]. Using the Gamow approximation (paragraph 1.4.2), the correlation functions are completely off. When considering the change of the shape of the wave function (see equation 1.25), the amplitude of the correlation signal is largely restored, but the too slow convergence of the Gamow factor as observed in Fig. 1.8 still severely affects the correlation function, particularly at higher k^* . The introduction of the Coulomb wave functions to the former calculation cures this issue, but is still not sufficient to describe the proper correlation function. Particularly in the repulsive model (right), the dip below unity is not yet described. This is, however, a very important feature as discussed in section 5.5.4. Dropping the large effective range in the triplet, a reasonable description is reached. In case of NLO19 [122], the depth of the dip below unity is mostly restored and in case of NSC97f [111, 131] an almost perfect agreement with the full calculation can be observed. One must, however, clearly note that in this case the here used source radius (1.2 fm) is the sweet spot of the calculations. At even smaller radii, the discussed modifications of the LL approach do not suffice anymore for the $p\text{--}\Sigma^+$ system, while at larger radii, the approximation of setting the effective range in the triplet channel r_t to zero becomes increasingly impractical. In any case, these findings are specific for the considered interaction and may not be generalized without caution. Since the source size in the analysis reported in this thesis is considerably smaller than 1.2 fm, a generic potential is used to extract the scattering lengths, as described in the next section.

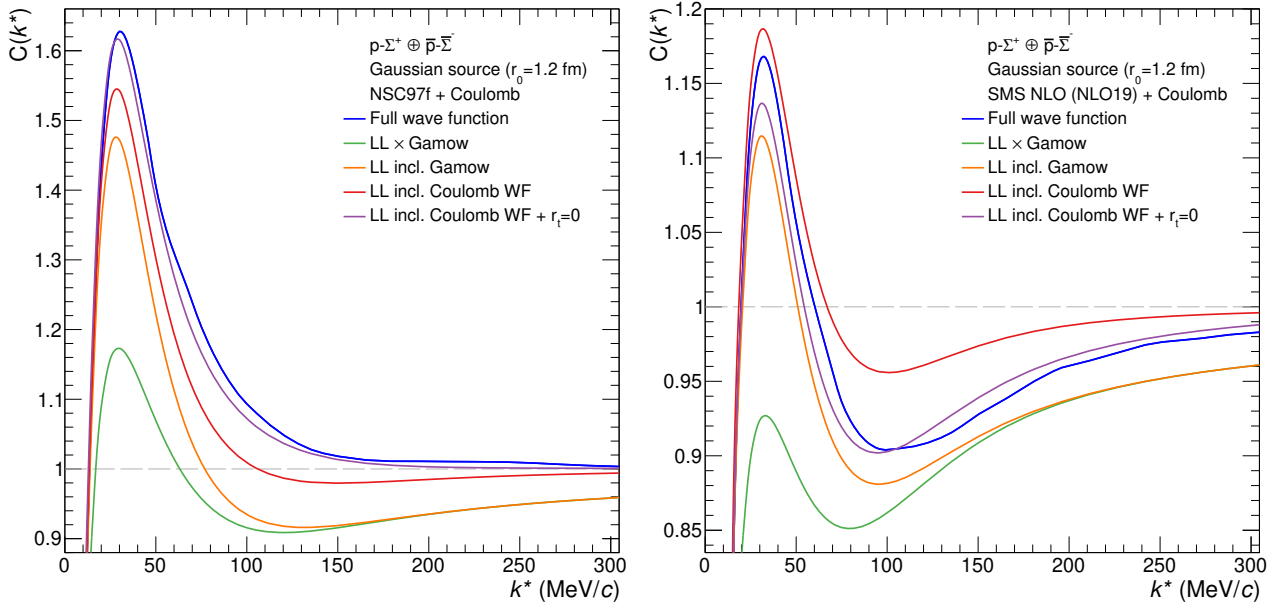


Figure 1.9: Theoretical correlation functions of protons and Σ^+ using the NSC97f [111, 131] (left) and SMS NLO (NLO19) [121, 122] (right) models for a Gaussian source with $r_0 = 1.2$ fm. The different computation methods introduced in this section are compared. The strong wave functions are provided by J. Haidenbauer [125] and the Coulomb wave functions are taken from GSL [201]. The full wave function calculations are performed in a finite binning. The visible artefacts come from the finite binning and the matching of the normalization to the asymptotic Coulomb wave function, which is done at a radius of 10 fm. The matching fails for some values of k^* if the strong wave function takes values close to zero. Such values are manually discarded and interpolated.

Generic potentials

Using the equations (1.31) and (1.6) it is possible to test a particular model calculation against data using full wave functions. Often, the corresponding wave functions are, however, not available. Also, one may seek to fit the obtained correlation function to extract the scattering parameters that fit the data best and determine their uncertainties. In these cases, the Lednický-Lyuboshits approach is commonly employed. Instead, generic potentials can be used to model the interaction among the particles. From these, the correlation functions can be calculated by solving the corresponding Schrödinger [207] or Lippmann-Schwinger [208] equations.

Several parametrizations of such potentials can be found in the literature. The potentials are typically phenomenological and based on the meson exchange

picture of the interactions, most prominently implemented in the Yukawa potential, which can be written as [109]

$$V_{Yukawa}(r) = -g^2 \frac{e^{-\lambda mr}}{r} \quad (1.32)$$

where g and λ are constants and λ is proportional to the mass of the exchanged meson. Later potentials like the Reid potential [209] build on this concept, but add terms to include repulsion at short distances. While this changes the shape of the potential at short ranges, the long-range shape is still dominated by the pion exchange. The arising free parameters of the potential models are fitted to the available data. In order to cope with the growing body of precise data, most recent potentials became increasingly sophisticated. In particular, one seeks to be able to describe the interactions among different baryons at the same time, such that the SU(3) flavor symmetry breaking needs to be considered.

Coming back to the correlation function, one has to consider that the scattering length is not very sensitive to the exact shape of the potential [132]. Thus, those sophisticated parametrizations may not be the best choice, particularly if the measured correlation function is limited by statistics and the exact shape cannot be resolved anyway.

A much simpler approach is the use of a Gaussian potential, which can be written as [210, 211]

$$V(r) = V_0 e^{-\frac{r^2}{b^2}} = V_0 e^{-m^2 r^2} \quad (1.33)$$

where b is the range parameter. It can be fixed - similarly to the Yukawa potential - to the inverse mass of the lightest meson that is exchangeable between the particles under study. In the case of p - Σ^+ , this is the pion.

In the presence of the Coulomb interaction, the well known Coulomb potential has to be added to the previous equation. For particles with charges q_i it reads [210]

$$V^C(r) = \alpha \frac{q_1 q_2}{r} \quad (1.34)$$

with α being the fine-structure constant. This leaves the potential depth V_0 as the only free parameter which needs to be fitted to the data.

Once V_0 is fitted, the scattering parameters can be determined from the asymptotic part of the resulting wave function using the effective range approximation

introduced earlier.

A study of the $p\text{-}\Sigma^+$ system with Gaussian and Reid-like potentials will be presented in section 5.5.5.

2 The ALICE experiment

The data presented in this thesis was measured with the ALICE detector, which is a large detector setup situated at the second interaction point of the Large Hadron Collider.

2.1 The Large Hadron Collider

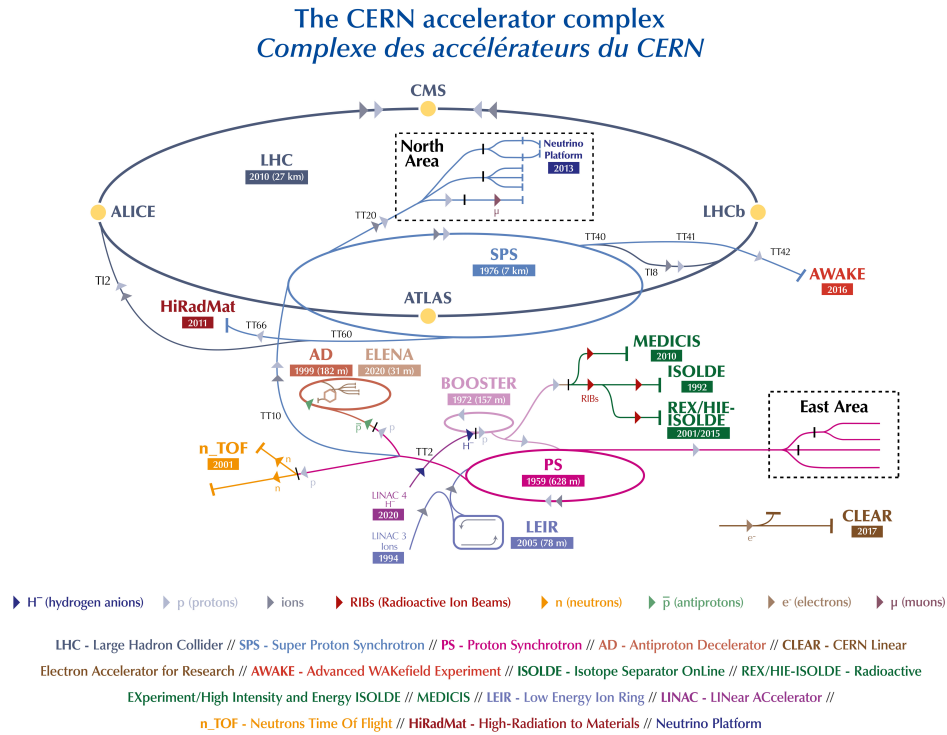


Figure 2.1: Schematic view of the accelerator facility at CERN. The LHC (uppermost ring) is fed by a chain of injectors. Numerous experiments are shown, including ALICE leftmost. Figure from Ref. [212].

The Large Hadron Collider (LHC) is the by far largest, most energetic, and most luminous particle accelerator worldwide [213]. It is located at the Conseil

Européen pour la Recherche Nucléaire (CERN) facility between Switzerland and France. A schematic diagram of the facilities at CERN is depicted in Fig. 2.1. One can see the large number of experiments, contributing to the very rich physics program of CERN. The various accelerators depicted in the figure have been built consecutively over a period of more than 50 year, with the LHC being the latest one, completed in 2008. The LHC is connected to the previous accelerators via transfer tunnels. These accelerators serve as injectors, which consecutively accelerate the particles to increasingly high energies. The LHC has a circumference of almost 27 km. It is installed in the tunnel that was previously built for the Large Electron–Positron Collider (LEP) [214], operating from 1989 to 2000. The LHC holds two counter-rotating beams in a common tube. It is not a perfect circle, but consists of straight and curved segments, eight each. In the curved segments, the particle beams are deflected by superconducting dipole magnets, which produce up to 8.33 T field strength. In each of the 528 m long straight sections an interaction point (IP), labeled IP1 to IP8, is located. At four of the interaction points the beams cross, allowing collisions. There, the four large experiments, ALICE, ATLAS, CMS, and LHCb are located. A diagram of the IPs is shown in Fig. 2.2.

The LHC can accelerate protons, lead ions, as well as lighter ions. In proton mode, the particles are injected from Linac 2 and are accelerated through the Proton Synchrotron Booster (PSB), Proton Synchrotron (PS), and Super Proton Synchrotron (SPS), before being injected into the LHC. The protons are packed in so-called bunches, each containing around 10^{11} protons, with up to 2808 bunches stored in the LHC. This results in a bunch crossing every 25 ns, which translates into a peak luminosity of $\mathcal{L} = 2 \cdot 10^{34} \text{ cm}^{-2}\text{s}^{-1}$, twice the design luminosity. In the second run period of the LHC (Run 2), which took place from 2015 to 2018, the protons were accelerated to a center-of-mass energy of $\sqrt{s} = 13 \text{ TeV}$.

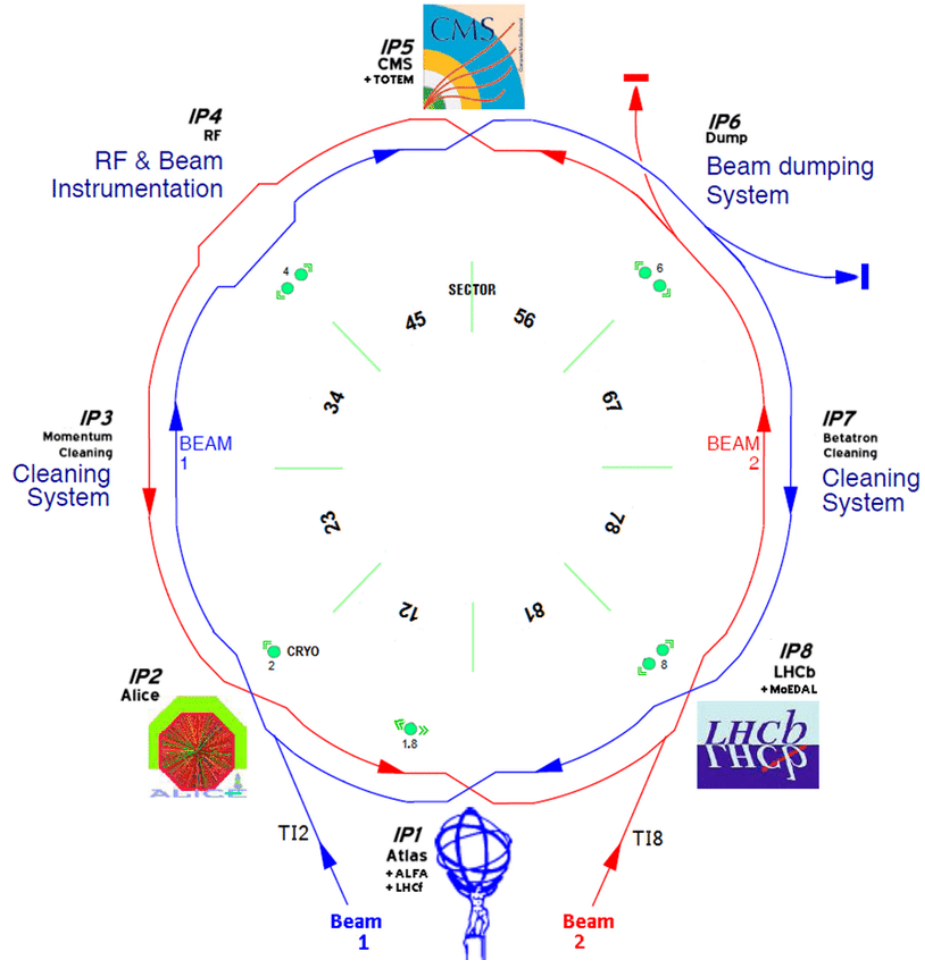


Figure 2.2: Schematic view of the LHC depicting the eight interaction points where the beams are manipulated and collisions take place. At IP2 and IP8 the beams are injected. Figure from Ref. [215].

2.2 The ALICE detector

In this section, the ALICE detector setup [216–218] will be introduced, mainly focussing on the subdetectors used in this thesis. ALICE is an acronym for “A Large Ion Collider Experiment”. The main aim of the experiment is the investigation of the quark-gluon plasma created in collisions of ultra-relativistic heavy ions. For this purpose, ALICE is equipped with versatile detectors, which are able to cope with the very high multiplicities present in central Pb–Pb collisions, while providing precise tracking and particle identification down to low transverse momenta.

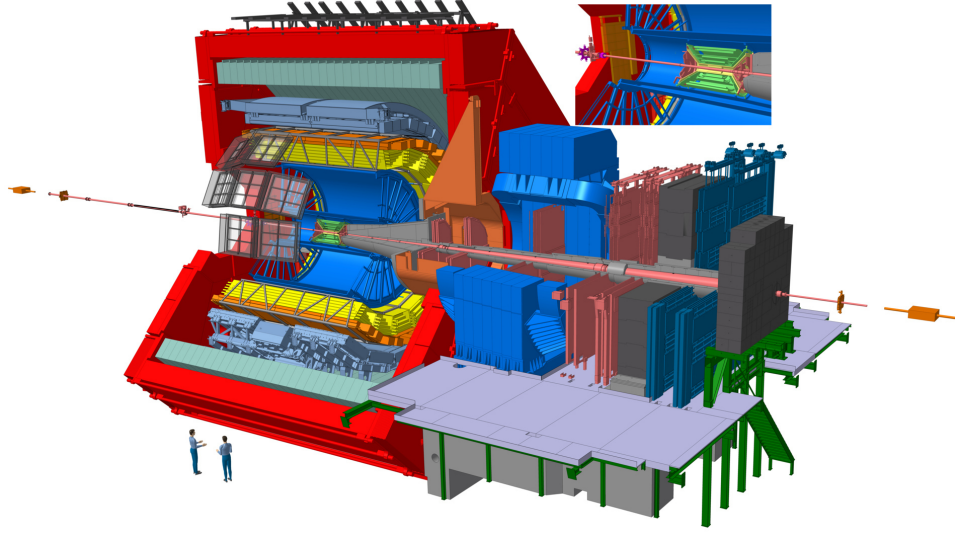


Figure 2.3: Schematic depiction of the ALICE detector as it was used during the LHC Run 2 data taking. The central barrel detector used in this thesis is seen in the left half of the figure within the L3 magnet [219] (red enclosure). In the upper right corner, a cut-out shows an enlarged view of the innermost subdetectors. Figure from Ref. [220].

The detector setup weighs around 10'000 t in total and measures around 16 m in height and width and 26 m in length. A schematic view of the setup is displayed in Fig. 2.3. On the left hand side of the figure, one can see the so-called central barrel detector. The central barrel detector consists of several subdetectors, which concentrically envelop the interaction point. The main subdetectors which are used for tracking and particle identification cover the full azimuthal angle of 2π . They are dimensioned such that a pseudorapidity¹³ coverage of

¹³Pseudorapidity $\eta = -\ln(\tan(\theta/2))$ where θ is the polar angle in spherical coordinates.

$|\eta| < 0.9$ is maintained for all events which occur within ± 10 cm around the nominal interaction point along the beam axis. This corresponds to an acceptance angle of slightly more than 90° in polar angle θ .

The central barrel detector is embedded in a 0.5 T magnetic field produced by the L3 [219] solenoid magnet.

To the right of the central barrel detector is the muon arm, which is specialized for the detection of muons in the forward direction at a rapidity of $-4.0 < y < -2.4$ stemming from the decays of charmed hadrons.

In the analysis presented in this thesis, only the detectors in the central barrel and the trigger detectors are used. The relevant subsystems will be described in detail in the following sections.

2.2.1 Inner Tracking System

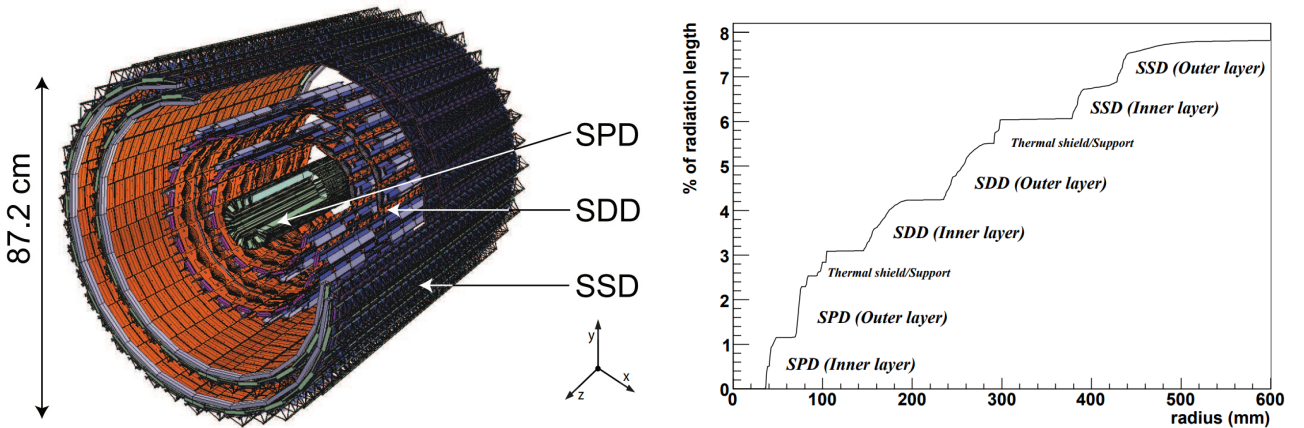


Figure 2.4: Cutaway diagram of the ALICE ITS detector, revealing its structure (left). On the right, the integrated material budget in percent of a radiation length is depicted as a function of the radius, showing an almost even distribution across the detector. Figures from Ref. [221] (left) and Ref. [216] (right).

The Inner Tracking System (ITS) [222] is the innermost detector in the central barrel. It is used for tracking and for the precise determination of the primary vertex by offering an outstanding spacial resolution of $12 \mu\text{m}$ in the $r - \varphi$ plane (i.e. perpendicular to the beam direction) and $100 \mu\text{m}$ in the beam direction z . The ITS improves the reconstruction of secondary vertices, the measurement of low-momentum tracks, and provides particle identification through the measurement of the specific energy loss. It consists of six cylindrical layers of silicon

detectors located at radii of 3.9, 7.6, 15.0, 23.9, 38.0, and 43.0 cm. The layers employ three different silicon detector technologies. The two innermost layers form the Silicon Pixel Detector (SPD), which consists of about 10 million individual reverse-biased silicon diode pixels. Since it is closest to the interaction point, a high granularity and radiation hardness are of particular importance. The short readout time of 300 ns makes these layers suitable for triggering on events with a high multiplicity at mid-rapidity.

The Silicon Drift Detector (SDD), comprised of the two middle layers, is characterized by a central cathode and two drift regions. The electrons created when a particle traverses the detector drift to the sides where they are read out. The position along the drift direction is computed from the arrival and the trigger time. The drift time makes this detector rather slow to read out (6.4 μ s).

The outer two ITS layers, the Silicon Strip Detector (SSD), consist of double-sided silicon detector strips and are most important for the matching between the tracks reconstructed in the TPC and in the ITS.

The material budget of the ITS is around 7.26% of a radiation length (including the enclosed air) [223]. The distribution on the layers can be seen in Fig. 2.4 on the right. In order to minimize energy loss and multiple scattering, which degrades the resolution especially at low p_T , one seeks to keep the material budget as small as possible. However, for the measurement of photons, and thus also for Σ^+ , a small material budget leads to a low reconstruction efficiency due to the low conversion probability. This will be discussed in section 4.2.

2.2.2 Time Projection Chamber

The Time Projection Chamber (TPC) [225] is the main detector of the ALICE experiment, most relevant for tracking and particle identification. It is sketched in Fig. 2.5. The TPC envelopes the ITS detector, extending from 85 to 247 cm in radius and 5 m along the beam axis. It is filled with a mixture of CO₂, noble gases (neon or argon) and nitrogen, while the composition changed during the years of operation. The TPC volume is split in half by a central high-voltage cathode, which provides a constant electrical field of 400 V/cm. When a charged particle traverses the TPC gas, it causes ionization, freeing electrons from the gas. These electrons consequently drift along the electrical field, eventually reaching the endplates of the TPC where they are read out. During Run 1 and

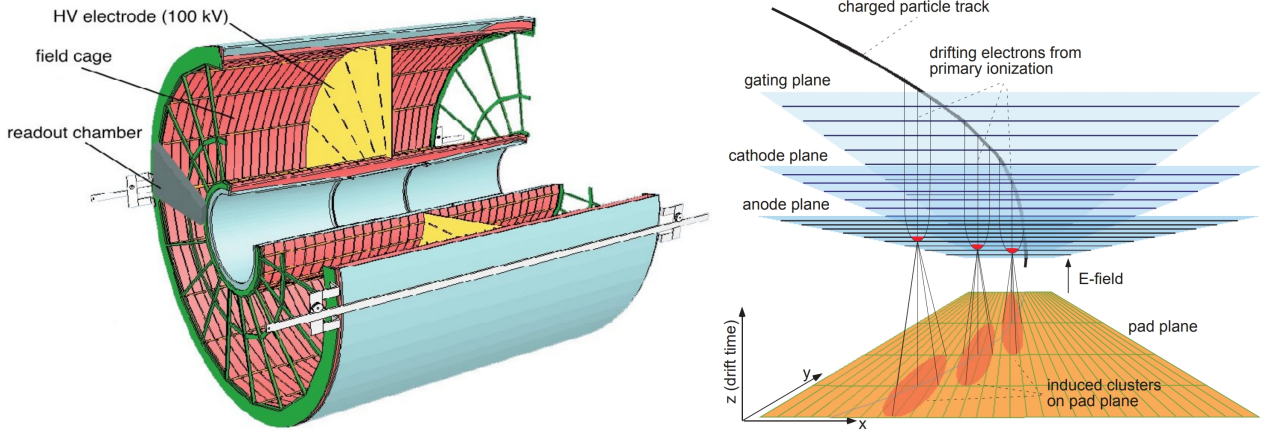


Figure 2.5: Schematic drawing of the ALICE TPC (left) and its readout plane (right). Figures from Ref. [224]. Left figure was modified.

Run 2, the readout consisted of multi-wire proportional chambers (MWPC), which amplify the incident electrons and direct them onto the pad plane where the signal is detected. The setup is sketched on the right side of Fig. 2.5. The endplates are partitioned into an inner and an outer chamber, each divided into 18 segments in φ and a total of 159 rows in the radius, totalling in more than $5.5 \cdot 10^5$ individual channels. By measuring both the position and the arrival time of the clusters on the pad plane, the TPC provides a three-dimensional picture of the particle trajectories crossing the detector. The maximum drift time amounts to around $100 \mu\text{s}$. After this time, the readout was closed by a gating grid for $200 \mu\text{s}$ to remove the ions from the volume. The readout of the TPC thus limited the rate capability of the ALICE detector to around 3 kHz. This has led to the replacement of the readout by a gas electron multiplier (GEM)-based continuous readout for the LHC Run 3 [226, 227].

In addition to position and time, also the amplitude of the TPC clusters is measured, allowing to identify particles by their specific energy loss (dE/dx) in the TPC gas. The energy loss is proportional to the square of the charge number and related to the velocity through the Bethe-Bloch equation. The velocity is, in turn, related to the momentum of the particles, which is determined from the curvature of the tracks in the magnetic field. The relation between the momentum p and the velocity β is given by

$$p = \beta\gamma mc = \frac{\beta}{1 - \beta^2} mc \quad (2.1)$$

where m is the mass of the particles and $\gamma = \beta/(1 - \beta^2)$ is the Lorentz factor. Measuring the momentum and the energy loss at the same time allows to identify particles by their mass and charge. The particle identification (PID) performance of the TPC is displayed in Fig. 2.6.

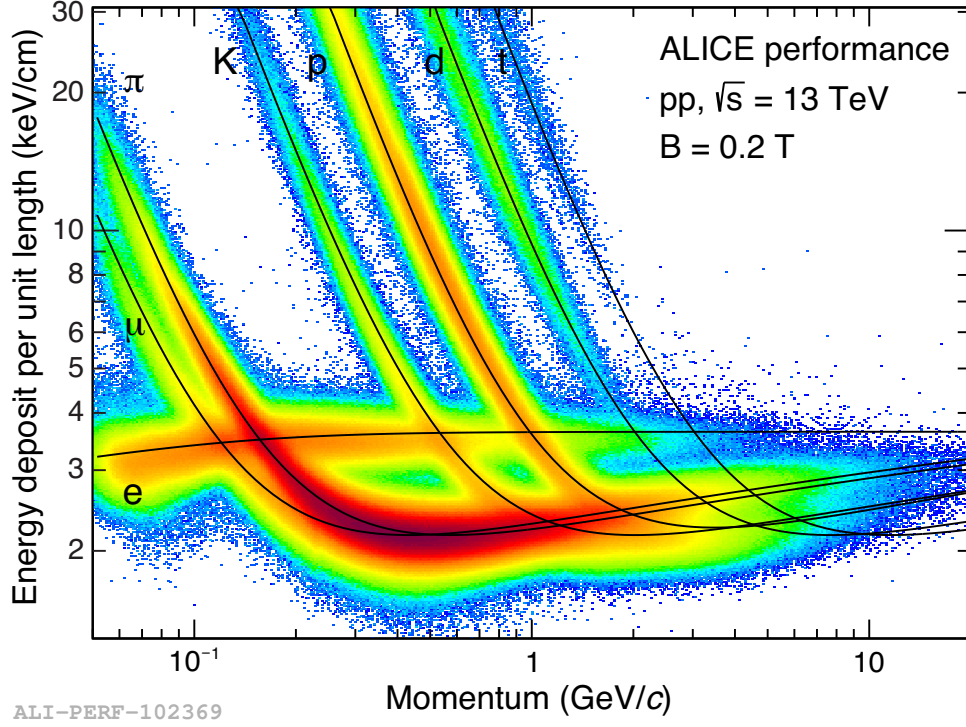


Figure 2.6: Performance plot of the PID in the TPC, showing the energy loss as a function of the momentum. The black lines correspond to parametrizations of the energy loss of various particle species, ranging from electrons (e) to tritons (t). The bands of the particles have a certain width due to the finite resolution of the measurement. The energy loss exhibits a characteristic minimum at a value of $\beta\gamma \approx 3$, resulting in a crossing of the bands, which limits the performance of the particle identification. Figure from Ref. [228].

2.2.3 Time-Of-Flight detector

The time-of-flight (TOF) [229] detector envelops the transition radiation detector¹⁴ (TRD), which in turn wraps around the TPC. It consists of an array of 1593 multi-gap resistive plate chambers (MRPC) placed at radii of 370 to 399 cm, providing an active area of around 140 m². It thereby covers the full

¹⁴The transition radiation detector is useful for the separation of electrons and hadrons and contributes to the tracking. It is not used in this analysis.

acceptance of the central barrel detector, except for the PHOS hole, which is explained in the next section. The time resolution amounts to 80 ps. The purpose of the TOF detector is to extend the particle identification capabilities to higher momenta where the energy loss bands of the particles overlap. It does so by measuring the flight time of the particles, which allows to infer their velocity by relating it to the integrated length of their trajectories. The velocity can again be related to the momentum using Eq. (2.1). Since the resolution of the calculated mass is momentum dependent, one often does not select based on the mass, but uses a so-called banana cut in the $p - \beta$ plane instead. This allows to select on the distance between the measured and the nominal flight time in multiples of the standard deviation (σ) of the resolution.

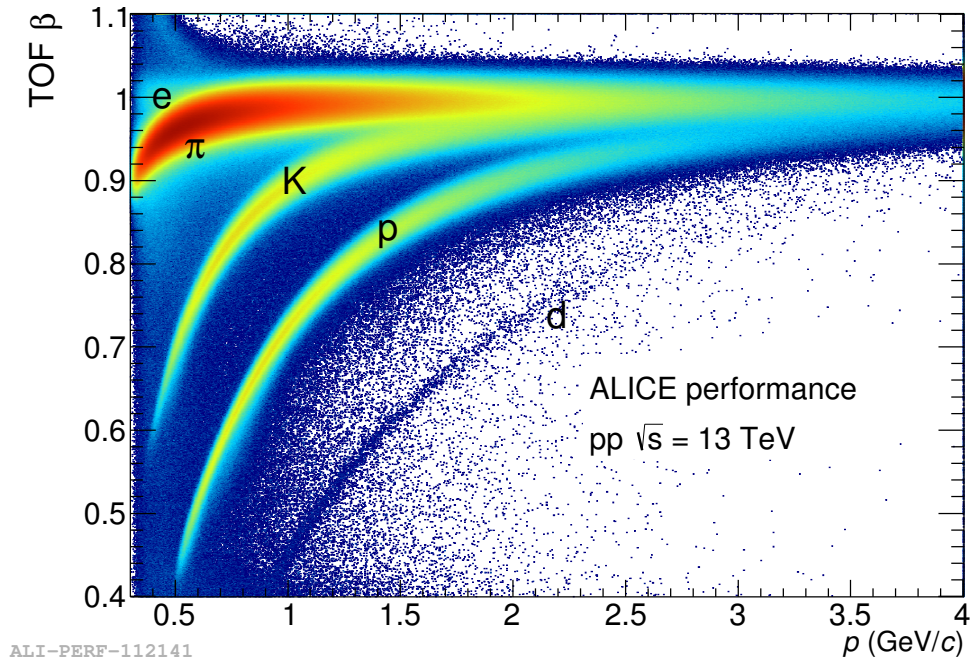


Figure 2.7: The velocity β , measured by the time-of-flight and the integrated length of the particle trajectories, is plotted against the particles' momenta derived from the curvature of the trajectories. The particles arrange in bands, which are separated due to their different masses. Velocities greater than c occur due to the finite resolution of the measurements. Figure from Ref. [230].

As depicted in Fig. 2.7, the particles converge to a common band one after another, with the protons being separable up to around 4 GeV/c. For even higher momenta there is another detector, the high momentum particle identification detector (HMPID), which makes use of the Cherenkov radiation to differentiate

between kaons and protons at momenta of up to 5 GeV/ c . However, it only covers 5% of the central barrel acceptance and is thus not used in this thesis.

2.2.4 Calorimeters

The central barrel detector of the ALICE setup contains three calorimeters, which form the outermost part of the central barrel. These are the photon spectrometer (PHOS) [231] and the electromagnetic calorimeter (EMCal) [232], where the latter comprises two subdetectors, the ECal and the di-jet calorimeter (DCAL) [233].

The purpose of ECal and DCal is to measure electromagnetic probes such as photons and improve the capabilities of ALICE to measure jets. The construction of ECal and DCal is the same, with both being lead polystyrene sampling calorimeters. The ECal has a pseudorapidity coverage of $|\eta| < 0.7$ and covers 110° in azimuth. The DCal has the same pseudorapidity range, but covers only 60° in azimuth. The DCal is placed back-to-back to the ECal, enabling the measurement of di-jets, hence the name.

The PHOS detector consists of lead tungstate crystals with a higher granularity than EMCAL. Located in between the DCal modules, it covers 70° in azimuth, but only $|\eta| < 0.12$ in pseudorapidity. Since the PHOS detector aims at measuring photons with low energies, it was necessary to reduce the material budget in front of it to a minimum. Therefore, the modules of the TRD and TOF detectors in front of the PHOS were omitted. This is referred to as the PHOS hole.

In total, the coverage of the calorimeters accumulates to roughly 40% of the full angular acceptance of the central barrel detector.

2.2.5 V0 detectors

The VZERO¹⁵ detectors [234] comprise two plastic scintillator arrays, called V0A and V0C, located at forward ($2.8 < \eta < 5.1$) and backward ($-3.7 < \eta < -1.7$) pseudorapidities. V0A is placed at a distance of 3.29 m to the interaction point, while V0C is located at only 0.88 m due to constraints from the muon arm. The VZERO detectors are used for triggering and the measurement of

¹⁵Also written as V0; not to be confused with the corresponding decay topology. In case of the decay topology, the 0 is written in superscript (V^0).

the luminosity.

The minimum-bias (MB) trigger requires at least one hit in both VZERO detectors. The events triggered in this way do not correspond to the total inelastic pp cross section, but the one which is visible to the VZERO detectors. The ratio between the two cross sections can be determined from so-called van-der-Meer scans [235]. One finds that the total inelastic cross section for pp collisions at a center-of-mass energy of $\sqrt{s} = 13$ TeV amounts to (77.6 ± 1.0) mb. The visible cross section is lower, as any trigger detector always has an efficiency below unity. In the case of the VZERO detectors, it amounts to (57.8 ± 1.2) mb, resulting in a ratio of 0.7448 ± 0.0190 .

The VZERO also provides a high-multiplicity (HM) trigger, which requires that the measured amplitude exceeds a threshold that is roughly 5 times larger than the average amplitude. Out of all events with at least one particle in $\eta < 1$, the events triggered in this way correspond to 0.17% of the ones with the highest multiplicity. A large data set with roughly 10^9 events was recorded this way and is eminently useful for femtoscopic analyses, as it provides particularly large statistics of particle pairs. In particular, high-multiplicity triggered events are also beneficial for studying systems containing strangeness, due to the enhanced production of strangeness compared to low-multiplicity events [10].

2.3 Data processing

The data set used in this thesis has been collected between 2016 and 2018 during Run 2 of the LHC. It comprises pp collisions at $\sqrt{s} = 13$ TeV using several triggers. As introduced in section 2.1, the upgrades performed during the precursory long shutdown 1 (LS1) allowed to use a tight bunch spacing of 25 ns, resulting in a luminosity of $2 \cdot 10^{34} \text{ cm}^{-2}\text{s}^{-1}$. A total integrated luminosity of 0.098 pb^{-1} has been collected using the minimum-bias trigger (at nominal and reduced magnetic field), 13 pb^{-1} using the V0 high-multiplicity (HM-V0) trigger, and an additional 1.1 pb^{-1} using the SPD high-multiplicity (HM-SPD) trigger [236]. Not all of the collected events are used for physics analysis. Event selections are applied to ensure a good vertex quality and to reject pile-up. This is done by a predefined physics selection macro using default selections. Additionally, events are rejected if the vertex position is further than 10 cm away from the nominal interaction point. Around 40% of the events are rejected by

the event selections. After the selections, around $1.8 \cdot 10^9$ MB events (at nominal field), $1 \cdot 10^9$ HM-V0 events and $3 \cdot 10^8$ HM-SPD events were available for analysis. Since the mean multiplicities of HM-V0 and HM-SPD triggered events are very similar and no sizeable correlation between the multiplicity in the SPD and the Σ^+ yield is expected, both triggers will not be distinguished in the following and will only be labelled as high-multiplicity (HM).

2.3.1 Tracking

The ALICE detector consists of several subdetectors, some of which have been introduced in sections 2.2.1 to 2.2.5. The subdetectors themselves comprise numerous individual channels, resulting in large amounts of raw data, which needs to be shipped, stored, and processed. The raw data is extremely high-dimensional, but has very low informational value. In the process of tracking, this data is converted to lower-dimensional objects like tracks, associated with physical particles, which have high informational value and allow to extract the relevant physics principles.

The tracking in the central barrel is a multi-stage process, which subsequently joins the individual detector data in an optimized way in order to make best use of it [218, 223, 237]. The procedure is performed within the AliROOT framework [238] and will be sketched in the following.

The reconstruction starts from individual detector clusters, characterized by position, time, and amplitude. At first, the two SPD layers are used to get a first estimate of the interaction vertex. This is done by pairing clusters in the SPD and fitting the intersection of those minimal tracklets. This preliminary vertex is used together with two clusters from the outermost part of the TPC as track seeds. The track seeds are then prolonged inwards through the TPC using a Kalman filter approach [218, 223, 239], which will be discussed in section 3.1. The resulting TPC-only tracks are subsequently propagated to attach the other detectors. Using the TPC-only tracks as seeds, the ITS clusters are added to the tracks layer by layer. In this step, multiple hypotheses of each track are preserved, fitted, and the best one is selected based on its χ^2 . Unused ITS clusters are used to build ITS-only tracks that have no prolongation to the TPC. Once the ITS information is included, the tracks are propagated back to the outer radius of the TPC and the TRD tracklets are added to the

tracks. Propagating further, the tracks are matched to hits in the TOF or the calorimeters, if available. During the outward propagation, the track length is determined by integration for PID purposes. Finally, the obtained so-called global tracks are propagated back to the interaction point. After removing outliers and secondaries, the primary vertex is fitted again with much higher precision using the global tracks. The distance of closest approach (DCA) between the tracks and the final vertex is calculated and stored to the tracks. Once all tracks are reconstructed, they are matched in the search for secondary decay vertices, as described in the following section. The reconstructed data is stored in the event summary data (ESD) format. To reduce the computational cost of user analyses, this data is filtered into the analysis oriented data (AOD) format [240].

2.3.2 Online secondary reconstruction

After the reconstruction of the tracks, the search for secondary vertices, stemming either from weak decays or photon conversions, is carried out. During Run 1 and Run 2, this was accomplished by the so-called on-the-fly finder during the tracking and an offline finder after the tracking [218, 223, 237]. Three kinds of topologies are thereby reconstructed. One stems from neutral particles decaying into two oppositely charged tracks, which suddenly appear¹⁶ from a common vertex, exhibiting a characteristic V-shaped topology, which is why they are referred to as V^0 s. The second one stems from short-lived charged particles, which exhibit an intermediate decay into a charged particle and a V^0 . This topology is referred to as a cascade decay, while the single charged track is called bachelor track. The third topology are kinked tracks. The particles exhibiting such decays are discussed later.

The finding of secondary vertices starts by pairing unlike-sign particles. To reduce the combinatorics and thus the CPU-time and to suppress primary particles, a minimum DCA of the used tracks to the primary vertex is required. Subsequently, the decay vertex is calculated as the point of closest approach (PCA) and selections are applied on the minimum distance of the tracks and on the cosine of the pointing angle (CPA) to remove unrelated pairs. Here, the pointing angle (PA) is the angle between the momentum vector and the vector pointing

¹⁶Since the mother particle is neutral, it is not visible in the detectors.

from the primary to the secondary vertex.

In the next step, the cascades are reconstructed by matching the previously found V^0 s with an additional bachelor track. Since the V^0 s are not primary in this case, the CPA selection is relaxed and a selection on the invariant mass of the Λ hyperon¹⁷ is used instead. Finally, a rather strong selection on the CPA of the cascade is applied [218, 223, 237].

The advantages of the reconstruction of secondaries already during the tracking are major, but there are also disadvantages, which will be discussed in the following. By reconstructing secondary vertices during the tracking when the information on the individual detector clusters is still present, tracks that are likely to originate from a decay can be refitted using this assumption, significantly improving the momentum resolution. Tracks stemming from the decay of a neutral particle may not cause hits before their decay vertex and one uses this causality information by requiring that the reconstructed decay vertex is closer to the primary vertex than any of the clusters associated to one of the two tracks stemming from this vertex. By doing so, one can make best use of the full detector information, which is not possible at the analysis level, where the individual clusters that contributed to the tracks are not preserved and a refitting of the tracks is not possible. Since storage is limited, tracks are only kept if they meet certain quality criteria. For instance, a maximum allowed DCA to the primary vertex is enforced. Secondaries, particularly soft electrons from photon conversions in the outer layers of the ITS, may fail to meet these requirements, severely affecting the achievable reconstruction efficiency. Therefore, the on-the-fly finder provides a significantly higher resolution and efficiency than offline finders [218, 223, 237].

The downsides of the online reconstruction are related to the fact that it makes use of information, which is not available anymore at the analysis level. This means that it is not possible to rerun the reconstruction procedure at any later moment to change the settings. Changing the settings is, however, useful for two particular reasons. On the one hand, variations of the selections are typically used to test how well the data is described by the Monte Carlo simulation and is thus used as a measure to quantify the systematic uncertainties of the efficiency correction [241, 242]. Such variations are still possible offline, but only in one direction, i.e. stronger selections. On the other hand, one might want

¹⁷As will be discussed later, for both particles exhibiting this decay topology, Ξ^- and Ω^- , the V^0 is a Λ [9].

to loosen or drop a selection which is unsuited for a particular analysis. This is the case for the analysis presented in this thesis. The selection on the CPA applied to the V^0 s is based on the assumption that the V^0 s originate from the primary vertex, which is not the case for the photons from the Σ^+ decay. Fortunately, the selection on the CPA was quite loose in pp collisions, and hence the reconstruction of the Σ^+ is still possible, as reported in this thesis.

It has been discussed [243] how the on-the-fly finding of secondaries could be improved in future runs. One option is to consider more particles in the reconstruction, i.e. widen the view from primary V^0 s and cascades to other eventually more complicated decay topologies. Also, it has been discussed [243] to drop the pointing angle selection for V^0 s which instead fulfil a selection on the invariant mass. This could significantly improve the efficiency of secondary photons and Λ s without causing unmanageable amounts of data.

3 Software tools

In this chapter, some of the software tools that have been used will be introduced. During Run 1 and Run 2, the reconstruction of the raw detector data as well as the detector simulations were performed within the AliRoot framework [238]. The code of the user analyses is contained in the AliPhysics framework [244] and runs on the reconstructed data. Both AliRoot and AliPhysics build on top of the ROOT framework [245] and were developed by and for the ALICE collaboration. ROOT is a very versatile framework for handling, analyzing, and visualizing large amounts of data and is therefore used by numerous experiments all over the world. As it is extensively documented [246], a dedicated introduction shall be foregone at this point. All figures in this thesis were created using ROOT unless stated differently.

In addition to these three frameworks, multiple libraries have been used at certain steps of the analysis. The KFParticle package [247] is used for the reconstruction of the Σ^+ . It is based on the Kalman Filter, which will be introduced in section 3.1.

For the particle selection in chapter 5, a machine learning approach is used. Therefore, Hipe4ML [248], Optuna [249], and XGBoost [250] were employed. These libraries will be further introduced in the corresponding chapters, while the principle concepts and considerations of machine learning will be addressed in section 3.2.

For the simulations and data comparison, the generator families PYTHIA and EPOS were used, while the detector simulations were handled by GEANT4 [251–253]. PYTHIA [62, 95] and EPOS [63, 96–99] were discussed in section 1.2.2 in the introductory chapter, while GEANT4 will be discussed in section 4.2.

3.1 Kalman filter

Detectors and sensors are not only used in experimental settings, but also used in many real-world technical applications to an increasing extent. Very often, one is faced with the difficulty that the quantities of interest are not directly observable and that the data of multiple detectors has to be combined to obtain the desired result. Aggravatingly, the systems are typically dynamical, i.e. change over time, and the sensor data is blurred by noise. In this regard, powerful algorithms are needed to combine the available information in an optimized way. One of these algorithms is the so-called Kalman Filter. The Kalman Filter is named after Rudolf Kalman [239] who introduced it in 1960, even though similar algorithms existed before [254]. It is well worth to note that it was very quickly and successfully used in the Apollo missions to calculate the trajectories of the flight to the moon [255].

Despite the technical name and the lengthly underlying mathematics, the concept of the Kalman Filter can be sketched quite easily. The calculation procedure is iterative. The whole information about the system is contained in a state vector, which contains its current state and its dynamics, as well as their uncertainty including all correlations, i.e. the covariance matrix. Therefore, information about previous iterations is not required, which reduces the memory requirements. Each iteration contains two distinct steps. Firstly, the current state is propagated by one time step by making use of an underlying motion model. The uncertainty is also propagated. The result is a prediction of the system state at this time step. Secondly, the new information is added by a weighted average, considering the uncertainty of the prediction and the one of the new measurement, respectively. With this, the state vector is updated accordingly. The proper treatment of the uncertainties is thereby of particular importance, as otherwise a new measurement would be given too much or too little weight, distorting the result.

In experiments like ALICE, one often seeks to reconstruct particle trajectories and derive quantities from them, for instance the momentum of a particle from the curvature of the trajectory. Considering the ALICE detector introduced in chapter 2, it becomes apparent that measurements of the particles' position are only available at discrete radii, for instance at the layers of the ITS or the rows of the TPC. These measurements naturally come with uncertainty and aggravat-

ingly it is a priori not known which data points belong to a given track. In this setting, the Kalman approach can be applied successfully [218, 223, 237, 256]. Starting from a seed, the track is propagated to the next layer using the motion model, which would in this case be the curvature in the magnetic field, and a prediction is made. At the next layer, it is checked if there is a compatible detector hit, and if so, it is added to the track and its state is updated accordingly. This procedure is continued until the full track is reconstructed.

The reconstruction of weakly decaying particles from daughter tracks can also be done in a similar way. Here, each contributing track, vertex, or mass constraint can act as a measurement and can be added to the mother particle consecutively using the Kalman approach. The Kalman Filter is implemented in the KFParticle package [247]. KFParticle has originally been developed for the CBM [257] experiment and is also used by the ALICE experiment by default. Meanwhile, it is furthermore used by a series of other experiments due to its versatile features, straightforward implementation, and outstanding performance. In KFParticle, each particle is represented by an 8-dimensional state vector, which contains the position and momentum (3 dimensions each), the energy, and the decay-length-over-momentum ratio. The covariance matrix is represented in the lower triangular form, thus containing 36 entries. The charge is also saved, yet not part of the state vector, as it is important for the propagation in a magnetic field, but remains unchanged. The same holds for additional parameters like track IDs or PDG codes [9] for MC purposes. The KF-particles can be initialized from a track object. Mother particles can then easily be created by adding the daughters and all relevant properties of the mother particle, including the covariance matrix, are automatically computed. The reconstruction automatically gives access to the decay vertex and the distances of the particles to this vertex. This information can for instance be used for the particle selection, which will be extensively discussed in the next chapters.

3.2 Machine learning

As explained in sections 2.3.1 and 2.3.2, tracking algorithms provide particle tracks and other pre-reconstructed topologies. For physics analyses, the analyzer is often faced with the task to select from these certain particles of interest.

In case of directly observed particles like protons, this is comparably straight forward as the number of observables is limited. These might, for instance, be PID information, DCA to the primary vertex, and the fit quality of the track. In case of reconstructed particles though, the amount of observables escalates. This is particularly the case for particles reconstructed in multiple steps. In these cases, not only the properties of the tracks used to build the particles are of interest, but also distances or angles between particles, pointing angles, invariant masses of intermediate particles, and others can be used to select the particles of interest. A good particle identification is crucial in these cases, as there is typically a large amount of combinatorics to be suppressed [258, 259]. The aforementioned variables are often directly or indirectly correlated with each other. For instance, the energy loss in the TPC gas is correlated with the velocity of the particle and its charge, while the velocity is again correlated with the particles' momentum through its mass. Any of such correlations can be visualized as a line in an n -dimensional hyperspace where a particle, fulfilling all correlations at the same time, would lie on a crossing point of all lines. Due to resolution effects, the crossing point is really rather an ellipsoid, but still it is often unlikely for background candidates to fulfil multiple correlations at the same time, leading to a superiority of a multivariate selection.

However, standard particle selections barely make use of correlations. This is because correlations between more than two variables are difficult to find and visualize and a multivariate selection is almost impossible to implement by hand. This, in turn, leads to non-optimal purities and selection efficiencies. In this regard, tools that recognize patterns in data in an automatized way appear to be very attractive. This has led to an increased interest in machine learning (ML) in the field of high-energy physics in the previous years [260–262]. In fact, machine learning tools are capable of significantly improving analyses. However, one needs to be aware of the limitations and pitfalls that there are. Any machine learning model will derive certain patterns in order to classify the data. How complicated a model has to be to obtain an ideal classification is an important question to be considered. In order to monitor this, a data set is typically divided into a training sample and a testing sample. While the model is trained on the training set, its performance is evaluated using the testing set. A too simple model will underfit the data, meaning that it is not capable of describing the present data patterns sufficiently. The result is a

high variance in the output and a non-optimal separation between signal and background. In contrast, a too complex model will fit the training data too closely. It will thereby “learn” properties that are specific to the training data set, i.e. fluctuations, that are not generalizable and lead to a bias. This case is called overfitting, while the general problem is referred to as bias-variance trade-off [263, 264]. Overfitting can lead to a situation where a model memorizes individual entries of the training set. In this case, the model will perform significantly better on the training than the testing set, which can be easily checked. In any case, both under- and overfitting will degrade the goodness of the classification, and therefore a thorough tuning of the algorithm-specific adjusting screws is required. Those adjusting screws are referred to as hyperparameters and will be discussed later [263–265]. It is very important to understand the meaning of the hyperparameters of a given model in order to optimize them. In most cases, however, there is no easy way to find the optimal settings and the optimization has to be done by the method of brute force [249, 263, 264]. There are tools that try to make the process as efficient as possible. The most simple one is a grid search, which uses a grid of discrete values. In this method, the number of necessary trials quickly escalates with the amount of hyperparameters, a problem known as “curse of dimensionality” [263]. Alternatively, gradient-based algorithms can be used, which try to descend into an optimum along the gradients calculated from previous trials. The issue with such algorithms is that they can get stuck in local extrema, rather than finding the global optimum. Therefore, more advanced algorithms use a combined method, making use of found gradients, but also exploring the surroundings at the same time [249, 266].

In any case, machine learning is not a “free lunch”, as it replaces a large number of easily interpretable parameters by a smaller amount of parameters, which are hard to interpret, no less correlated, and computationally costly to tune. This has to be taken into consideration before using machine learning for an analysis [249].

Machine learning is a broad field and many algorithms and implementations exist. The algorithms can be roughly divided into supervised, unsupervised, and reinforced learning. In case of high-energy physics, Monte Carlo simulations are available, providing labelled data sets. This allows the usage of supervised learning models [263]. Examples for these are artificial neural networks

and boosted decision trees (BDT). The following section will focus on boosted decision trees, as these are used in this thesis.

3.2.1 Boosted decision trees

A decision tree is a simple and intuitive concept of classification¹⁸ [263, 264]. It consists of a sequence of questions, so-called nodes, with two paths originating from each node. The topmost node is called root node, while the bottommost node is called leaf node and represents the output. Due to this structure, each node depends on all previous ones. The advantage of using (boosted) decision trees is that they are rather easy to interpret and thus allow to include domain knowledge by placing interaction constraints. They also perform rather well on small data sets, which is important when the statistics of the simulations is limited. The main drawback is that such models are highly prone to overfitting, which needs careful consideration [263–265]. In order to understand the training of a decision tree and “unpack” the black box, one first of all needs to understand what a “model” actually is. A model is just a mathematical function, which relates input parameters x_{ji} to a target variable y_i [265]. Here, the predicted output value is commonly represented by a hat (\hat{y}_i). A simple example of such a function is a linear combination of the input parameters multiplied by weights θ_j [250, 265]

$$\hat{y}_i = \sum_j \theta_j x_{ji}. \quad (3.1)$$

Here, j is the index of the input parameters going into the calculation of target variable y and i is the index of the data point. In this example, the weights θ_j are the parameters to be trained. In order to do so, one defines a so-called objective function which consists of two terms. The first one is the so-called loss function and the second one is the regularization term. The loss function quantifies the predictiveness of the model. One choice of the loss function L , common for fitting problems, is the mean square error (also called L2), which can be written as [250, 265]

$$L(\theta) = \frac{1}{N} \sum_i^N (\hat{y}_i(\theta) - y_i)^2 \quad (3.2)$$

¹⁸For a review of the rich history of decision trees for classification and regression problems see for instance Ref. [267].

where N is the number of data points in the training sample. The second term of the objective function, commonly referred to as the regularization term, is rather abstract, but vividly its purpose is to give complexity a prize. The loss function alone would, by construction, quickly lead to overfitting and thus needs to be balanced. With the objective function defined, training the machine learning model comes down to an optimization problem.

Since it is difficult to come up with a complicated classification model from scratch, so-called ensemble techniques are used to build a decision tree from multiple simple ones. While multiple variations of this technique exist, this section will only focus on one of them, the boosting method. Boosting is an iterative procedure in which in every step a so-called weak learner is trained and sequentially added [250]. A weak learner often only includes one feature of the data and only performs slightly better than a random guess. Every new weak learner tries to correct the mistakes that the current model made. The new tree is then added to the current model to improve it. In order to avoid overfitting, the weak learner is not added fully, but is weighted by a factor. This factor is called learning rate or shrinkage and is one of the hyperparameters of the boosted decision tree. A smaller value increases the number of iterations needed to fit the model to the training data, but also makes it more robust against overfitting. Typical values are 0.1 or less. The learning rate is connected to another hyperparameter, which is the number of estimators, i.e. the number of weak learners that are trained. A small learning rate requires a higher number of estimators for successful training. The third hyperparameter is the maximum depth of the tree, which adjusts the complexity. The maximum reasonable depth equals the number of variables minus one, which would mean that all variables are correlated. Typically, smaller values are recommended [264, 265]. Furthermore, many other hyperparameters exist, which might be used. For instance, it is possible to subsample the data in every iteration or to add weights to the loss or regularization term [265].

Gradient boosting [268, 269] is an advancement of boosting, which fits so-called pseudo-residuals instead of standard residuals that correspond to gradients of the loss function with respect to the prediction. The method requires the loss function to be differentiable, but allows it to be otherwise arbitrary, increasing the flexibility of the model.

Once the training is done, the model outputs a score for each particle candidate,

indicating the likelihood of being signal. The cut-off value used in the analysis might be tuned for the particular need, for instance optimal significance or optimal purity. The value might also be momentum dependent.

In order to tune the hyperparameters, it is useful to condense the goodness of the classification into a single parameter. This is typically done by scanning over the output scores (from 0 to 1) and thereby plotting the true positive rate against the false positive rate. The true positive rate is also called sensitivity; it resembles the efficiency of the selection. The false positive rate gives the fraction of background counts in the selected sample, i.e. 1-purity. The result is a characteristic curve known as the receiver operating characteristic (ROC) curve. The area under the curve (AUC) is thereby referred to as the ROC-AUC score [263, 265]. A perfect classification has a value of 1, while a purely random selection has a value of 0.5. One must note that the ROC-AUC score depends on the composition of the training and testing sample and is thus specific to a given use case. Therefore, caution is advised if one wants to draw general conclusions on the goodness of the classification from it. Also, one must note that the ROC-AUC score has a statistical uncertainty, which is often not shown. There is no point in optimizing the score on a level which is not statistically resolved, as the best value found this way is random.

In this thesis, the machine learning library XGBoost [250] is used. In the recent years, XGBoost has gained popularity, particularly in the field of high-energy physics after winning the “HEP meets ML” award during the “Higgs Machine Learning Challenge” in 2014.

The library Hipe4ML [248] is a minimalistic python interface, easing the use of XGBoost by providing an interface to ROOT [245] files and ROOT tree objects.

For the optimization of the hyperparameters, the framework Optuna [249] is at hand, which uses a sampler based on the tree-structured Parzen estimator (TPE) [266] that builds a so-called surrogate probability model from previous trials to estimate the dependence of the ROC-AUC score on the hyperparameters, which allows to guess the next promising trial efficiently.

A common drawback of machine learning is the lack of interpretability. A model might produce a single value from a set of parameters and it is not obvious how the parameters contributed to this value. This makes it challenging for third parties and the analyzer itself to judge if the model is reasonable. One

way to interpret a model is to consider the feature importances, which indicate the impact of the input parameters on the total output. A popular concept uses so-called shapley (or shap¹⁹) values, which originate from game theory and are named after Lloyd Shapley [270]. The value measures the mean impact of the parameter on the output, given all combinations of the other parameters. Considering this value is interesting, as it does not only probe the individual importance of the parameters, but also the synergies that come by adding the particular parameter. The open-source framework shap [271] allows a straight forward calculation of the shap values for various tree-based machine learning models, including XGBoost.

Pitfalls

Despite the advantages of machine learning, one needs to carefully consider the pitfalls that come with it. As discussed, any tuning of the hyperparameters is a trade-off between bias and variance, i.e. a bias can generally not be completely avoided without ruining the variance. Thus, a model will typically perform at least slightly better on the training sample than on the testing sample. Since this could bias the efficiency correction and the purity evaluation, one should abstain from evaluating such quantities with the same data set used for the training. Since this cuts down the available statistics to evaluate the efficiency, which might be a bottleneck in some analyses, one may consider a cross training, similar to a cross validation optimization [248]. Therefore, the data is partitioned in two so-called folds, each containing half of the statistics and two models are trained independently using one of the folds. The models are subsequently applied to the other fold and finally the folds are merged.

Apart from model biases, one also needs to consider biases stemming from the simulation. As it will be discussed in section 4.3.4 in more detail, simulations are only capable of reproducing the reality with a finite accuracy, leading to systematic uncertainties. A machine learning model might make odd selections that one would not do by hand, potentially enhancing the systematic uncertainties [272]. In any case, one needs to vary the selections to quantify the uncertainty. In machine learning this can be challenging, as there is only a single value to modify and there is no linear response of any of the observables

¹⁹Abbreviation or acronym for “Shapley additive explanation” [271].

on the output score [263, 264, 272]. Thus, the systematic uncertainty can easily be underestimated.

For these reasons, classical selections are used instead of machine learning for the analysis of the production spectra of Σ^+ presented in chapter 4. For the analysis of the p - Σ^+ correlation function presented in chapter 5, however, the advantages of machine learning outweigh its drawbacks and thus it will be used there.

4 Measurement of the Σ^+ production

Heavy-ion experiments are optimized for the measurement of particles that are charged. Such particles interact with the tracking detectors losing energy, allowing to reconstruct their trajectories, given that their lifetime is long enough to traverse sufficient detector material. Sufficient in this regard means that at least three detector hits need to be measured, as otherwise no curvature can be determined. This is the case for frequently measured particles like electrons, muons, pions, kaons, protons, and also for light nuclei. However, if a particle is neutral, it is not possible to track it directly. On the other hand, some particles might still be measured if they decay into charged particles within the detector, exhibiting a V^0 topology, as described in section 2.3.2. Essentially, only three particle species exhibit such a topology; the Λ baryon decaying into a proton and a π^- , the K_S^0 decaying into two oppositely charged pions, and the photon converting into an electron–positron pair [9]. One may note that some rare probes like the hypertriton can also decay in a V^0 topology [9]. Similarly, charged particles which are too short-lived to be tracked directly might be reconstructed as a cascade. This is the case for the Ξ^- baryon decaying into a Λ and a π^- and the Ω^- decaying into a Λ and a K^- [9]. In addition, long-lived neutral particles like (anti-)neutrons might be measured in calorimeters, although this has limited application due to limitations in the resolution and the identification of such particles.

The ground-state Σ baryons, namely the Σ^- , Σ^0 , and Σ^+ , fall into a gap between those cases. They are too short-lived to be measured directly (Σ^\pm) or neutral (Σ^0) and they do not have a purely charged decay channel²⁰. The Σ^- only decays into a π^- and a neutron [9] that cannot be measured by ALICE. However, it has been demonstrated that anti-neutrons can eventually be measured in the PHOS calorimeter, which will be discussed later. The Σ^0 decays almost exclusively

²⁰One may note that rare semi-leptonic decay channels exist which do not feature neutral daughters. However, their branching ratios are extremely low and not well known, making them rather unsuited for precise measurements [9].

into a Λ and a photon [9], which themselves can be measured as discussed. However, this comes with the pitfall that the Σ^0 is so short-lived [9] that its daughters cannot be distinguished from primary particles, which itself limits the maximum achievable purity to the Σ^0/Λ ratio. This makes the peak extraction complicated and hinders femtoscopic measurement, which will be addressed in chapter 5. For these reasons, this thesis focusses on the reconstruction of the Σ^+ . It decays into a proton and a neutral pion with a branching ratio of 51.57% [9]. The neutral pion decays almost instantly into two photons. The lifetime ($c\tau$) of the Σ^+ amounts to 2.4 cm [9], which is sufficiently long to reconstruct the decay topology, enabling high purities. The caveat in this case is the extremely low reconstruction efficiency. The reason for this will be discussed in section 4.2.2. Within this thesis, it was possible to increase the reconstruction efficiency by several orders of magnitude, enabling the measurement of the production cross section and the interaction of Σ^+ with protons for the first time.

As already elaborated above, the Σ^+ is reconstructed by exploiting its decay into a proton and a pion, i.e. $\Sigma^+ \rightarrow p + \pi^0$ with $\pi^0 \rightarrow \gamma + \gamma$ [9].

Particles and anti-particles are produced in roughly equal amounts at the LHC and their reconstruction and selection is no different. Thus, in the following “proton” (p) will be used for protons and anti-protons (\bar{p}) and “ Σ^+ ” for Σ^+ and its anti-particle $\bar{\Sigma}^-$. Likewise, the tuple “p- Σ^+ ” will refer to p- Σ^+ as well as \bar{p} - $\bar{\Sigma}^-$, unless stated differently.

4.1 Σ^+ reconstruction

The measurement of the Σ^+ strongly relies on the reconstruction of its decay vertex, which allows to suppress the background by applying topological selections and also allows to construct an energy correction, as explained in section 4.1.2. Therefore, one can make use of the relatively long lifetime of the Σ^+ of $c\tau = 2.4$ cm and the extremely short lifetime of the π^0 of $c\tau = 25.5$ nm [9]. The path length of the π^0 is far below the experimental resolution and thus one can assume that the proton and the photons originate from a common vertex that will in the following be referred to as the secondary vertex.

The secondary vertex is reconstructed using a Kalman Filter [239] implemented in KFParticle [247] as described in section 3.1. For this, it is of course necessary to know the momentum components of at least one of the photons by

measuring it through its conversion into an electron–positron pair as elaborated in section 2.3.2. In fact, there is no major difference in the resolution of the secondary vertex using one or two conversion photons, as the proton track strongly dominates the fit due to its smaller covariance matrix and the much shorter propagation distance.

For the proton, the position and momentum vector as well as the covariance matrix are taken at the primary vertex, while for the photons these quantities are taken at the conversion vertex. Within KFParticle, the protons are propagated outwards and the photons inwards towards their point of closest approach.

In the case of the calorimeter photons, where the momentum components are not directly accessible, they are constructed by the connecting line between the secondary vertex and the position of the calorimeter cluster. This vector is then normalized and scaled by the energy deposited in the calorimeter to find the momentum vector.

The selections have been tuned to the MC simulation described in section 4.2.1. The proton selection will be discussed in section 4.1.1 and the photon and subsequent π^0 selection in section 4.1.2. The protons and pions are paired to construct the Σ^+ . The final selections will be discussed in section 4.1.3.

The distributions of the discussed quantities will be spared in this chapter; a comprehensive collection of these distributions can be found in Fig. 5.6, 5.7, and 5.17 on page 148, 149, and 162, respectively.

4.1.1 Proton selection

The protons for the reconstruction of the Σ^+ are selected from the track array using the selections specified below. These selections are rather coarse and prioritize efficiency over purity, providing a preselection that enhances secondaries. The main selection of the Σ^+ is done via the topological selections described in section 4.1.3.

The proton tracks are required to be in the detector acceptance ($|\eta| < 0.9$) and have at least 60 clusters in the TPC. This ensures a reasonable track quality, while one may note that in the filtering of the ESDs to the AODs (see section 2.3.1) also additional quality selections are applied. For the identification, the particles are selected by their specific energy loss in the TPC within a 3σ

band around the parametrized value. Above a momentum of $0.9 \text{ GeV}/c$ where the TPC bands start to cross, a 3σ TOF selection is applied. However, the TOF selection is only applied if the track has an associated TOF hit, which holds true only for a fraction of the protons that is as low as 30% at $0.9 \text{ GeV}/c$. To make best use of the weak nature of the Σ^+ decay, the DCA to the primary vertex in the xy -plane (DCA_{xy} , i.e. perpendicular to the beam direction) is required to be larger than $100 \text{ }\mu\text{m}$, which effectively suppresses primary protons. The distributions of the proton features are displayed in Fig. 5.17 on page 162.

4.1.2 π^0 measurement

ALICE generally provides two possibilities to measure photons [273]. One is to measure the photons in the calorimeters (see section 2.2.4) and the other is the so-called photon conversion method (PCM) [273]. PCM is based on the fact that photons, even though they are stable in vacuum, can convert into an electron–positron pair in the presence of an external electrical field through a process called photon conversion. A strong electrical field is present in the proximity of a nucleus, which will take the recoil momentum, thus allowing the fulfilment of the conservation of momentum and energy at the same time. The converted photons form a V^0 topology, which is found by the V^0 finder as outlined before. The advantages of PCM over calorimetry are major. These include the reach to lower momenta, the higher resolution, and the significantly better particle identification and thus higher purity. Moreover, PCM gives access to the momentum components, i.e. the direction of the photon, which enables the separation of primary and secondary photons as well as the reconstruction of the secondary vertex from which the photon originated. Such advantages come with the price of a very low reconstruction efficiency due to the low conversion probability, which comes from the purposely minimized material budget [216, 223].

Two methods of photon reconstruction result in three options to measure the neutral pion, one using PCM alone, one using only the calorimeters, and a combined method, reconstructing one photon via PCM and one in the calorimeters. All of these methods have been successfully applied for measuring the π^0 and also the η meson that also decays into two photons [273].

Considering the low conversion probability, a precursory study investigated the

possibility to reconstruct the Σ^+ using only the PHOS detector [274]. Indeed, a peak in the invariant-mass spectrum could be seen, however, it only contained $\mathcal{O}(100)$ signal counts situated on an overwhelming background. Consequently, only 2 bins in p_T could be extracted, starting at 3.25 GeV/ c , making it difficult to draw any quantitative conclusions from this data, not least because of the sizeable statistical and systematic uncertainties. Thus, for this work, it was concluded that at least one PCM photon is necessary for a significant measurement of Σ^+ .

The combined method is thereby particularly attractive since it combines the advantages of both methods. PCM opens up the low-momentum regime, while the calorimeters improve the overall efficiency. One may also note that the fact that both photons can convert, but only one conversion is required, improves the efficiency again by almost a factor of two. If the conversion probability is p , the probability that exactly one photon converts is given by $2 \cdot p \cdot (1 - p)$, which compares to a probability of p^2 for two conversions. Assuming a conversion probability of 8%, this results in a 23 times higher probability to have one instead of two conversions.

In case of Σ^+ , however, most of the momentum is carried by the proton. A study using a phase space simulation²¹ found that on average only 11% of the momentum is carried by each photon. Therefore, a low momentum reach of the photon reconstruction is of major importance. Furthermore, the momentum components of the photons are indispensable to reconstruct the decay vertex of the Σ^+ , which is important to obtain a high purity. Also, the higher resolution must be taken into account. With these considerations, choosing the PCM-only method seems most reasonable. It will be referred to as the PCM-PCM method in the following. While it was possible to obtain a clear peak of the Σ^+ and determine its integrated yield with this method for the first time at LHC energies, the statistics is severely affected by the low reconstruction efficiency, which can be seen in Fig. 4.15 on page 124.

Due to the low statistics, the first measurable transverse-momentum bin starts at 1.5 GeV/ c using the high-multiplicity trigger, while in minimum bias only a coarse binning with a bin width of 1 GeV/ c could be used. Both results in sizeable uncertainties of the integrated yields. Also, only around 10'000 Σ^+ could be reconstructed in total, making a femtoscopic measurement unfeasible.

²¹The study was performed using “TGenPhaseSpace” which is implemented in ROOT [245].

Therefore, also the combined method was studied. It has been found that the secondary vertex can be reconstructed using only the momentum components of one photon. Using this vertex, it is possible to use selections for the calorimeter clusters that differ significantly from the standard selections and to construct an energy correction, which restores the resolution, thereby improving both the efficiency and the resolution substantially. This will be discussed in the following sections.

Because of its superior performance, the combined method is used as a default for the p_T spectra; it will be referred to as the PCM-Calo method in the following. Nevertheless, the PCM-PCM method serves as a valuable cross check. In the following sections, the selections applied to the photons are discussed. The selected photon candidates are paired to construct the π^0 s. The π^0 s are selected by their invariant mass, requiring a lower limit of $0.1 \text{ GeV}/c^2$. As the upper limit, $0.15 \text{ GeV}/c^2$ is used for the PCM-PCM method and $0.16 \text{ GeV}/c^2$ for the PCM-Calo method.

Conversion photons

The conversion photons are reconstructed as V^0 s, as explained in section 2.3.2. Their selection is comparably easy and allows very high purities without the need for drastic selections. This is due to the distinct topology and kinematic relations, which allow to distinguish the V^0 s from the background and from one another without the need for prior track selections. Thus, V^0 s can be used in the calibration of the PID, as they can provide almost pure samples of electrons (from γ), pions (from Λ and K_S^0), and protons (from Λ) in data. Following this approach, the selections on the V^0 candidate daughters are coarse. A 5σ selection in the TPC PID is applied and already rejects a sizeable fraction of the background from Λ and K_S^0 . Only 30 TPC clusters are required and also the selection in the pseudorapidity η is relaxed to 1.1 from the usual value of 0.9. This considers that the photon daughter tracks are often shorter in length and curled more due to their low momenta.

The kinematic relation of the V^0 daughters can be well visualized in the so-called Armenteros-Podolanski plot [275]. The plot opposes the asymmetry in the longitudinal momentum p_L^\pm of the V^0 , $\alpha = (p_L^+ - p_L^-)/(p_L^+ + p_L^-)$, and the transverse momentum q_T , where both quantities are considered with respect to

the flight direction of the V^0 . It is depicted in Fig. 4.1. As visible in the figure, particles of different identities form semi-ellipses, which are centered around $\alpha = 0$ for symmetric decays (γ , K_S^0) and shifted for asymmetric ones (Λ , $\bar{\Lambda}$). In this plane, photons are located around $q_T = 0$. The reason for this is that any transverse momentum q_T must come from the energy released in the decay. This is 0 in the case of photons, as their rest mass is smaller than the one of the decay daughters, making them stable in the absence of an external field. Following this consideration, the photons are selected within $q_T < 0.03 \text{ GeV}/c$ and $|\alpha| < 0.9$. Additionally, the opening angle of the V^0 is restricted to 0.3 rad and the difference in the θ coordinate, which gives the angle between the track and the magnetic field, is restricted to 0.1 rad. Assuming the electron mass for both tracks, the invariant mass of the V^0 is calculated and is required to be less than $0.06 \text{ GeV}/c^2$. Interestingly, the mass of the photons does not have to be strictly 0 due to the presence of Dalitz decays of the π^0 s involving virtual photons [9]. However, those cannot be distinguished from conversions within the resolution and thus they are treated equally.

The selections stated above seem similar, raising the question of their informational value. However, except for q_T and the invariant mass, no strong correlations are present between the selected quantities, which is well visible in Fig. 5.4 on page 145. Thus, selecting on all of these quantities helps to suppress the background.

Calorimeter photons

As elaborated in section 4.1, the reconstruction of the Σ^+ only makes use of the position of the clusters. A rough selection on the energy is made through the selection on the invariant mass of the pion, the exact energy is, however, not required. Furthermore, the reconstruction of the secondary vertex and the thus possible topological selections eliminate the need for a high photon purity in the cluster sample. Therefore, the selections used to select the calorimeter clusters differ substantially from standard cuts [273], which will be discussed in the following.

High-momentum charged particles traverse the calorimeters depositing a fraction of their energy, while low-momentum particles might be stopped completely depositing all of their energy. Photons deposit their energy in the calorimeter

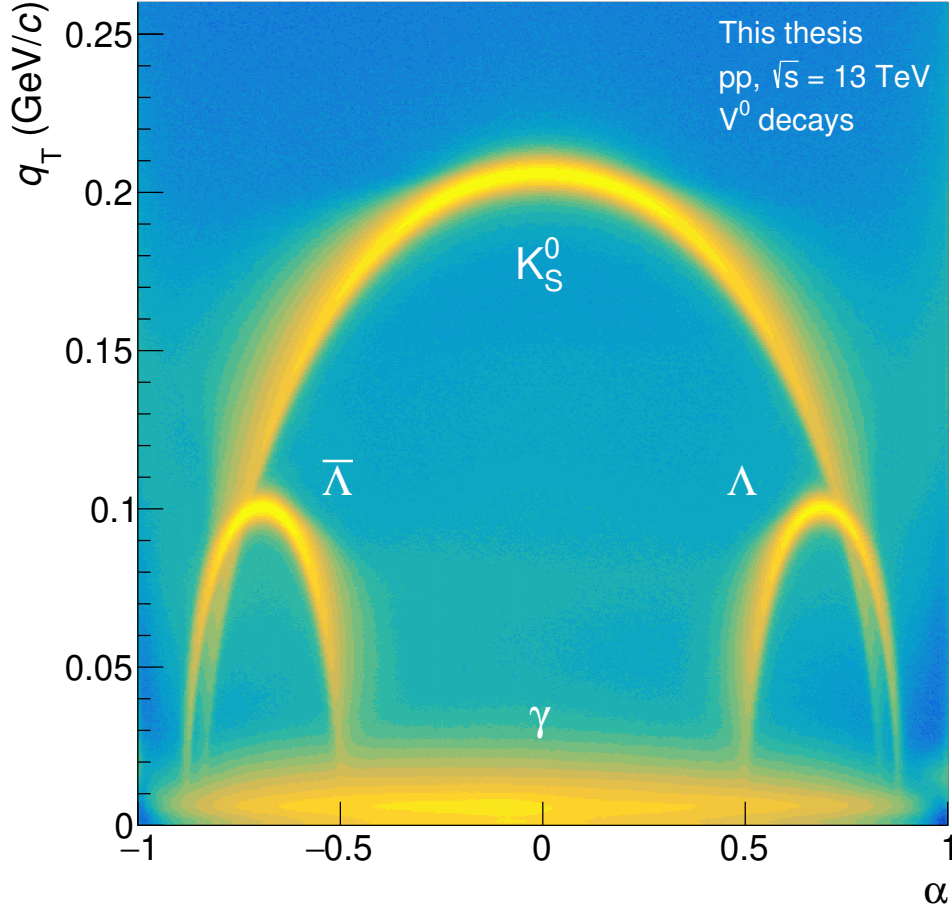


Figure 4.1: Armenteros-Podolanski plot [275] of V^0 candidates. It opposes the longitudinal momentum asymmetry α of the daughter tracks and their transverse momentum q_T with respect to the mother particle. The ellipses of photons, Λ , $\bar{\Lambda}$, and K_S^0 are well visible.

in an electromagnetic shower [276]. Depending on their energy, the shower can occur in a single cell of the calorimeter or spread over several neighbouring cells forming a so-called cluster. A cluster finding algorithm runs during tracking to identify such clusters. The algorithm works by finding cells with an energy deposition well above the noise level as seeds and consequently aggregates neighbouring cells which also show a signal.

While PCM allows to obtain a very pure photon sample by making use of the numerous topological, kinematic, and PID observables, the selections applicable to the calorimeter clusters are limited, particularly at low energies.

Photon clusters can be identified by their energy and shape. The shape of a

cluster can be quantified by the shape parameter M_{02} , which can be pictured as the semi-major axis of an ellipse around the cluster. Photons have rather round clusters, resulting in a smaller yet energy-dependent M_{02} [276]. Of course, a selection on the cluster shape can only be applied if the cluster has a shape in the first place, which is only the case for clusters consisting of more than one cell. However, one must note that low-energy photons - those interesting for this analysis - are very likely to deposit their energy in a single cell, making shape selections inapplicable.

Often, also a rather large minimal energy is required. Typical values for EMCal analyses are 500 or even 700 MeV for the seeding cell and 100 MeV for the aggregation of neighbouring cells [273]. Such selections guaranty a distinctive cluster shape and also suppress minimum ionizing particles (MIPs) [273, 276] to a high degree. However, as elaborated in section 4.1.2, the photons stemming from the Σ^+ decays have very low energies, making those selections prohibitive for this analysis.

Thus, only a minimal selection is applied. The cut-off value in the energy, applied by the framework, is 100 MeV for the EMCal and 70 MeV for PHOS. No further selections are applied on the energy.

Concerns have been discussed that the calorimeter response may not be well described in MC at low energies. If that was the case, however, one may consider that the minimum energy for the aggregation of cells would also need to be increased in a similar way, making the calorimeter practically useless for most analyses. To ensure that the description in the simulation is proper, multiple checks have been performed, which will be discussed in section 4.3.3.

To reduce the contamination by charged particles, all tracks in the event are propagated to the calorimeter plane and for each cluster the distance to the closest track is computed. A minimum of 10 cm is required, suppressing most of the charged-particle background.

Usually, a timing selection is applied to ensure the cluster belonged to the considered event. This is necessary due to the modest time resolution of the calorimeters. In this case, however, the combination with particles that are measured in detectors with a better time resolution effectively anchors the reconstructed particle to a specific event. Thus, clusters that did not belong to the event are suppressed by the other selections and eventually only contribute to the combinatorial background.

Not all calorimeter cells are functional. A fraction of the cells is dead, i.e. does not produce any signal. Other cells can have a higher noise level. In both cases, the corresponding cell is classified as bad. The information about which cells are affected is stored in maps in the offline analysis database (OADB). The maps eventually change over time. For the periods used in this analysis, the percentage of affected cells is displayed in Fig. 4.2. If there are multiple entries, the maps were updated during a period.

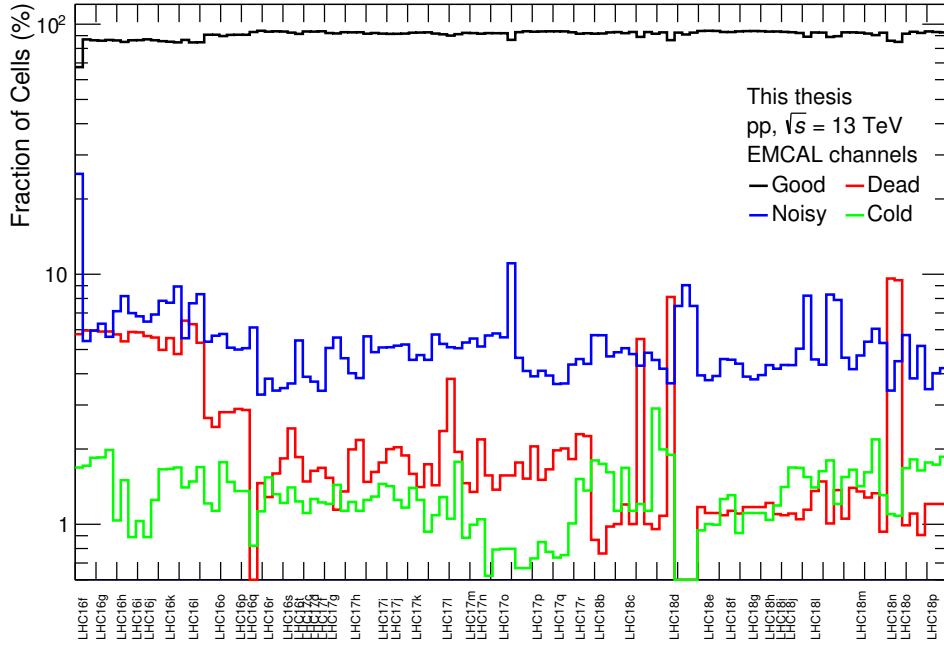


Figure 4.2: Fractions of noisy, cold, and dead cells for the used periods.

As visible, a sizeable fraction of dead cells was present in early 2016. The reason for this is that several calorimeter modules were switched off. Luckily, only a small fraction of the data was recorded at that time, such that the average number of dead cells is below 1%. To obtain the correct reconstruction efficiency, the dead cells must be removed from the simulation. Other than for most other subdetectors, this is not done automatically in the anchoring of the simulations, but must be done manually using the maps in the OADB.

Energy correction

The energy resolution of the calorimeters is only modest, particularly at low energies. This of course also affects the invariant-mass spectra of the π^0 and

finally the Σ^+ by broadening the peaks significantly. This is inconvenient, as it exacerbates the peak extraction and also worsens the momentum resolution, both resulting in larger uncertainties. In order to avoid such negative effects, the energies of the calorimeter clusters are corrected by making use of the known topology as described in the following.

Since photons are massless, the equation for the invariant mass of the π^0 (m_{π^0}) simplifies to

$$m_{\pi^0} = \sqrt{2 \cdot |\vec{p}_1| \cdot |\vec{p}_2| \cdot (1 - \cos(\alpha))} \quad (4.1)$$

where \vec{p}_1 and \vec{p}_2 are the momenta of the photons and α is the angle they enclose. A selection can be applied to the invariant mass calculated in this way to eliminate candidates which are kinematically not in line. After the selection, the invariant mass of the pion is fixed to its nominal value of 134.98 MeV/ c^2 [9] and Eq. (4.1) is solved for the momentum or energy of one of the photons. One finds

$$E_{\text{Calo}} = \frac{m_{\pi^0}^2}{2 \cdot |\vec{p}_{\text{PCM}}| \cdot (1 - \cos(\alpha))} \quad (4.2)$$

whereby the momentum of the conversion photon \vec{p}_{PCM} as well as the angle α are kept constant. The integrated invariant-mass spectrum of the Σ^+ with and without applying the energy correction is depicted in Fig. 4.3.

4.1.3 Σ^+ selection

After selecting the proton and π^0 candidates, the Σ^+ are constructed and their invariant mass and momentum \vec{p} is computed. From the momentum and the reconstructed secondary vertex \vec{r} , the pointing angle is calculated as

$$PA = \arccos \left(\frac{\vec{r} \cdot \vec{p}}{|\vec{r}| \cdot |\vec{p}|} \right). \quad (4.3)$$

The pointing angle²² is a very effective selection to suppress the combinatorial background. For the PCM-PCM method the pointing angle is required to be below 20 mrad. The selection is relaxed to 30 mrad below a Σ^+ momentum of 5 GeV/ c and relaxed further to 40 mrad below 3 GeV/ c . The momentum

²²Often the cosine of the pointing angle is used, eliminating the need for trigonometric calculations.

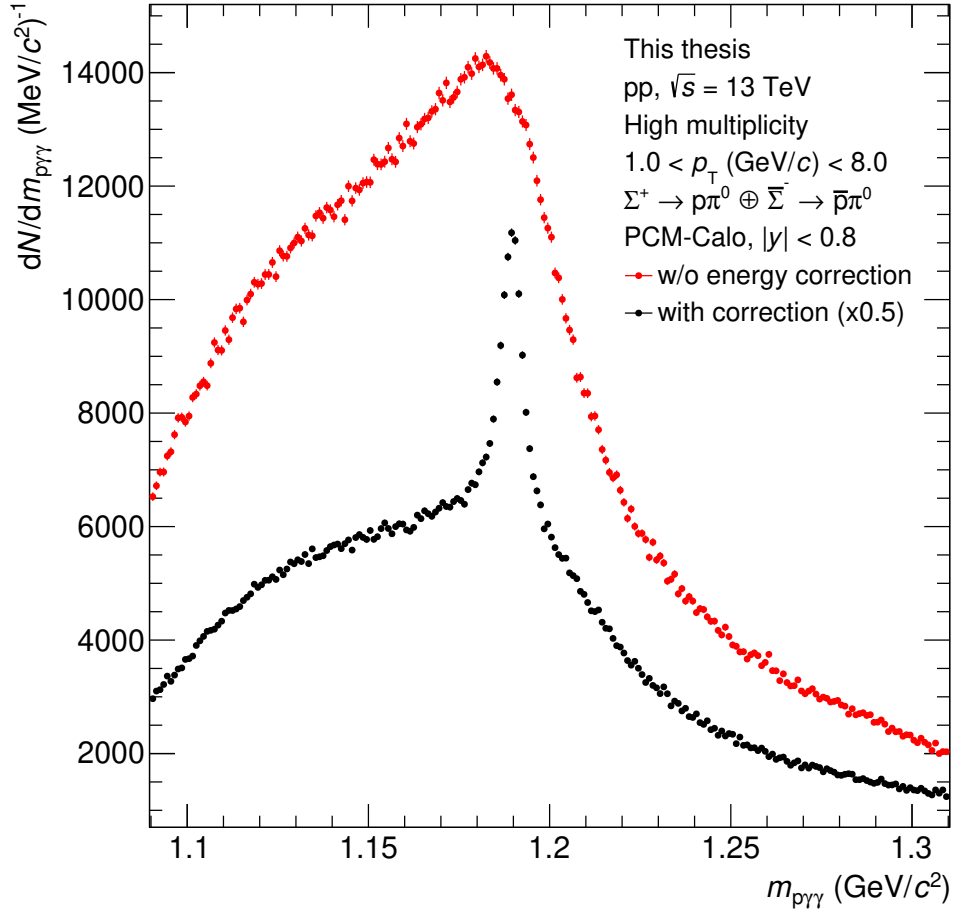


Figure 4.3: Invariant-mass distribution of Σ^+ reconstructed with the PCM-Calo method showing the effect of the energy correction using the mass constraint of the intermediate π^0 decay. In the uncorrected case, the signal peak is barely visible and the maximum is shifted from the nominal Σ^+ mass. After the correction, a clear and narrow peak is visible at the proper invariant mass.

dependence is given rise to by the strong momentum dependence of the pointing angle resolution and also by the trade-off between purity and efficiency.

For the PCM-Calo method, a stricter value of 12 mrad is chosen, which is relaxed to 24 mrad below 2 GeV/ c .

4.2 Reconstruction efficiency

Only a small fraction of the Σ^+ produced in the collision is principally available for reconstruction and again only a small fraction is actually reconstructed and

selected. Due to the composite nature of the Σ^+ , the number of sources of inefficiency is much larger compared to particles that can be tracked directly. These sources are the branching ratio, conversion probability, tracking efficiency, V^0 finding efficiency, cluster finding efficiency, and selection efficiency. In order to be able to make quantitative statements about the abundance of Σ^+ in the collisions, the total reconstruction efficiency containing all these sources must be known with precision. The reconstruction efficiency is determined by means of Monte Carlo simulations.

Before a detector is even built and data is recorded in a heavy-ion experiment, simulations of the heavy-ion collisions and the interactions of the particles with the detectors are crucial for designing the experiment for the best performance. At the analysis level, simulations also have broad application, as they give access to otherwise inaccessible quantities. For instance, simulations are used to tune the particle selections or to study the reconstruction efficiency and the resolution of the detectors. The simulations are typically carried out by the Monte Carlo method, which is based on the repeated drawing of random numbers to simulate certain processes [94]. A hadronic collision is simulated in multiple steps. First of all, the collision itself needs to be simulated by an event generator as introduced in section 1.2.2. Unless stated differently, PYTHIA 8 [62] with the Monash 2013 [277] tune is used for this purpose in this thesis.

In order to compare to data, the response of the detectors needs to be simulated too. This is done by a dedicated software package, which is also based on the Monte Carlo method. Commonly, the geometry and tracking (GEANT) framework [251–253] developed at CERN is used for this purpose. In this thesis, the latest release (GEANT4) is used in all simulations. Within GEANT, the whole ALICE detector is implemented. GEANT propagates the created particles through it and simulates the interactions of the particles with the matter including the detector response. The thus created data points are then plugged into the reconstruction framework used to reconstruct the particle trajectories from the individual detector data. The simulations are anchored to real data in order to reproduce the detector status, which is subject to change over time. Such simulations are computationally extremely costly. Often, only a fraction ($\lesssim 50\%$) of events in data is simulated, which is sufficient for most analyses and can be used for general purpose. However, if one wants to study probes which are rare or not at all produced in the simulation, difficulties arise in aggregating

enough statistics. The same holds for particles like the Σ^+ which has a very low reconstruction efficiency. In the case of Σ^+ , this is aggravated by the fact that strangeness is generally underproduced by PYTHIA [7, 8].

For the discussed reasons, the available simulations have been found to be insufficient for the analysis presented in this thesis. Therefore, a custom simulation had to be developed, which will be discussed in the following section.

4.2.1 Custom Monte Carlo simulation

Several possibilities exist to aggregate sufficient statistics in cases where a general purpose simulation is not suited or too costly.

One is to trigger the simulated events on certain conditions, for instance on a high multiplicity in a certain rapidity interval or the presence of a particle of interest. While this reduces the demand on storage and produces realistic spectra, all events still need to be simulated before triggering, resulting in large computational cost. For the high-multiplicity triggered data used in this thesis, this was done by demanding a certain multiplicity at forward rapidity, effectively replaying the trigger conditions of the V0 detectors (compare section 2.2.5). Around $6 \cdot 10^8$ events have been produced this way, roughly half of the amount recorded in data. Together with the underestimated production of strange hadrons, this simulation represented the statistical bottleneck of this analysis. Furthermore, the simulation was only produced for the first reconstruction pass²³ (pass1) and not for the one used in data (pass2). Rerunning the simulation with the latest pass and with more statistics was not an option, considering the high cost of the simulation; it consumed around 3323 years of CPU-time and produced 614 TB of data output.

Alternatively, the particles of interest can be injected into a minimum-bias event. Often, the injection follows uniform distributions in the transverse momentum and in the rapidity within suitable limits, e.g. 0 to 10 GeV/ c in p_T and $|y| < 1$. Several particles can be injected per event without effecting the efficiencies, in particular in pp collisions. While this strategy works well for instance for light nuclei, it is still not well suited for Σ^+ . Due to the strong momentum dependence of the reconstruction efficiency, low-momentum particles

²³The calibration of a large detector setup like ALICE is a complicated endeavour, which takes time and improves over time. Thus, the data is often reconstructed multiple times in order to improve for instance the tracking and the PID performance.

are only rarely reconstructed, leading to a similarly high demand on events as a minimum-bias simulation. A flat injection scheme is hence not an asset.

Therefore, a different injection scheme has been developed within the scope of this thesis, which utilizes a combination of generators merged in a so-called generator cocktail.

A realistic p_T spectrum has the inverse p_T dependence as the reconstruction efficiency, compensating the declining efficiency towards lower p_T . To tune this realistic p_T dependence, a preliminary spectrum was measured using the existing simulations and fitted with a Lévy-Tsallis distribution as described in section 1.2.1. From this fit function, 10 Σ^+ and 10 $\bar{\Sigma}^-$ were sampled per event. This injection scheme just struggles at very low and high p_T , which can, however, be patched by injecting 1 additional particle and anti-particle each per event flat in p_T . A minimum-bias event was used as the underlying event. The resulting p_T distribution leads to roughly uniform²⁴ distribution in the reconstructed spectrum and thus provides equally large statistical uncertainties in all p_T bins. The reconstructed spectra for the two reconstruction methods are displayed in Fig. 4.4.

Using the described injection scheme, it is possible to improve the statistics of the simulated Σ^+ considerably compared to the high-multiplicity simulation while keeping the computational cost tolerable. The simulation produced for this analysis consumed roughly 54 CPU-years and produced 3 TB of data, which amounts to around 1.6% in terms of CPU-time and 0.5% in terms of memory usage compared to the high-multiplicity simulation.

4.2.2 Efficiency results

With the simulation at hand, the reconstruction efficiency can easily be calculated by applying the selections to the reconstructed MC particles and dividing the obtained reconstructed p_T spectrum by the generated one. Both the reconstructed and the generated particles are considered within $|y| < 0.8$. Fig. 4.5 showcases the obtained reconstruction efficiencies for the PCM-PCM and the PCM-Calo method.

The reconstruction efficiency of the PCM-Calo method is roughly one order of

²⁴“roughly uniform” means “in the same order of magnitude” in this regard. This compares to a spread of the statistics across several (>2) orders of magnitude when injecting using a uniform distribution in p_T .

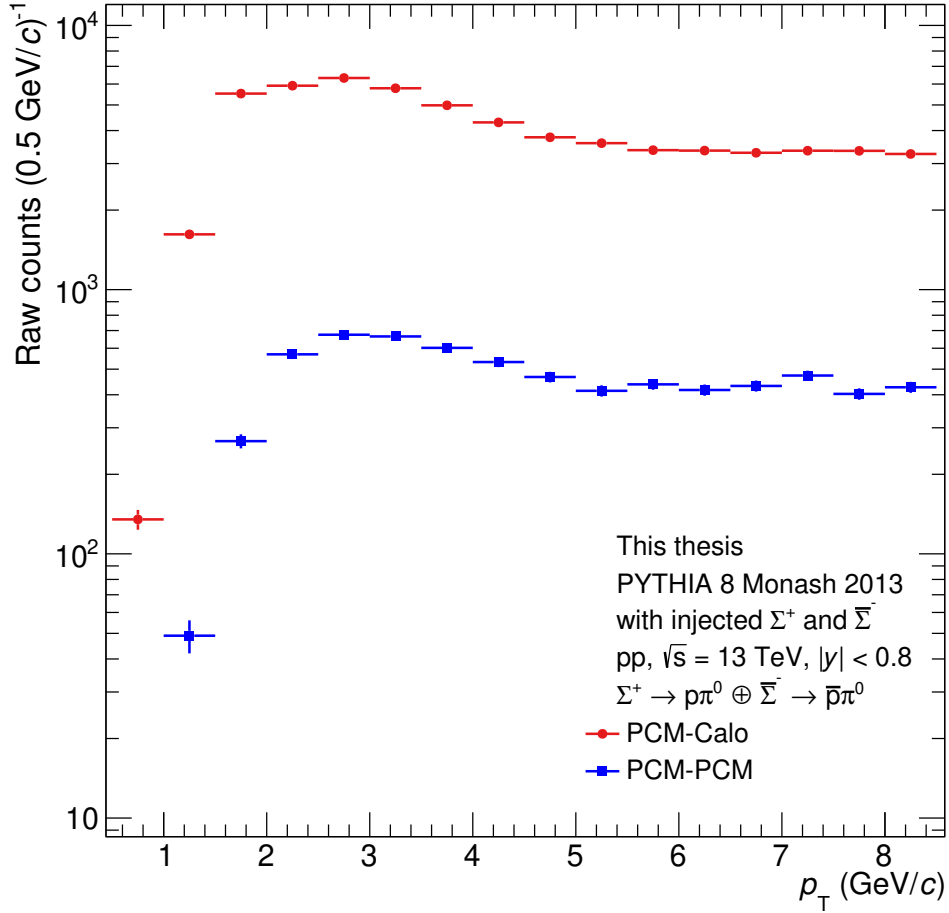


Figure 4.4: Raw spectrum of reconstructed Σ^+ in the MC simulation produced with the injection scheme described in the text. A roughly uniform distribution is reached, resulting in similar statistical uncertainties over the used p_T range.

magnitude higher than the one of the PCM-PCM method, but in both cases the efficiency is rather low. This particularly holds towards low momenta, where the efficiencies exhibit a steep decline. Clearly, it is of interest where the loss of efficiency comes from. This can again be studied in the simulations.

One may consider first that depending on the reconstruction method, 4 or 5 particles need to be measured in the final state to reconstruct the Σ^+ . Each of these particles is reconstructed and selected with a certain efficiency, which is always smaller than unity. Moreover, in case of more particles in the final state, each particle carries a smaller fraction of the Σ^+ momentum, making it harder to reconstruct. Since in the case of the Σ^+ photons are involved, the conversion probability is also major source of inefficiency. Putting these considerations

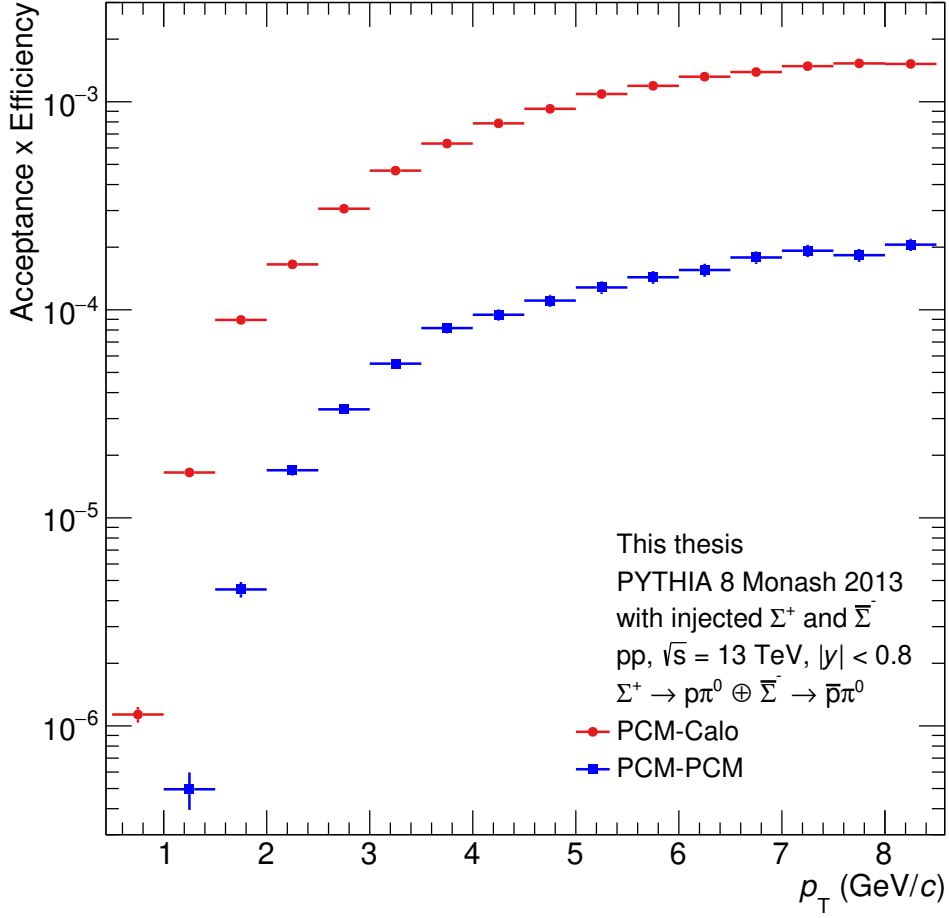


Figure 4.5: Acceptance \times efficiency of Σ^+ as a function of p_T for the PCM-PCM and the PCM-Calo method.

into numbers, one finds that above 1 GeV/ c between 90 and 95% of the protons from the Σ^+ decays could be reconstructed as tracks in the TPC. While this number decreases quite drastically below 1 GeV/ c , it still amounts to around 50% at 0.5 GeV/ c . Since the proton carries most of the momentum of the Σ^+ , the proton is clearly not the bottleneck.

The probability that a primary photon converts into an electron–positron pair is shown in Fig. 4.6 together with the probability that the photon is reconstructed by the on-the-fly V^0 finding algorithm introduced in section 2.3.2.

One can see that the conversion probability amounts to around 8.5%, corresponding to 11.4% of a radiation length, given by the material budget of the beam pipe, the ITS layers, the supporting structures, as well as the inner containment and the inner field cage of the TPC [223]. The probability that the

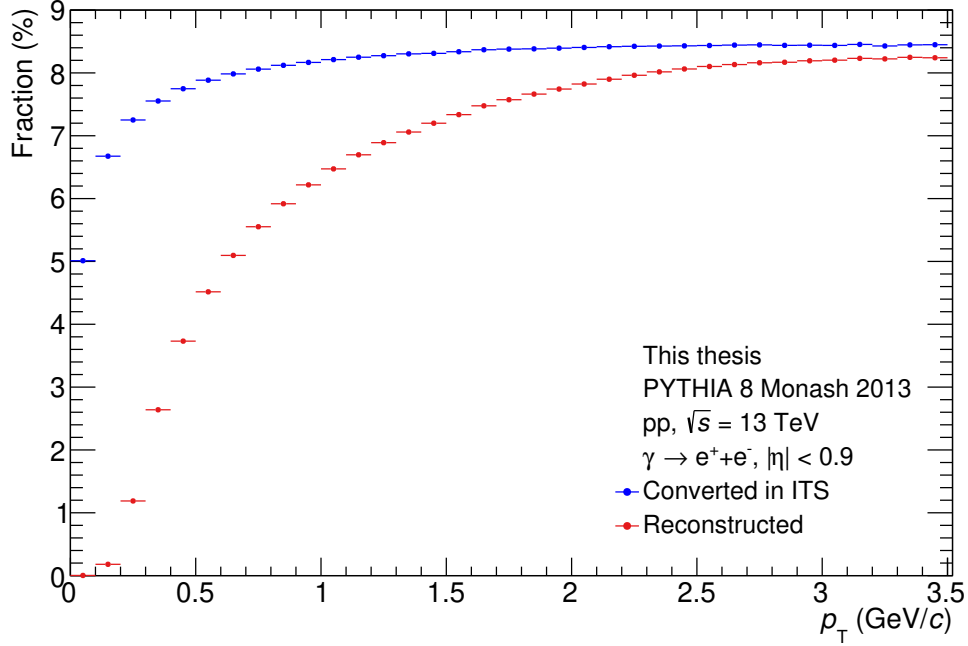


Figure 4.6: Conversion probability of photons within the ITS (blue) and their reconstruction efficiency with the on-the-fly V^0 finder (red). The conversion probability amounts to around 8% with little p_T dependence. The reconstruction efficiency shows a strong p_T dependence, reaching almost 100% at momenta above 3 GeV/ c and vanishing towards 0.

converted photon is found by the V^0 finder reaches almost 100% at higher momenta, but exhibits a drastic drop towards low momenta, reaching virtually 0 below 100 MeV/ c . The reason for this is the tracking efficiency of the electron tracks. In the case of very low momenta, the electron tracks are strongly curved, eventually curling back in the direction of the primary vertex (so-called loopers). Since there is a sizeable background of low-momentum electrons, these must be discarded.

In case of the Σ^+ , the conversion probability is further decreased by the fact that the Σ^+ baryons may traverse the beam pipe and potentially several layers of the ITS before they decay, effectively reducing the material budget ahead of the photons. In fact, the probability that none of the two photons converted increases from roughly 84% in case of primary π^0 s to 93% in case of π^0 s from Σ^+ decays.

The probability that a photon that did not convert is seen in the calorimeters amounts to around 15% with little momentum dependence, explaining the

much higher efficiency when including the calorimeters.

Lastly, the absorption of $\bar{\Sigma}^-$ in the detector material may not be described correctly in the simulation. In order to investigate this, the reconstruction efficiency is considered separately for particles and anti-particles, which is displayed in Fig. 4.7 for the PCM-Calo method. It can be seen that the efficiency of particles and anti-particles is almost equal. Below 2 GeV/ c , the efficiency of anti-particles is slightly reduced, which hints towards absorption of anti-particles. However, the difference is not significant. This behavior is also present in data. It can thus be concluded that absorption of $\bar{\Sigma}^-$ is negligible in the considered momentum region and well described by the simulation.

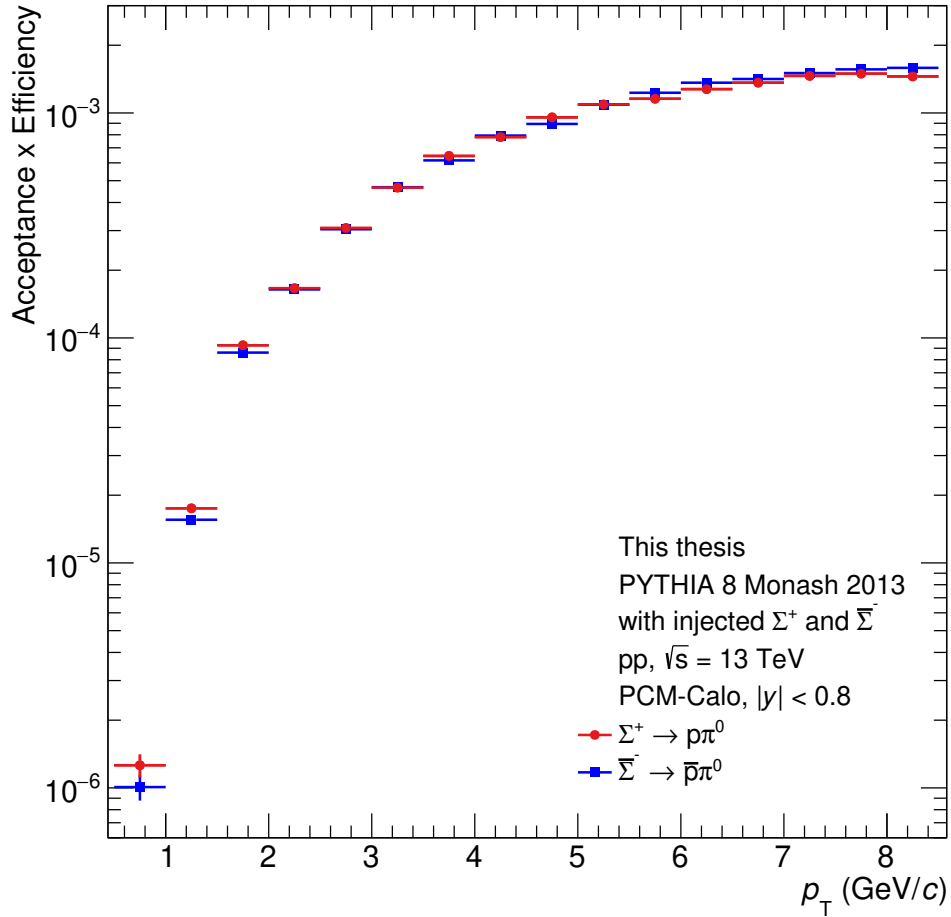


Figure 4.7: Acceptance \times efficiency of the PCM-Calo method with Σ^+ and $\bar{\Sigma}^-$ shown separately.

4.3 Invariant-mass spectra

Following the reconstruction and selection, the Σ^+ can finally be identified by their invariant mass. To calculate the invariant mass, the curved proton track is propagated to the reconstructed decay vertex to obtain the momentum components at that point. The invariant-mass distributions are displayed in Fig. 4.8 for the PCM-PCM method and in Fig. 4.9 for the PCM-Calo method. In both cases, the signal peak is well visible at the correct invariant mass of the Σ^+ of $1.189 \text{ GeV}/c^2$ [9]. The peak sits on top of a combinatorial background that needs to be described to extract the number of counts and proceed to the p_T spectra. The procedure will be discussed in the following.

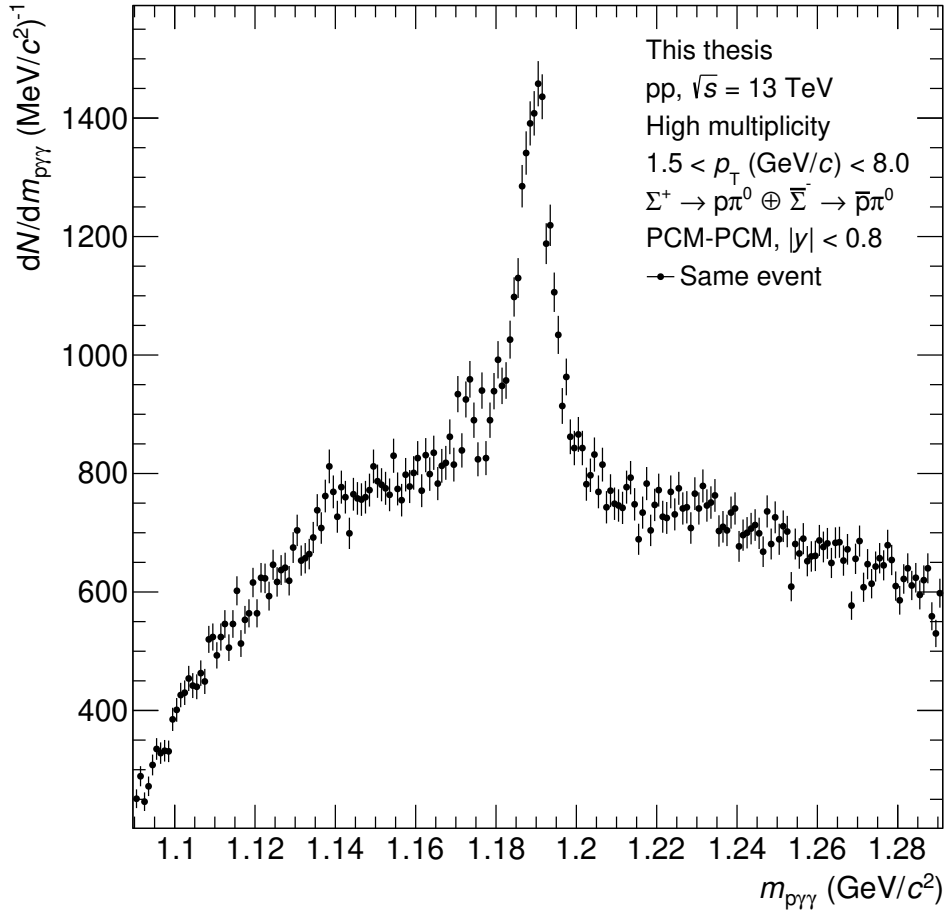


Figure 4.8: Invariant-mass distribution of Σ^+ reconstructed with the PCM-PCM method.

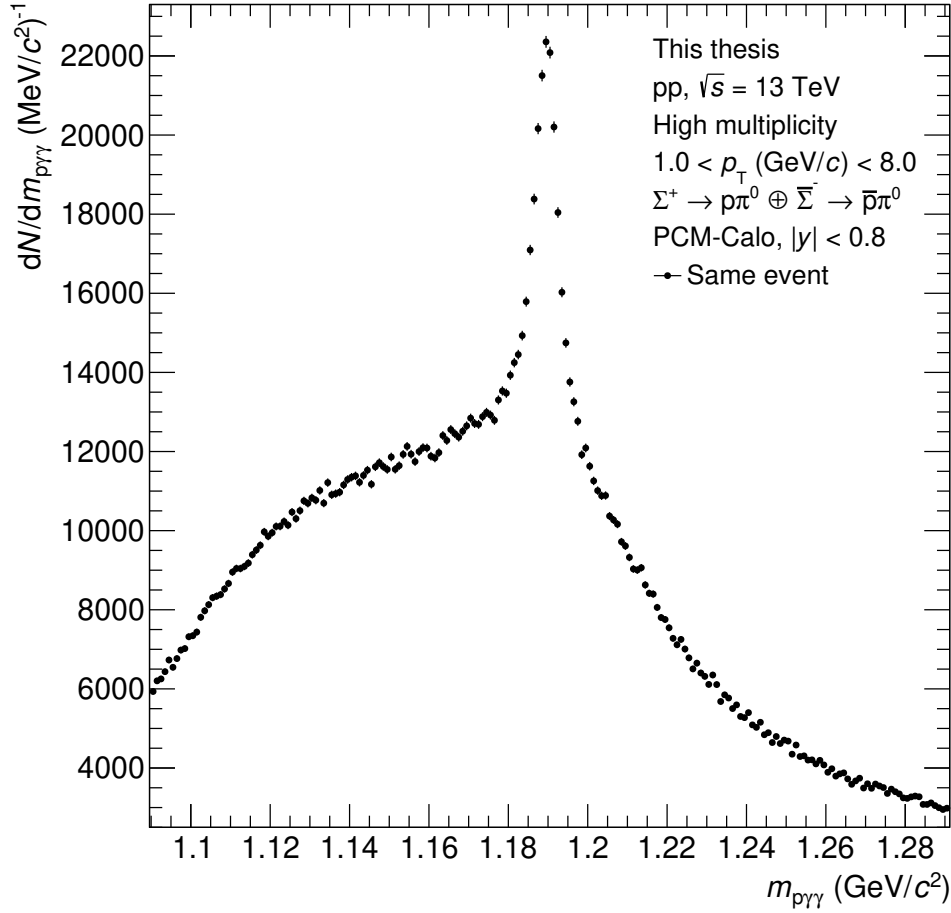


Figure 4.9: Invariant-mass distribution of Σ^+ reconstructed with the PCM-Calo method.

4.3.1 Background description

For a given number of particles in an event, the sheer combinatorics potentiates with the number of daughters of the particle of interest. This also holds for the Σ^+ and it cannot be fully mitigated by selections without affecting the efficiency in a detrimental way. Therefore, close attention needs to be given to a proper description of the background.

For the description of the combinatorial background, several techniques are commonly used. These include the use of a simulated background, fitting with a function, like-sign spectra, rotational methods, and event mixing. While the Monte Carlo background seems most attractive, this requires a very good description of the momentum spectra of all used particles, which is not always given, resulting in an insufficient description of the background. In case of in-

jected particles, the background from the simulation is of course unusable, as it is unphysical. Fitting the background with a function is the most straight forward method. Potentially, a physically motivated function is at hand or one may use a simple polynomial or exponential. This is feasible if the background is monotonic in the peak region and the peak width is not too broad. In case of Σ^+ , the background has an odd shape with a momentum-dependent maximum. As one can see in Fig. 4.9, the peak is close to a drop in the distribution, making it difficult to extrapolate the background into the peak region. In such cases, it is recommendable to choose a different background estimation. A common conception is to break the correlation between particles originating from a decay, while preserving the momentum spectra [278]. One of those techniques is the rotation method where particles are rotated around certain axes. Caution is advised if the acceptance of the detector is not uniform, as one easily creates particles which could not have been measured. Also, rotating in θ changes the transverse momentum of the particles. In case of the calorimeters in ALICE, the acceptance is limited and highly non-uniform, making the rotation method challenging. For these reasons, in this thesis the event mixing technique is used. In this method, the particles are taken from different events.

The actual phase space distribution of the particles is not known, but several samples from it, the events. It is justified to assume that any set of such samples is representative for the full distribution and can thus be used as a proxy for the phase space distribution [279]. Given that the particles stem from different events, they cannot be correlated. A major advantage of this method is that it is possible to mix an event with several others, increasing the statistics of the background distribution. However, one must consider that there are pitfalls. First of all, it has to be made sure that the acceptance of the mixed events is indeed equal. Typically, one therefore requires the events to have similar vertex positions (along the beam direction). This is also done in this analysis by requiring the vertices to have a maximum distance of 1 cm. However, the effect of this requirement is negligible. Given the sheer size of the TPC and the rather small range of vertex positions, this is easy to visualize. A much more important mixing parameter is the multiplicity of the events. Events with a high multiplicity have harder spectra, i.e. the particles have higher average momenta than low-multiplicity ones and this of course effects the derived invariant-mass spectra. Therefore, the maximum difference in the total number of tracklets

within the acceptance is restricted to 4.

In a reconstruction using more than two particles, one furthermore has to consider which particles to mix. In case of the PCM-PCM method, it is found that keeping the reconstructed pions fixed and mixing the protons is most practical and describes the background well. In case of the PCM-Calo method, however, this concept failed. The reason for this is related to the fact that the energy correction that is applied to the calorimeter photon depends on the reconstructed decay vertex, which is in turn a property of the tuple of the proton and the PCM photon. Breaking this correlation apparently leads to an unphysical background. Keeping the tuple of the proton and the PCM photon and mixing the calorimeter cluster instead has been found to be a working solution which describes the background well.

After drawing the mixed pairs, the particles are shifted by their original primary vertex position, as otherwise the inter-particle distances would be strongly biased. The reconstruction is done and the selections are applied as if the particles originated from the same event. Up to 10 events are mixed, which helps to improve the statistics. In order to describe the background quantitatively, a scaling factor has to be introduced, which is momentum dependent. It is computed by calculating the ratios of the same and the mixed-event distributions and fitting these ratios in the sideband region of the peak. In Fig. 4.10 this is plotted for one p_T bin. The resulting integrated invariant-mass spectra in the same and mixed events can be seen in Fig. 4.11 for the PCM-PCM method and in Fig. 4.12 for PCM-Calo method.

4.3.2 Peak extraction

The p_T spectra of the Σ^+ baryons are obtained by extracting the number of counts from the invariant-mass spectra. For each p_T bin, the scaled mixed-event background is subtracted from the same-event distribution and the residual spectrum is fitted with a Gaussian distribution to determine the mean and width of the peak. This is exemplarily plotted in Fig. 4.13 for one p_T bin.

The nominal rest mass of the Σ^+ as reported by the PDG [9] is well reproduced. The width of the peak is related to the momentum resolution of the protons and the photons and shows a momentum dependence. In order to check the consistency with the MC simulation, the invariant-mass spectrum of the re-

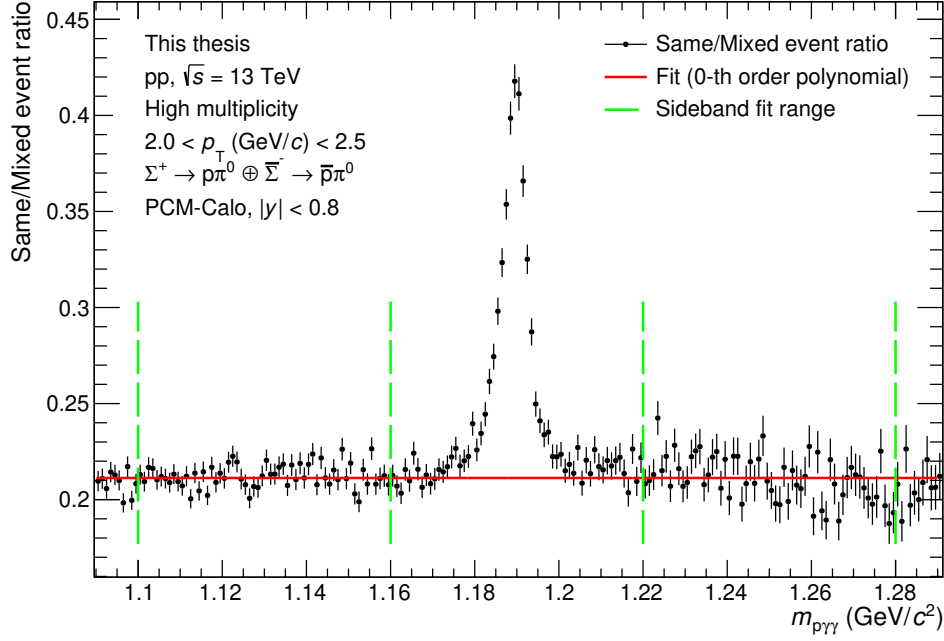


Figure 4.10: Ratio of the invariant-mass distributions in same and mixed events shown for one p_T bin. The fitting interval for the normalization and the resulting fit are also shown.

constructed Σ^+ from the simulations is superimposed over the data. This is shown in Fig. 4.14. The distribution from the simulation is scaled such that the number of entries in the data and the MC distribution match. This allows a straight forward comparison. A good agreement is found, indicating that the momentum resolution of the particles is well reproduced by the simulation and that the energy correction works there just as in data. This is of particular importance, as the resolution directly affects the selection efficiency of the Σ^+ . This will be discussed further in section 4.3.4.

To extract the number of counts, again several approaches exist. One is to integrate the Gaussian distribution. This seems appealing, as the fit smoothes out fluctuations, providing a more stable result, particularly in bins where the statistics are scarce. However, this is based on the assumption that the distribution is in fact normally distributed, which is not necessarily the case. In case of the Σ^+ , the energy correction modifies the distribution, leading to deviations in the tails of the peaks. Also, the amplitude of the fit is most sensitive only to the central bins of the peak, wherefore the statistical uncertainty of the integral is not simply given by the square root of the total number of counts. For these

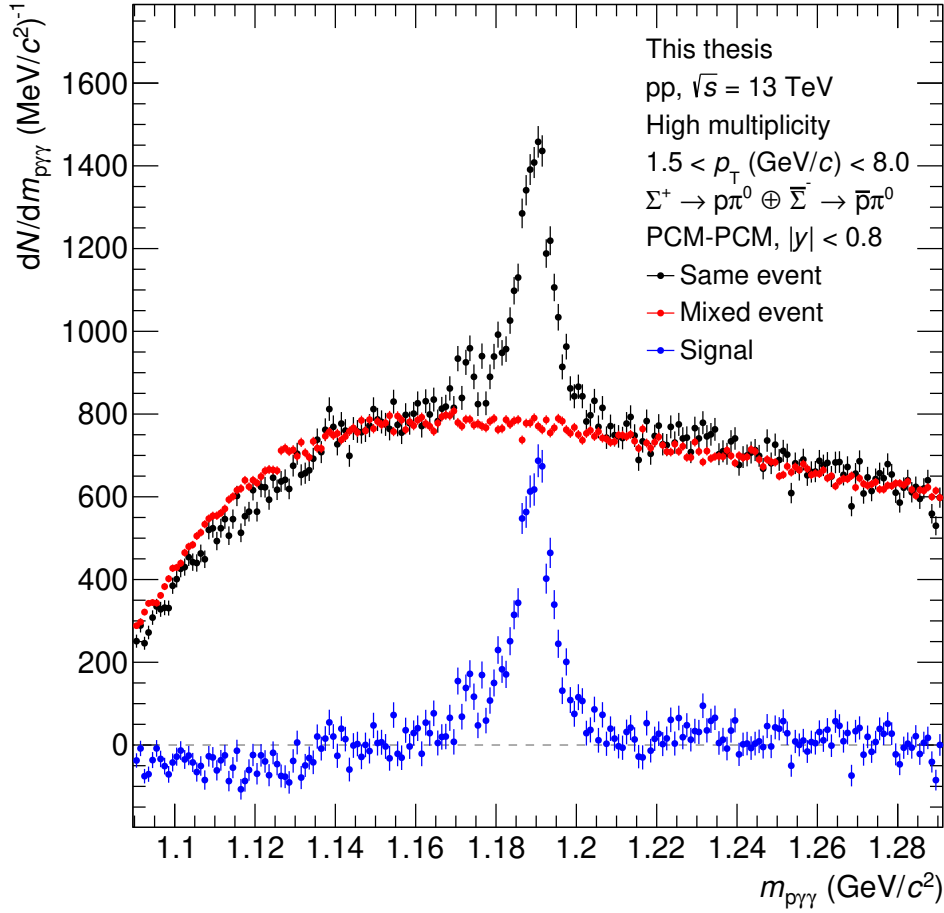


Figure 4.11: Integrated invariant-mass distribution of Σ^+ reconstructed with the PCM-PCM method in the same events (black markers) and the mixed events (red markers), as well as the signal (blue markers) calculated by subtracting the same- and mixed-event distributions.

reasons, the number of counts is determined by means of bin counting, i.e. by adding the contents of the bins in a given range. The range is defined such that it corresponds to a 3σ interval.

The raw p_T spectra are plotted in Fig. 4.15. Subsequently, the spectra are corrected for the reconstruction and selection efficiency as described in section 4.2. Additionally, the spectra are divided by the number of events, the rapidity range, and by the bin width.

Often, one needs to consider feed-down from other particles if one wants to obtain the primary p_T spectra. In case of feed-down from weak decays, the particles do not point to the primary vertex anymore, but have an offset that results

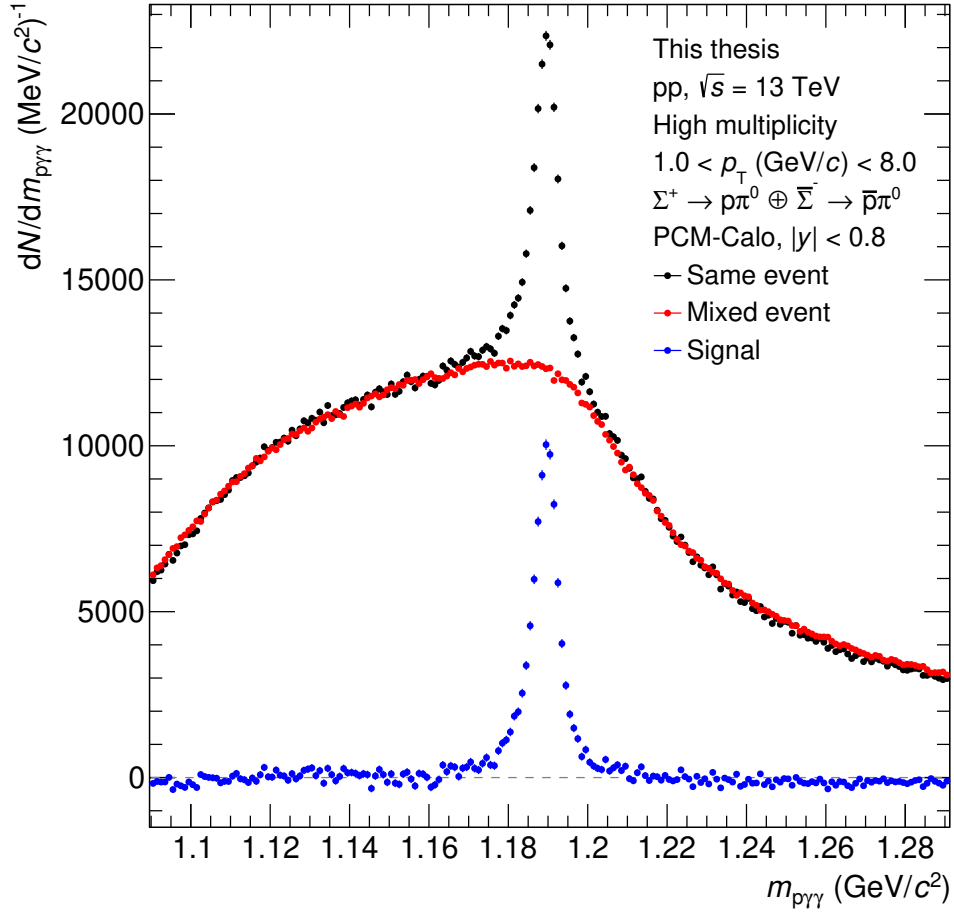


Figure 4.12: Integrated invariant-mass distribution of Σ^+ reconstructed with the PCM-Calo method in the same events (black markers) and the mixed events (red markers), as well as the signal (blue markers) calculated by subtracting the same- and mixed-event distributions.

in a larger DCA to the primary vertex for tracks and a larger pointing angle for V^0 s and cascades. The feed-down fractions are then obtained by fitting the distributions of those observables with templates from a MC simulation [15]. In case of the Σ^+ , advantageously no feed-down needs to be considered, since no baryons decay weakly into Σ^+ [9]. Thus, all Σ^+ are primary by definition²⁵. The fraction of primordially produced Σ^+ amounts to 63.17%, while the remainder stems from strongly decaying resonances [280]. A more comprehensive discussion about the strong feed-down will be made in section 5.5.1 in the context of the femtoscopic source.

²⁵Particles that originate directly from the collision or from strong or electromagnetic decays (of primary particles) are defined as “physical primaries” in ALICE [238].

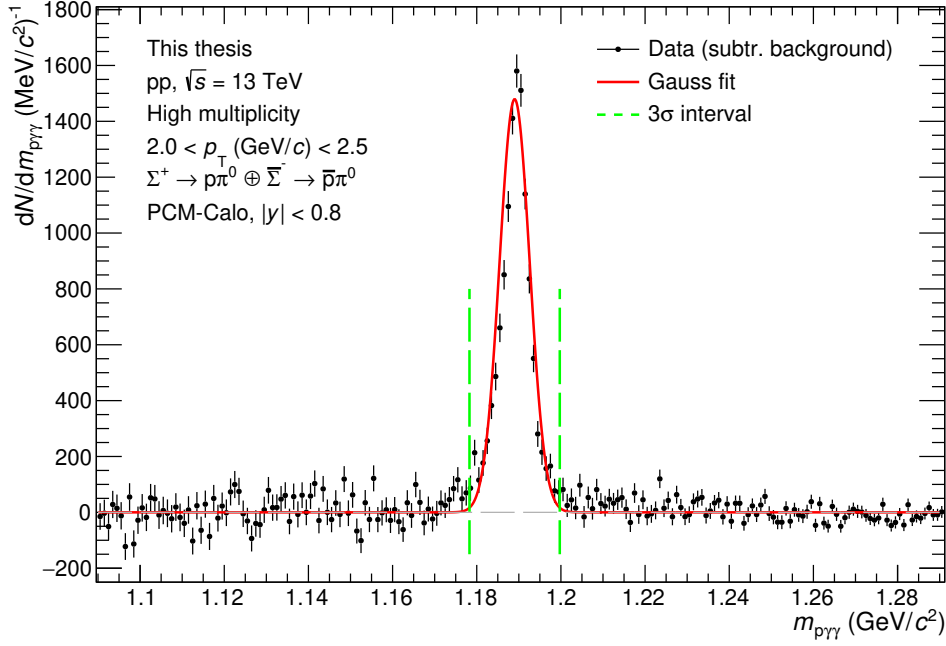


Figure 4.13: Invariant-mass distribution of Σ^+ candidates with $2 < p_T$ (GeV/c) < 2.5 with subtracted background in high-multiplicity events with the PCM-Calo method fitted with a Gaussian function. The 3σ interval is indicated by the dashed green lines.

For the minimum-bias trigger, the spectra are divided by the factor that relates the V0 visible cross section to the total inelastic cross section of pp collisions (see section 2.2.5). This allows a comparison with other results and particularly with MC generators.

Finally, the systematic uncertainties are evaluated, as explained in section 4.3.4. The resulting p_T spectra are shown in section 4.4.

4.3.3 Cross checks

In order to cross check the results and in particular to verify a proper description of the calorimeter performance in the MC simulation, two independent checks are performed.

Firstly, the spectrum using the PCM-Calo method is compared to the one using the PCM-PCM method. The comparison for the high-multiplicity triggered data is shown in Fig. 4.17. The spectra are in good agreement within the uncertainties and no systematic deviation is identifiable. This indicates that the reconstruction efficiency and in particular the conversion probability are

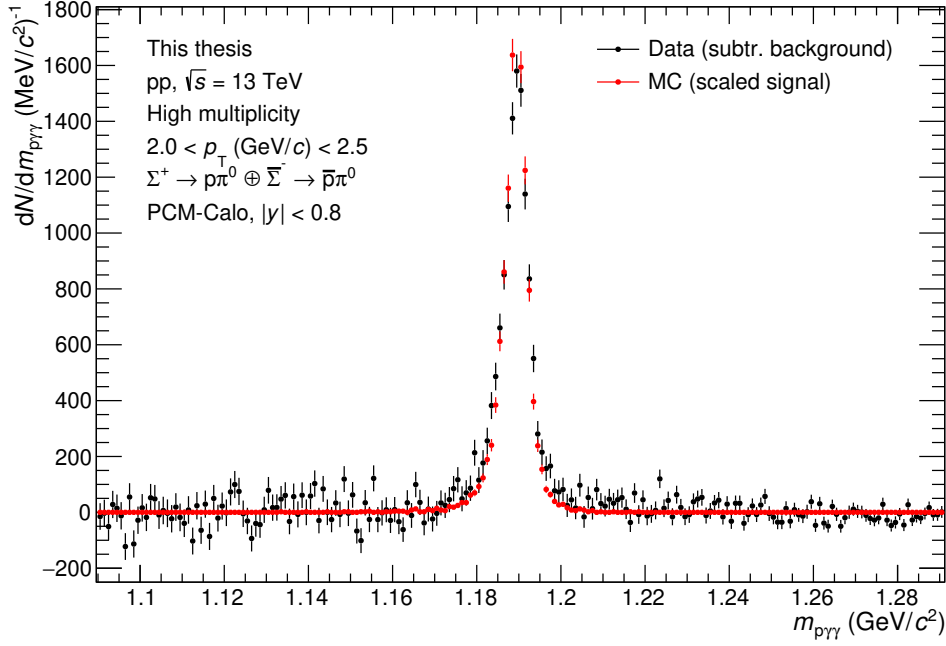


Figure 4.14: Invariant-mass distributions of Σ^+ candidates within $2 < p_T$ (GeV/c) < 2.5 with subtracted background in high-multiplicity events, reconstructed with the PCM-Calo method. The MC signal distribution is also shown. Position and width of the signal peak are well reproduced.

well described by the Monte Carlo simulation. In case of the minimum-bias triggered data, the results are also compatible, but due to the coarser necessary binning for the PCM-PCM method, the reduced p_T reach, and the much larger uncertainties, a comparison of these data points is not fruitful. Since a poor description of the calorimeter efficiency, particularly at low energies, would lead to a wrong momentum dependence of the reconstruction efficiency, a purely coincident agreement of the spectra from low to high momenta is very unlikely. However, a single comparison with a spectrum which is itself not well established is not enough to be considered proof. Thus, a selection setting was found, which gets as close as possible to the established selections, while preserving enough statistics for a reasonable comparison. For this, the minimum energy was chosen to be 200 MeV for the seed cell and 100 MeV for cell aggregation with a minimum number of 2 cells per cluster. The efficiency loss of this setting is sizeable and as large as 98% in the first bin, which can thus not be evaluated. The comparison is shown in Fig. 4.16. No systematic deviation or trend in p_T is observed. A linear fit yields a deviation from zero of around 1%, which

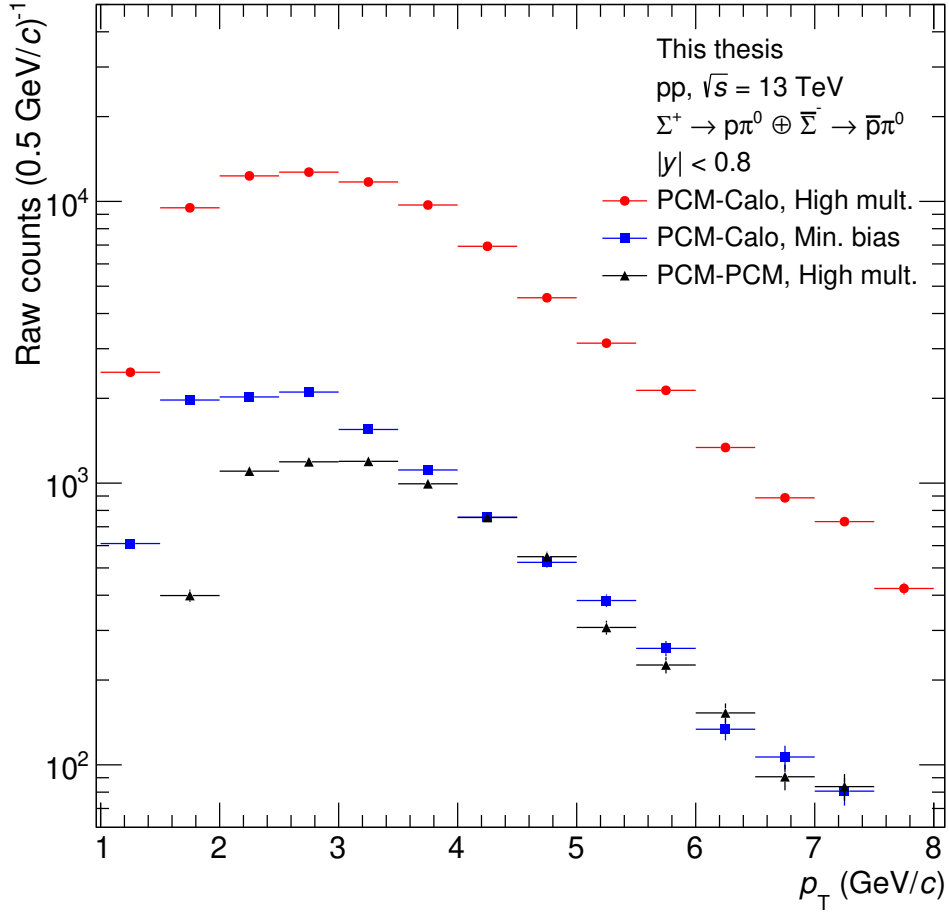


Figure 4.15: Raw p_T spectra of Σ^+ in high-multiplicity events (both reconstruction methods) and minimum-bias events (only PCM-Calo). At high multiplicity, the maximum of the distribution is shifted to higher momenta due to the hardening of the spectra. The much higher efficiency of the PCM-Calo method is visible.

is compatible with zero within the statistical uncertainties. Precautionally, an additional uncertainty is added, which is presumed to be a constant value of 3%. It shall cover all uncertainties coming from the description of the calorimeter efficiency in the simulation and thus it is listed as “cluster efficiency” in the systematic uncertainties plot (see Fig. 4.18).

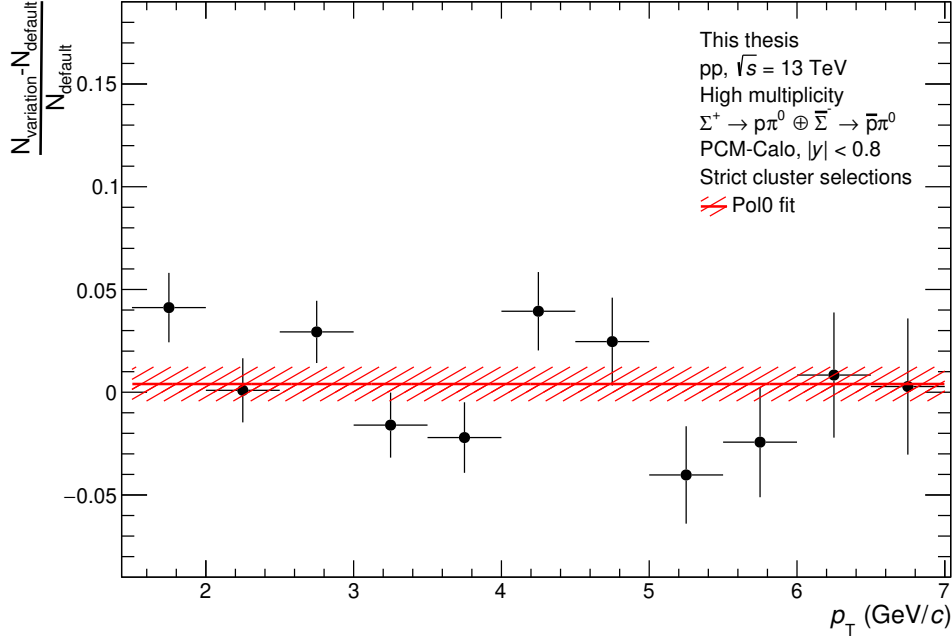


Figure 4.16: Ratio of the corrected yields of Σ^+ using the default selections for the clusters and the strict ones (see text). The shown statistical uncertainty is calculated as the square root of the difference in the raw counts divided by the default number of counts. One may also note the increased systematic uncertainty in the peak extraction when using the strong selections, which results from the much lower statistics and the different background shape. A good agreement is still found within the statistical uncertainties, suggesting that the efficiency of the calorimeters is well described by the MC simulations even at low energies.

4.3.4 Systematic uncertainties

Monte Carlo simulations are only capable of reproducing the reality to a certain extent. This finite accuracy leads to systematic uncertainties of the efficiencies used to correct the raw p_T spectra. While it is not possible to avoid such uncertainties completely, it is important to quantify them. For this, variations of the selections are made. In the following, the selections are not varied individually, but in groups, which also takes into account possible correlations of the selections and at the same time gives access to the full probability distributions. The selection groups and the ranges are listed in Tab. 4.1. The number of variations per group is 600 for the topological selections, 200 for the kinematic selections, 150 for the PID selections, and 50 for the track selections. These numbers are tuned to roughly scale with the number of selections per group and the impact of the selections. The range in which each selection is varied is defined

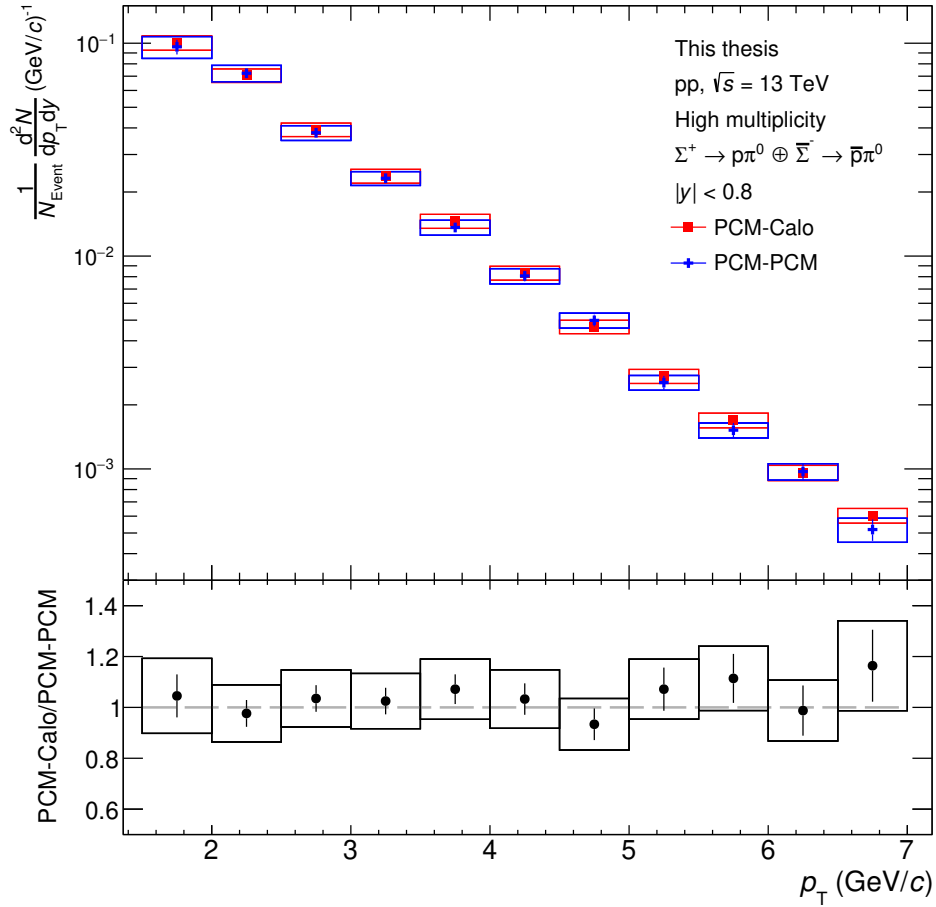


Figure 4.17: Comparison of Σ^+ spectra using the PCM-PCM and the PCM-Calo method. Correlations of the uncertainties are neglected. Even though the reconstruction efficiencies of both methods are approximately one order of magnitude apart, a good agreement is found, indicating that the reconstruction efficiencies are well described in the MC simulations.

such that it corresponds to half a unit of standard deviation for the (roughly) normally distributed observables and around 10% for the others. Defining too large ranges does not make sense in this case, as every deviation from the default values decreases the significance of the signal by construction and thus increases the difficulty of the peak extraction. At some moment, this would only create outliers and does not help in determining the systematic uncertainties. Within the groups of selections, different sets of selections are randomly chosen from uniform distributions such that each setting is equally likely. The raw spectra and the corresponding efficiencies are automatically evaluated for each variation and the residual to the default setting is saved. The distributions

obtained by this procedure are fitted with Gaussian distributions in order to determine the mean and the width. Using the width of many variations as a proxy for the systematic uncertainties makes this method rather insensitive to outliers compared to using a single variation. The distributions of the variations are not necessarily centered at zero, which indicates that the default value is not the most probable one. This, in turn, gives rise to asymmetrical error bars. One must clarify that if one defines the systematic uncertainty as one unit of standard deviation, this only means that roughly 68% of the variations are within these limits. It does not state that there is an equally large probability that the true value is within the error bars. In fact, selection variations cannot give access to this information, as this requires completely independent measurements by different methods or experiments.

In addition to the variational systematic uncertainties, uncertainties arise from the conversion probability, i.e. the material budget, the ITS-TPC matching efficiency, and the mixed-event normalization. The uncertainty of the material budget is reported to be 0.5% of a radiation length, corresponding to 4.5% of the total material budget [223]. A recent study uses a data-driven approach to reduce the uncertainty to 2.5% [281]. While the procedure is not yet implemented in this analysis, it paves the way for future improvements of the measurement. The total uncertainty of the ITS-TPC matching efficiency is estimated at 4% based on previous analyses [282] and considering that in the PCM-Calo method 3 tracks have to be measured in the final state. The uncertainty stemming from the mixed-event normalization is assumed to be 2%. The aforementioned contributions are assumed to be momentum independent. Finally, the total uncertainties are calculated by adding the contributions quadratically. The contributions to the systematic uncertainty are displayed in Fig. 4.18. The uncertainties caused by the material budget and the ITS-TPC matching efficiency clearly dominate the systematic uncertainties at intermediate momentum, while the impact of the topological and kinematic selections increases towards low p_T . One may note that systematic uncertainties evaluated by variations always contain a statistical admixture. Given a finite amount of statistics, the number of particles fulfilling a certain selection set is statistically distributed, both in data and in the simulation. Consequently, one would observe non-zero deviations of the yields, even if there was no systematic uncertainty at all. Thus, in the case of large statistical uncertainty, one may ask to which extent the observed devia-

tions are really systematic in nature. A well known check is the so-called Barlow criterion [283], which relates the deviation of a given variation to the statistical uncertainty to probe whether it is significant. In case of the here made random variations, this check is non-trivial and not necessarily meaningful. While Fig. 4.18 depicts the uncertainties for the high-multiplicity spectrum using the PCM-Calo method, the values of the contributions show striking similarities for the minimum-bias spectrum and the PCM-PCM method as well, despite the vastly different statistics. This implies that the evaluated uncertainties are indeed of systematic origin. Therefore, all systematic contributions are considered to be significant over the full p_T range, which is the most conservative assumption.

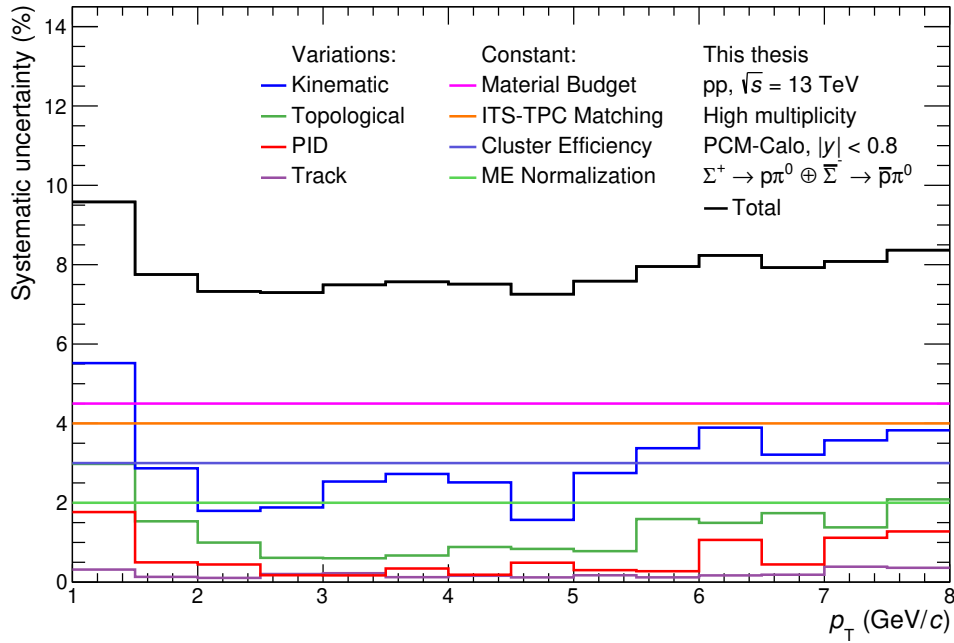


Figure 4.18: Different contributions (in different colors, where the quadratic sum is shown in black) to the systematic uncertainty as a function of p_T for the high-multiplicity spectrum of Σ^+ using the PCM-Calo method.

Group	Selection	Default value	Minimum	Maximum
Topological	Track $ \eta $	0.9	0.8	1.0
	Photon opening angle	0.30 rad	0.27 rad	0.33 rad
	Photon $\Delta\Theta$	0.10 rad	0.09 rad	0.11 rad
	Photon radius (lower)	3.0 cm	2.7 cm	3.3 cm
	Photon radius (upper)	220 cm	210 cm	230 cm
	Proton DCA _{xy} (lower)	0.010 cm	0.009 cm	0.011 cm
	Proton DCA _{xy} (upper)	2.0 cm	1.5 cm	2.5 cm
	PA (PCM) ($p_T < 3$ GeV/ c)	0.040 rad	0.036 rad	0.044 rad
	PA (PCM) ($p_T > 3$ GeV/ c)	0.030 rad	0.027 rad	0.033 rad
	PA (PCM) ($p_T > 5$ GeV/ c)	0.020 rad	0.018 rad	0.022 rad
	PA (Calo) ($p_T < 2$ GeV/ c)	0.024 rad	0.022 rad	0.026 rad
	PA (Calo) ($p_T > 2$ GeV/ c)	0.012 rad	0.011 rad	0.013 rad
	Flight distance (lower)	1.0 cm	0.9 cm	1.1 cm
	Flight distance (upper)	50 cm	45 cm	55 cm
	DCA (track-cluster)	10 cm	9 cm	11 cm
Kinematic	Photon $ \alpha $	0.9	0.8	1.0
	Photon q_T	0.03 GeV/ c	0.027 GeV/ c	0.033 GeV/ c
	Photon invariant mass	0.06 GeV/ c^2	0.05 GeV/ c^2	0.07 GeV/ c^2
	π^0 mass (lower)	0.10 GeV/ c^2	0.09 GeV/ c^2	0.11 GeV/ c^2
	π^0 mass (upper)	0.16 GeV/ c^2	0.15 GeV/ c^2	0.17 GeV/ c^2
	Minimum cluster energy	0.10 GeV	0.10 GeV	0.15 GeV
PID	Electron TPC n_σ	5.0	4.5	5.5
	Proton TPC n_σ	3.0	2.5	3.5
	Proton TOF n_σ	3.0	2.5	3.5
Track	Proton TPC clusters	60	50	70
	Electron TPC clusters	30	20	40

Table 4.1: Selections of Σ^+ with systematic variation ranges. The number of variations for each group is given in the text.

4.4 Integrated yields

In order to compare to model calculations, the total yield of the Σ^+ is of interest. The comparably high cut-off of 1 GeV/ c is caused by the vanishing reconstruction efficiency of the photons. Consequently, the unobserved fraction of the production yield is sizeable. To determine the total yield, it is thus crucial to fit the spectra with a proper fit function. Several fit functions are tested, which have been introduced in section 1.2.1. The simple models, namely Maxwell-Boltzmann, m_T exponential, p_T exponential, and Fermi-Dirac all come with only two free parameters, the slope parameter and the normalization. The p_T exponential is tested just for completeness and in spite of the fact that the underlying assumption ($p_T \gg m$) is not fulfilled. As expected, the models only provide a reasonable fit in the intermediate p_T region and show sizeable deviations at low and high p_T as seen in Fig. 4.19. In contrast, the more sophisticated Lévy-Tsallis [86, 91, 92] and Boltzmann-Gibbs blast wave [84, 85] functions both allow to fit the data well.

As expected for pp collisions, the Lévy-Tsallis function describes the data best over the full considered p_T range and is thus used for the extrapolation. The integration of the spectra is performed by adding the data points in the measured region and by a numerical integration of the fit function in the unobserved region. This procedure effectively limits the dependence of the fit quality to the extrapolation region.

The statistical and systematic uncertainties of the extrapolated yield are determined by performing random variations of the data points within their uncertainties. In case of the statistical uncertainties, the uncertainties of the data points are uncorrelated, giving rise to an individual variation. In case of the systematic uncertainties it is, however, a legitimate question if this also holds. One may consider that it is well possible that the efficiency of a certain selection is underestimated by the simulation at low momenta and overestimated at high momenta or vice versa. Thus, an individual variation is also justified for the systematic uncertainty. Generally, an individual variation does not only shift the fit up or down, but also changes the shape, which yields a more conservative estimation of the uncertainty. Therefore, this approach is followed. Each variation of the spectra is fitted and the obtained array of curves is displayed in Fig. 4.20. The yield is calculated for each fit function and the standard devi-

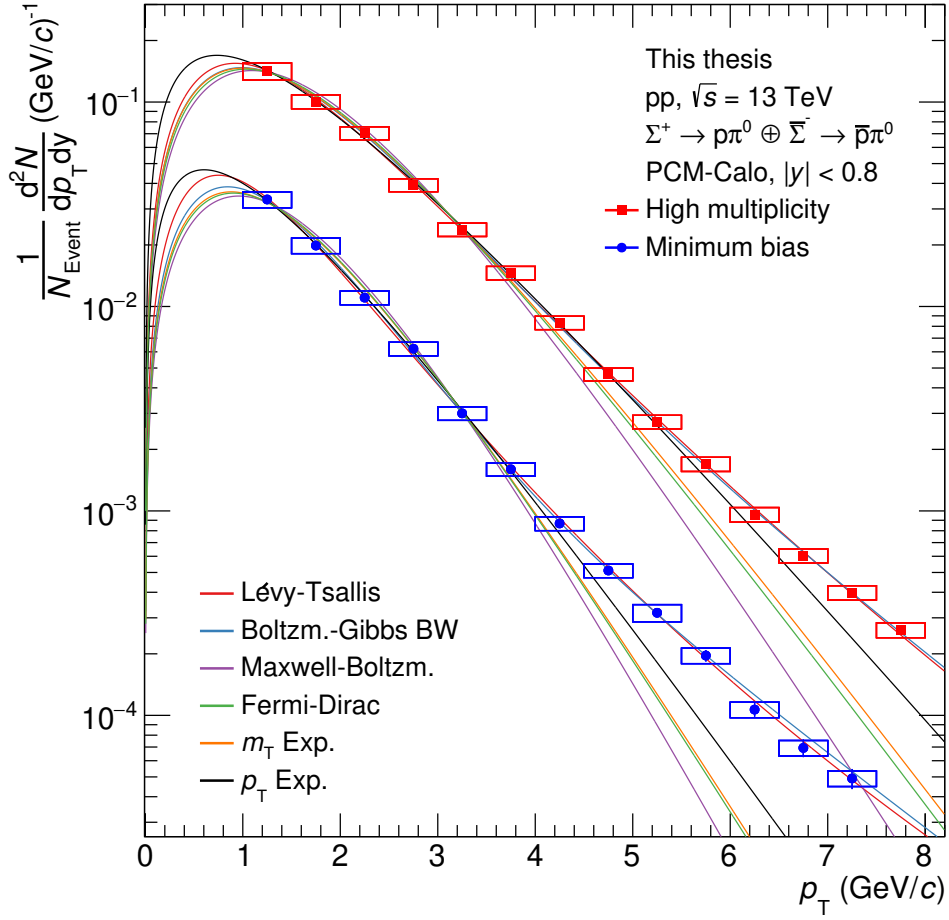


Figure 4.19: Corrected p_T spectra of Σ^+ with different fit functions. The Lévy-Tsallis function describes the data best and is used to extrapolate the spectra to the unobserved region ($p_T < 1$ GeV/c).

ation of these yields is considered as the uncertainty of the extrapolation. This procedure is done individually for the statistical and systematic uncertainties. The results are given in Tab. 4.2.

It is apparent that the contribution of the extrapolated yield is around 4/9 in case of the minimum-bias spectrum, but only 1/3 in case of the high-multiplicity spectrum. This is due to the hardening of the p_T spectrum with increasing multiplicity as discussed before.

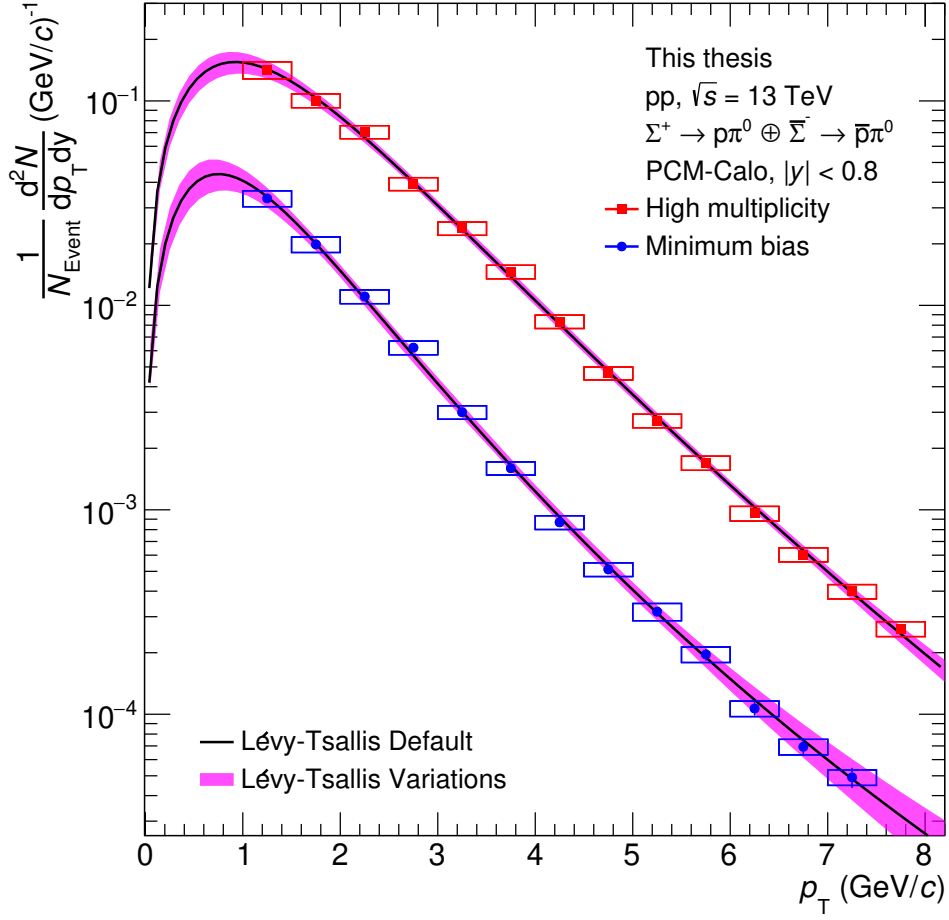


Figure 4.20: Array of curves resulting from the variations of the fit. The standard deviation of the extracted yields is considered as the uncertainty of the extrapolation.

Trigger	Minimum bias	High multiplicity
Data ($p_T > 1$ GeV/c)	$0.0387^{+0.0014}_{-0.0014}(\text{stat})^{+0.0032}_{-0.0034}(\text{syst})$	$0.2054^{+0.0045}_{-0.0045}(\text{stat})^{+0.0154}_{-0.0185}(\text{syst})$
Fit ($p_T < 1$ GeV/c)	$0.0325^{+0.0012}_{-0.0011}(\text{stat})^{+0.0046}_{-0.0043}(\text{syst})$	$0.1077^{+0.0021}_{-0.0022}(\text{stat})^{+0.0112}_{-0.0139}(\text{syst})$
Total	$0.0711^{+0.0026}_{-0.0025}(\text{stat})^{+0.0077}_{-0.0077}(\text{syst})$	$0.3131^{+0.0066}_{-0.0067}(\text{stat})^{+0.0265}_{-0.0324}(\text{syst})$

Table 4.2: Yields dN/dy of Σ^+ and $\bar{\Sigma}^-$ for the two considered triggers. The yields of the measured region (data points) and the extrapolated region (fit) are given separately as well as the sum of both.

4.5 Thermal model comparison

The obtained yields of the Σ^+ are compared to thermal model calculations. Therefore, the γ_s CSM model [80, 284] is used, which was introduced in section 1.2.1. The calculation is performed using a canonical and a grand-canonical approach, where in the canonical approach slightly different values for the different multiplicities are found. For the comparison to the data, the ratio to Λ baryons is considered. This is practical, since many dependences cancel out [80]. Also, it allows a comparison to Σ^0 baryons, since the Σ^0/Λ ratio was measured in a previous analysis in ALICE [2]. The yields of Λ baryons in pp collisions at 13 TeV are measured and publicly available [242, 285]. This data is given in multiplicity classes, which do not equal the multiplicities of the triggers used in this analysis. However, the yields can be inter- or extrapolated, making use of the roughly linear scaling of the yields with multiplicity. To do so, the mean tracklet multiplicities in $|\eta| < 0.5$ are evaluated for the used triggers. These amount to $dN_{ch}/d\eta = 30.8 \pm 0.4$ for the high-multiplicity trigger and $dN_{ch}/d\eta = 6.9 \pm 0.1$ for the minimum-bias trigger. The resulting yields of the Λ baryons and the resulting ratios of Σ^+ and Λ are given in Tab. 4.3.

Trigger	$\frac{dN}{dy} (\Lambda \oplus \bar{\Lambda})$	$\frac{\Sigma^+ \oplus \bar{\Sigma}^-}{\Lambda \oplus \bar{\Lambda}}$
Minimum bias	$0.26150 \pm 0.00047(\text{stat}) \pm 0.01848(\text{syst})$	$0.272^{+0.010}_{-0.010}(\text{stat})^{+0.035}_{-0.035}(\text{syst})$
High multiplicity	$1.13467 \pm 0.00380(\text{stat}) \pm 0.07700(\text{syst})$	$0.275^{+0.006}_{-0.006}(\text{stat})^{+0.030}_{-0.034}(\text{syst})$

Table 4.3: Yields of Λ and $\bar{\Lambda}$ at the mean multiplicities corresponding to the used triggers. From these, the given ratios are computed. Values for Λ inter- or extrapolated as described in the text using the data from Ref. [242, 285].

Apparently, the Σ^+/Λ ratios are practically identical for the two considered multiplicities. This might seem surprising, considering the large systematic uncertainty of the ratios. However, one needs to keep in mind that these are almost fully correlated, since the same efficiencies are used to correct both Σ^+ yields. The uncertainty of the material budget for instance affects the yields at both multiplicities in the same way. Similar considerations also hold for the measurement of Λ [242]. Thus, for the comparison of the ratios, only the statistical uncertainty is of interest, which is considerably smaller.

In the canonical thermal model calculation, a ratio of 0.2714 for minimum bias and 0.2847 for high multiplicity is found. The grand-canonical calculation, in turn, gives a value of 0.2731. Interestingly, the grand-canonical value is not above the high-multiplicity value, which is due to the non-monotonicity of the model parameters [80]. In both cases, the values are close to the 1:3 ratio which one would expect from the pure isospin consideration in the absence of a mass splitting between Λ and Σ baryons. While the data slightly favours the grand-canonical calculation, this conclusion cannot be made, given the uncertainty of the data. However, clearly a very good agreement of the data and the thermal model calculation is found.

For the Σ^0/Λ ratio, a preliminary value of 0.319 ± 0.065 is reported [2]. While this is in slight tension with the values found here, one needs to note that this data was taken at 7 instead of 13 TeV and that it is still compatible within the combined uncertainty.

Due to the present uncertainty, no conclusive statement about strangeness enhancement for Σ baryons can be made yet. However, the ratios at the two multiplicities are in very good agreement, which supports the assumption that the same strangeness enhancement at high multiplicities, which is seen in Λ baryons (see Fig. 1.4), is also present for Σ baryons.

4.6 MC comparisons

The spectrum of Σ^+ is compared to the spectra of multiple commonly used MC generators. Comparing the high-multiplicity spectrum would require to replay the trigger conditions in the simulation which is not trivial. As mentioned in section 4.2.1, this has been attempted using PYTHIA 8 Monash 2013 events. However, it was found that the multiplicity does not match the one in data exactly, which is apparently related to an error in the implementation of the trigger conditions found later. A comparison of this production to data is therefore not particularly meaningful. More naturally, the minimum-bias spectrum is used for the comparison with the generators. First of all, PYTHIA 8 Monash 2013 [62, 277] is tested, as it is the standard event generator for pp collisions in ALICE. Another frequently used generator is EPOS LHC [63]. Moreover, an older version of PYTHIA is used, namely PYTHIA 6 [95] with the tune Perugia 2011 [286]. Lastly, the recently published fourth version of

EPOS (EPOS4) [96–99] is considered. At least one reconstructed track is required in all events for the determination of the number of events for the normalization, which puts the data and the simulation on a common ground. The measured mean multiplicities found in data and in the generators match within 2%, providing a reasonable comparison. The obtained spectra and the ratios to data are depicted in Fig. 4.21. Generally, a reasonable description of the data is achieved by all generators. The yields are underestimated by around 1.5 to 2, which is a common finding for strange hadrons [7, 8]. The spectral shape is more or less captured, with EPOS LHC [63] performing best and PYTHIA 6 [95] worst. Notably, the shape of the MC spectra is closer to the one of Λ s, implying that the generators have been tuned to these, as this data is readily available. This, however, results in a comparably flat Σ^+/Λ ratio as a function of p_T . A similar finding was made for Σ^0 [2]. This again leads to a ratio of the integrated yields of around 0.4, both in PYTHIA and in EPOS, which is neither supported by thermal model calculations, nor by the data presented in this thesis (see previous section). This finding underlines the importance of the Σ baryon p_T spectra to tune those models.

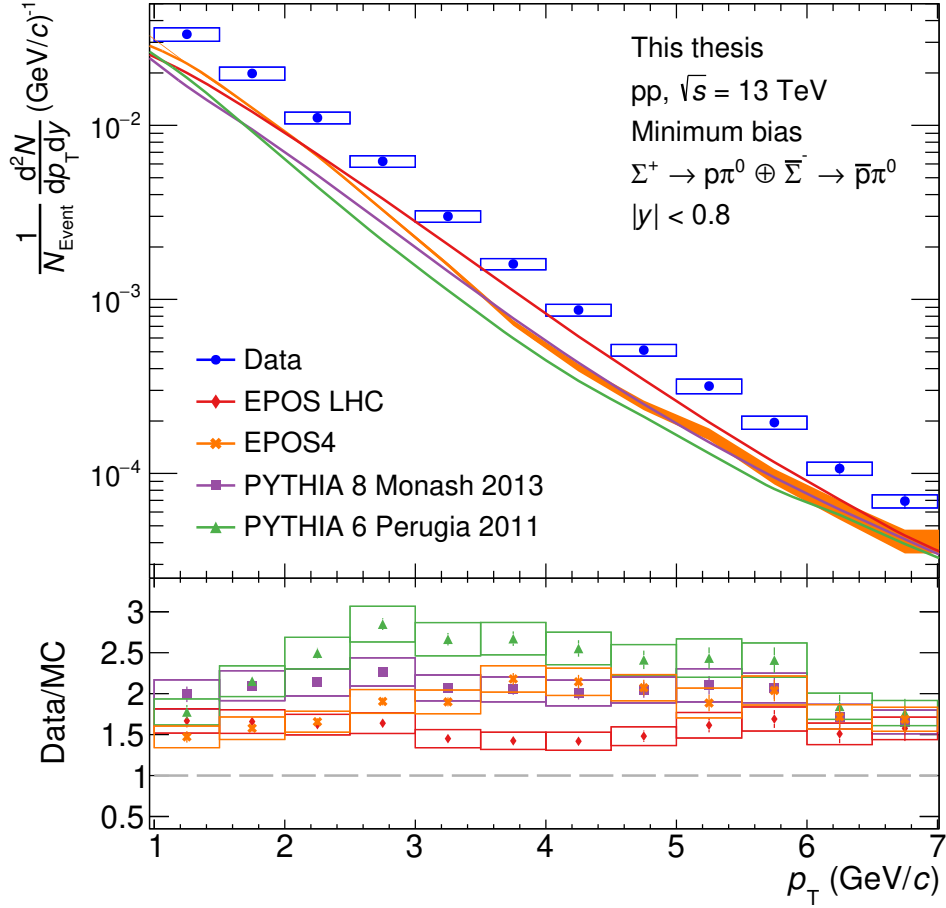


Figure 4.21: Comparison of the minimum-bias Σ^+ p_T spectrum in pp collisions at $\sqrt{s} = 13$ TeV with PYTHIA 6 [95], PYTHIA 8 [62], EPOS LHC [63], and EPOS4 [96–99] event generators. Generally, the p_T shape is reasonably well described, while all generators underestimate the production of Σ^+ by a factor of around 2.

5 Measurement of the $p\text{--}\Sigma^+$ correlation function

In this chapter, the measurement of the correlation function of protons and Σ^+ and its comparison to theory is presented. As already discussed, the partially Pauli-forbidden decuplet channel is inaccessible by the $N\text{--}N$ and $N\text{--}\Lambda$ systems [20], which leads to a large uncertainty on the nature of this interaction. Extending the femtoscopic studies to the Σ sector is thus inevitable to complete the picture. In the context of neutron stars, the Σ^- baryons are most interesting to study, as these would presumably occur first [12–14]. Experimentally, however, their decay into a neutron makes them almost inaccessible, at least for femtoscopic measurements (compare section 5.1.6). The Σ^0 is, in contrast, relatively easy to reconstruct, as it decays into a Λ and a photon [9] that can both be measured. Consequently, the $p\text{--}\Sigma^0$ was measured in a previous analysis [22, 23]. However, multiple caveats are present in this channel. Firstly, the purity of the Σ^0 is low due to its short lifetime as discussed earlier. The genuine contribution to the correlation function is only 22% in the given analysis, while the dominant contribution is the $p\text{--}\Lambda$ correlation function, smeared by an uncorrelated photon. Together with the limited statistics, this results in insignificant and not particularly meaningful results; the measured correlation function is in good agreement with both the $p\text{--}\Lambda(\gamma)$ baseline as well as all considered models within less than 1σ [22, 23]. Furthermore, the presence of coupled channels ($p\Sigma^0 \leftrightarrow p\Lambda$ and $p\Sigma^0 \leftrightarrow n\Sigma^+$) imposes an additional complication.

The Σ^+ allows much higher purities due to its weak decay and additionally coupled channels at low k^* are completely absent. Following these considerations, one can conclude that the $p\text{--}\Sigma^+$ channel is the best suited one to study the interaction between Σ baryons and nucleons.

Nonetheless, one needs to take another look at the reconstruction of the Σ^+ . As shown in section 4.2, the inclusion of the calorimeters and consequently the

omission of the demand of two photon conversions significantly improved the reconstruction efficiency. However, one must recall that the acceptance of the calorimeters in ALICE is rather small and does not nearly cover the full acceptance of the central barrel detector [231–233]. This limits the efficiency and leads to a non-isotropic acceptance, which is not well suited for femtoscopic measurements. In fact, it is found that the statistics obtained by the reconstruction method presented in chapter 4 is still insufficient for a significant femtoscopic signal. The reason for this is that the region of interest in femtoscopy is at (very) low relative pair momenta. In order to have such low pair momenta, the particles not only need to have similar momenta, but also need to enclose a small angle. This two-dimensionality leads to a very high demand on the statistics. In case of protons and Σ^+ , this is aggravated by the completely different p_T dependences of the reconstruction efficiencies, which limits the overlap in momentum space. For this reason, it was necessary to improve the reconstruction even further, which will be presented in section 5.1.1.

Beyond the particle reconstruction, new methods for the determination of the λ parameters and the phase-space contribution to the correlation function have been developed within the scope of this thesis. They will be presented in section 5.3 and 5.4.1, respectively. The purpose of these measures is to mitigate common issues and minimize systematic uncertainties, ultimately optimizing the significance of the measurement.

5.1 Σ^+ sample

As already seen in section 4.2, the bottleneck of the reconstruction efficiency are the photons. Removing one of the conversion photons and replacing it with a calorimeter cluster greatly helped improving the efficiency, so it seems natural to follow this idea and drop the second photon completely. Such missing-mass analyses are not uncommon in high-energy physics and might be employed if an unobservable particle like a neutron or neutrino occurs at any point in the decay chain [287]. In such cases, the information on the unobserved particle is missing. This adversely affects the momentum resolution of the mother particle, which is, nonetheless, crucial for the calculation of the correlation function. In case of Σ^+ , however, one can use domain knowledge on the decay to derive the missing momentum components, which will be described in the following.

5.1.1 Missing-mass reconstruction

In section 4.1 it was discussed that one can make use of the short lifetime of the neutral pion to reconstruct the decay vertex of the Σ^+ using only the proton and one of the photons. This is also done here. Once the topology is known, one can make use of momentum conservation and the fact that the Σ^+ decay consists of two consecutive two-body decays to derive the momentum components of the unobserved photon. The transverse momentum of the proton with respect to the flight direction of the Σ^+ equals the corresponding transverse momentum of the pion. The same holds true for the transverse momenta of the two photons with respect to the flight direction of the pion. This already allows to eliminate two of the momentum components of the unobserved photon. The third one can then be calculated from the known invariant mass of the π^0 .

The laboratory system is not well suited to solve the constraints outlined above. Instead, one might consider the following orthonormal basis with the unit vectors \vec{e}_1 , \vec{e}_2 , and \vec{e}_3 . The vector \vec{e}_1 points in the flight direction of the Σ^+ and can be constructed from the decay vertex and the primary vertex. The vector \vec{e}_2 is perpendicular to the decay plane of the Σ^+ and is constructed by the cross product of the (normalized) momentum vector of the proton and \vec{e}_1 . The vector \vec{e}_3 is then perpendicular to \vec{e}_1 and \vec{e}_2 and points in the direction of the transverse momentum component of the proton with respect to the flight direction of the Σ^+ . Due to the choice of this coordinate basis, the problem to solve effectively becomes a two-body problem in each dimension, which is straight forward to solve using the conservation of momentum.

Let $\vec{p}_p = \{p_{x_p}, p_{y_p}, p_{z_p}\}$ be the momentum vector of the proton in the basis described above and $\vec{p}_{\gamma 1} = \{p_{x_{\gamma 1}}, p_{y_{\gamma 1}}, p_{z_{\gamma 1}}\}$ and $\vec{p}_{\gamma 2} = \{p_{x_{\gamma 2}}, p_{y_{\gamma 2}}, p_{z_{\gamma 2}}\}$ be the momentum vectors of the observed and the unobserved photon, respectively. In this nomenclature, p_{z_p} is the transverse momentum of the proton with respect to the flight direction of the Σ^+ . Obviously, this needs to be compensated by the photons, which implies

$$p_{z_{\gamma 2}} = -(p_{z_p} + p_{z_{\gamma 1}}). \quad (5.1)$$

The same holds for the second component, which is, however, zero for the proton. Vividly, the second momentum component points outside of the plane of the proton and the π^0 , thus it needs to be carried by the photons alone,

which then implies that

$$p_{y_{\gamma 2}} = -p_{y_{\gamma 1}}. \quad (5.2)$$

For the third component, one may consider Eq. (4.1), which relates the invariant mass of the pion to the momentum of the photons and the angle they enclose. With this one finds

$$m_{\pi^0}^2 = 2 \cdot (|\vec{p}_{\gamma 1}| \cdot |\vec{p}_{\gamma 2}| - |\vec{p}_{\gamma 1} \cdot \vec{p}_{\gamma 2}|). \quad (5.3)$$

Equation (5.3) can now be solved for $p_{x_{\gamma 2}}$. A closed-form solution exists and can be written as

$$p_{x_{\gamma 2}} = \frac{a \cdot b}{1 - b^2} \pm \frac{\sqrt{a^2 \cdot b^2 - (b^2 - 1) \cdot (a^2 - c)}}{b^2 - 1} \quad (5.4)$$

with

$$\begin{aligned} a &= \frac{m_{\pi^0}^2}{2} + \frac{p_{y_{\gamma 1}} \cdot p_{y_{\gamma 2}} + p_{z_{\gamma 1}} \cdot p_{z_{\gamma 2}}}{|\vec{p}_{\gamma 1}|} \\ b &= \frac{p_{x_{\gamma 1}}}{|\vec{p}_{\gamma 1}|} \\ c &= p_{y_{\gamma 2}} \cdot p_{y_{\gamma 2}} + p_{z_{\gamma 2}} \cdot p_{z_{\gamma 2}}. \end{aligned} \quad (5.5)$$

One may note that in Eq. (5.4), the second term may have a positive or negative sign with only one of them being physical. It is - faute de mieux - assumed that the one that leads to an invariant mass closer to the nominal Σ^+ mass is the correct one, which is also backed up by the simulations. No adverse effect on the background is observed and no signal peak is faked.

Finally, one only needs to transform the momentum vector of the unobserved photon back to the laboratory system.

Having the momentum of the unobserved photon, one can calculate the momentum and invariant mass of the Σ^+ just as before. The invariant mass is shown in Fig. 5.1. The reconstruction method described above will be referred to as PCM (single γ) or simply single- γ method in the following.

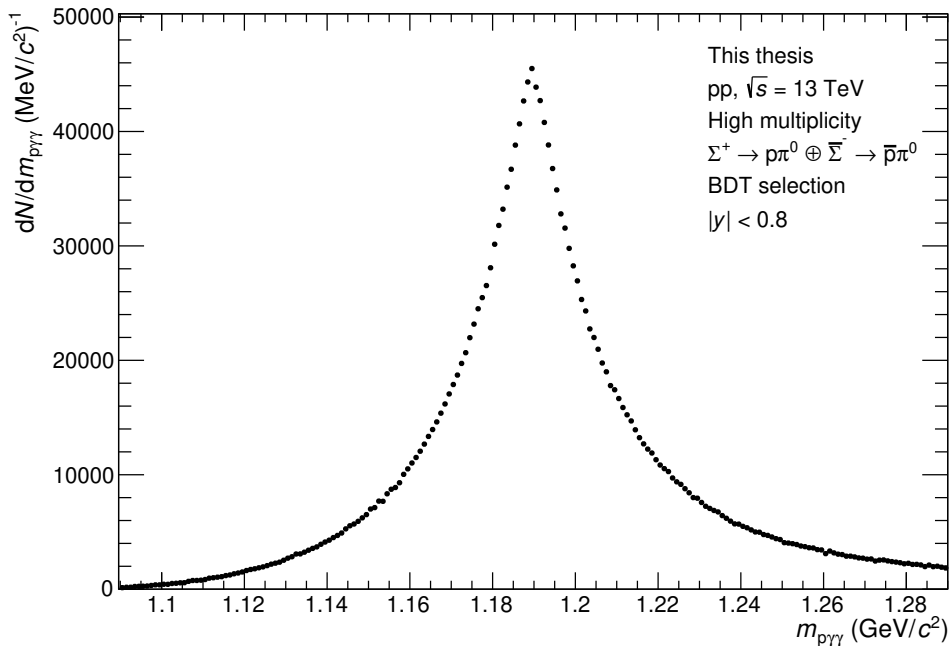


Figure 5.1: Invariant-mass distribution of Σ^+ reconstructed with the method described in the text. The visible broadening of the peak is not caused by the missing momentum, but rather by the resolution of the secondary vertex. This will be treated in section 5.1.2.

5.1.2 Resolution improvement

Apparently, the resolution is worse than in the previous methods, which is the result of information loss. In concrete terms, it is found that the limiting factor is the resolution of the secondary vertex. One might ask why this issue was not encountered in the method presented in section 4.1, which also made use the secondary vertex for the construction of the second photon. The reason is the different length scale. In the PCM-Calo method, the photon is constructed as the connecting line between the secondary vertex and the calorimeter cluster, which are several meters away from each other. Therefore, the resolution of the secondary vertex, which is in the order of millimetres, is negligible. In fact, the method even produces reasonable results when not using the secondary vertex at all and assuming that the photons originate from the primary vertex. In the single- γ method, however, the distance between the primary and the secondary vertex, which is only a few centimetres, is the scale of interest, and thus the resolution of the secondary vertex has a sizeable effect. The limited resolution also affects the momentum resolution of the reconstructed Σ^+ baryons. This is

of course not optimal for investigating small momentum differences of particle pairs, which is the goal of the analysis. This led to the idea to fix the momentum resolution by using the known mass of the Σ^+ baryon as an additional constraint, i.e. to find a correction of the secondary vertex that optimizes the invariant mass, as this also optimizes the momentum. To do so, a coordinate transformation into spherical coordinates is performed. In order to understand why this is useful, one may consider the orthonormal basis used before. Here, the base vector \vec{e}_1 points into the flight direction of the Σ^+ and hence contains the information about the secondary vertex. Since it is a unit vector, the radius of the secondary vertex, i.e. the length of the vector cancels. Advantageously, the radius of the secondary vertex is the coordinate with the worst resolution. Thus, only θ and φ remain as error prone parameters. Their resolution can be obtained from the simulation and is displayed in Fig. 5.2. Since there is no closed-form solution for the optimization, an iterative algorithm is applied to find the corrections $\Delta\theta$ and $\Delta\varphi$ that optimize the invariant mass of the Σ^+ . The search window for both $\Delta\theta$ and $\Delta\varphi$ is chosen to be ± 20 mrad. The momentum resolution before and after the correction is shown and discussed in Fig. 5.3. The resulting resolution in k^* , which is of interest for the correlation function, is shown in section 5.4.3.

By construction, the resolution correction shapes the invariant-mass distribution to the nominal Σ^+ mass. In the limit of infinite iterations, the distribution would resemble a delta-like function and this holds for the signal and the background in equal ways. The determination of the purity is therefore performed using the uncorrected distributions and is described in section 5.1.4.

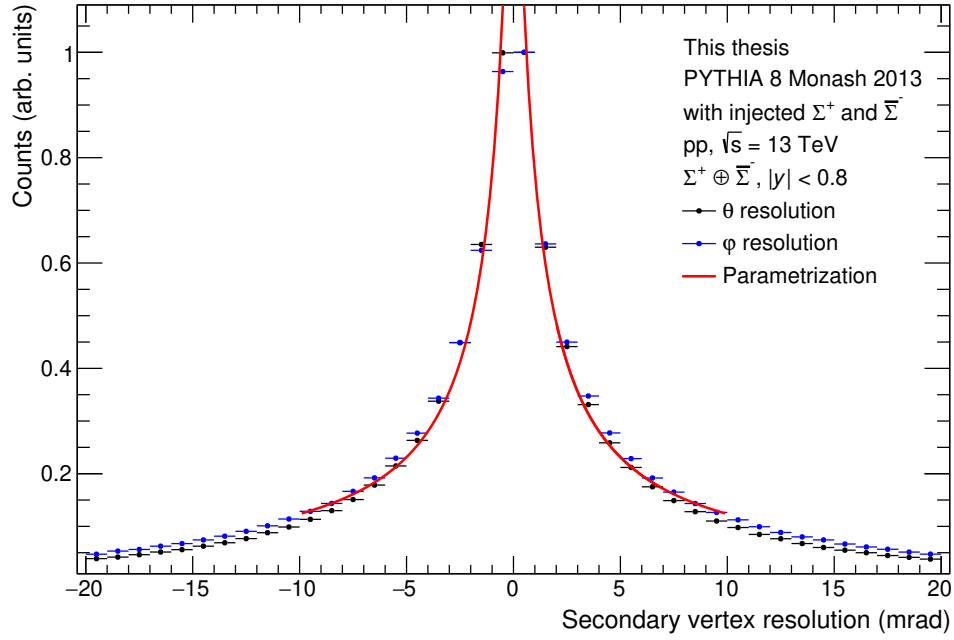


Figure 5.2: Resolution of the secondary vertex reconstructed using KFParticle[247]. θ and φ can both be parametrized by a phenomenological function that is given by $a \cdot (|x| + b)^{-1}$ and provides a good description in the relevant interval. The shown parametrization (red line) is a combined fit, making use of the almost equal resolutions of θ and φ .

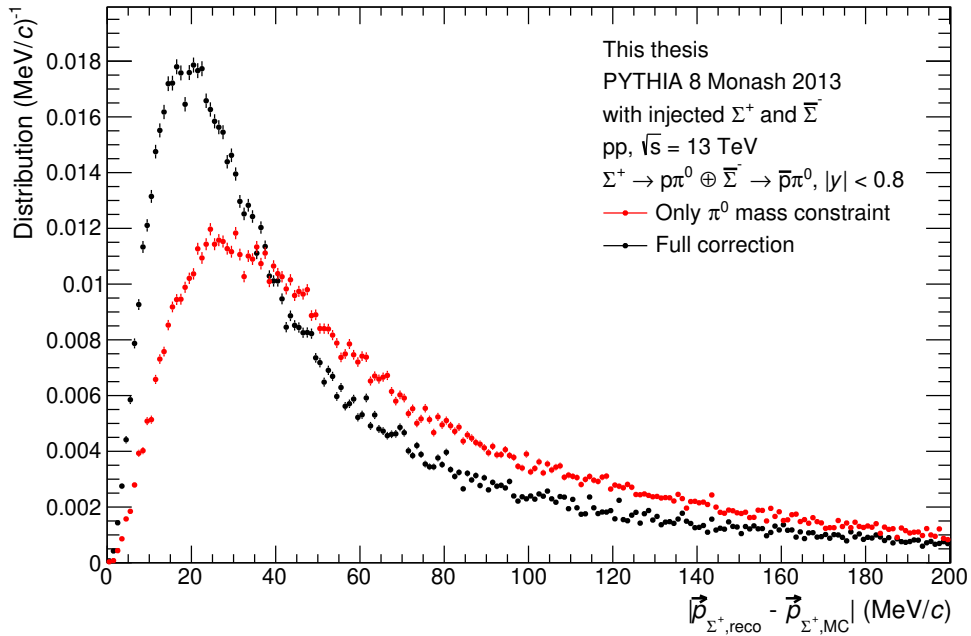


Figure 5.3: Resolution of the momentum of the reconstructed Σ^+ before (black markers) and after (red markers) the correction described in the text.

5.1.3 Σ^+ selection

The particle selection is much more challenging in case of the single- γ method compared to the previous PCM-Calo method, as the most important selection, the pointing angle, cannot be used anymore. This coincides with a high demand on the purity, as impurities in the particle sample degrade the significance of the femtoscopic signal, which will be discussed in section 5.3. Advantageously, femtoscopy does not require precise knowledge about the reconstruction efficiency. In fact, it therefore equalizes the major drawbacks of machine learning that are biases in the efficiency correction and difficulties of quantifying its systematic uncertainties as discussed in section 3.2. Consequently, femtoscopy is an ideal use case for machine learning.

Following these considerations, a boosted decision tree [250], which was thoroughly introduced in section 3.2.1, is used to select the Σ^+ .

For the training of the model, one needs a signal and a background sample. The signal is generally taken from a MC simulation. For the background sample, different approaches exist. A common one is to use the sidebands of the invariant-mass peak from the data. This is preferable if the background is not well described by the simulation or particularly if there is hardly any background in case of injected particles. However, one must take care that the data is very well described by the simulation, as otherwise a model could be accidentally trained on the differences between the data and the simulation rather than learning actual signal characteristics, which can result in very poor performance.

In any case, the reconstruction method presented here does not allow the use of sidebands, as the peak is too broad and the observables depend indirectly on the invariant mass. Therefore, a simulation is required that produces a physical background.

Fortunately, a large data set was produced that can be used for this purpose. This simulation comprises around $6 \cdot 10^8$ PYTHIA 8 events which are triggered for high-multiplicity. The triggering was done by checking the multiplicity in the rapidity region of the V0 detectors. The threshold was set such that the average multiplicity roughly corresponds to the one in the high-multiplicity triggered data set in data.

The distributions of the Σ^+ features used for training the model are shown in

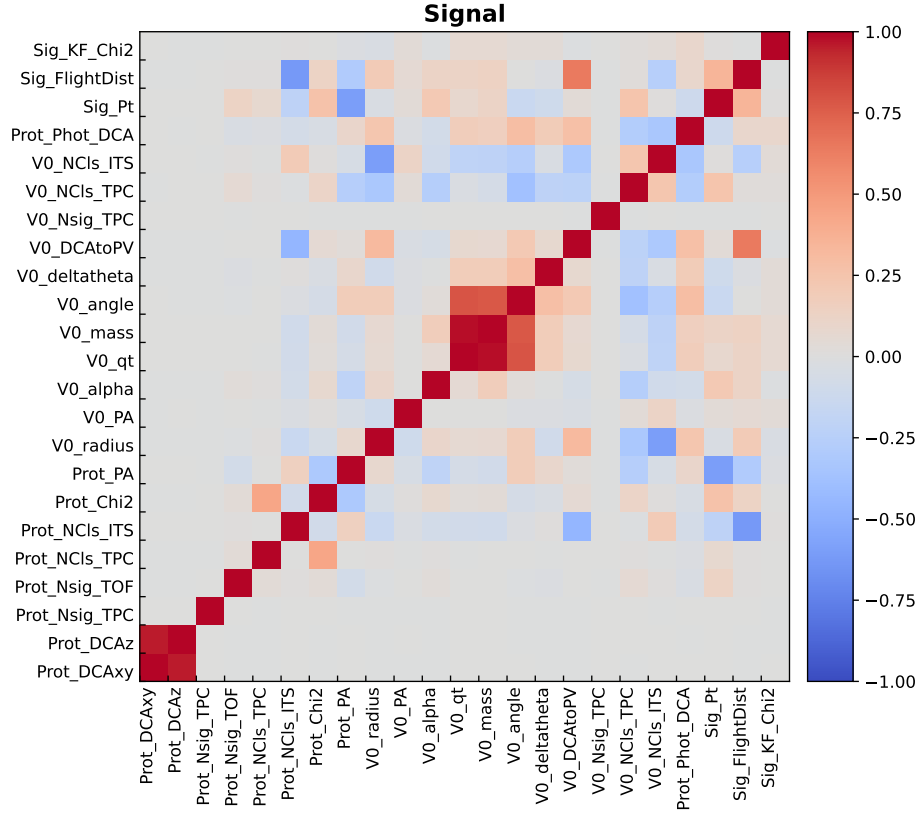


Figure 5.4: Correlation plot of the Σ^+ features used for the training of the boosted decision tree [250]. Figure created with Hipe4ML [248].

Fig. 5.6 and 5.7. As it is visible, the features are plentiful and the signal is not well separated from the background in any of the features, which calls for the use of a multivariate selection. An important figure to look at is the correlation plot that is shown in Fig. 5.4. If a feature is fully (anti-)correlated with another feature, it brings no value to the selection. To the contrary, it can corrupt the model in certain machine learning implementations. Boosted decision trees are, however, rather robust to those correlations [265]. Two correlations are visible by eye. The DCA parameters of the protons are correlated, as both DCA_{xy} and DCA_z grow with an increasing decay length of the Σ^+ . This is different in the case of primary protons, where these values are randomly distributed within their resolution as seen in Fig. 5.17. Moreover, there is a correlation between the invariant mass of the V^0 candidates and the transverse momentum q_T within the V^0 candidates, which is a consequence of the kinematic relation that is exploited in the Armenteros-Podolanski plot [275] (see Fig. 4.1).

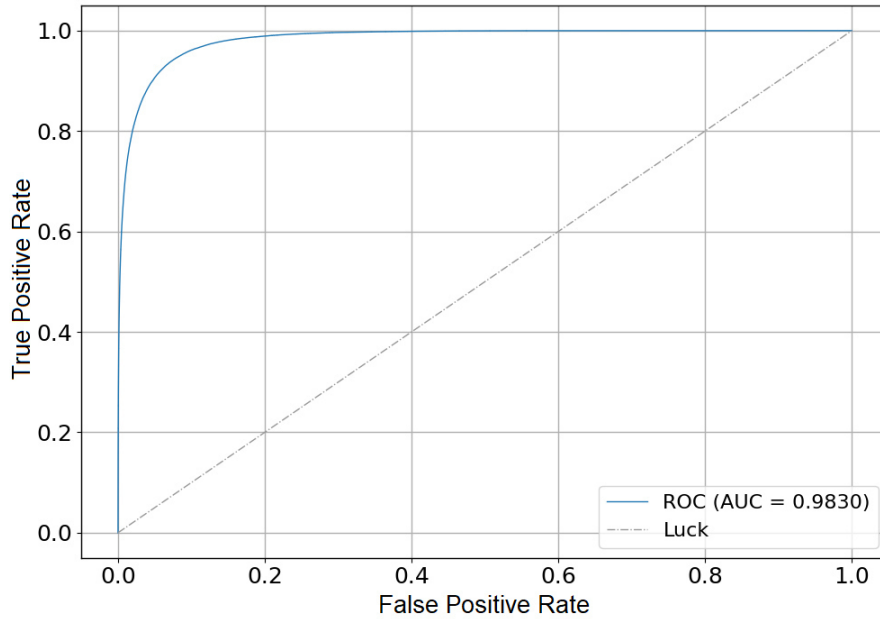


Figure 5.5: ROC-AUC curve of the Σ^+ selection for the testing sample. Figure created with Hipe4ML [248].

The tuning of the hyperparameters is done using both a custom grid search²⁶ as well as the optimization framework optuna [249]. It is found that the ROC-AUC score is rather stable as long as the hyperparameters remain in a reasonable regime.

The learning rate is chosen to be 0.01 and the maximum tree depth to be 8. These parameters reflect the complexity of the classification as well as the predisposition for overfitting. Due to the low learning rate, 2000 estimators are needed. A saturation effect is observed in this parameter. To further suppress overfitting, a subsampling is introduced which draws a unique random subset of half of the candidates for each estimator.

The performance of the Σ^+ selection can be probed as usual by considering the ROC-AUC curve (Fig. 5.5) and the distributions of the BDT scores for signal and background (Fig. 5.8). The ROC-AUC value amounts to around 0.98, a very good value, considering that it ranges from 0.5 (random selection) to 1 (ideal selection). The curves are very similar for the training and testing sample, indicating little overtraining. The Σ^+ are selected above a BDT score of

²⁶The optimization using optuna [249] runs quite slowly and aggressively consumes computing resources. It was found to be beneficial to reduce the search window by a simple grid search before running the sophisticated TPE [266] approach.

0.6, aiming for a purity of 90%. The purity is calculated using a data-driven approach introduced in section 5.1.4. Below 1 GeV/ c the cut-off value is relaxed by 0.1, as the efficiency is already affected quite severely. Still, a purity of 75% can be preserved in the lowest bin. The same cut-off value is also used above 4 GeV/ c , as there is only little background. Nonetheless, the region above 4 GeV/ c hardly contributes to the correlation function, as there is little overlap with the protons and the phase space is large, resulting in a very low probability to produce a low- k^* pair.

The feature importances measure the impact of a given parameter on the output score. They are shown in Fig. 5.9 for the Σ^+ as shap [271] values (see section 3.2.1). The highest value is found for the TPC PID of the decay daughters of the V^0 candidates. The reason for this is that no preselection is implied on this parameter. The distribution of the parameter is seen in Fig. 5.6. Apparently, a sizeable amount of background entries can be rejected purely based on this parameter, boosting the shap value. It must thus be considered as an artefact of the preselection. Apart from that, the most important parameters are the topological features, which allow to distinguish the signal from random combinatorial background. This finding is expected from the classical selection in section 4.1.3, where also the topological selections were most impactful, particularly the pointing angle.

Around $1.8 \cdot 10^6$ Σ^+ are selected for further analysis. The raw p_T distribution of the selected Σ^+ is shown in Fig. 5.20 together with the selected protons. The distribution of the Σ^+ in η and φ is shown in Fig. 5.10. Due to the composite nature of the Σ^+ , non-uniformities in the efficiency are washed out, resulting in a mostly uniform distribution in η and φ .

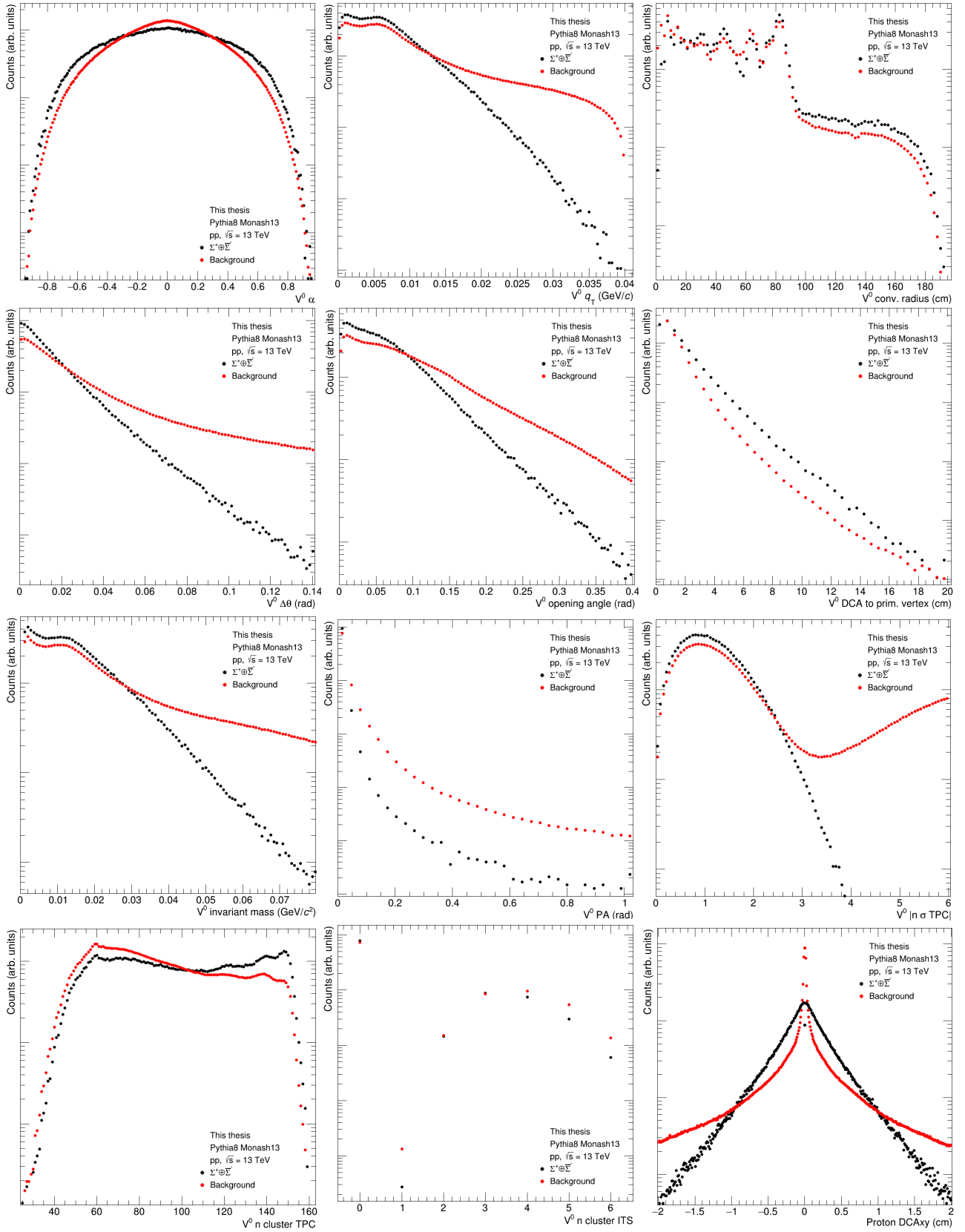


Figure 5.6: Features of the Σ^+ used for the training of the boosted decision tree [250]. Continued on page 149.

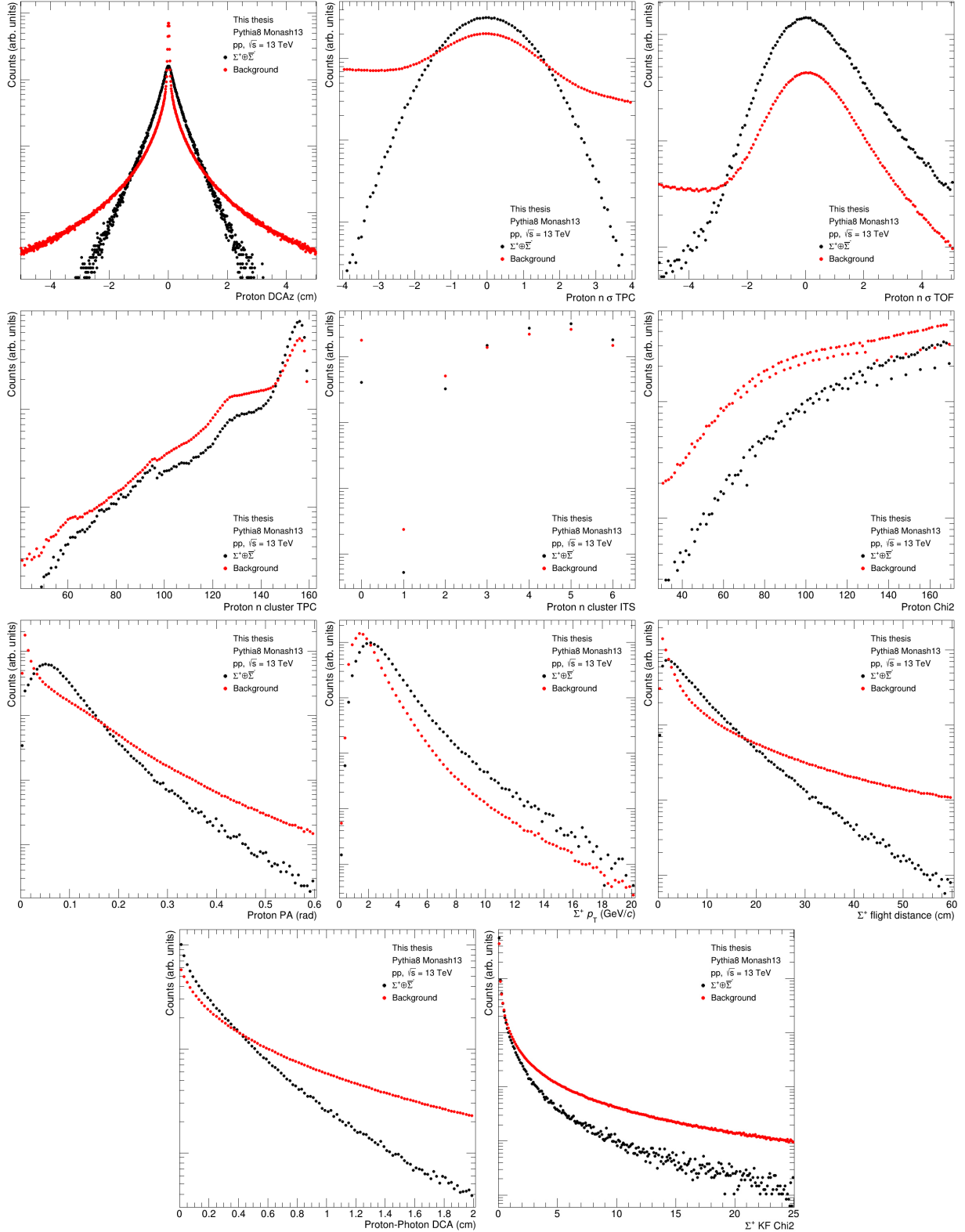


Figure 5.7: Features of the Σ^+ used for the training of the boosted decision tree [250] (continuation). All distributions are normalized to the total number of entries. The background contains all combinations of proton and photon candidate pairs which fulfil a coarse preselection.

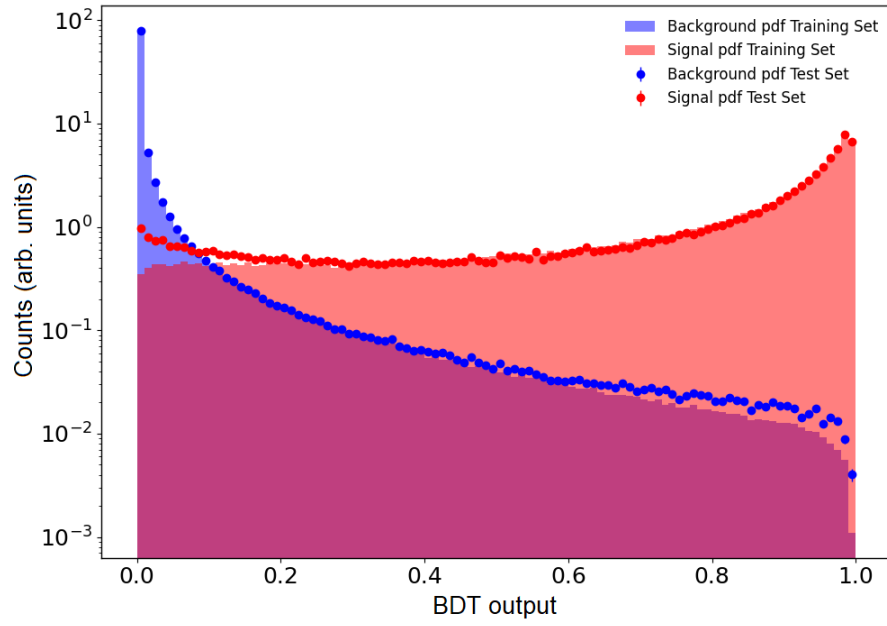


Figure 5.8: Distributions of the BDT scores for the signal and the background of the Σ^+ . Figure created with Hipe4ML [248].

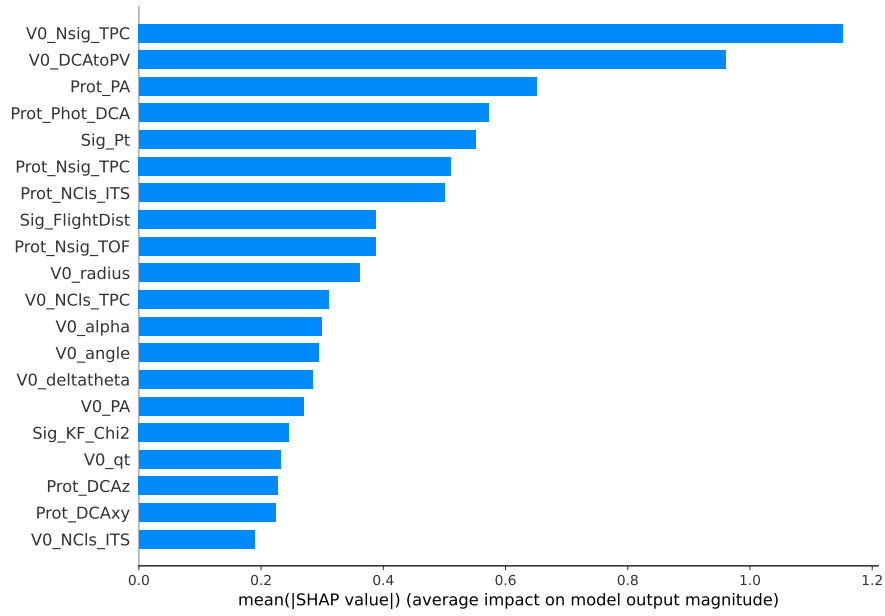


Figure 5.9: Importance of the Σ^+ features calculated as shap [271] values. Figure created with Hipe4ML [248].

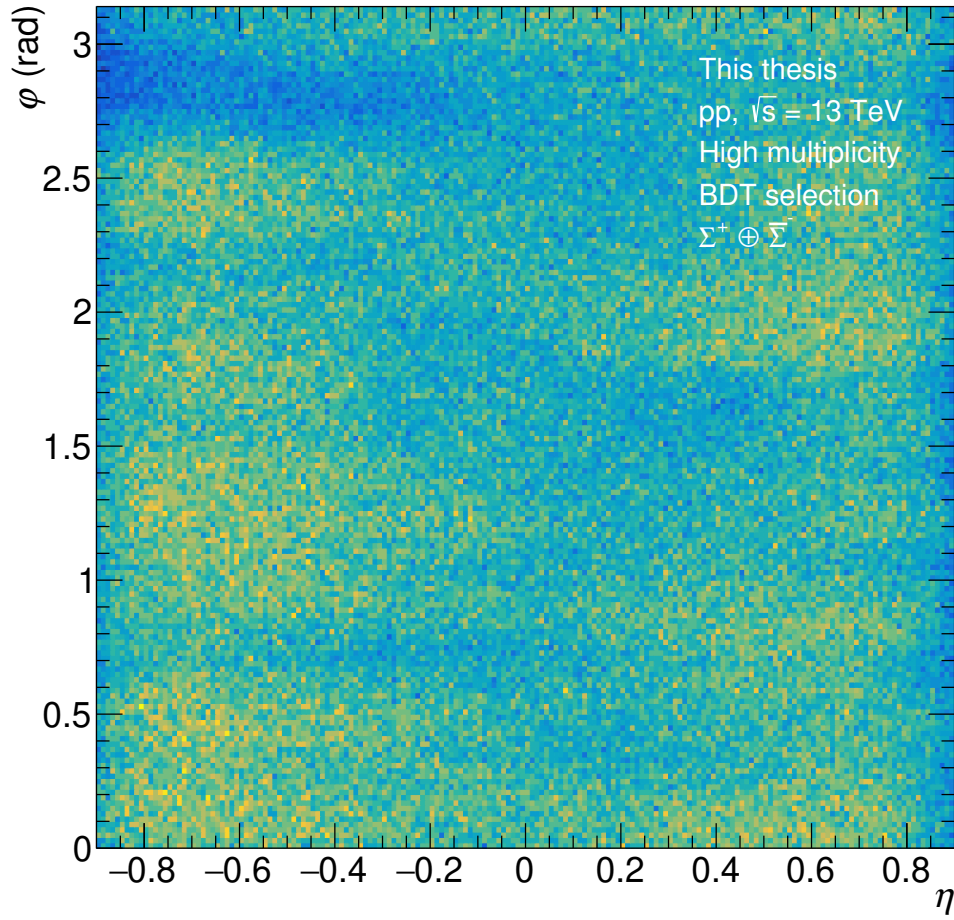


Figure 5.10: Distribution of selected Σ^+ in η and φ .

5.1.4 Purity determination

Knowledge about the purity of the selected particle sample is crucial for femtoscopy, as it enters the so-called λ parameters [15], necessary to compare the experimental correlation function to theory. This will be further discussed in section 5.3.

As already elaborated, the purity is evaluated with the uncorrected invariant-mass spectra. Regarding the background description, the same considerations that were discussed in section 4.3.1 hold. Since there is no calorimeter cluster that could be mixed, event mixing would require to mix the proton and the PCM photon. This is not straight forward, as there is sizeable correlated background in this pair, e.g. from Σ^0 or Δ^+ decays [9], which would need proper consideration. Therefore, this approach is not followed. Instead, the purity is evaluated by fitting the data momentum differentially with templates of the signal and background distributions taken from the simulation.

Naturally, this method works only up to a certain purity due to the vanishing statistics in the background template, leading to an increasing number of invariant-mass bins to remain empty. Thus, fitting the templates on a bin-by-bin basis is found to be rather unstable.

Alternatively, one can make use of the dextral tail of the background to scale the templates by defining two distinct regions in the invariant mass, the peak region (PR) from 1.17 to 1.21 GeV/ c^2 and the tail region (TR) from 1.25 to 1.35 GeV/ c^2 . Within these regions, the number of counts in the signal template (S), background template (B), and total data distribution (T) are evaluated by means of bin counting. The weights of the background (w_B) and signal (w_S) templates can then be easily evaluated as the solutions of the corresponding system of linear equations given below.

$$\begin{aligned} w_B &= \frac{S_{\text{PR}} \cdot (T_{\text{TR}} - T_{\text{PR}}) / (S_{\text{TR}} - S_{\text{PR}}) - T_{\text{PR}}}{S_{\text{PR}} \cdot (B_{\text{TR}} - B_{\text{PR}}) / (S_{\text{TR}} - S_{\text{PR}}) - B_{\text{PR}}} \\ w_S &= \frac{T_{\text{TR}} - T_{\text{PR}} - (B_{\text{TR}} - B_{\text{PR}}) \cdot w_B}{S_{\text{TR}} - S_{\text{PR}}} \end{aligned} \quad (5.6)$$

This method produces stable results without any need for fitting. Furthermore, the systematic uncertainties can be evaluated by varying the width of the used regions, in addition to considering the residuals between the template sum and

the data.

For a quantitative description, the templates need to be normalized and scaled by the weights and the total number of counts in the data distributions. This is shown exemplarily for one p_T bin in Fig. 5.11.

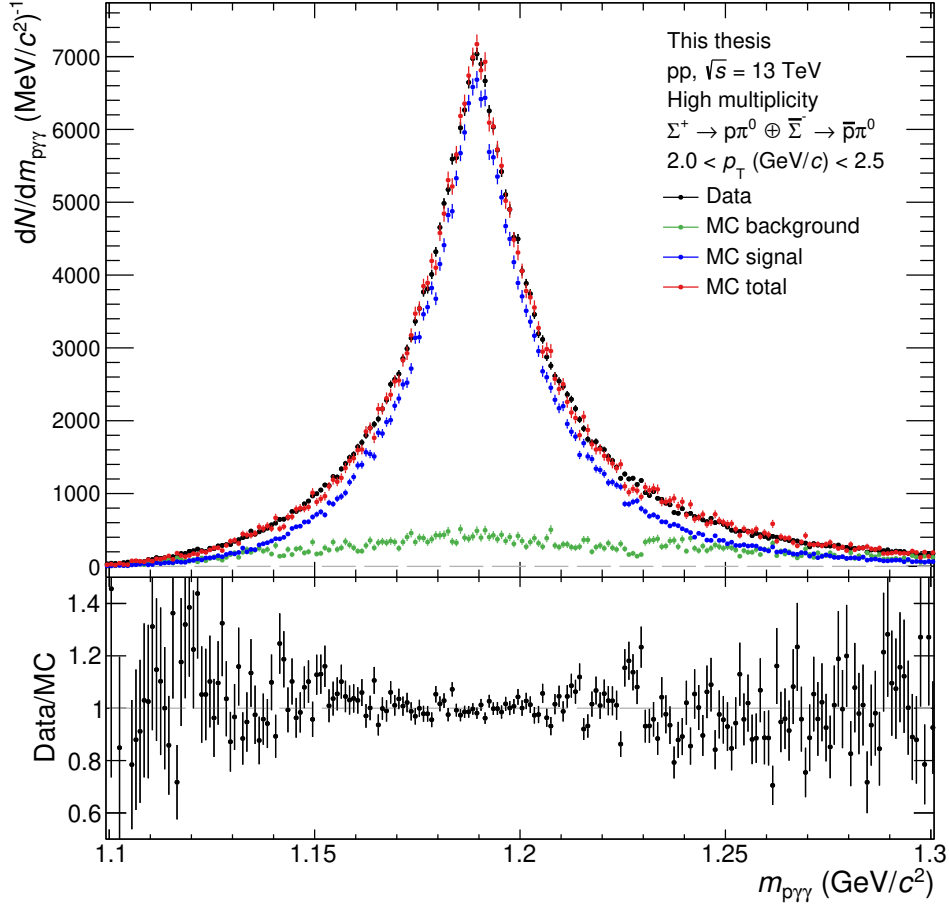


Figure 5.11: Invariant-mass distribution of Σ^+ candidates with $2.0 < p_T$ (GeV/c) < 2.5 with fitted MC signal and MC background templates. In the lower panel, the ratio between the data and the sum of the MC templates is shown.

Apparently, the sum of the scaled signal and background distributions represents the data very well, indicating that the templates indeed resemble the corresponding data distributions.

The Σ^+ are selected in the invariant-mass region from 1.15 to 1.23 GeV/c^2 and are subsequently subjected to the resolution correction described earlier. The signal and background counts are evaluated by summing the bins of the scaled templates in the given region. Finally, the purity is evaluated from the signal

and background counts. It is displayed in Fig. 5.12. For comparison, the purity of the PCM-Calo method is also shown.

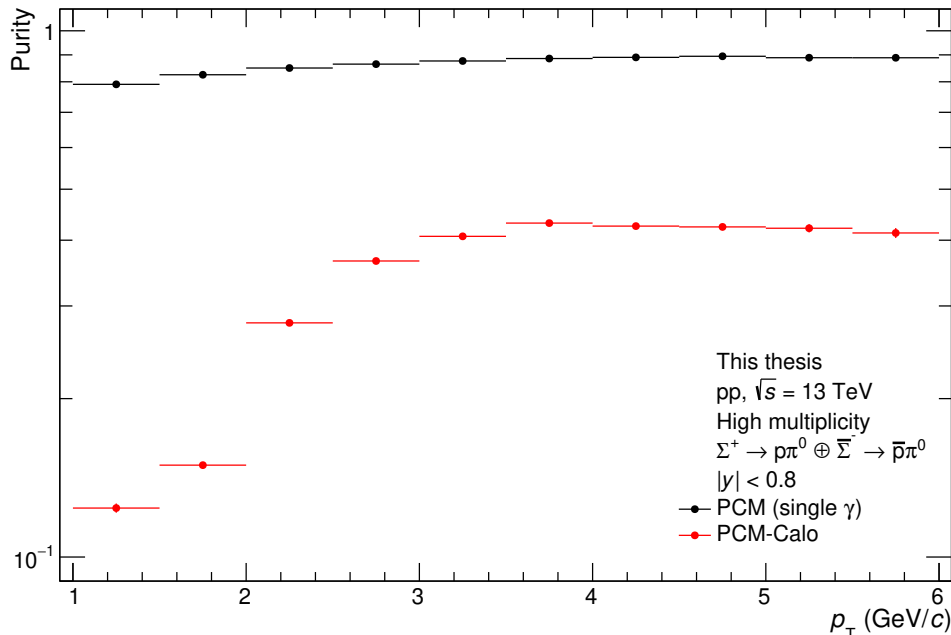


Figure 5.12: Purity of the selected Σ^+ . For the PCM-Calo method, the purity is evaluated in a 3σ interval around the nominal mass, while for the single- γ method an interval of 1.15 to 1.23 GeV/c^2 is used, which roughly corresponds to a 2σ interval.

5.1.5 Reconstruction efficiency and cross check

The reconstruction efficiency using the single- γ method is depicted in Fig. 5.13. The overall improvement compared to the PCM-Calo method is around one order of magnitude. Particularly at low momenta, an even more significant improvement can be achieved. This is not surprising, considering the low acceptance of the calorimeters and the energy cut-off. Since the second photon is not measured at all, its energy can have virtually any value down to 0. Also, it might propagate perpendicular to the direction of flight of the Σ^+ due to the low boost and thus out of the acceptance of the central barrel detector. In terms of the central barrel acceptance, this yields a virtual reconstruction efficiency above 100%, which is not achievable with any other method.

Nevertheless, in the lowest momentum bins at $p_T < 1 \text{ GeV}/c$, the efficiency of this method also drops steeply. This is dominantly related to the declining

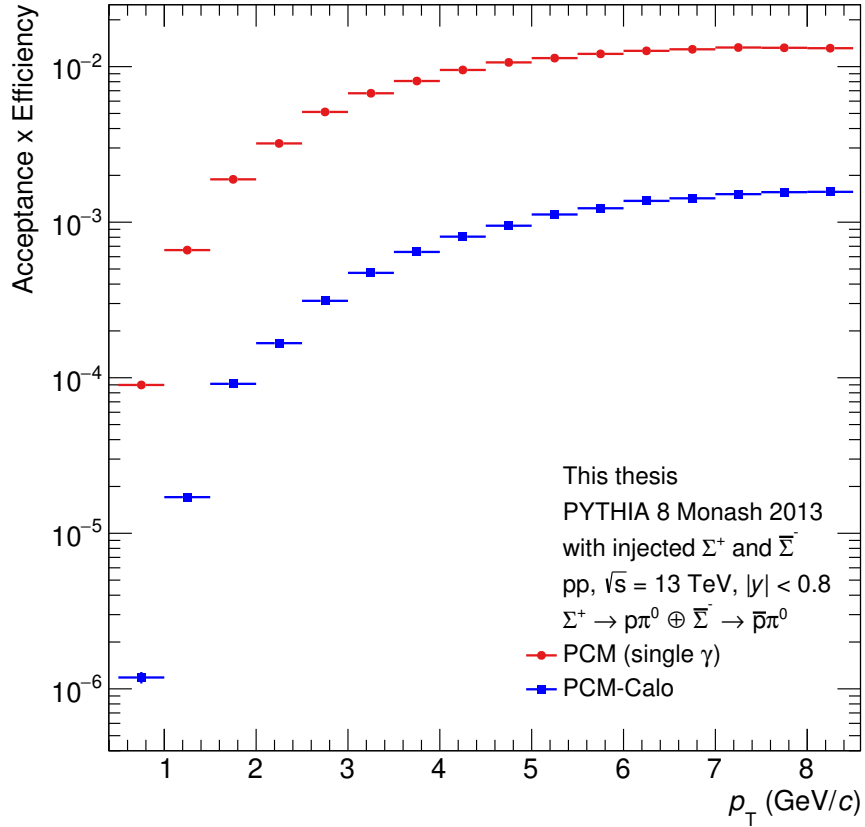


Figure 5.13: Acceptance \times efficiency of Σ^+ using the single- γ method and the PCM-Calo method. A more than tenfold improvement is achieved with the single- γ method.

selection efficiency. Most of the background is situated in the low-momentum region and also the secondary vertex is much closer to the primary vertex, making it much more challenging to discriminate between signal and background, even with the help of machine learning. When demanding purities above 70%, as desired for femtoscopy, selection efficiencies in the single-digit percentage range occur.

Having calculated both purity and efficiency allows to produce a p_T spectrum with this method. The purpose is to cross check with the previously obtained spectrum, which was measured using established methods, to verify that the new method produces reasonable results. In particular, it must be made sure that the observed signal is not fake, that the selection is not (strongly) biased, and that the purity determination using the template method works well over the full momentum range. The comparison is depicted in Fig. 5.14. Obviously, the spectra are in very good agreement with each other. It must be noted

that the depicted systematic uncertainties only correspond to the ones of the PCM-Calo method; still they suffice to explain the deviations, implying that the previous analysis steps work as desired.

It seems compelling to use this method also to obtain an integrated yield, but caution is advised as discussed in section 3.2.1. Despite the good agreement with the PCM-Calo method, there is quite some systematic deviation above 3.5 GeV/ c , and below 1 GeV/ c no comparison can be made. The deviations could stem from a bias in the efficiency correction and also the purity estimation is a source of uncertainty. In any case, the systematic uncertainties are difficult to handle properly and would be larger than in the PCM-Calo method. Since the systematic uncertainty already exceeds the statistical one in the PCM-Calo method, no benefit arises in terms of the p_T spectra. For femtoscopy, however, the much higher statistics makes this method favorable.

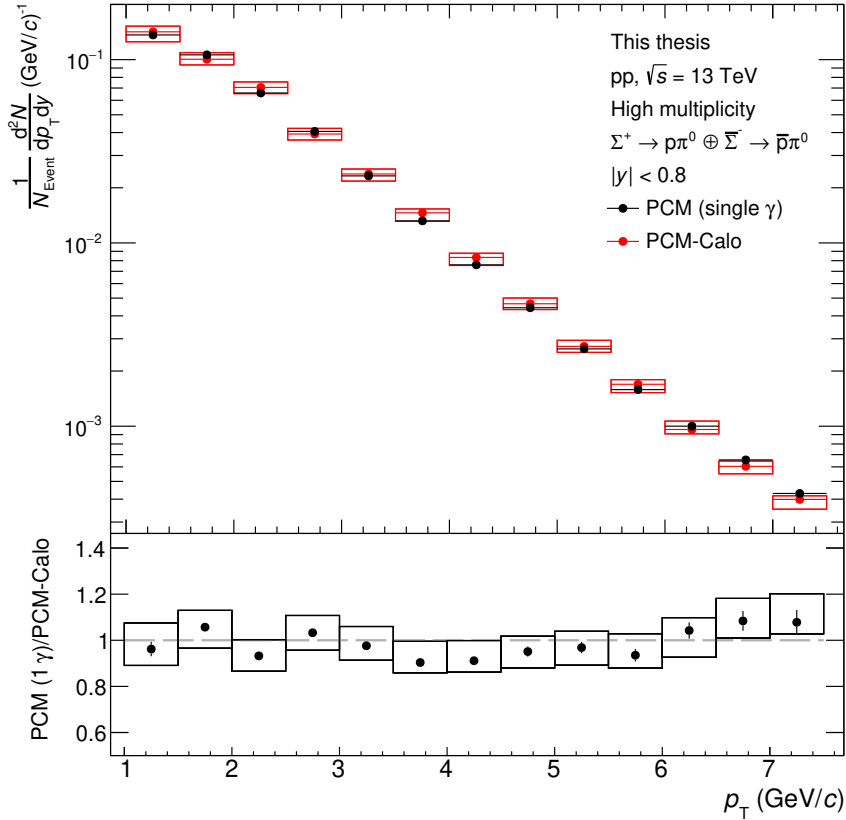


Figure 5.14: Comparison of the Σ^+ p_T spectra obtained with the single- γ method and the PCM-Calo method. The lower panel shows the ratio, indicating a very good agreement.

5.1.6 Alternative reconstruction methods

In addition to the reconstruction methods presented in this work, two other reconstruction methods of the charged Σ baryons have been developed by other ALICE collaborators²⁷ during the course of this thesis.

The first one exploits the decay of the charged $\bar{\Sigma}$ baryons into an anti-neutron and a charged pion [288]. The anti-neutron is measured by the annihilation in the PHOS detector that gives a characteristic signal. As this implies, only the anti-particles can be measured. However, this also gives access to the $\bar{\Sigma}^+$ (anti-particle of the Σ^-) that is inaccessible for the reconstruction methods presented in this thesis. The major drawback of this method is that the resolution is poor, reportedly 1 GeV/ c in the momentum²⁸, which is because the energy of the neutron can only be calculated either from the deposited energy or from the time of flight, which both have a rather modest resolution. This is completely prohibitive for femtoscopy, considering that one seeks to measure very small momentum differences. Moreover, the secondary vertex cannot be reconstructed, which limits the purity, and lastly the low acceptance of the PHOS detector must be considered (see section 2.2.4). All in all, this makes this method unsuited for femtoscopic measurements.

Another method also exploits the decay into a (anti-)neutron and a charged pion by measuring only the pion. This gives access to all charged Σ baryons and anti-baryons²⁹. The method makes use of the fact that the neutron carries most of the momentum of the Σ , which causes the pion track to exhibit a so-called kink topology. This of course requires the Σ to be measured directly, which apparently became possible with the upgraded ITS in LHC Run 3, whose first layer is closer to the interaction point [289]. It is, however, still very unlikely for the Σ s to traverse several layers of the ITS, which is necessary for a precise momentum measurement, particularly for low-momentum particles. Even more importantly, the method is not able to distinguish between particles and anti-particles, since only the charge of the pion and not the baryon number of the neutron is known. That rules out this method for femtoscopy.

Similarly, the proton could be measured in the TPC instead of the pion, which would allow to distinguish between particles and anti-particles. In this case,

²⁷I was not personally involved in the analyses outlined in this section.

²⁸Personal communication with the analyzer P. Gordeev.

²⁹The analysis is not published.

however, the kink angle is extremely small, since the proton carries most of the momentum, which is further aggravated by the boost at high momenta. Consequently, the resolution and efficiency of this approach is limited.

In summary, it can be concluded that the reconstruction scheme of the Σ^+ presented in this thesis remains the only one, which is (currently) well suited for femtoscopy with charged Σ baryons.

5.2 Proton sample

Other than the Σ^+ baryons, the protons are stable particles [9]. They are thus reconstructed as tracks, readily at hand for analysis, and common values exist for their selection [15, 282]. Typically, a 3σ selection is applied on the dE/dx in the TPC. Above around 0.9 GeV/ c , where the dE/dx bands start to overlap, an additional selection of 3σ is applied on the TOF response. A cut-off is applied at 4 GeV/ c , as also the other bands in the TOF start to overlap with the proton band at that point. This selection leads to a very good purity of around 99% [15]. In order to reject protons from weak decays, a selection on the DCA to the primary vertex is introduced. Typical values for femtoscopic analyses are 1 mm in the xy -plane and 2 mm in z [15]. Even though commonly used, one must note that fixed selections on the DCAs to the primary vertex neglect their sizeable momentum dependence, leading to a by far non-optimal selection. The reason for the usage of fixed selections is that it is otherwise challenging to use template fits to determine the primary fraction as outlined in section 5.3. With the DCA selections stated before, contamination fractions of the proton sample as large as 12.8% are found, with 9% coming from Λ decays and 3.8% coming from Σ^+ [15]. Thus, the contribution of the feed-down exceeds the contamination by misidentification by more than one order of magnitude. Therefore, it is compelling to apply machine learning also to the selection of the protons in order to improve these values. Machine learning optimizes the proton selection in several ways. The machine learning model naturally takes into account the momentum dependence of the DCA to the primary vertex, significantly improving the primary fraction. Moreover, also the efficiency and the reach of the particle selection is improved. As one may see in Fig. 2.6, the dE/dx band of the protons overlaps with the electron band first, which is then followed by a region where no overlapping takes place. A ML model

can identify those regions, allowing to improve the efficiency by loosening the TOF selection automatically. The range of the PID can also be extended beyond 4 GeV/ c without sacrificing a good purity by an asymmetric selection, rejecting the incoming kaons. Finally, also correlations between the DCA and the PID information can be exploited, making use of the different DCA distributions of the particle species and their different corresponding momentum dependencies.

The approach is similar to the one described in section 5.1.3. The only difference is that instead of a binary classification (“signal” and “background”), three classes are used. These are “primary protons”, “secondary proton”, and “non-protons”. The hyperparameters are tuned again in the described way. Also here it is found that the dependence of the ROC-AUC score on the hyperparameters is not very strong in a reasonable regime. The optimal parameters are found to be again 0.01 for the learning rate, 7 for the tree depth, and 1200 for the number of estimators.

As input parameters, DCA_{xy} and DCA_z to the primary vertex, the number of ITS and TPC clusters, the absolute momentum, and the TPC and TOF PID information is used. The PID information is presented both parametrized (n_σ) and unparametrized (β , dE/dx). The distributions of the features are displayed in Fig. 5.17. The correlations of the features are shown in Fig. 5.15. As expected, β and $n_{\sigma, \text{TOF}}$ are correlated with each other. Other sizeable correlations are not visible. The performance of the model can again be studied using the ROC-AUC curve, which is displayed in Fig. 5.16. The plot is more challenging to interpret than in the binary case as there are now 3×2 curves displayed. What one can still easily see is that the particle identities are easier to disentangle than their origin, characterized by a larger area below the orange and green curves. This behavior is expected, considering that the contamination from feed-down is much larger than from misidentification when using standard selections [15] as discussed above. This is also clearly a consequence of the momentum distribution of the protons. The particle identification becomes challenging only at higher momenta where the PID bands converge, resulting in lower purity. High momenta are, however, exponentially suppressed, giving them less weight when calculating average purities. The plain average of the ROC-AUC scores is found to be 0.968, automatically evaluated in the figure by Hipe4ML [248]. This, however, also includes the discrimination between

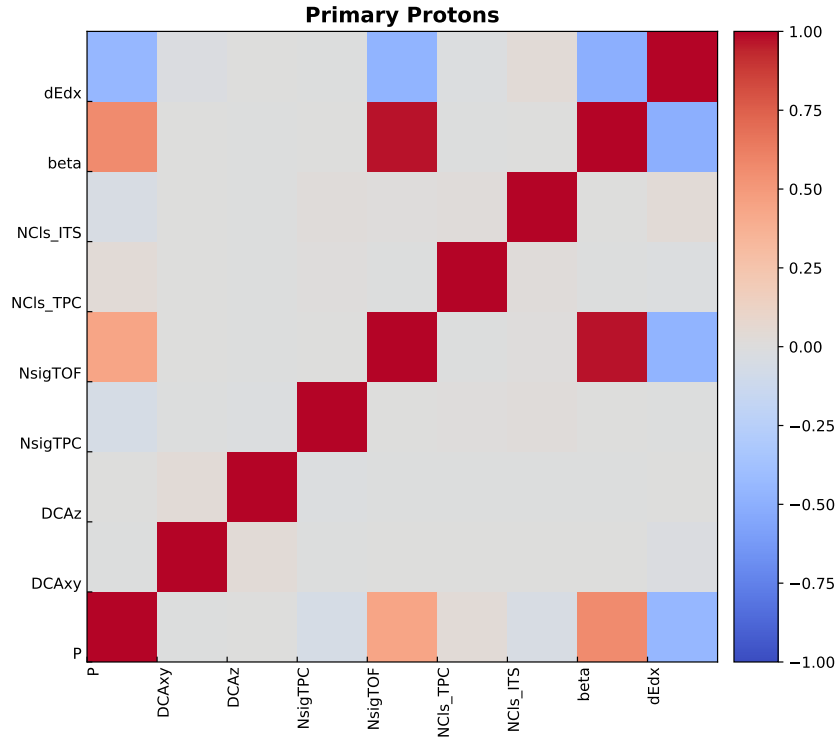


Figure 5.15: Correlation plot of the proton features used for the training of the boosted decision tree. Figure created with Hipe4ML [248].

secondary protons and misidentified particles, which is not interesting for this analysis. The proper value is thus slightly lower.

The resulting BDT output distribution for primary protons is displayed in Fig. 5.18. A cut-off of 0.5 is chosen, above which primary protons are dominant. One may note here the log-scale. The feature importances are again calculated as shap [271] values and are displayed in Fig. 5.19. The importances are plotted as a stack plot, where the size of the colored bars indicates the importance of the given feature for a given class, e.g. dE/dx for misidentified particles. Not surprising, the PID values are more important for the identification of the particles and the DCA values are more important for the discrimination between primaries and secondaries. Nonetheless, the importance of the DCAs for the misidentified is not negligible, as is the importance of the PID for secondaries. This indicates that indeed the particle selection benefits from the combination of topological and PID information, which was one of the motivations of using machine learning for the proton selection in the first place.

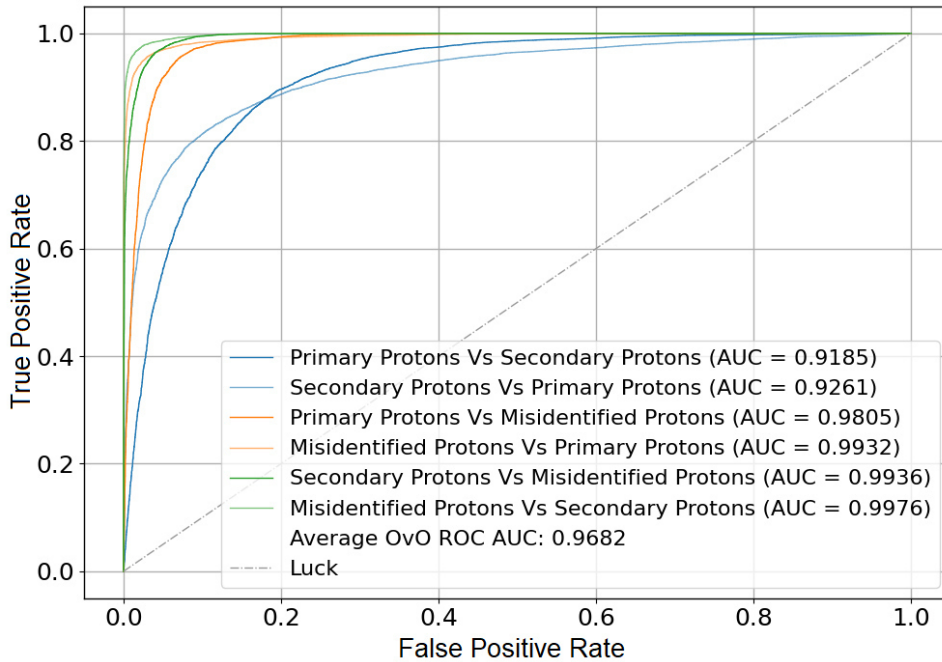


Figure 5.16: ROC-AUC curves (One vs. one, OvO) of the BDT proton selection. As explained in the text, 3 classes have been used, resulting in 6 distinct ROC-AUC curves. Figure created with Hipe4ML [248].

Around $2.7 \cdot 10^6$ protons are selected for further analysis. This includes only protons from events³⁰ with at least one selected Σ^+ . Fig. 5.20 shows the p_T distribution of the selected protons and the selected Σ^+ . The mean p_T of the protons amounts to roughly 1.4 GeV/ c . While this is significantly lower than in the Σ^+ sample (2.7 GeV/ c), still a sizeable overlap is present as seen in the figure. The overlap is crucial for femtoscopy, as particles with similar or equal masses require similar momenta to have small relative momenta k^* in the pair rest frame. Luckily, the Σ^+ is almost 27% heavier than the proton [9], consuming some of the mean p_T difference.

The distribution of the protons in η and φ is shown in Fig. 5.21. Non-uniformities in the efficiency are more pronounced compared to Σ^+ , particularly the vanishing acceptance above $|\eta| > 0.8$ is visible.

The evaluation of the purity and the primary fractions is presented in section 5.3.

³⁰Due to the vast number of protons in the full data set, only events with at least one Σ^+ candidate were stored offline for further processing. The events were further filtered offline to contain a Σ^+ that passed the final BDT selection. Only those events are considered in the following.

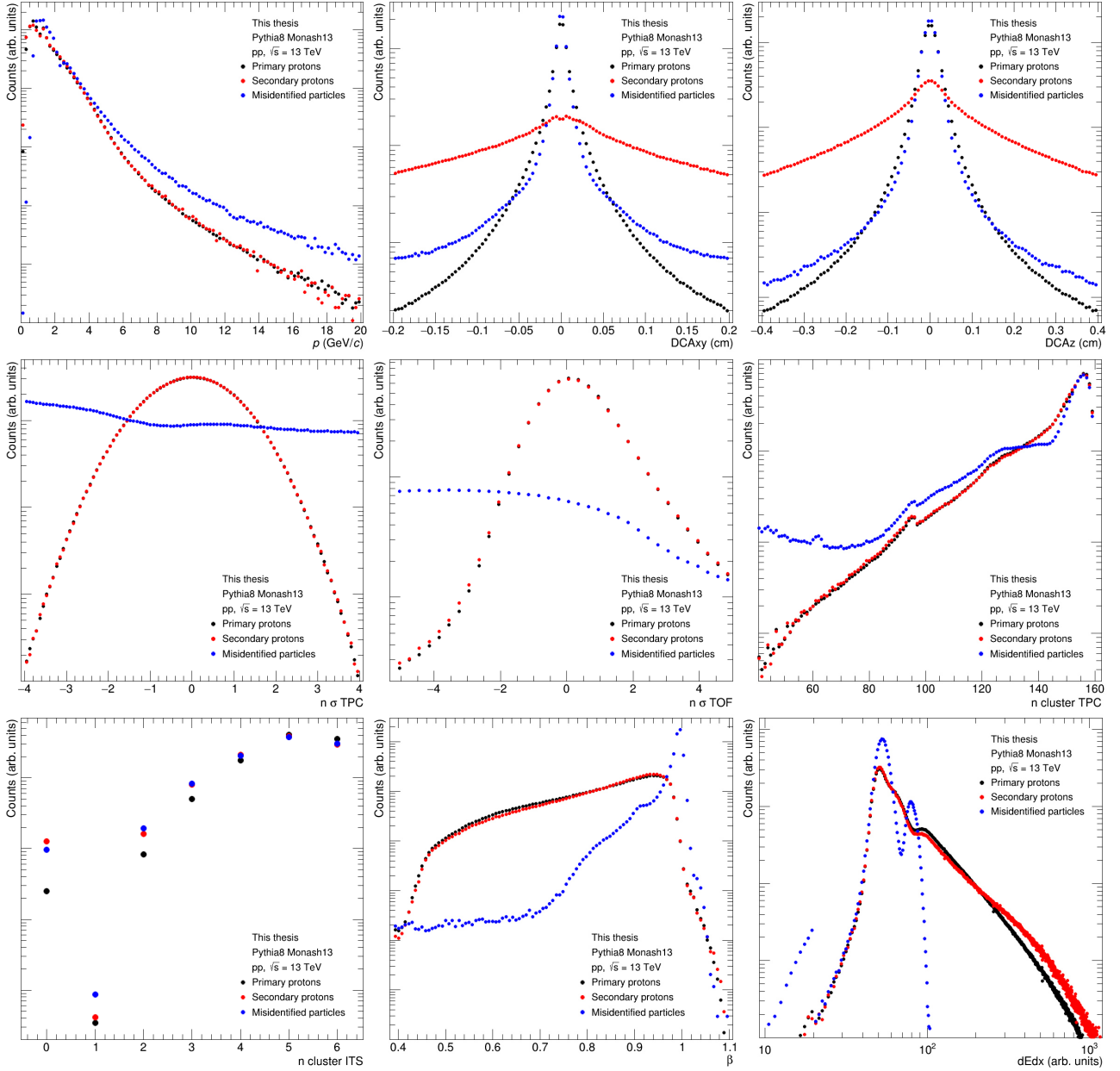


Figure 5.17: Proton features used for the training of the BDT model. The distributions are shown for the three used classes “primaries”, “secondaries”, and “misidentified”.

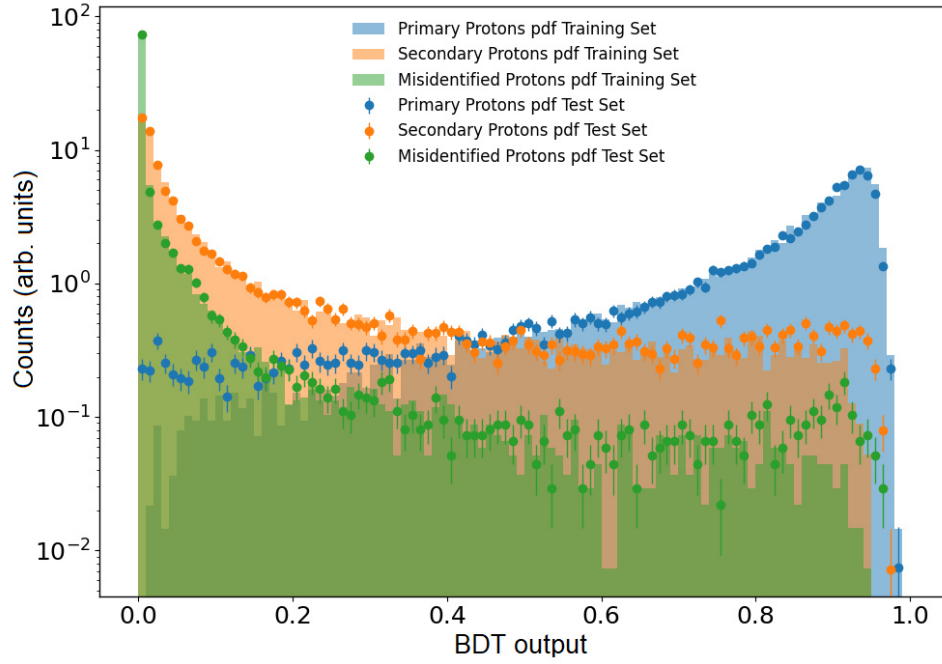


Figure 5.18: Distributions of the BDT scores for primary protons, secondary protons and misidentified particles. Figure created with Hipe4ML [248].

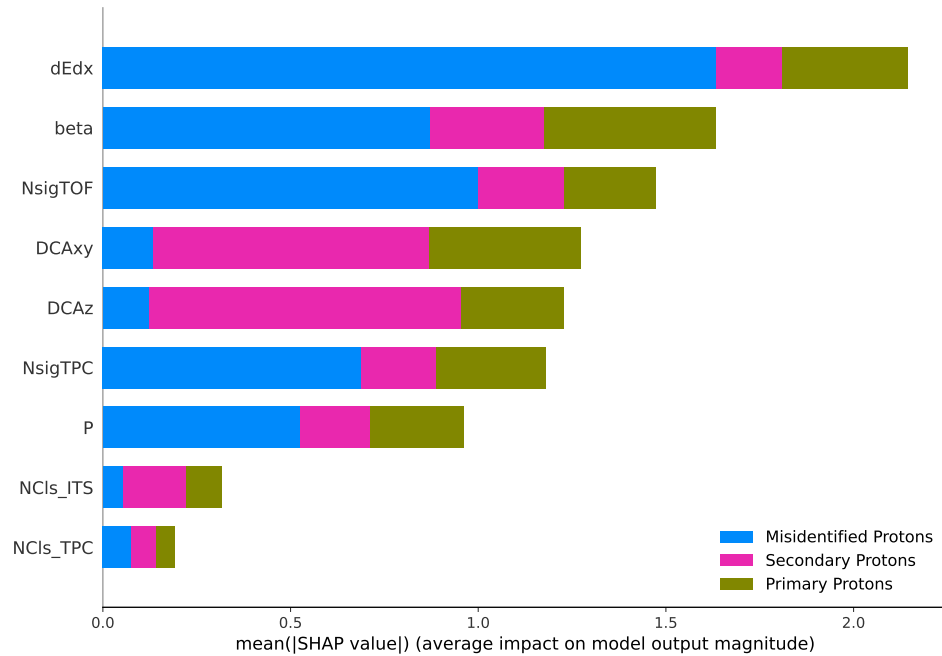


Figure 5.19: Importances of the proton features calculated as shap [271] values. Figure created with Hipe4ML [248].

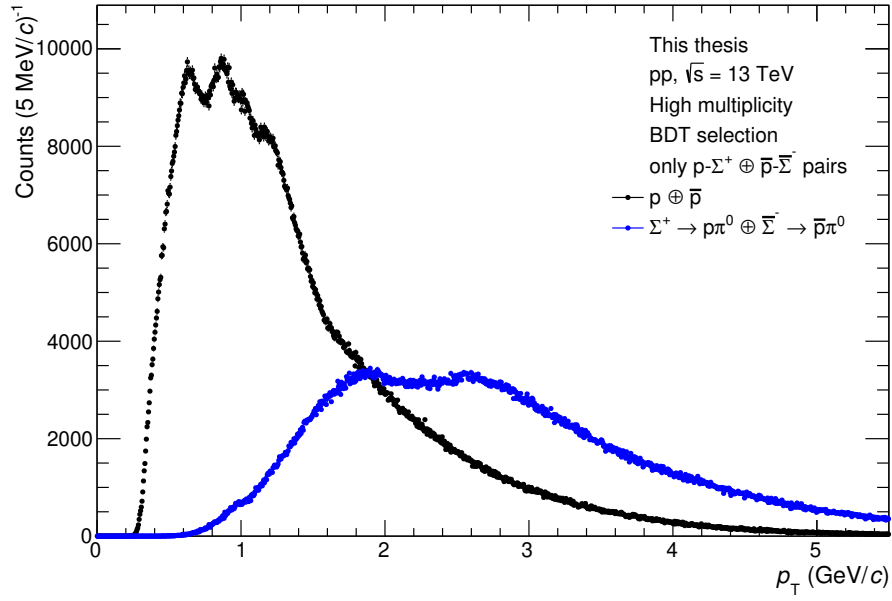


Figure 5.20: Raw p_T distributions of selected protons and Σ^+ . Only particles from events with at least one p - Σ^+ pair are shown.

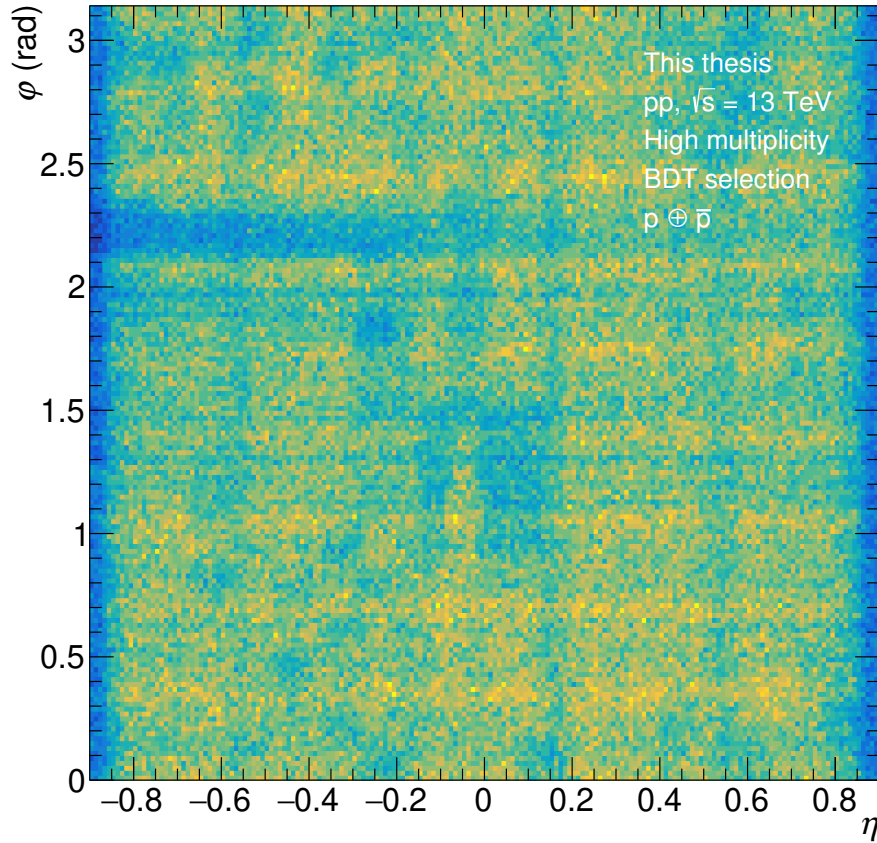


Figure 5.21: Distribution of selected protons in η and φ .

5.3 λ parameter determination

Every sample of particles contains a finite fraction of particles that are misidentified or originate from feed-down or knock-out from the detector material [15]. This particularly holds for composite particles, which always have a finite combinatorial background. If one is only interested in the yield, one can simply fit or construct the background (compare section 4.3.1) and subtract it. For a single particle, however, one cannot make a definite statement about its origin or identity. Thus, an experimental correlation function is always a superposition of multiple contributions.

In order to disentangle the measured correlation function, it is crucial to know its composition. In the terminology of femtoscopy, the probability that a given pair is of a certain type is often expressed in terms of λ parameters [15]. With these, the total (measured) correlation function $C(k^*)$ can be written as [15]

$$C(k^*) = \sum_{i,j} \lambda_{i,j} C_{i,j}(k^*) \quad (5.7)$$

where $C_{i,j}(k^*)$ are the correlation functions if all pairs would be of type i and j . By construction

$$\sum_{i,j} \lambda_{i,j} \equiv 1. \quad (5.8)$$

One must note that the λ parameters are not constant values, but they are certainly a function of the momenta of the particles. This momentum dependence translates into a k^* dependence, which needs to be considered to avoid biases. However, often only average values are given.

In any particle sample, typically two kinds of contaminations are present, which are misidentification and feed-down. Misidentification is when a particle is confused with a different particle species, for instance a kaon is assumed to be a proton, or in case of a composite particle, a background candidate is assumed to be signal. Feed-down, in turn, is a well identified particle, which, however, originated from a weak decay; for instance a proton stemming from a Λ decay. Often, the purities P_i and the primary fractions f_i of the paired particle samples are evaluated individually and separately for the two particles of interest. It is then assumed that these quantities factorize such that the λ parameters can be

computed by [15]

$$\lambda_{i,j} = f_i P_i f_j P_j. \quad (5.9)$$

While this should always hold at lowest order, higher order correlations might be present, but are typically neglected as there is no straight forward way of obtaining them.

Eq. (5.7) implies that in order to obtain the contribution of interest from the measurement, one needs to know all other contributions beforehand. While these are readily available for pairs that have already been measured or whose interaction is well known, often not all contributions are at hand. This is particularly the case for feed-down contributions. If a particle originates from feed-down of a weakly decaying particle, it does not exhibit a final-state interaction with other particles, as the decay occurred too far from the primary vertex. The mother particle, however, might show signs of a final-state interaction. This signal is then washed out by the decay, leading to a non-flat correlation function [15]. Similarly, residual correlations can occur in the case of electromagnetic decays, for instance in the p- Σ^0 system, where the Σ^0 decays into a Λ and a photon. The Σ^0 is extremely short-lived, such that the Λ daughters cannot be distinguished from primaries. In these cases, the sidebands of the invariant-mass peak are often taken as a proxy for the contribution of the combinatorial background [23]. Also, attempts have been made to transform the known underlying correlation functions kinematically to describe the feed-down contributions, firstly investigated in Ref. [290]. The procedure was already successfully applied to various systems [15], including p- Σ^0 [22], based on the methods developed in Ref. [291]. For all other contributions, in particular for knock-out, the correlation function is often assumed to be flat [15]. This seems reasonable if the contribution is not large, but one should be aware that it might create a bias if unchecked.

In any case, one first of all needs to consider which contributions are significant. As discussed in section 4.3.2, the only background contribution in the Σ^+ baryon sample is the combinatorial background. This purity is obtained from the MC template fits presented in section 5.1.4. The feed-down from strong resonances is treated via the source size as discussed in section 5.5.1.

In case of the protons, typically misidentification, feed-down from Λ , feed-down from Σ^+ , and knock-out from the detector material are considered, while feed-

down from rare probes is neglected [15]. This strategy is followed also in this thesis. The fraction of misidentified particles is typically obtained from a MC simulation. Taken accurately, this only works if all relevant p_T spectra are reproduced exactly by the simulation, which might not be the case. For the protons, however, this MC method gives results that are consistent with the method used in this analysis as shown in Fig. 5.25. For the feed-down, template fits of the DCA_{xy} distributions are typically used to access the secondary fractions [15]. This is, however, challenging to do p_T differentially, as this requires sufficiently large statistics in all p_T bins of the templates, both in data and in the simulation. In case of a machine learning selection, it is not possible at all, since there is no fixed selection on the DCA distributions. Additionally, template fits make it complicated to derive an uncertainty on the ratios, which is why they are rarely shown [15]. Nevertheless, the secondary fractions are highly error prone. For these reasons, a completely new method was developed within this thesis. The idea of this method is simple and can be illustrated with an example.

In order to find the feed-down fraction from Λ s to the protons, one can take the measured spectrum of Λ baryons [242, 285] as a starting point. This is then scaled by the branching ratio of the decay into protons and subsequently folded by the momentum distribution of the protons as a function of the Λ momentum, which results in an effective spectrum of protons from Λ decays. To this end, the phase space of the decay is simulated using “TGenPhaseSpace” from ROOT [245]. The effective spectrum is further weighted by the reconstruction efficiency of protons from Λ decays. This reconstruction efficiency differs from the reconstruction efficiency of Λ baryons, as it is not necessary to correctly reconstruct the Λ in order to measure its decay proton. Furthermore, the reconstruction efficiency is lower compared to primary protons, as secondary protons are suppressed due to their larger DCA to the primary vertex. A comprehensive plot of all relevant efficiencies is given in Fig. 5.22.

One can finally take the ratio of those spectra and the sum of the spectra to obtain the fraction of the respective contribution as a function of p_T . The same procedure is repeated for protons from Σ^+ decays.

Advantageously, the spectrum of Σ^+ with the high-multiplicity trigger is measured within this thesis and is thus readily available for the method outlined above. For the Λ s this is not the case, since there is no measurement of the Λ

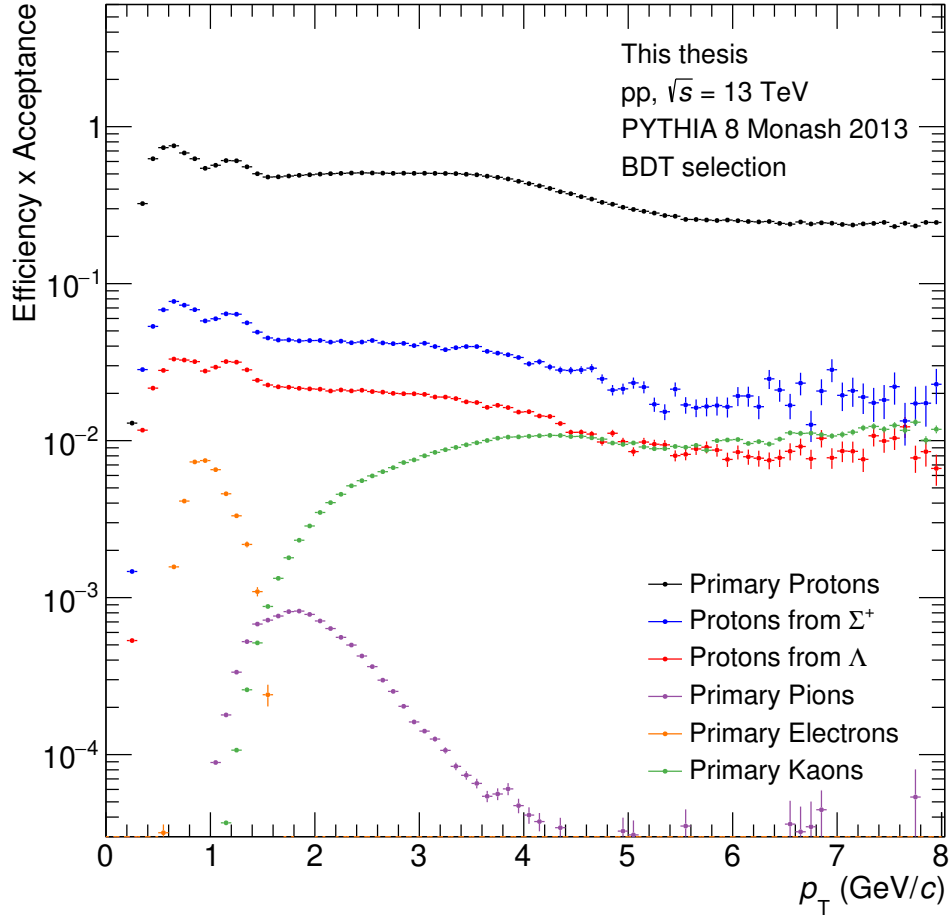


Figure 5.22: Acceptance \times efficiency of various primary particles and protons from feed-down relevant for the determination of the λ parameters.

p_T spectrum using the high-multiplicity trigger. Instead, the Λ baryons have been measured in several multiplicity classes, the so-called V0M classes, ranging from high multiplicity in class I to low multiplicity in class X [242, 285]. Here, I and X are roman numerals³¹. The average multiplicity corresponding to class I is almost as high as in the high-multiplicity triggered data set, but not exactly. This makes it necessary to extrapolate these spectra to the correct multiplicity. It can be shown that the integrated yield scales linearly with the multiplicity [292], but this does not hold for the full spectrum. This is, because the yield does not increase equally in all bins, but the spectra get harder with multiplicity, i.e. the yield increases overproportionally at high momenta. Therefore, the

³¹The roman numerals correspond to multiplicity intervals defined by the ALICE collaboration. The intervals can for instance be found in Ref. [242] and Ref. [282].

extrapolation is performed on a bin-by-bin basis. As a cross check, the class I spectrum is reproduced from the class II and class III spectra and is found to be consistent with the measured class I spectrum. Thus, it is justified to assume that this scaling holds also at slightly higher multiplicities. The spectra for the 3 multiplicity classes and the two extrapolated spectra are shown in Fig. 5.23 for the protons [282, 293] and the Λ s [242, 285]. The resulting effective spectra are displayed in Fig. 5.24. From this, the primary fractions are evaluated and are shown in Fig. 5.25.

A similar procedure is done for the kaons and pions (both from Ref. [282, 293]), which allows for a MC independent evaluation of the proton purity. It also allows a cross check of the data-driven method described above. The resulting purities for both methods are displayed in Fig. 5.25. A very good agreement is evident. The minor deviation around 1.5 GeV/ c can be attributed to electrons, which are not considered in the data-driven method since there are no suitable spectra available. Since their contamination is small, they are neglected.

The obtained quantities are functions of p_T and need to be projected onto k^* . This is done using the matrices displayed in Fig. 5.26. The matrices are evaluated in the mixed events to improve the statistics. Finally, the λ parameters are evaluated using Eq. (5.9). The results are shown in Fig. 5.27.

The genuine contribution amounts to roughly 79% in the femtoscopic region. A very good value that underlines the superiority of the p - Σ^+ channel compared to p - Σ^0 , where a value of only 22% was found [22, 23]. The main contamination is the combinatorial background of the Σ^+ , which alone makes up more than 80% of the total contamination. The k^* dependence is only modest, as the spread in the purity of the Σ^+ is only 15% and is washed out in the projection onto k^* . The second most important contamination stems from the feed-down into the protons, which contributes by around 2% in absolute terms. All other contributions reside in the sub-percent regime. Thus, higher order contaminations (e.g. misidentification of secondary pions) can be neglected. Furthermore, the contamination from knock-out is also negligible in pp collisions [15].

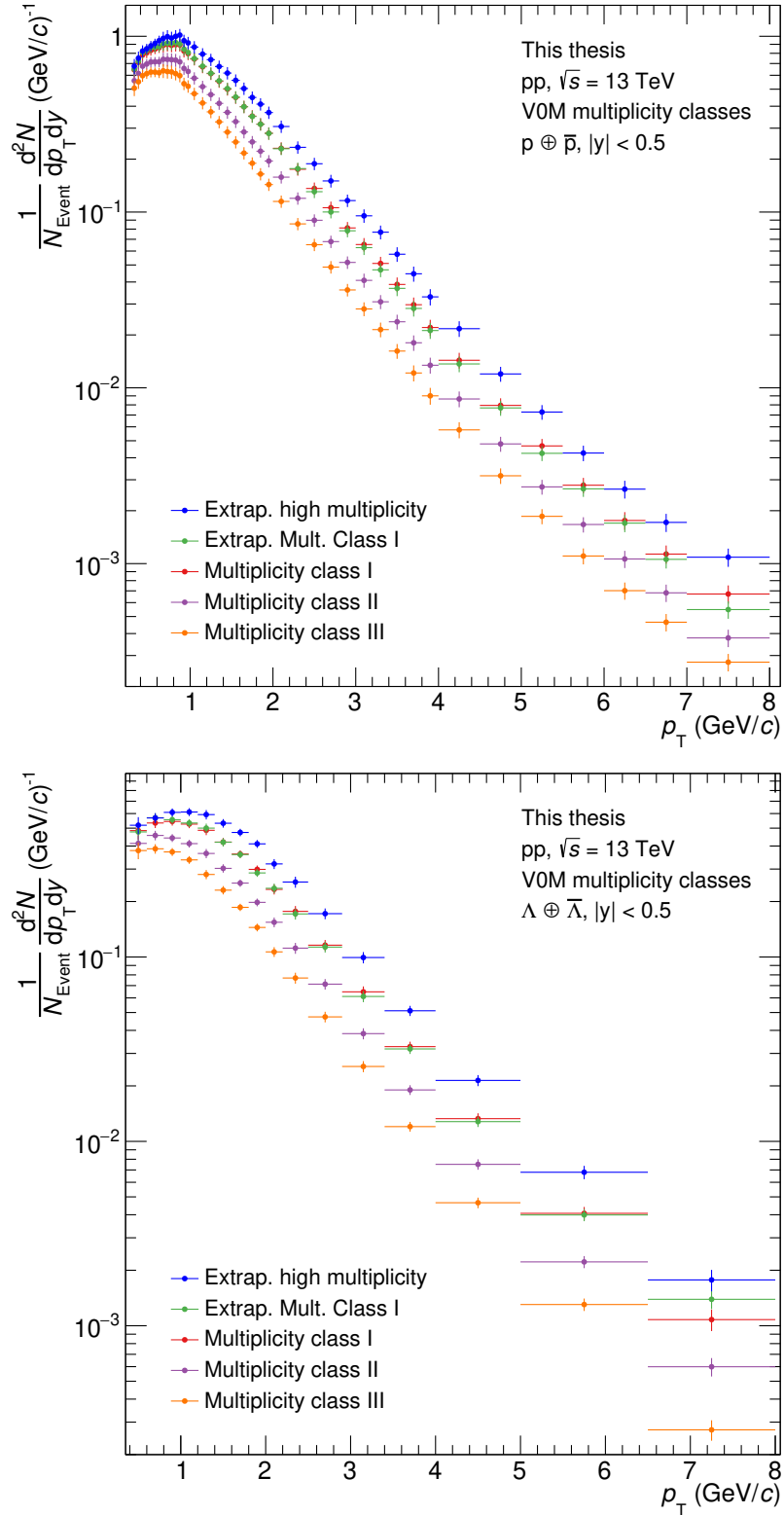


Figure 5.23: Measured and extrapolated p_T spectra of protons (upper) and Λ s (lower) in the highest multiplicity classes. Proton data taken from Ref. [282, 293] and Λ data taken from Ref. [242, 285].

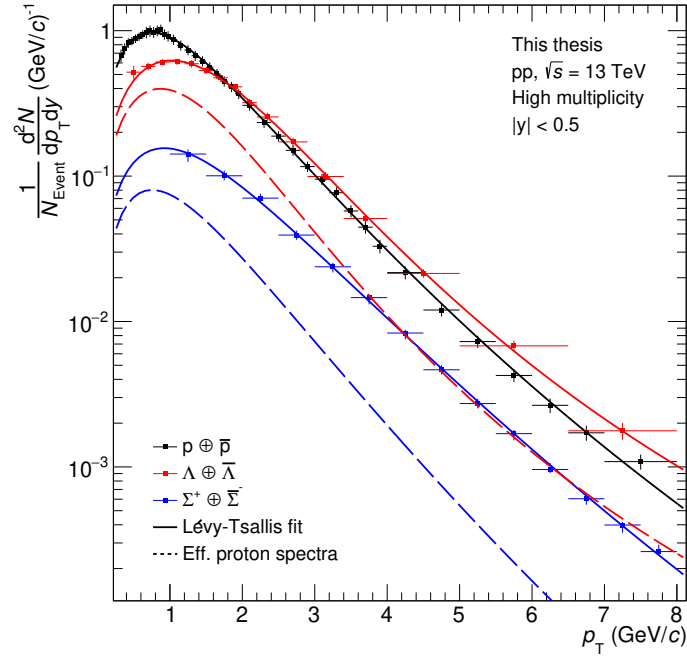


Figure 5.24: Effective spectra of protons from Λ and Σ^+ decays plotted together with the original spectra of primary protons, Λ , and Σ^+ . The efficiencies are not yet considered.

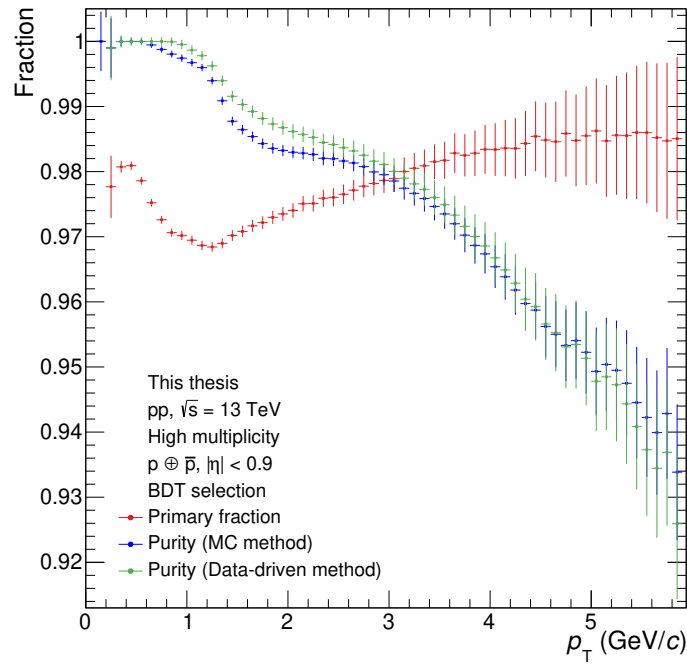


Figure 5.25: Purities (green, blue) and primary fraction (red) of selected protons. The purities are evaluated using MC simulations (blue) as well as the data-driven method described in the text (green). For the primary fractions, a comparison with MC is not fruitful since the spectra of Λ and Σ^+ are not well reproduced.

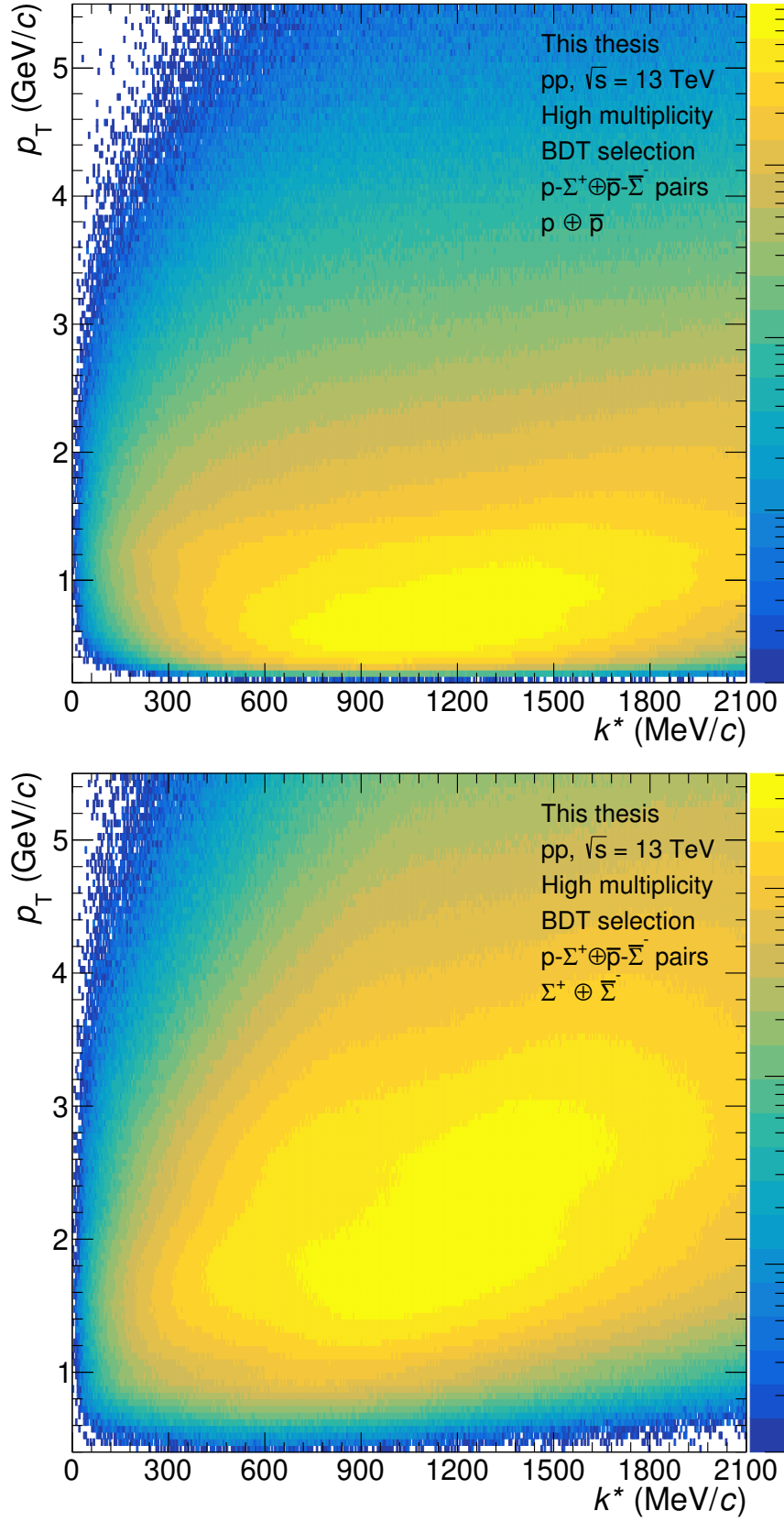


Figure 5.26: k^* vs. p_T matrices for protons (upper) and Σ^+ (lower) evaluated in mixed events.

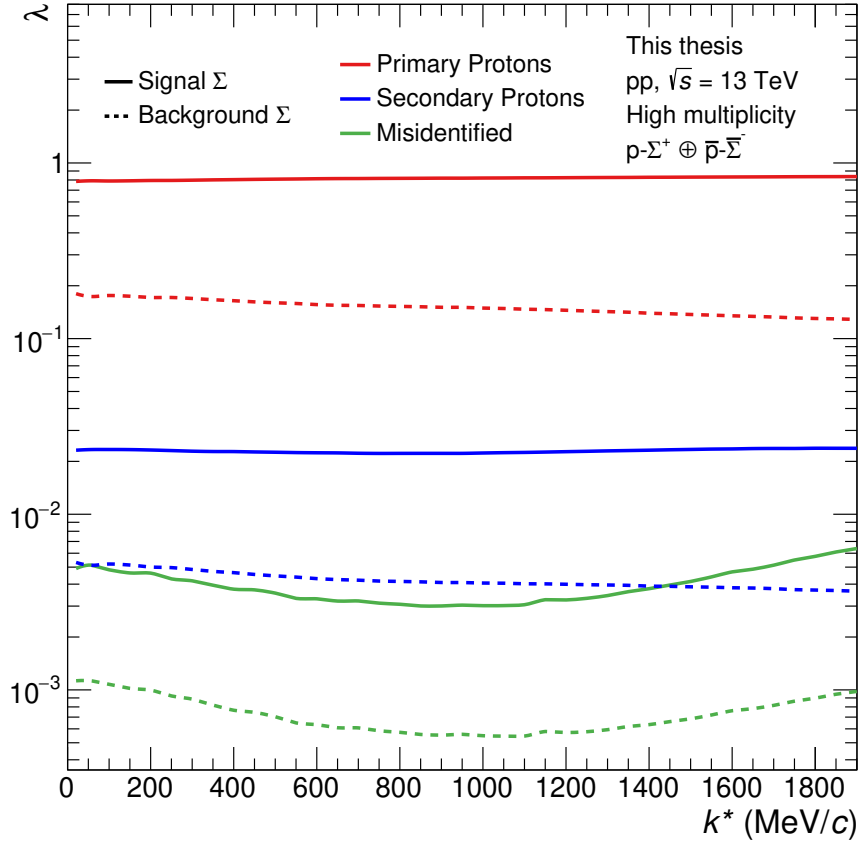


Figure 5.27: λ parameters of the main contaminations of the p - Σ^+ pairs. The line style indicates if the Σ^+ candidate is signal (solid) or background (dashed), while the line color indicates if the proton is primary (red), secondary (blue), or misidentified (green). Thus, the genuine p - Σ^+ contribution is given by the solid red line.

5.4 Experimental correlation function

In this section, the experimental correlation function will be discussed. As discussed in section 5.3, a rather high genuine fraction is achieved. Also, the relative momentum resolution does not pose a problem, which will be discussed in section 5.4.3. Even though the reconstruction efficiency could be improved by several orders of magnitude, the statistics clearly remains the limiting factor. Nonetheless, given the large spread of model predictions, the data is very constraining and allows to draw conclusions, which will be discussed in section 5.5. For the k^* distributions, firstly a reasonable binning has to be chosen. With a too course binning, one is not able to resolve the correlation signal, while a too fine binning has no significance in case of low statistics. It is found that a bin width of 40 MeV/ c is a reasonable trade-off for the p - Σ^+ correlation function given the available statistics. The first 30 MeV/ c are spared as there are hardly any entries in this region. Considering the model predictions, a strong rise of the correlation function is expected below 100 MeV/ c . To resolve this region better, the width of the first two bins is reduced to 35 MeV/ c which allows to accommodate two bins below 100 MeV/ c .

Given the rather large bin width, the center of gravity within each bin might deviate from the bin center, which needs to be considered in order to compare to theory calculations. Sometimes this is accounted for by shifting the markers to the center of gravity, evaluated in the mixed events. However, clearly the proper approach is to integrate the model under test over the unbinned phase space distribution (i.e. mixed events) and compare the obtained distribution to the same-event distribution. Nonetheless, it is found that shifting the bin center to the center of gravity of the mixed event and evaluating the model at that point gives almost identical results. Thus, a shifting of the bin centers in the aforementioned way is justified, at least for esthetic purposes. In any case, the shift is only visible in the first two bins and negligible in all others.

In order to obtain a correlation function from the relative-momentum spectrum, one needs to construct an uncorrelated sample. This sample should ideally resemble the phase space distribution of the particles under study including all detector effects, but break the correlation induced by the final-state interaction. The correlation function is then simply given by the normalized ratio of the pair-momentum distributions [11] as stated in Eq. (1.5). The construction

of the uncorrelated sample is done in twofold ways, which will be elaborated in the following sections.

5.4.1 Uncorrelated sample

The construction of the uncorrelated sample has similarity to the construction of the invariant-mass background, which was discussed in section 4.3.1, and the same considerations hold. In the standard approach of femtoscopy, the uncorrelated sample is built by taking the particles from different events [11]. Thereby, the events are required to have similar vertex positions in z and similar multiplicities, where the used mixing parameters are equal or similar to the ones stated in the aforementioned section. Even though this is a common practise, it is known that it does only work well in large collision systems like Pb–Pb and not in small ones like pp [11, 15]. Ideally, the correlation function should be unity outside of the region where the final-state interaction is visible, i.e. larger than $\mathcal{O}(100 \text{ MeV}/c)$. This is, however, not the case in small collision systems where the correlation function exhibits a rise in the order of 10% at relative momenta of about $1 \text{ GeV}/c$ [15, 23]. The effect is present in some Monte Carlo generators, yet they fail to describe it quantitatively [15].

The increase is usually fitted with a simple polynomial up to third order. The fit is carried out outside of the region of interest, starting from around $300 \text{ MeV}/c$. The fit is subsequently multiplied to the femtoscopic fit and provides a reasonable yet phenomenological description [15].

Particularly in the case of large statistical uncertainties, the background fit introduces a sizeable contribution to the systematic uncertainty. Therefore, a different approach to construct the uncorrelated sample was developed in the scope of this thesis, which is described in the next section. It is used complementary to the standard method, which is described in the following, by providing a fit-independent comparison.

In the standard method, the particles are taken from different events. Similarly to the event mixing for the invariant mass analysis (section 4.3.1), the difference in the total number of tracklets in the acceptance is restricted to 4 and the difference in the z -position of the primary vertices is required to be no more than 1 cm. The mixing is done on a run-by-run basis to avoid biases stemming

from the change of the detector status over time. Within the runs, all selected particles from compatible events are mixed. Considering the model predictions (section 5.5.2), the normalization region cannot extend lower than 300 MeV/ c , as a sizeable deviation from unity is expected there. Above 500 MeV/ c , the increasing trend clearly impacts the correlation function. Thus, the normalization region ranges from 340 to 500 MeV/ c . This region is varied by 40 MeV/ c in both directions for the systematic uncertainties as described in section 5.4.4. The small number of data points in the normalization region limits the choice of usable fit functions. A constant function (0-th order polynomial) is chosen to fit the data in this region. This is based on the assumption that the minijet³² background vanishes towards low k^* , which was also observed in the case of the p - Σ^0 correlation function [22, 23]. Indeed, the data points can be described by a constant within the statistical uncertainty in the given region. Moreover, the correlation function converges to the one obtained with the alternative method in the normalization region, giving further evidence that the choice of the normalization is reasonable. The resulting correlation functions for both methods, the standard and the alternative one, are shown in Fig. 5.28 and 5.29. One may note that in both cases the statistical uncertainties of the uncorrelated samples are small (yet not negligible) compared to the one in the same events. This explains the striking similarity of the fluctuations in both correlation functions that stem mostly from the same-event distribution in both cases.

5.4.2 Alternative method

The idea of event mixing is to describe the distribution stemming from the phase space and the detector acceptance as accurately as possible, while at the same time breaking the correlation of interest, such that the ratio of the correlated and uncorrelated sample exhibits only the correlation of interest [278]. However, the final-state interaction is not the only correlation present in a particle collision. Collective phenomena and hard parton interactions for instance contribute to a non-uniform emission pattern of particles in an event [294, 295]. Such correlations are typically also broken in a mixed event and thus reflect in a non unity-valued correlation function referred to as non-femtoscopic background [15]. While this is easily comprehensible, a quantitative theoretical de-

³²See paragraph 5.4.2 on page 177.

scription is missing. Event generators like PYTHIA [62, 95] show similar features, but fail to describe the effect quantitatively [15]. It has been pointed out that the simulated correlation function could be reweighed to describe the data [188]. In baryon–anti-baryon systems, where the minijet background is very pronounced, attempts have been made to model the background using PYTHIA by separating pairs stemming from common and unrelated partons [296]. While a satisfactory description could be achieved, these approaches are still model dependent and come with free parameters causing uncertainty. Thus, an alternative method is desired, which is introduced in this section. Often, the increase at large relative momenta is attributed to the conservation of energy and momentum, which is obviously violated when a particle is artificially introduced to an event [15, 184]. Occasionally, also the term “minijet” (or “mini-jet”) arises, which has - as jets in general - no clear definition. In this regard, a minijet refers to particles stemming from the hadronization of a common parton [297]. In an ultra-relativistic pp collision, the partons are resolved, i.e. it is in fact a superposition of parton-parton collisions. Due to the conservation of momentum, the colliding particles are thereby emitted in a back-to-back direction, leading to preferential directions. Therefore, the emission of particles in a pp collision is not isotropic. In a mixed event, where particles are taken from different events, preferential directions are not preserved. If the two particles of interest originate from the same parton scattering, they might be emitted in a similar direction or in the opposite. In the former case, they might have a small or large relative momentum k^* , depending on their individual momenta, while in the latter, they can only have a large relative momentum due to their opposite direction of flight. This could explain the higher abundance of pairs at large relative momenta.

The issue of the preservation of jet-axes in small systems was already pointed out earlier [11] and multiple solutions were proposed, mostly based on the reversing or flipping of momentum components with respect to the jet-axes.

One may consider that the correlation signal from the final-state interaction depends on the angle and the momenta of the particle pair, while for instance the correlation from minijets is dominantly of angular nature, at least at first order. This might be used to preserve the correlations which are not of interest in the denominator sample (i.e. the now partially correlated sample) and thus eliminate them from the correlation function.

The relative momentum of any pair depends, apart from the particle masses, only on 3 parameters, which are the absolute values of the particle momenta $|p_1|$ and $|p_2|$ and the angle α they enclose. With these, one may write the relative momentum of the pair in its rest frame k^* as [173]

$$k^* = \sqrt{\frac{(\Delta p^2 + m_1^2 + m_2^2 - \Delta E^2)^2/4 - m_1^2 \cdot m_2^2}{(\Delta p^2 + m_1^2 + m_2^2 - \Delta E^2) + m_1^2 + m_2^2}} \quad (5.10)$$

with

$$\Delta p^2 = p_1^2 + p_2^2 - 2 \cdot p_1 \cdot p_2 \cdot \cos(\alpha)$$

and

$$\Delta E^2 = \left(\sqrt{p_1^2 + m_1^2} - \sqrt{p_2^2 + m_2^2} \right)^2$$

where m_1 and m_2 are the masses of the particles.

One may take for any particle pair in the same event the exact angle and construct one or multiple mixed pair(s) from it by changing the particle momenta only. The momenta are thereby taken from distributions filled from the same events beforehand. Since the momentum spectra become harder with increasing multiplicity, the momentum distributions are considered in several multiplicity bins, similar to a standard event-mixing approach.

By construction, the angular distribution of the mixed pairs constructed in this way exactly resembles the one in the same events. The same holds true for the momentum distributions. Since in this method the angles are kept fixed, it is referred to as fixed-angle mixing in the following. The resulting correlation function is plotted in Fig. 5.28 and 5.29 together with the one using the standard event mixing. Obviously, the very pronounced increase at large relative momenta is missing in the fixed-angle mixing technique, implying that it in fact originates from a purely angular correlation which is now preserved. It remains, however, to be checked that remnants of the final-state interaction are not also preserved, which would wash out the femtoscopic signal and thus bias the result. It should be noted that this procedure cannot be applied for identical particles with peaked momentum distributions. If k^* is small, so is the angle. If one does now draw two momenta from the same distribution, most likely similar ones will be drawn, in which case the mixed pair will again have a small k^* . This

kind of autocorrelation can luckily not occur in the case of protons and Σ^+ , as the reconstructed momentum distributions are very different.

In terms of uncertainty, the new background construction is also advantageous. Since the number of mixed pairs per same-event pair is known, the normalization of the correlation function is trivial. An uncertainty stemming from the fitting of the non-femtoscopic region and the choice of the fit function does not occur.

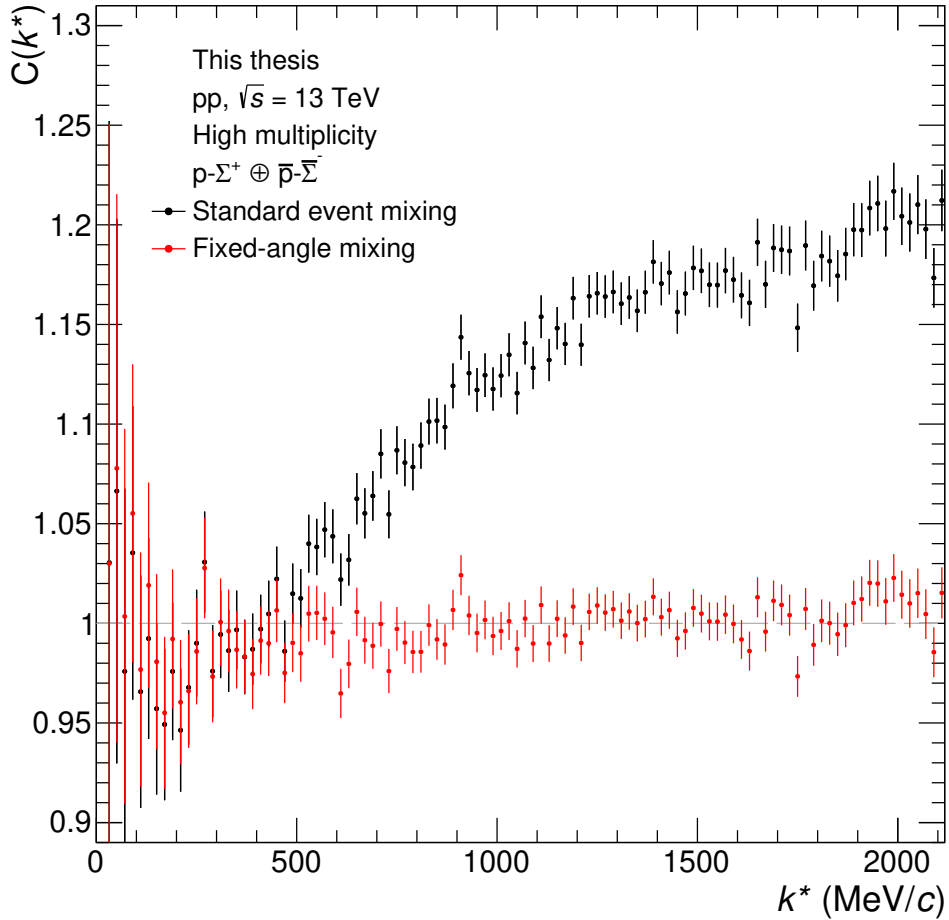


Figure 5.28: Comparison of the correlation function of protons and Σ^+ using the standard (black markers) and the fixed-angle method (red markers) to construct the uncorrelated sample of particle pairs. With the fixed-angle method, no increase of the correlation function at high k^* is observed.

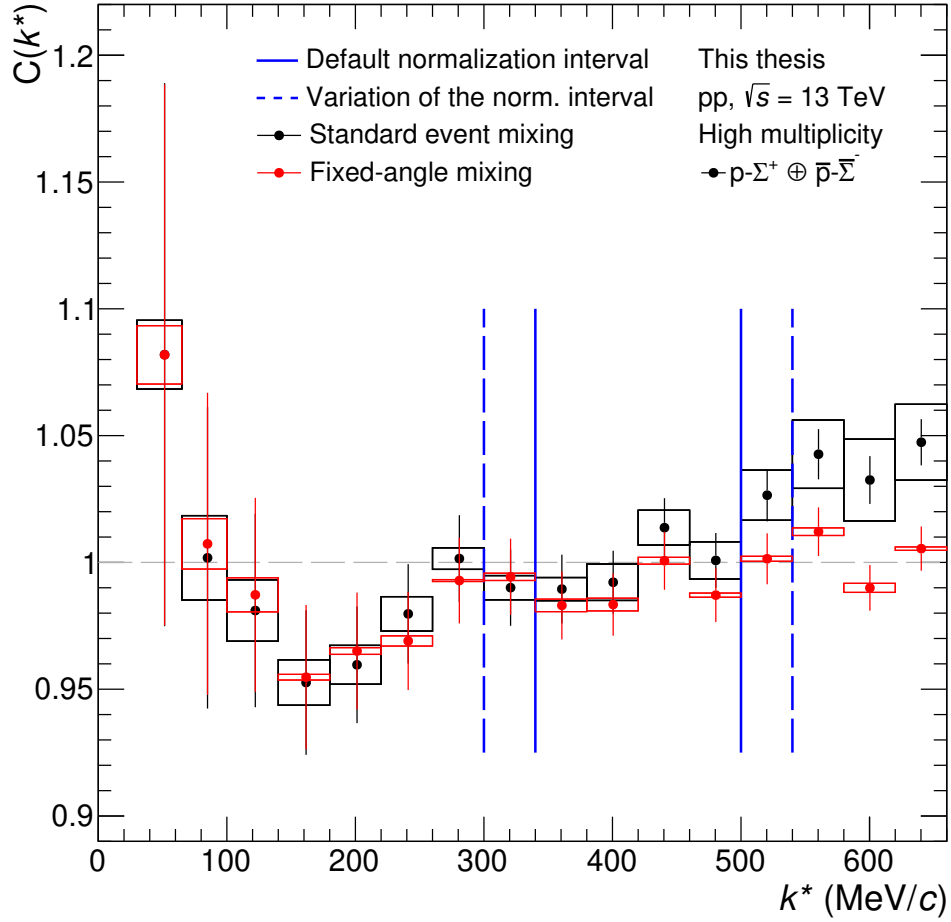


Figure 5.29: Comparison of the correlation function of protons and Σ^+ using the standard (black markers) and the fixed-angle mixing (red markers) to construct the uncorrelated sample of particle pairs. The normalization region for the standard method and its variations are also shown. A very good agreement in and below the normalization region is visible.

5.4.3 k^* resolution

The k^* resolution is related to the momentum resolution of the particles and in case of the p - Σ^+ correlation function it is dominated by the momentum resolution of the Σ^+ . The k^* resolution is evaluated by comparing the k^* values calculated from the reconstructed momenta to the ones calculated from the true values obtained from the Monte Carlo simulation. Technically, the matrix spanned by the true and the reconstructed k^* values is sliced in bins of the reconstructed k^* with a bin width of 5 MeV/c. This is done in the mixed events, as otherwise not enough statistics could be aggregated. There is no

difference between same and mixed events in terms of resolution. The obtained resolution as a function of k^* is depicted in Fig. 5.30. A k^* dependence is visible, with the relative resolution ranging from roughly 10% at low k^* to around 1% at high k^* . In the femtoscopic region, the resolution is around 6 MeV/ c , which is not a limiting factor considering the bin width of the correlation function. Interestingly, the k^* resolution of a pair of tracks, for instance two protons, is around 4 MeV/ c [22], underlining that the momentum correction discussed in section 5.1.2 is indeed capable of restoring the momentum resolution to a very high degree.

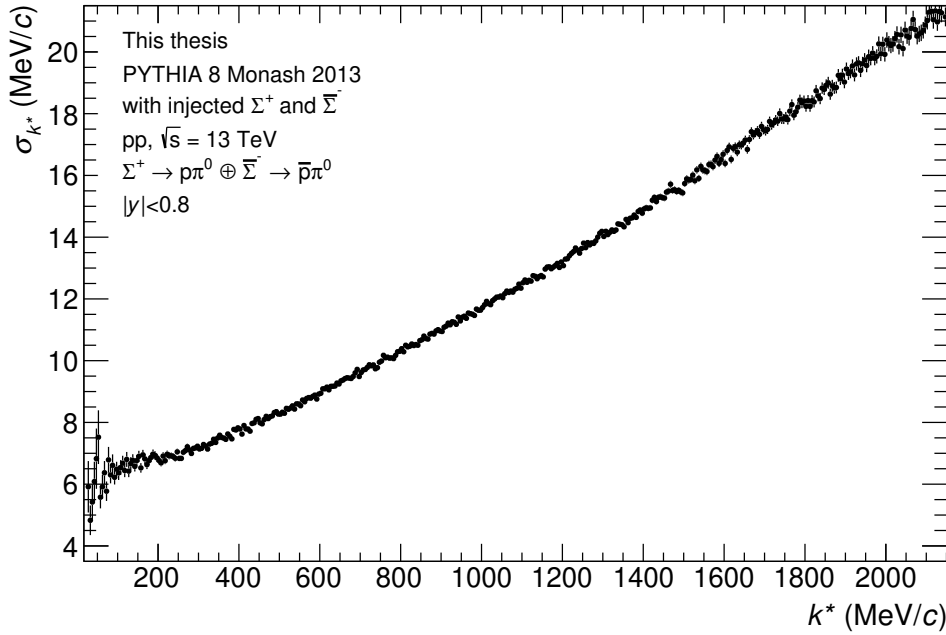


Figure 5.30: Resolution of k^* as a function of k^* . In the femtoscopic region, a resolution of around 6 MeV/ c is reached.

5.4.4 Systematic uncertainties

Similar to section 4.3.4, the systematic uncertainties of the experimental correlation function are calculated by making variations to the particle selection and comparing the resulting correlation functions to the default one. In addition, also the construction and fit of the uncorrelated sample is considered as a source of uncertainty.

For the particle selection, the uncertainty does not arise from the selection itself,

but from the treatment within the calculation of the λ parameters. Ideally, a stricter selection leads to an enhancement of the signal, where the enhancement equals the increase of the genuine λ parameter. Any excess or shortfall of the enhancement compared to the change of the genuine λ parameter can then be classified as systematic uncertainty. In the case of p - Σ^+ , the cut-offs of the BDT scores of protons and Σ^+ are each increased or decreased by 10%. Since there is no linear dependence of the purity on the BDT scores, the effect of these variations is evaluated by repeating the procedure explained in section 5.3 for the different selections. Overall, genuine λ parameters between 75.5% and 82% are found, where in any case the change of this value is mostly driven by changes in the Σ^+ purity as the largest source of contamination. Given the shallowness of the interaction, the expected change of the femtoscopic signal amounts to no more than around 0.01, which cannot be resolved within the limited statistics. Nonetheless, the described variations are kept as a proxy for the uncertainty of the genuine λ parameter.

As already discussed in section 5.4.1, the fit range is varied by one bin in both directions to account for the uncertainty stemming from the choice of the fit range. Changing the fit function or choosing an even wider fit range is not fruitful for the reasons discussed in the aforementioned section. In addition to the fit range, the alternative construction method for the uncorrelated sample is considered as a variation. The variations of the fit are done for all variations of the particle selections to account for possible correlations. It is assumed that the distribution of the variations is uniform, and thus the total uncertainty of the data points is evaluated by dividing the difference between the maximum and the minimum value by $\sqrt{12}$. The individual contributions to the systematic uncertainty are shown in Fig. 5.31, where each contribution is evaluated by keeping the others at the default and dividing the resulting deviation by $\sqrt{12}$ each.

Another major source of systematic uncertainty is the source size that is evaluated in section 5.5.1. While this does not affect the experimental correlation function and is thus not included in the uncertainty of the data points, it is crucial for the comparison with model calculations and gives rise to uncertainty bands around the model curves. The average width of the bands is also shown in Fig. 5.31 for comparison.

By construction, the choice of the fit range leads to a constant uncertainty due

to the usage of a constant function. In contrast, the other contributions of the systematic uncertainty vanish towards high k^* , which can be attributed to the correlation function trending to unity. However, it also hints towards an increasing statistical admixture of the evaluated systematic uncertainties at low k^* as discussed in section 4.3.4. The contribution of the different mixing methods is small, highlighting their good agreement, particularly in the first bins. The contribution of the BDT selection is similar at high k^* but increases further towards low k^* . As discussed above, the uncertainty induced by the uncertainty of the source size is only shown for comparison and does not affect the measured correlation function. Nonetheless, it is apparent that this contribution is crucial for the comparison between data and theory and contributes considerably to the overall systematic uncertainty, even being the largest contribution in the first measured k^* bin.

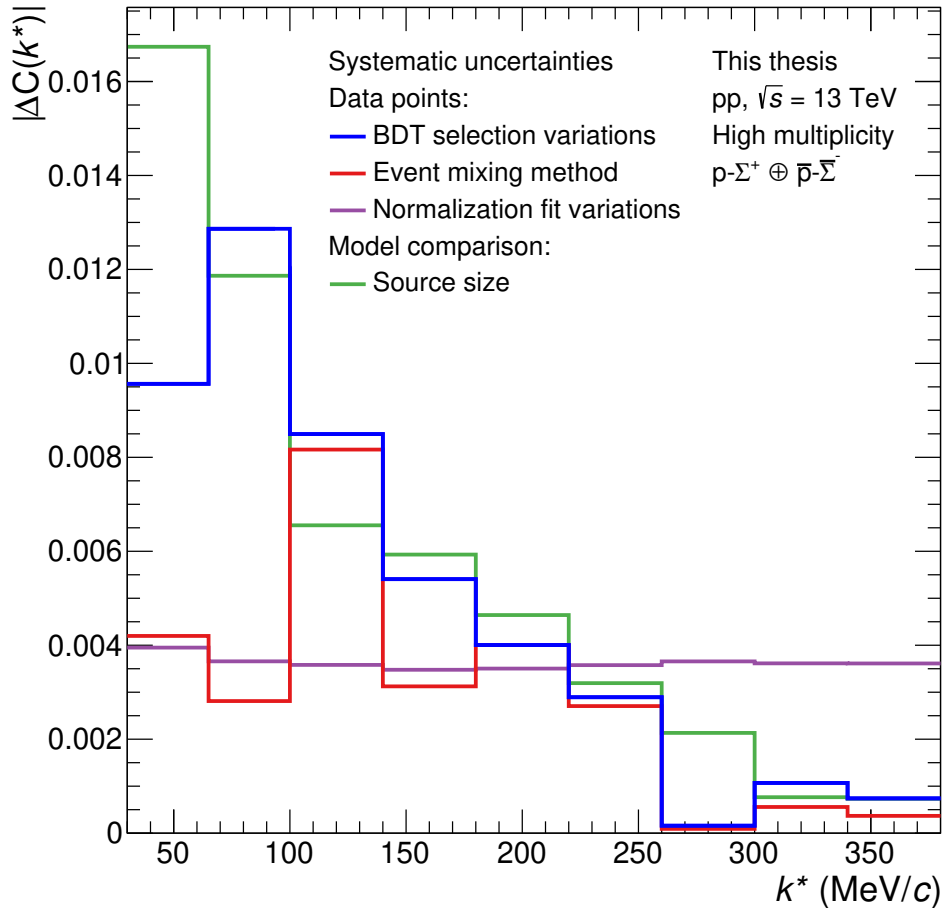


Figure 5.31: Contributions of the systematic uncertainties of the correlation function as a function of k^* . The uncertainty of the model comparisons induced by the uncertainty of the source size (green line) is also shown for comparison.

5.5 Theoretical correlation function

In the following, the obtained correlation function is compared to theory predictions to draw conclusions about the p - Σ^+ interaction, particularly on the less-known triplet channel. Beforehand, the source size must be constrained as good as possible, making use of the extensive work invested in the study of the particle emitting source in ALICE [182, 183].

5.5.1 Source size

The determination of the source size is based on the procedure that was developed within the ALICE collaboration [182, 183]. The source size was calculated in collaboration with M. Korwieser [298], who provided the resonance source distribution. The procedure is sketched in section 1.4.2.

Firstly, the mean m_T is calculated. Therefore, the m_T is calculated for all particle pairs using Eq. (1.8). As seen in the equation, m_T depends on the p_T of the particles as well as on their masses. If no restriction on the relative momentum is applied, m_T can take any value above the mean mass of the pair particles. This is because the p_T is considered in vector form, which allows the particle momenta to cancel. If one, in turn, limits the relative momentum of the particles to a small value, this implies that the particles move roughly collinearly. The minimum pair p_T is then limited by the onset of the measurement. Thus, the onset of the m_T distribution is shifted to a higher value in this case. On the other hand, the phase space of high- p_T particles is larger, resulting in a lower probability to form pairs with low k^* . Thus, the distribution in m_T is also narrower for low- k^* pairs. Consequently, the mean m_T is a function of the cut-off in k^* , and so is the source size. However, at low k^* , this dependence is minimal and it is sufficient to restrict oneself to evaluating the mean m_T in the femtoscopic region ($k^* < 200$ MeV/ c) and treat the residual k^* dependence as an uncertainty. The normalized distributions of m_T are displayed in Fig. 5.32 in same and mixed events for various cut-off values in k^* : 100 MeV/ c , 200 MeV/ c , and 300 MeV/ c . In this region, the evaluated means are very stable among the shown distributions and even at 500 MeV/ c the mean m_T remains within the uncertainties given below. Also, the same- and mixed-event distributions are in good agreement. Using the mixed-event distribution with $k^* < 200$ MeV/ c as

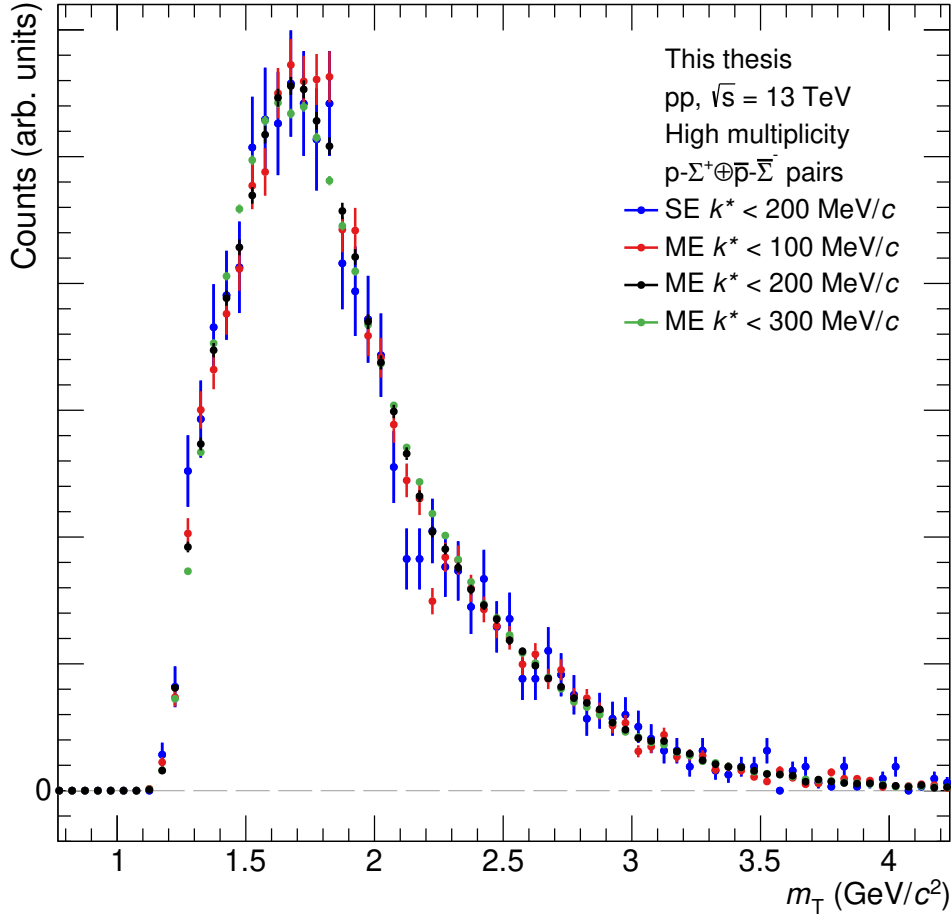


Figure 5.32: Distributions of m_T of the p - Σ^+ pairs shown for same (SE) and mixed events (ME) and for multiple cut-off values of k^* as described in the text. A bin width of $50 \text{ MeV}/c^2$ is used in the plot, while for the evaluation of the means the unbinned distributions were used. The distributions are normalized to the number of entries for comparability.

default, one finds a value of $\langle m_T \rangle = (1.94 \pm 0.03) \text{ GeV}/c^2$, where the uncertainty gives the full difference of the default to the minimal and maximal values of $\langle m_T \rangle$ of the distributions shown in Fig. 5.32.

The mean m_T is comparably large, which is caused by the relatively large rest mass of the Σ^+ and by the high average p_T of the Σ^+ , which is in turn related to the p_T dependence of the reconstruction efficiency.

From the mean m_T , the core radius is evaluated using the parametrization seen in Fig. 1.7. Fortunately, the mean m_T is situated in a region where the m_T dependence is almost flat [183], such that the effects of the uncertainty of $\langle m_T \rangle$ as well as the width of the m_T distribution have minimal effect on r_{core} . Thus,

the uncertainty of r_{core} is driven by the uncertainty of the parametrization. The evaluated value amounts to $r_{\text{core}} = (0.85 \pm 0.05)$ fm.

The enlargement of the source size due to resonance decays is modelled using the framework that was worked out in Ref. [182]. In a nutshell, the procedure works as follows. One has to consider that several scenarios are possible for the origin of the particle pair under study. For simplicity, only 4 are considered, which are that both particles are primordial, both stem from resonances, as well as the two mixed cases. To evaluate the probabilities of the aforementioned scenarios, a list of resonances is produced from the thermal model toolkit Thermal-FIST [280] using the latest PDG list [9] of currently known resonances. The decay kinematics of the resonances are simulated based on the masses of the resonances using an EPOS [63] simulation. Hereby it is assumed that all resonances only decay in a two-body decay into a baryon and a pion. With this basis, the total source distribution is obtained using a sampling procedure. Firstly, a random core radius is drawn from a Gaussian distribution with the width obtained from the $\langle m_T \rangle$ parametrization. Then, one of the emission scenarios is chosen using the probabilities obtained before. With the masses and the lifetimes of the resonances at hand, the flight distances prior to their decay can be sampled from an exponential function. The orientation of the resonances is taken from the EPOS simulation. With this, the total source size is calculated as the modulus of the vector sum of the core radius and the flight distance of the resonances.

The uncertainty of the source size is evaluated by making variations to the input parameters, namely the core radius, the fraction of the resonances, the masses of the resonances, as well as their lifetimes. The core radius is varied within the uncertainty of the parametrization, while the other parameters are varied by 10% each. This value is chosen rather conservatively to anticipate later changes of the PDG list and also to accommodate the uncertainties of the resonance properties. In order to quote numbers, the obtained full source is fitted with a Gaussian distribution in the region from 0.5 to 4.5 fm, which results in an effective Gaussian parametrization of the source. This is done for all variations and, assuming a uniform distribution, the deviation between the smallest and largest source radius is taken and divided by $\sqrt{12}$. With this, a radius of $(0.98^{+0.03}_{-0.02})$ fm is found. The resonance contribution thus only amounts to 0.13 fm, a comparably small value, which is related to the fact that the pri-

mordial fraction of the Σ^+ is more than 63% and thus almost twice as high as the primordial fractions of protons or Λ s [280].

Fig. 5.33 displays the full source, the Gaussian core, as well as the effective Gaussian source. The effective parametrization describes the full source well at small distances, but converges much faster towards 0. Due to the exponential decay of the resonances, the resonance source still has a finite contribution even at very large values of r , where no interaction is expected. The effect of this behavior is studied in the light of the theoretical calculations and will be discussed in section 5.5.3.

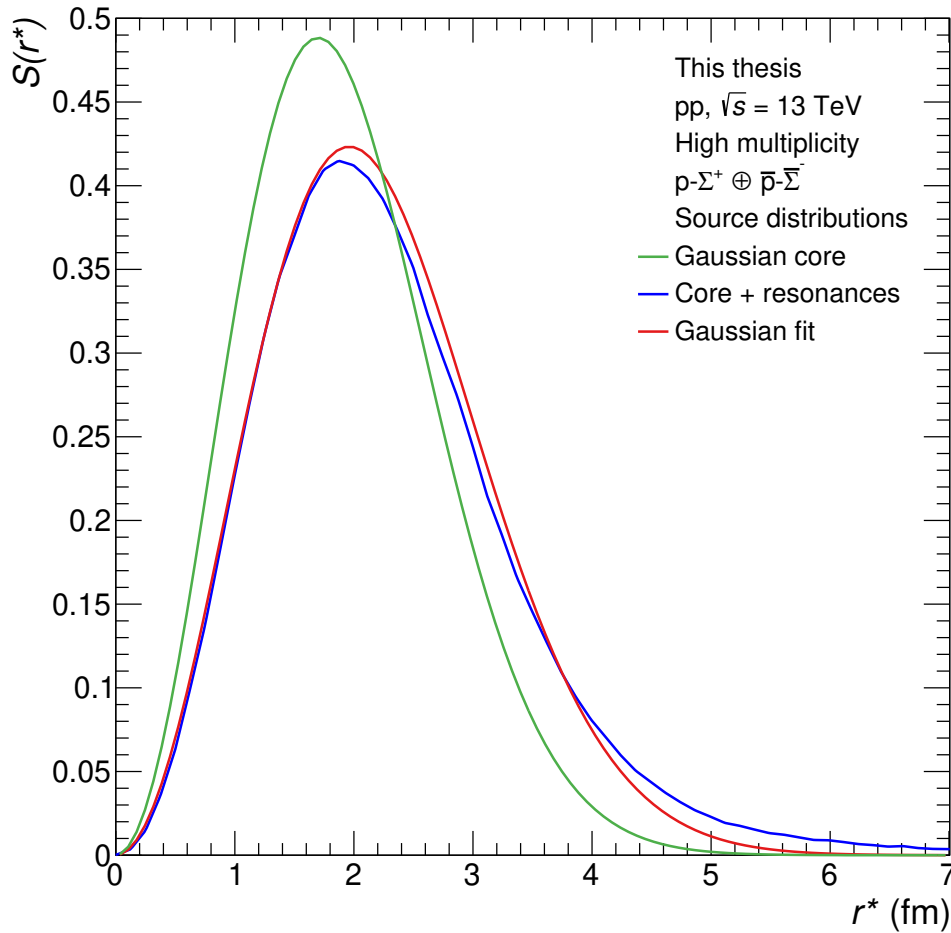


Figure 5.33: Gaussian source distribution (Eq. (1.16)) for the core radius obtained from the m_T scaling (green), full resonance source (blue), and the effective Gaussian parametrization of the full resonance source (red). Resonance source provided by M. Korwieser [298].

5.5.2 Comparison with theoretical calculations

The model predictions for the scattering parameters are given in Tab. 1.2. Clearly, one can see that the large effective ranges hinder the use of the Lednický-Lyuboshits [190, 193] approach. In particular, the small source correction turns negative in all but two models. Therefore, the full wave functions are used to compute the theoretical correlation functions. Taking the Koonin-Pratt [11, 185] (Eq. (1.6)) and the wave function including Coulomb (Eq. (1.31)), the full calculation reads

$$C(k^*) = 1 - \lambda(k^*) + \lambda(k^*) \sum_{i=1,2} j_i \int dr^* S(r^*) \times \left[|\Psi_i^{SC}(k^*, r^*)|^2 + \sum_{L=1}^{\infty} (2L+1) \left(\frac{F_L(\eta, \rho)}{\rho} \right)^2 \right] \quad (5.11)$$

where $S(r^*)$ is either the effective Gaussian source (Eq. (1.16)) or the resonance source described in section 5.5.1. The function $\lambda(k^*)$ is the genuine λ parameter that is introduced in the calculation to make it comparable to the data. It is hereby assumed that the correlation functions of all non-genuine contributions equals unity. The factors j_i are the statistical weights, which amount to 1/4 for the singlet and 3/4 for the triplet [123]. The Coulomb wave functions F_L are adopted from the GSL [201] library. The sum over L is evaluated up to $L = 50$. The strong wave functions in the presence of the Coulomb interaction $\Psi^{SC}(k^*, r^*)$ were provided by J. Haidenbauer [125]. As one of the authors of the χ EFT model NLO19 [122], he was not only able to provide the desired wave functions, but could also make modifications to the model, which will be discussed later. Moreover, he also had the source code of the NSC97f [111, 131] and ESC16 [113] models available, allowing to calculate the wave functions from these models in the same framework. While the constituent quark models were not available, NLO(sim) [122] simulates the same behavior and provides very similar scattering parameters as discussed in section 1.3.1. It is thus possible to explore the full range of predictions, from the most repulsive to the attractive triplet interactions, without the need for crude approximations. The wave functions are provided in a discrete form, i.e. binned in k^* and r^* . In the latter, a 20 am binning was used in the range of 0 to 10 fm. In k^* , a variable bin width was used with a finer binning towards low k^* and a total of 51 bins

in the interval between 1 and 469 MeV/ c , corresponding to center-of-mass energies between 1 keV and 200 MeV. The resulting calculations are shown in Fig. 5.34. The correlation function with the Coulomb interaction only is also shown. Since the interaction is shallow, the model calculations are close to the Coulomb-only expectation as well as to unity. Nonetheless, it is clearly visible that the inclusion of the strong interaction allows to describe the shape of the data much better.

The real and imaginary part of the used singlet and triplet wave functions Ψ^{SC} are exemplarily shown for the SMS NLO (NLO19) calculation in Fig. 5.35.

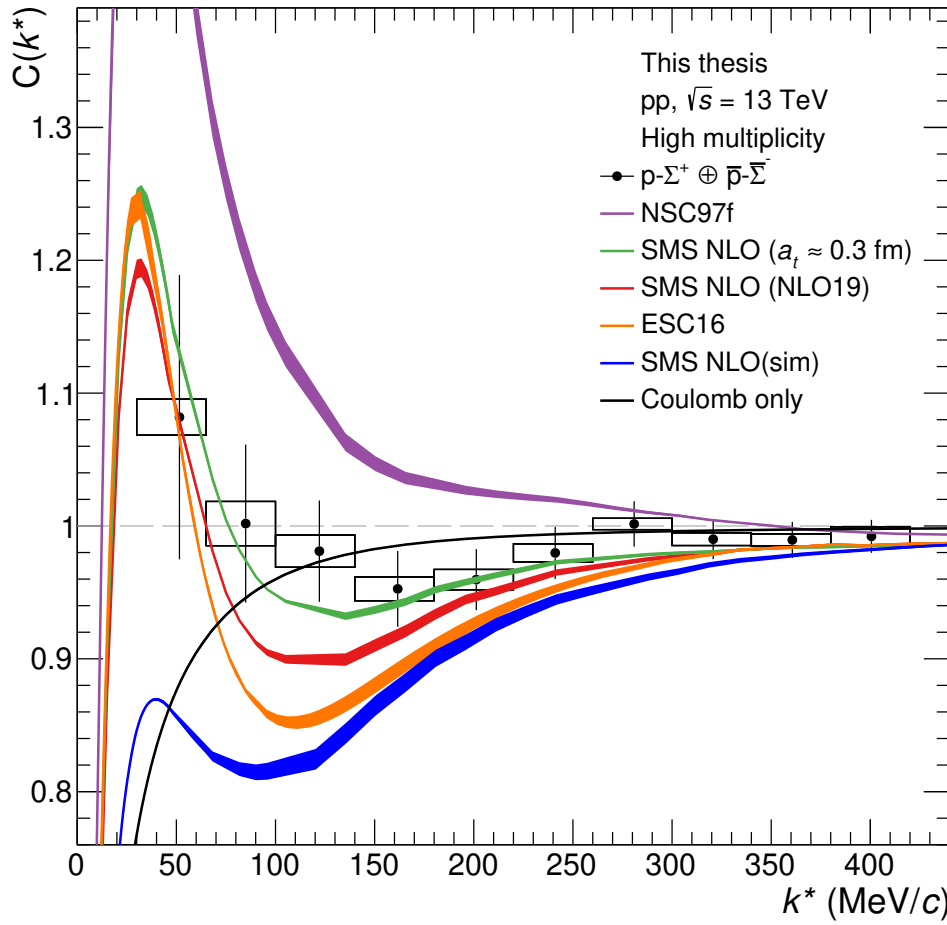


Figure 5.34: Correlation function of $p\text{-}\Sigma^+$ with several model calculations using the full wave functions and the effective Gaussian parametrization of the source. The green curve depicts a version of the SMS NLO (NLO19) [121, 122, 125] calculation where the triplet scattering length was tuned to approximately 0.3 fm. The uncertainty bands arise from the uncertainty of the source size (see section 5.5.3).

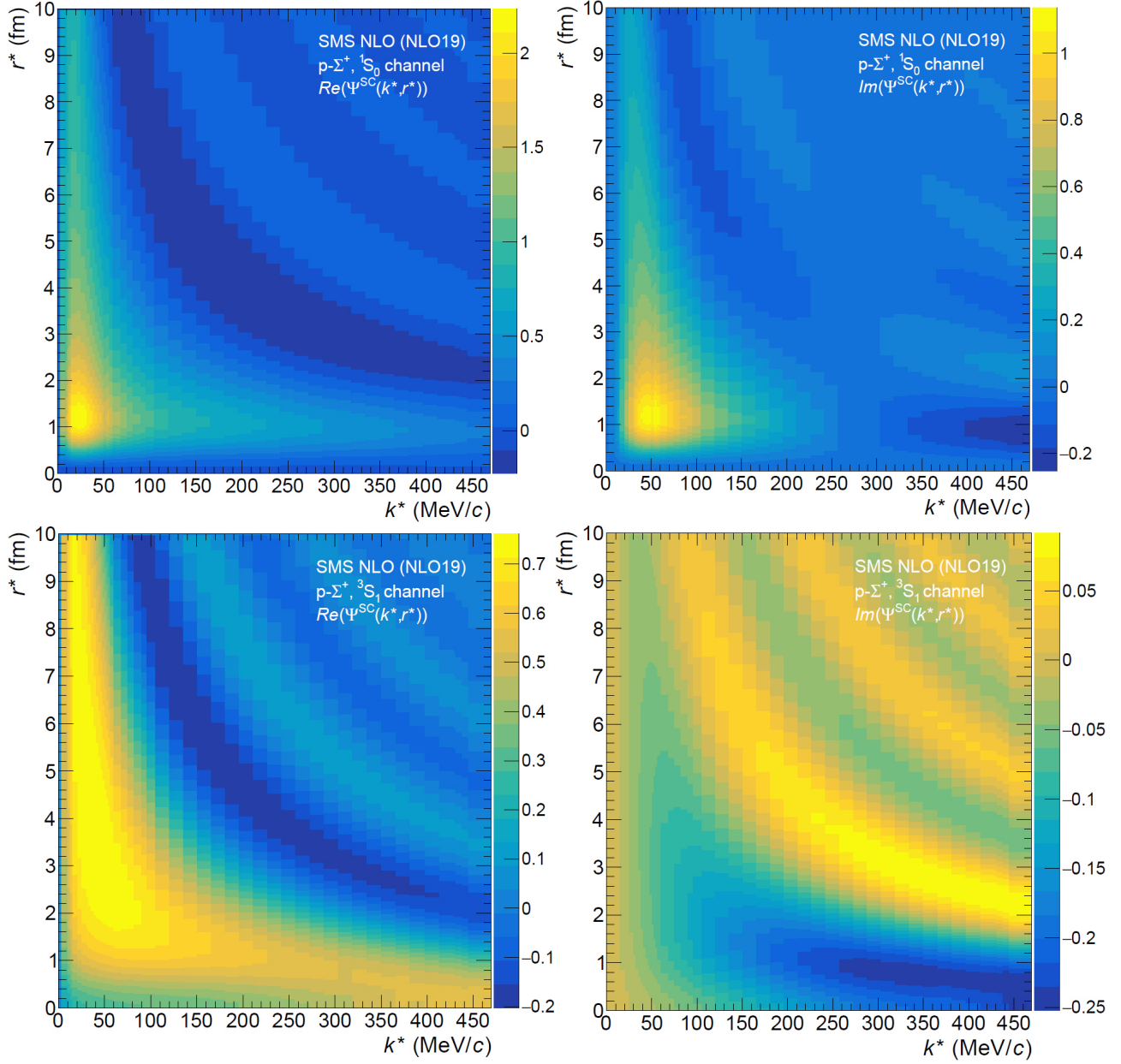


Figure 5.35: Real (left) and imaginary (right) part of the strong wave function Ψ^{SC} for the singlet (upper) and the triplet (lower) channel of the $p\text{-}\Sigma^+$ interaction in the SMS NLO (NLO19) [121, 122] model calculation. Wave functions provided by J. Haidenbauer [125].

5.5.3 Source size dependence of the correlation function

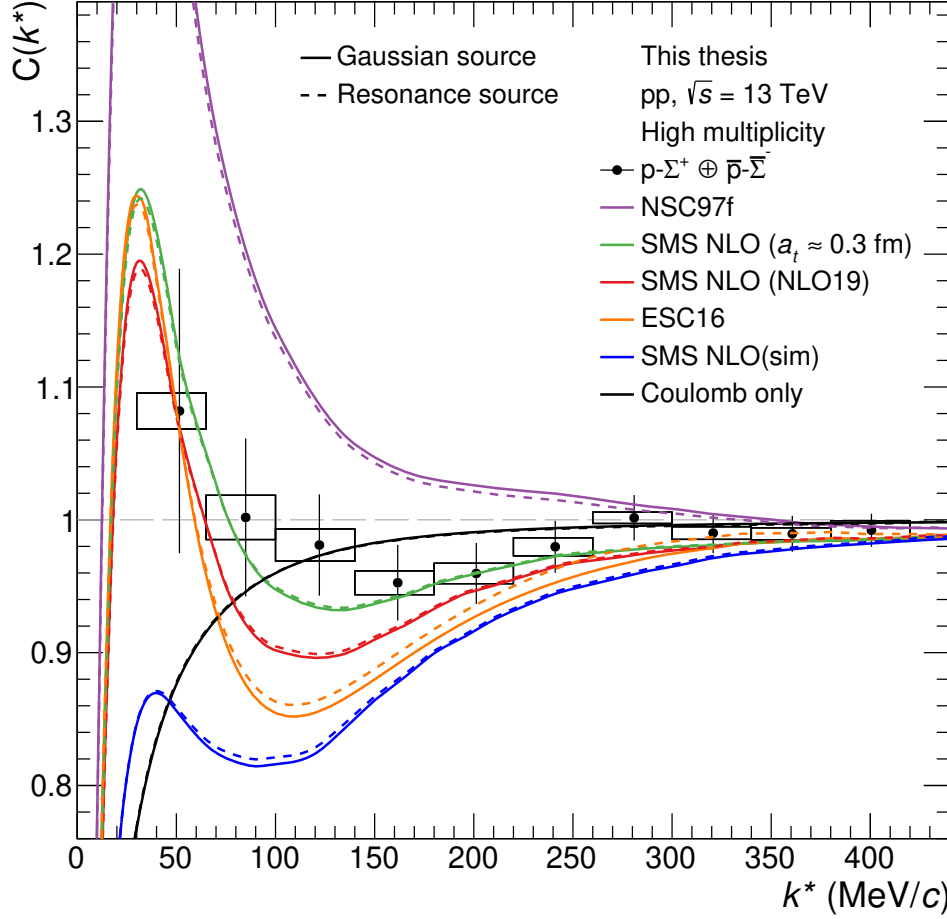


Figure 5.36: Correlation function of $p\text{-}\Sigma^+$ with several model calculations using the full resonance source (dashed) and the effective Gaussian parametrization (solid).

As already touched in section 5.4.4, the source size is a sizeable source of systematic uncertainty when comparing the data to model calculations. The uncertainty gives rise to uncertainty bands in the model calculations, which are shown in Fig. 5.34. Here, the Gaussian parametrization is used and the radius is varied as described in section 5.5.1. While the uncertainty bands decrease the significance a bit, still a reasonable comparison is possible. Nonetheless, it underlines the importance of a solid source size determination for future measurements. As elaborated in section 5.5.1, the full source extends to large radii due to the resonance decays. While the effects of the interaction are negligible at such distances, care must be taken with the proper normalization, particu-

larly when the wave function is only available up to a certain distance, which potentially causes undesired artefacts. This can be mitigated by the usage of a Gaussian parametrization which converges more quickly. In order to verify that the parametrization produces the same results as the full source, a comparison is shown in Fig. 5.36. As visible, the differences are very small, in particular for the NLO calculations they are negligible. In fact, the differences are well covered by the uncertainty of the source size. As expected, the tails at large radii have no sizeable effect on the correlation function as long as the small radii are well described [182, 183]. This finding is practical, as a Gaussian parametrization allows for the use of the Lednický-Lyuboshits approach in interactions where it is applicable.

5.5.4 Decomposition of the correlation function

In order to understand the correlation function better, it is interesting to look at its decomposition into the singlet and triplet contribution. This is depicted in Fig. 5.37 for two versions of the SMS NLO [122] calculation and for NSC97f [111, 131]. Here, the contributions are weighted by their statistical weights j_i . Additionally, the Coulomb-only correlation function is added, weighted by $1 - j_i$. This representation makes it easy to see by eye where and to which extend the respective contribution influences the total correlation function. In particular, one can see that the singlet and triplet contributions impact the correlation function at different values of k^* . Looking first at the singlet contribution, it is apparent that the shapes are very similar for the considered models and that they only differ in the amplitude of the peak. Above 120 MeV/ c the difference becomes negligible. The singlet correlation function is peaked at around 30 MeV/ c . A data point in this region would allow to study the amplitude. Unfortunately, the statistics available for this thesis does not allow to explore this region. Nonetheless, one can see that the singlet contribution alone already captures the shape of the data quite well, while being systematically above it. This implies the presence of a shallow repulsive triplet interaction, contradicting the attractive triplet interaction predicted by NSC97f. In the repulsive models, the triplet leads to a dip below unity around 100 MeV/ c , where the position and depth depend on the strength of the repulsion. With more repulsion, the dip is shifted to lower values of k^* and is deeper. This obser-

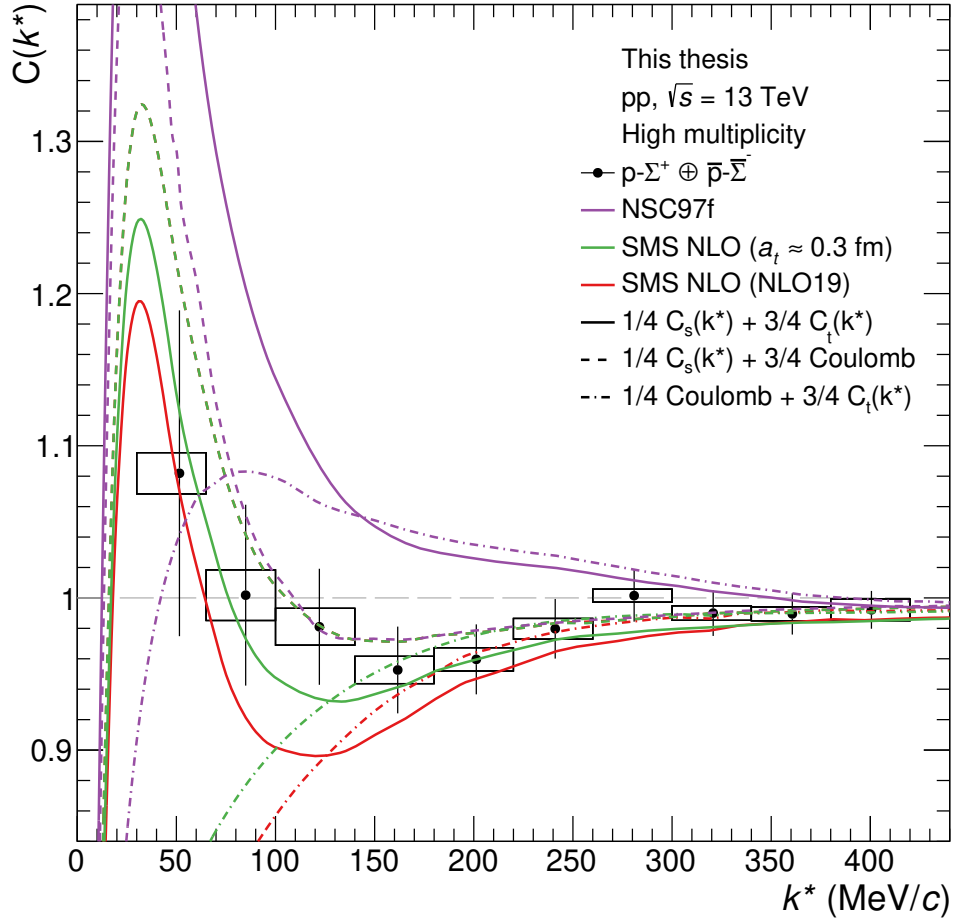


Figure 5.37: Decomposition of the theoretical correlation functions into the singlet and triplet contribution for various models. The contributions are weighted by their statistical weights, which allows to observe their influence on the total correlation function.

vation is most interesting, as it allows to probe the strength of the less-known triplet interaction at higher values of k^* where the statistical uncertainties are smaller. However, this underlines, why reliable calculations at high k^* are essential and the Lednický-Lyuboshits approach is not useful. In the data a dip is found, again contradicting the attractive model. However, the dip is very shallow and situated slightly above 150 MeV/ c . This is in tension with the models predicting a stronger repulsion, fss2 [115, 116] and Nagels73 [130]. This finding is supported by the scattering data of KEK E40 [20], which also found fss2 to be too repulsive to describe the differential cross sections and the phase shifts. Since also SMS NLO (NLO19) is seemingly too repulsive, Haidenbauer retuned the LECs of the NLO19 model to reduce the repulsion in the triplet,

leaving the singlet untouched [125]. This is also plotted in Fig. 5.34 as well as in Fig. 5.37 as the green line. As stated in the legend, the triplet scattering length amounts to roughly 0.3 fm in this case. Apparently, this tune describes the data better than all other models. Without also retuning the strength of the singlet, the resulting cross sections would be lower. This is, however, not necessarily in tension with existing data. To the contrary, KEK E40 found lower cross sections than previous experiments as discussed in section 1.3.1. However, one must be aware that the low-energy behavior is not strongly correlated with the one at higher energies anyway and that the chiral calculations are themselves not too reliable at the energies reached in KEK E40. At lower energies, at $p_{\text{lab}} < 200$ MeV/ c , still only 4 data points exist and these are not very constraining due to their large uncertainties [154, 155].

Concluding, the correlation function found in this thesis supports the assumption of a very shallow repulsion in the triplet channel of the p - Σ^+ interaction, very similar to the one in the Jülich04 [110] model. Nevertheless, it contradicts a strong repulsion as found in quark constituent models, just as it contradicts a modest attraction found in the NSC97f model.

5.5.5 Generic potential fits

In addition to the previous model comparisons, the data is fitted with correlation functions obtained from several potentials (see section 1.4.2). This work was done in collaboration with Y. Kamiya [299], who provided the correlation functions (Fig. 5.38) and their relationship to the scattering lengths (Fig. 5.40), and with J. Haidenbauer [125], who provided advice.

In this analysis, a Gaussian and a Reid-like potential are used. The use of a Gaussian potential is appealing due to the minimal number of parameters. However, it is also purely phenomenological and its radial dependence is clearly unphysical. The Reid potential, in turn, is physics-motivated and thus closer to the natural truth, while having more free parameters to be tuned to data. It is not obvious that both potentials yield equal or even similar results. Using both potentials can therefore serve as a valuable cross check to answer the question whether a simple phenomenological potential is indeed capable of capturing the relevant dynamics of the system.

For the Gaussian potential, two different ranges are used. Firstly, as touched in

section 1.4.2, the inverse pion mass is used. This amounts to a value of 1.46 fm. While this assumption seems natural, a recent study of the pp interaction found that this choice is not optimal [300]. In fact, since the radial dependence of a Gaussian potential differs from a Yukawa-like one, a different range parameter must be used in this case to reproduce roughly the shape in the relevant distance region. In the aforementioned study, a value of about 1.8 fm was found, which is also used here.

The original version of the Reid potential was tuned to describe the N - N interaction. For the singlet, it is given by [209]

$$V(^1S) = -10.463 e^{-x}/x - 1650.6 e^{-4x}/x + 6484.2 e^{-7x}/x \quad (5.12)$$

where $x = mcr/\hbar$ with m being the pion mass in this case (compare Eq. (1.33) and (5.13)). The prefactors are given in MeV. The first term corresponds to the long-range part described by the single pion exchange. The second term constitutes the intermediate range described by the exchange of heavier pseudoscalar mesons, while the third term is the short-range part described by the (heavy) vector meson exchange [125, 209]. The Reid-like potential used in this analysis to describe the N - Σ interaction is obtained by the modification of the prefactors of these terms. Due to the different masses of the exchanged mesons, the three terms are affected differently when going from the N - N to the N - Σ system, which motivates a different treatment in the fitting procedure [125, 299].

In case of the pion exchange, the strength needs to be adjusted by the difference between the $NN\pi$ and the $\Sigma\Sigma\pi$ coupling constants. In accordance with the $SU(3)$ flavor symmetry, the term is scaled by a factor of 0.8, twice the $SU(6)$ value of 0.4 [120, 125, 301]. The effects of the other pseudoscalar mesons (η , η' , and K) are suppressed due to their larger masses and are effectively absorbed by the phenomenological short-range part of the potential. For the third term, one can assume that it is not very different in the N - Σ case due to the large masses of the vector mesons. It is therefore kept constant. This leaves the intermediate-range term to be modified by the introduction of a phenomenological fitting parameter β , which incorporates the effects of the $SU(3)$ flavor symmetry breaking. This will be called version 1 (V1) in the following. Additionally, the calculation is repeated by multiplying both the second and the third term by a common parameter β , referred to as version 2 (V2). In the latter, however, the different signs of the terms lead to a delicate in-

terplay, which causes the scattering length to reach a characteristic maximum that corresponds approximately to the pion exchange alone. This artefact will be discussed later. Nonetheless, it is used as a cross check.

In the triplet, the original Reid parametrization is rather complex. It is given in Eq. (30) in Ref. [209] for the $^3S_1\text{--}^3D_1$ coupled state. It contains a central, a tensor, and a spin-orbit term. For the S-wave triplet state alone, only the central potential is relevant. For the N–N interaction, however, the coupling to the D-wave is most important, as a sizeable part of the attraction that leads to the deuteron bound state can be attributed to the tensor coupling [209]. On the other hand, for the Reid-like parametrization of the N– Σ interaction only the central part will be considered. It contains four terms, where the first one again corresponds to the long-range pion exchange. As in the singlet, this term is treated by multiplying it by 0.8, whereby in this case the isospin factor implies an additional factor of $-1/3$ [125, 299]. The second term possibly corresponds to the two-pion exchange, as used also in the Usmani potential [302]. It is treated again by introducing the fitting parameter β . The other terms are not considered. The used triplet potential is consequently given by [125, 209, 299]

$$V(^3S) = \frac{0.8}{3} 10.463 e^{-x}/x - \beta 105.468 e^{-2x}/x. \quad (5.13)$$

Again, the potential is given in MeV. For all of the considered potentials, the wave functions are obtained by solving the Schrödinger equation in the given potential for a discrete set of values of the fitting parameter. From these, the correlation functions are calculated, again using the Gaussian source with a radius of 0.98 fm as determined in section 5.5.1. Finally, the relation between the fitting parameter and the S-wave scattering length is evaluated. In the following, the full fitting procedure will be exemplarily shown for the Gaussian potential with the range parameter of 1.8 fm. It is likewise employed for the other potentials. The potential depth V_0 of the Gaussian potentials and the parameter β of the Reid-like potentials are solely used as phenomenological fitting parameters and otherwise meaningless. In practice, both fitting parameters are treated equally. At the end of this section, a comparison of the results obtained with the different potentials is shown and discussed.

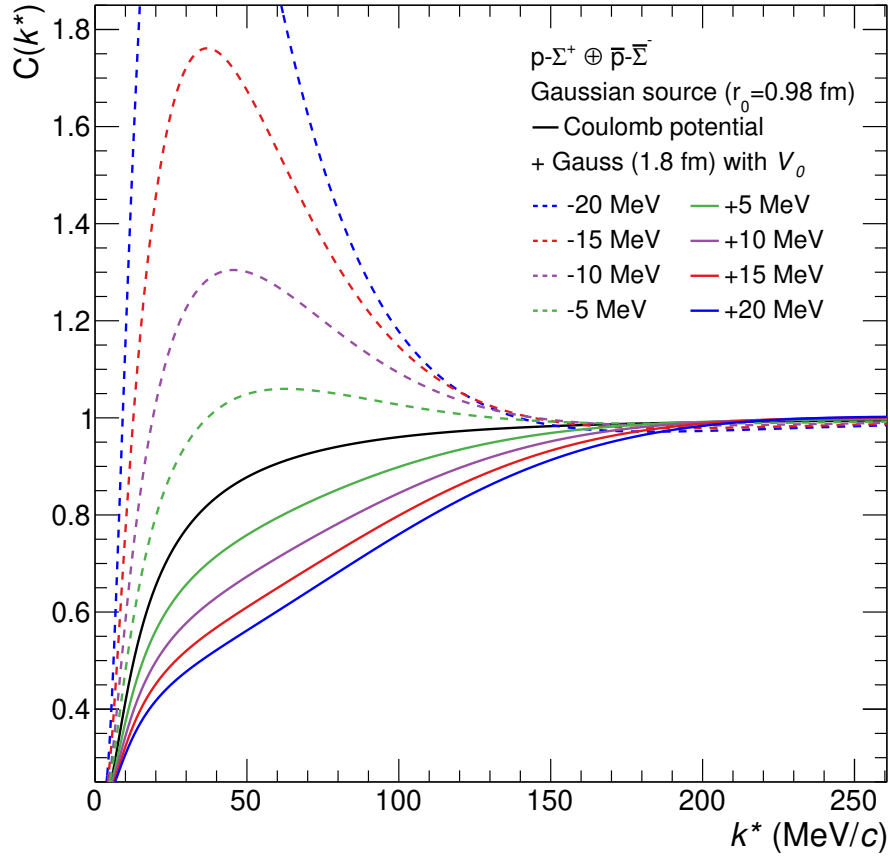


Figure 5.38: Correlation function of $p\text{-}\Sigma^+$ calculated by solving the Schrödinger equation for a Gaussian (1.8 fm) + Coulomb potential (see section 1.4.2) for various values of the potential depth V_0 . Coulomb only (i.e. $V_0 = 0$) is also shown. A Gaussian source with $r_0 = 0.98$ fm is used.

Fig. 5.38 shows the correlation functions for selected potential depths. The shown correlation functions are already weighted by the genuine λ parameter, similar to Eq. (5.11).

In the case of the $p\text{-}\Sigma^+$ system, two spin configurations matter, the singlet and the triplet, and thus two values of the fitting parameter (V_0 or β) need to be determined. This is done by adding two correlation functions from the array, weighted by the respective statistical weight. All combinations are then compared to data.

The comparison of the data with the model curves is done by calculating the χ^2 , which is defined by

$$\chi^2 = \sum_i^n \left(\frac{C_{i,\text{data}} - C_{i,\text{model}}}{\sigma_i} \right)^2 \quad (5.14)$$

where i is the index of the data points, $C_{i,\text{data}}$ is the value of data point i , $C_{i,\text{model}}$ is the model value evaluated at data point i , and σ_i is the combined statistical and systematic uncertainty of data point i . The number n is the amount of data points considered.

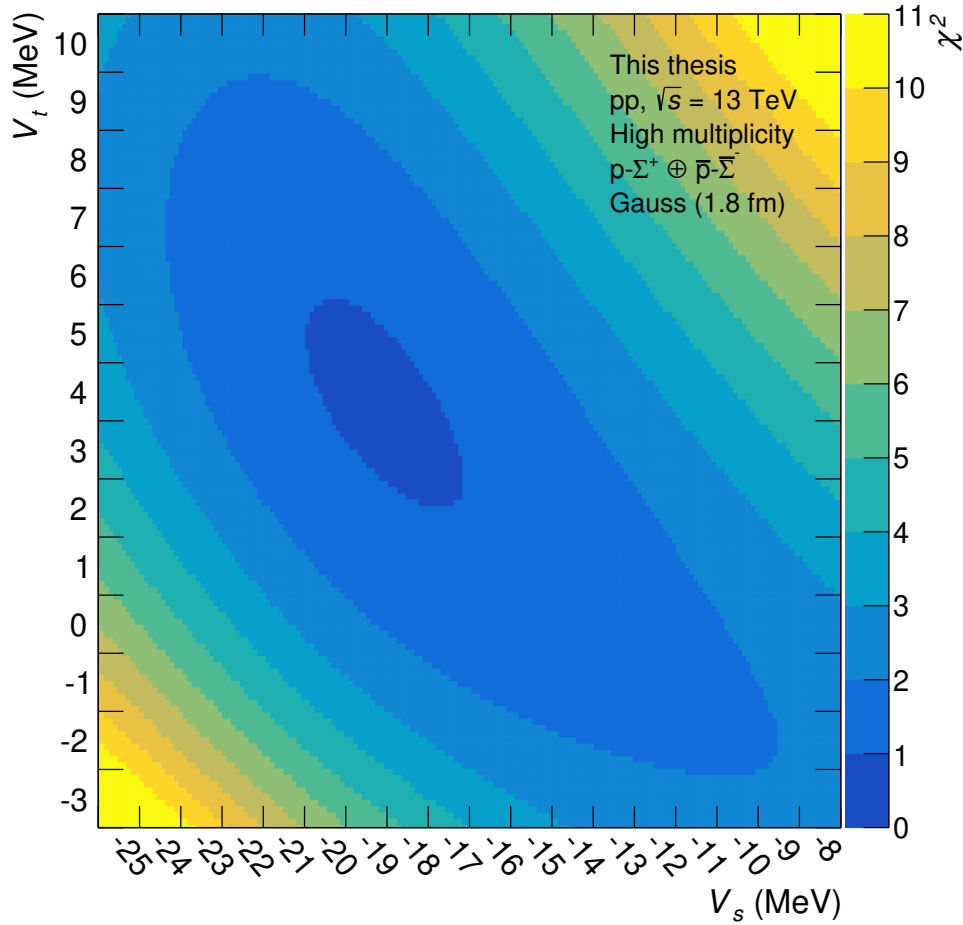


Figure 5.39: χ^2 as a function of the singlet and triplet potential depths for the Gaussian (1.8 fm) potential.

Only the first four data points are considered. This is because the model curves fail to describe the data at higher k^* , possibly due to the large effective ranges of the $p\text{-}\Sigma^+$ interaction and the fact that only the S-wave is considered. The

model curves converge at around $k^* = 180 \text{ MeV}/c$ as visible in Fig. 5.38. Adding up the χ^2 values above this value would be pointless and only shift up the χ^2 baseline. The Reid-like potentials describe the data generally better at larger k^* , yet they also converge at a similar value. Therefore, also here only the first four data points are used. The resulting values of χ^2 are plotted in Fig. 5.39 as a function of the singlet and triplet values of V_0 .

The well in χ^2 is clearly visible³³ and is analyzed further in the following. Obviously, a correlation between the singlet and triplet potential depths is present and results in ellipsoidal isohypses oriented along the diagonal. Consequently, the evaluation of the triplet scattering length would profit from more stringent constraints of the singlet scattering length.

Since the fitting parameters (V_0 or β) are specific to the here used potentials, they cannot be easily generalized. A more meaningful value is the (S-wave) scattering length a_0 . The relation between the fitting parameter and a_0 can be made through the procedure outlined in section 1.4.2. The relation is shown for the Gaussian potential in Fig. 5.40. Since the ranges of the used potentials are fixed, only the scattering length is meaningful in this case.

The scattering length saturates for repulsive potentials and diverges for attractive ones. A similar finding is made both for the Gaussian and the Reid-like potentials. Thus, a given uncertainty in the evaluation of V_0 or β translates into a smaller (larger) uncertainty in the scattering length if the interaction is repulsive (attractive). On the other hand, attractive potentials lead to a more pronounced signal as seen in Fig. 5.38, increasing the sensitivity for such potentials. In case of the singlet of $p\text{-}\Sigma^+$, however, this is washed out by the small statistical weight, such that the overall sensitivity on the triplet scattering length is higher.

The χ^2 values in Fig. 5.39 have to be related to the p-values of the underlying distribution in order to determine the uncertainty interval. This is done using a bootstrapping procedure that was already used in a similar analysis for this purpose [303]. To this end, the correlation function which fits the data best, i.e. which has the lowest χ^2 , is considered as the true value. From this correlation function, artificial data points are sampled. This is done by evaluating

³³It has to be noted that the fact that only the sum of the singlet and the triplet can be fitted inevitably leads to a secondary minimum with a moderately attractive triplet, counterbalanced by a strongly repulsive singlet. This solution is believed to be an artefact and is not considered further in this analysis [299].

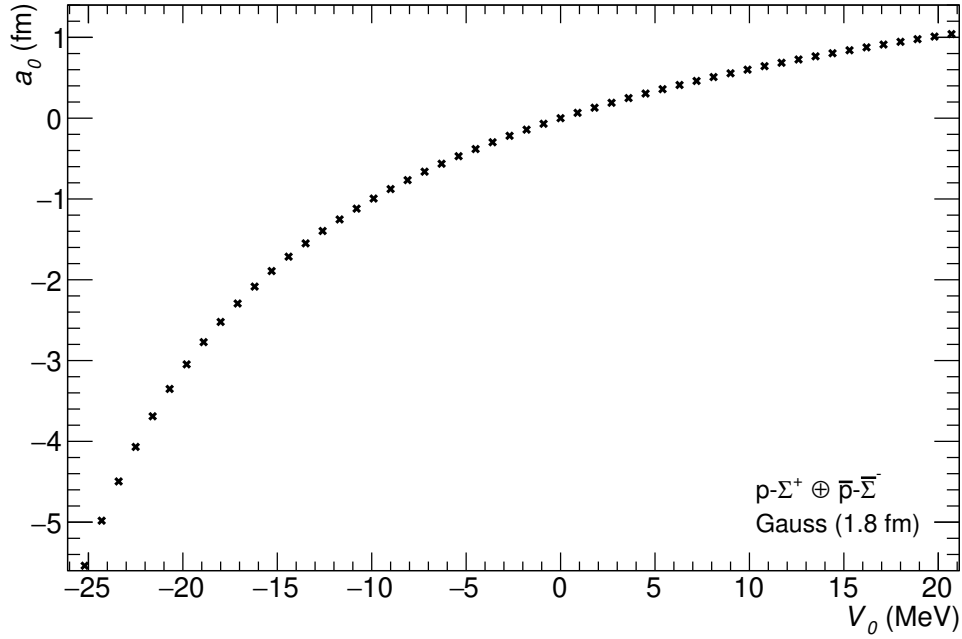


Figure 5.40: S-wave scattering length a_0 as a function of the potential depth V_0 for the Gaussian (1.8 fm) potential.

the model curve at the center of each of the real data points and modifying these values with a random value drawn from a Gaussian distribution with a standard deviation corresponding to the combined uncertainty of the respective data point. A total of 10^5 correlation functions are generated this way. In principle, a similar procedure could be done by sampling from the real data points, however, one has to consider that any data point could be an outlier itself, in which case one would not sample around the center of the underlying distribution. This aspect is mitigated by taking the central value from the fit. For each of the resulting artificial data sets, the new minimum in χ^2 is determined.

The normalized distribution of the minima is displayed in Fig. 5.41.

Combined with the χ^2 distribution (Fig. 5.39), the distribution of the variations allows to find the desired relation between $\Delta\chi^2 = \chi^2 - \chi^2_{\min}$ and the p-value by plotting the fraction of included variations as a function of the cut-off in $\Delta\chi^2$. This is displayed in Fig. 5.42.

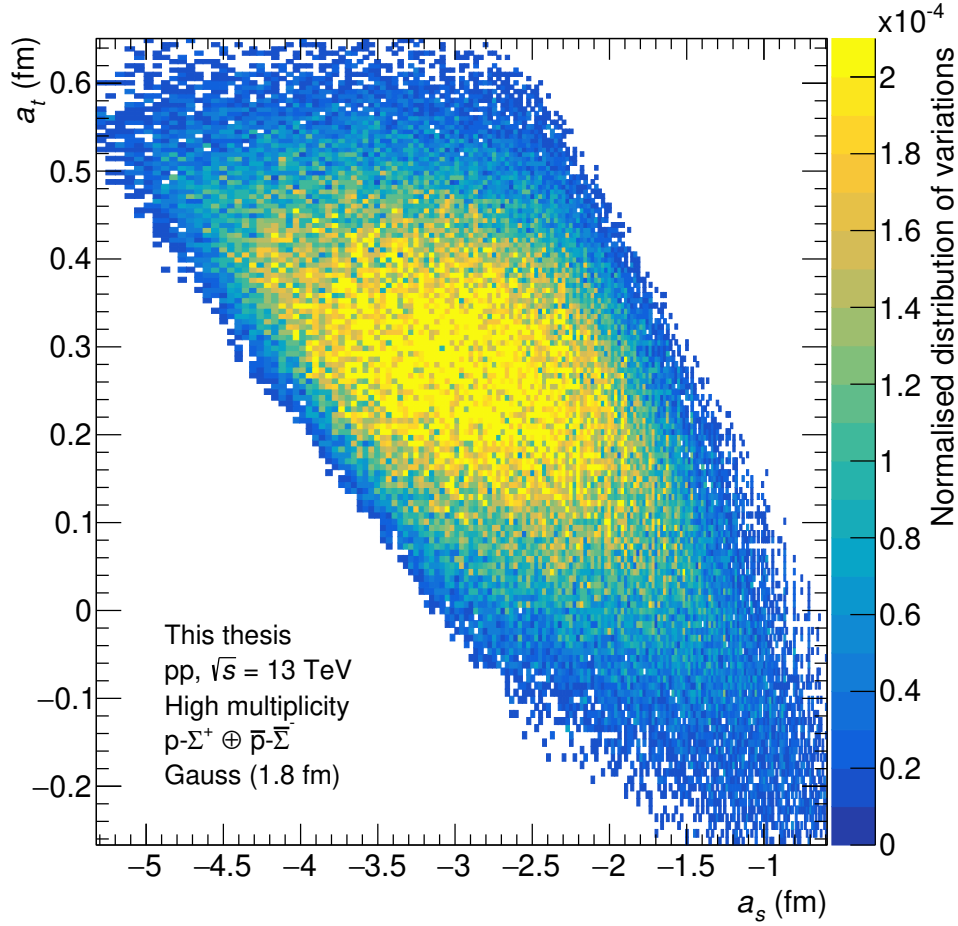


Figure 5.41: Distribution of fits from the bootstrapping procedure for the Gaussian (1.8 fm) potentials.

For a normal distribution, the relation between the distance from the central value in multiples of the standard deviation $n\sigma$ and the p-value is given by [303]

$$\text{p-value} = \text{erf}\left(\frac{n\sigma}{\sqrt{2}}\right) \quad (5.15)$$

where erf is the Gaussian error function. The resulting p-values for 1, 2, and 3σ are indicated in Fig. 5.42 as dashed lines. The crossing of the data points with these lines is evaluated using a spline interpolation that allows to translate the χ^2 distribution into multiples of the standard deviation.

With the former results, one can arrive at the exclusion plot, showing the agreement with the data as a function of the singlet and triplet scattering lengths in multiples of the standard deviation. It is displayed in Fig. 5.43 for all considered potentials. The figure also contains the model predictions given

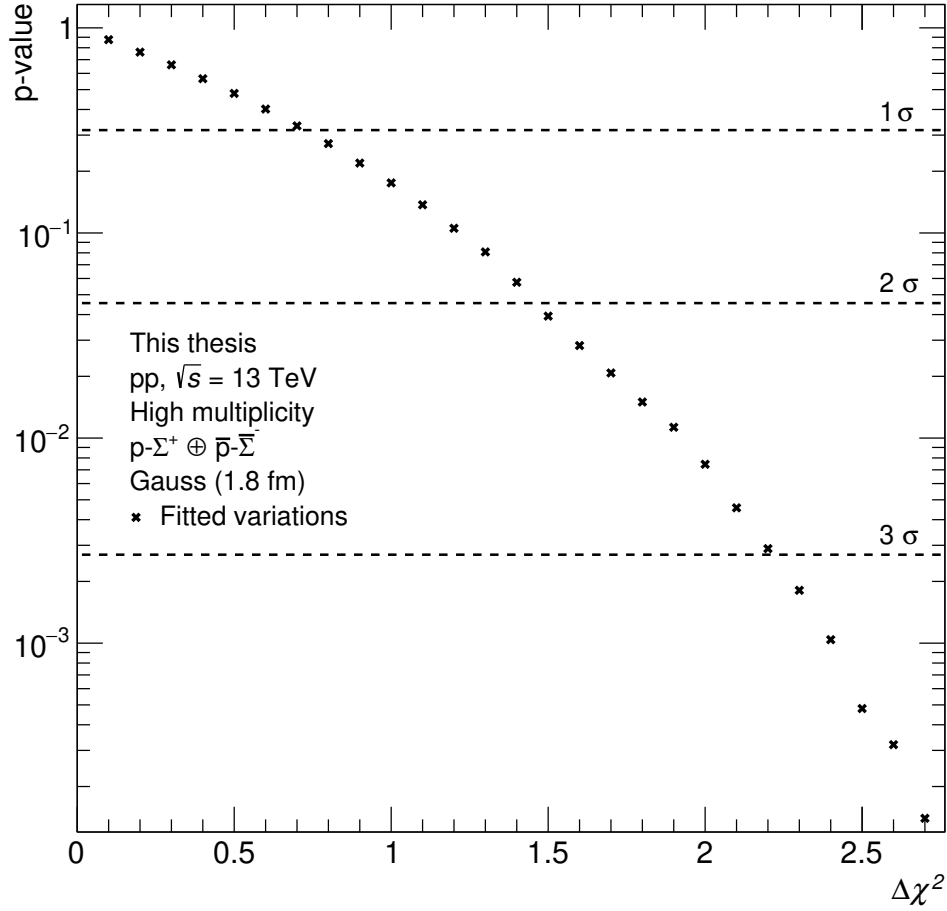


Figure 5.42: p-values of the bootstrapping variations as a function of $\Delta\chi^2$ for the Gaussian (1.8 fm) potentials.

in Tab. 1.2. The source size uncertainty is considered by calculating the χ^2 for each bin for both the lowest and the highest possible source radius and using the lower value of χ^2 , which is the most conservative estimate of the $n\sigma$ contours. Apparently, the ellipsoidal contours differ among the models, both in shape and in width. Most strikingly, the 3σ contour of V2 of the Reid-like potential is seemingly cut-off. As discussed earlier, this is a direct consequence of the interplay between the second and the third term in this parametrization of the singlet, which does not allow for values of the scattering length above around -0.9 fm. Despite the differences, a sizeable overlap of the allowed regions is present, indicating that the results are in agreement. This will again be discussed later.

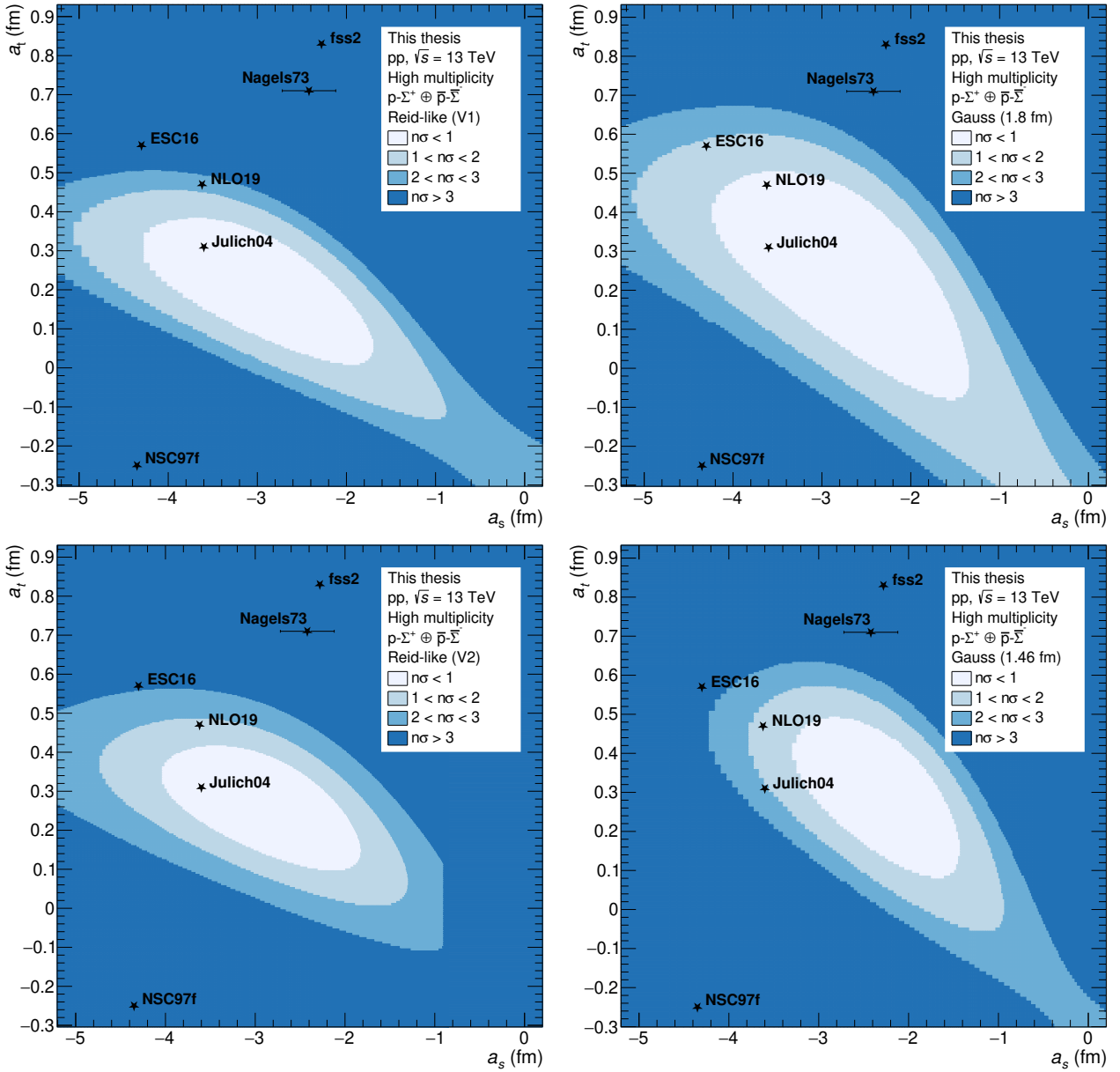


Figure 5.43: Exclusion plots showing the agreement with the data as a function of the singlet and triplet scattering lengths in multiples of the standard deviation for the four considered potentials: Reid-like V1 (upper left), Gauss 1.8 fm (upper right), Reid-like V2 (lower left), Gauss 1.46 fm (lower right). Several model predictions (see Tab. 1.2) are shown. One may note the specific characteristics of the used potentials (see text), which lead to the cut-off artefact in the Reid-like (V2) potential and the shift in the Gauss (1.46 fm) potential.

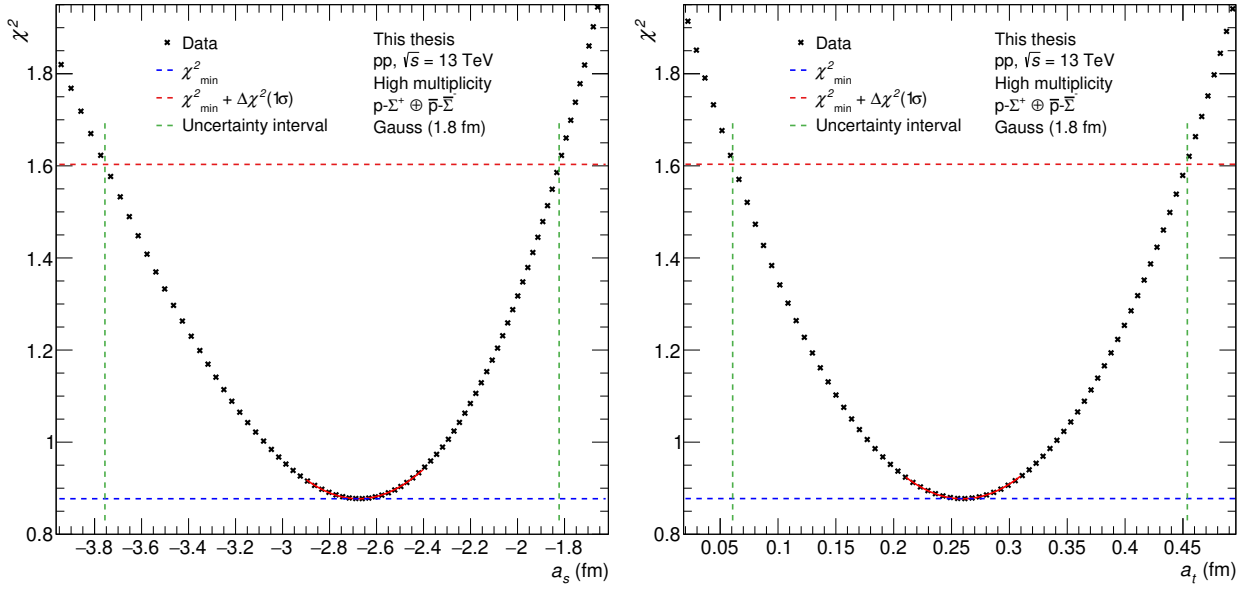


Figure 5.44: Projections of the χ^2 distribution onto the singlet (left) and triplet (right) axis for the Gaussian (1.8 fm) potentials. The lowest 10 data points are fitted with a second order polynomial function (solid red line) to determine the position and value of the minimum in χ^2 . The dashed blue lines indicate the minimum χ^2 value χ^2_{\min} and the dashed red line $\chi^2_{\min} + \Delta\chi^2(1\sigma)$. The uncertainty interval (dashed green lines) is defined as the crossing of the data distribution and the dashed red line.

To determine the uncertainties in the singlet and triplet channel separately, projections of the χ^2 distribution onto the singlet and triplet axes are made at the global minimum. The projections are shown in Fig. 5.44 for the singlet (left) and the triplet (right). The minimum of the projections is determined by means of a quadratic fit (solid red line) of the lowest 10 data points. This is necessary because of the finite binning of the fitting parameters. The resulting minimum χ^2 is indicated by the dashed blue line. The uncertainty interval is evaluated as the crossing of the data distributions and the line at $\chi^2_{\min} + \Delta\chi^2(1\sigma)$ (dashed red line). A linear spline is used to interpolate between the data points. The resulting uncertainty intervals are indicated by the dashed green lines. The results are summarized in Tab. 5.1 for the considered potentials. The uncertainties given in the aforementioned table also include the uncertainty of the source size, which is evaluated by repeating the former procedure for the different source sizes and quadratically adding the resulting uncertainty to the statistical and systematic one.

Potential	Reid-like (V1)	Gauss (1.8 fm)	Reid-like (V2)	Gauss (1.46 fm)
a_s (fm)	$-2.94^{+0.82}_{-0.96}$	$-2.67^{+0.85}_{-1.08}$	$-2.86^{+0.79}_{-0.98}$	$-2.31^{+0.63}_{-0.72}$
a_t (fm)	$0.21^{+0.13}_{-0.13}$	$0.26^{+0.19}_{-0.20}$	$0.27^{+0.13}_{-0.13}$	$0.31^{+0.15}_{-0.16}$

Table 5.1: S-wave scattering lengths including Coulomb effects of the singlet (a_s) and triplet (a_t) channel of the $p\text{-}\Sigma^+$ interaction evaluated using Gaussian and Reid-like potentials.

The correlation function with uncertainty bands superimposed over the data is shown in Fig. 5.45 for the Gaussian (1.8 fm) potential. One may note that in this plot the correlation between the singlet and triplet uncertainties has been considered, i.e. only parameter sets within the 1σ contour of Fig. 5.43 are used. The data is well described in the k^* region used for the fitting procedure. At higher values tension arises as discussed earlier.

The results of the fits with the used potentials are summarized in Tab. 5.1. The results are in agreement with each other within the given uncertainties, both for the singlet and the triplet and for all considered potentials. This finding highlights that the $p\text{-}\Sigma^+$ correlation function is not sensitive to the exact shape of the potential, at least not within the current statistics. This result is not surprising, considering the discussion in section 1.4.2. Despite the small source size, the wave function is mostly probed at relatively large separations of more than 2 fm. The similarity of the wave functions at these distances is essentially guaranteed if the effective range expansion parameters are similar and vice versa. This holds for even simpler models like a square well potential [125]. If, however, the phase shifts of the interaction are large or exhibit a sign change as a function of the energy, a simple potential will break down and will not be able to reproduce such details. For the $N\text{-}\Sigma$ system, this is not the case, allowing for the use of a rather simple approach.

Apparently, the singlet scattering length of the Gaussian potential with a range parameter of 1.46 fm deviates noticeably. This might be related to the small source size, which leads to a larger overlap with the wave function in a more confined potential. This is in agreement with the finding in Ref. [300], where also a larger signal with a decreasing range parameter was found. The stronger signal is compensated by a smaller scattering length in the fit, explaining the deviation. Similarly, the two Reid-like parametrizations have a slightly different range dependence, influencing the shape of the correlation function at higher

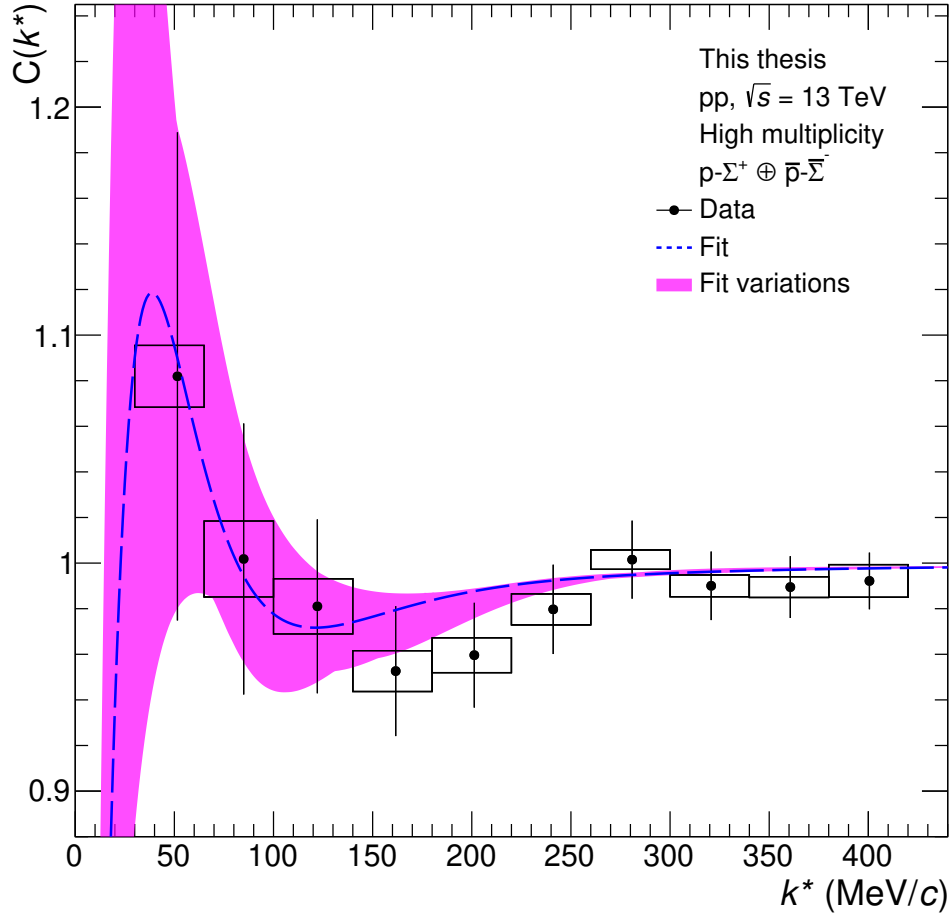


Figure 5.45: Best fit of the data (dashed blue line) and the uncertainty band for the Gaussian (1.8 fm) potentials. The uncertainty band is the superposition of all parameter sets within the 1σ contour. The values are reported in Tab. 5.1.

values of k^* . This, in turn, leads to a difference in the obtained triplet value. For a more precise determination of the scattering parameters, one would need to introduce more free parameters to the potential. In particular, one would need to fit the range parameters as well. In this analysis, however, the small number of data points and their large uncertainties do not allow this operation. Thus, the differences between the considered potentials need to be considered as a model uncertainty.

Nonetheless, a comparison with the theoretical predictions summarized in Tab. 1.2 is fruitful and reveals that the found values are clearly in the expected range. Indeed, the singlet scattering length is well compatible with all but two models given in the table within less than 1σ . NSC97f[111, 131] and ESC16[113]

predict a rather large singlet scattering length of -4.35 or -4.3 fm, respectively, which, however, is still compatible with the here shown results within less than 2σ .

In the triplet channel, a value of around 0.3 fm is found. This is consistent with the finding from section 5.5.2, where the chiral calculation with a triplet scattering length of roughly 0.3 fm also had the best agreement with the data. Consequently, the same conclusion can be drawn here that most model calculations overestimate the repulsiveness of the p - Σ^+ triplet interaction. Moreover, the higher sensitivity in the triplet channel allows to disfavor an attractive triplet interaction by almost 2σ and the triplet scattering length predicted by NSC97f by more than 3σ . At the same time, a strong repulsion, as predicted by fss2 [115, 116], is disfavored by also more than 3σ .

Concerning these model comparisons, one must recall the correlation between the singlet and the triplet scattering lengths, which affects the overall compatibility between the models and the data. This can best be seen in Fig. 5.43. While a stronger repulsion in the triplet paired with a stronger attraction in the singlet, as predicted for instance by NLO19 [122], is still compatible within $2 - 3\sigma$, this is not so in the case of NSC97f and fss2. In fact, given attraction in the triplet channel, the data requires a very shallow attraction in the singlet, while NSC97f predicts quite the opposite. On the other hand, a stronger repulsion in the triplet also implies more attraction in the singlet, whereas fss2 predicts the least attraction in this channel among the considered models. This behavior might be related to the fact that the models are fitted to a certain set of measured scattering cross sections and a stronger amplitude in the triplet requires a shallower one in the singlet or vice versa to reproduce the given experimental scattering cross sections. Thus, also here a correlation between the channels is present. In fact, the model predictions roughly lie on one line across the $a_s - a_t$ plane. This line has the opposite slope than the correlation implied by the fit of the correlation function, highlighting that the combination of scattering and correlation data can give valuable additional insight. With this consideration, both NSC97f and fss2 are disfavored with even higher confidence. Among the considered models, the best agreement is found with the Jülich04 [110] model, which is the only one that resides within the 1σ contour.

Summary

The work presented in this thesis is about the first measurement of the Σ^+ in pp collisions at $\sqrt{s} = 13$ TeV at the LHC. This particle has gained only little attention in the previous years, not because of a lack of interest, but because it is particularly challenging to measure. In fact, a sizeable part of the thesis revolves around the reconstruction strategies that were developed within this scope.

The general principle of reconstruction involved the determination of the decay vertex of the Σ^+ from the proton track and the PCM photon using a Kalman Filter [239] approach. Hereby, the weak nature of the Σ^+ decay and the short lifetime of the π^0 were exploited.

Clearly, the low reconstruction efficiency of the photons proved to be the bottleneck of the analysis, being particularly prohibitive for the application of the femtoscopy [11] method. To overcome this issue, more and more information about one of the photons was sacrificed, going from PCM through the calorimeters to no reconstruction at all. By including the available topological information and the constraints imposed by the intermediate decay, missing information could be patched and the resolution was restored.

The existing simulations were found to be the bottleneck in terms of the statistical uncertainty. Therefore, a generator cocktail was developed to produce a new custom simulation. With this, it was possible to significantly increase the statistics at a fraction of the computational cost of the previous simulation.

This made it possible to successfully measure of the first Σ^+ p_T spectra at the LHC in minimum-bias and high-multiplicity pp collisions.

The comparison of the Σ^+/Λ ratio was found to be independent of the multiplicity well within uncertainties, implying an equal scaling of the yields of Σ and Λ baryons. A particularly good agreement of the ratios with the γ_s CSM thermal model [80] was found. The comparison with PYTHIA [62, 95] and EPOS [63, 96–99] event generators found a qualitatively good description of the spectral shape

of Σ^+ , while the yields are underestimated by a factor of roughly 2 in all considered models and tunes.

The successful measurement of the Σ^+ production spectra was encouraging to go further and also measure the interaction of Σ^+ with protons via the femtoscopy method. This required the development of a missing-mass reconstruction of the Σ^+ , measuring only one of the decay photons. The overwhelming combinatorial background could be successfully tamed by the inclusion of state of the art machine learning techniques [248, 250]. This method allowed to increase the reconstruction efficiency by more than one order of magnitude at a more than twofold improvement of the purity.

The machine learning selection was also employed for the selection of the protons, for which typically hard selections are used. It could be shown that the ML selection particularly increases the primary fractions, while also increasing the momentum reach.

The multivariate selection required the development of a novel data-driven approach to determine the λ parameters using effective spectra. This has gained particular interest, as it reduces the dependence on MC simulations, is intrinsically multi-differential, and potentially reduces systematic uncertainties. With more and more statistics being collected, the systematic uncertainty inevitably outgrows the statistical one. Thus, the consideration of systematic effects will need particular attention in future measurements.

Consequently, also a novel approach for the construction of the uncorrelated background sample was developed, seeking to mitigate the known issue of momentum conservation in small systems. The technique named fixed-angle mixing worked surprisingly well, being simple, fit- and model-independent, and computationally cheap. While further investigation is needed to build trust in the method and to understand potential limitations, it paves the way for the significant improvement of already measured correlation functions, reducing the systematic uncertainties significantly.

Using these developments it was possible to measure the p - Σ^+ correlation function down to 35 MeV/ c in k^* , achieving a k^* resolution of 6 MeV/ c , a genuine fraction of 79%, and reasonable statistics. This is a success, which was not believed to be possible within the first year of this work, considering the starting point, the efficiency of the PCM-PCM method, and the large number of

developments and improvements needed.

For the interpretation of the correlation function, the source size had to be evaluated precisely for the p - Σ^+ system. A source size of slightly less than 1 fm was found [182, 183]. The smallness of the source and the shallowness of the interaction hindered the usage of the typically employed simplistic approach of Lednický and Lyuboshits [190, 193]. It was possible to perform the necessary calculations using full wave functions. This allowed - despite the still limited statistics - to draw a conclusive picture of the interaction between Σ^+ and protons. The little known triplet interaction was found to be very shallow and repulsive, as predicted by some meson exchange models [110], contradicting both stronger repulsion [115, 116, 130] and attraction [111, 131] in this channel. Additionally, a fit of the data using Gaussian and Reid-like potentials was possible. Not only did this underline the previous findings, but also represents first direct experimental measurement of the p - Σ^+ scattering parameters.

Going back to the initial motivation of the measurement of the p - Σ^+ interaction - the potential presence of Σ baryons in neutron stars - a comparison with p - Λ is fruitful. One has to recall that the hyperon puzzle arose from the fact that the Λ baryon is less than 19% heavier [9] as the neutron and that the N - Λ interaction is quite strongly attractive [15, 16]. This implies that at a certain density it would become energetically favorable to substitute neutrons by Λ s and this is only overturned by repulsive three-body forces [18, 19]. Comparing the found scattering parameters of p - Σ^+ with the ones from p - Λ , a striking similarity in the singlet scattering length is apparent. Even though the singlet N - Λ ($I=1/2$) channel is not purely resident in the 27-plet, this is still clearly the dominant contribution ($\sqrt{0.9}$) as seen in Tab. 1.1. On the contrary, the triplet channels of the former interactions are completely unrelated and thus it is not surprising that the scattering lengths are different. While the p - Λ triplet interaction is found to be attractive, the one of p - Σ^+ is apparently repulsive. Additionally, the Σ baryons are considerably heavier than the Λ and consequently the neutron. The data presented in this thesis has sizeable uncertainties and thus no definite conclusion on this topic shall be made. Nonetheless, one may conclude that the presence of Σ baryons inside neutron stars is even less likely than the presence of Λ baryons and hence no “ Σ hyperon puzzle” arises.

Within this thesis, the production spectra of Σ^+ baryons in high-energy pp collisions at $\sqrt{s} = 13$ TeV and the p - Σ^+ correlation function were measured for the first time; and like all first measurements, those are the best there are - currently. As technology advances, future experiments will provide more precise data. Already now, ALICE is taking unprecedented statistics in the ongoing Run 3 of the LHC, which will only be surpassed by later runs. Thus, one has to state, as a matter of fact, that every result will be outdated sooner or later. Nonetheless, these results are based on the tremendous work of their predecessors. So, it remains to be hoped that the methods and the thoughts introduced in this thesis are useful for the young scientists to come.

Bibliography

- [1] **ALICE** Collaboration, B. B. Abelev *et al.*, “Production of $\Sigma(1385)^\pm$ and $\Xi(1530)^0$ in proton-proton collisions at $\sqrt{s} = 7$ TeV”, *Eur. Phys. J. C* **75** (2015) 1.
- [2] **ALICE** Collaboration, A. Borissov, “Production of Σ^0 Hyperons at LHC with ALICE”, *EPJ Web Conf.* **222** (2019) 02002.
- [3] **HADES** Collaboration, J. Adamczewski-Musch *et al.*, “ Σ^0 production in proton nucleus collisions near threshold”, *Phys. Lett. B* **781** (2018) 735–740.
- [4] **DELPHI** Collaboration, P. Abreu *et al.*, “Strange baryon production in Z hadronic decays”, *Z. Phys. C* **67** (1995) 543–554.
- [5] **OPAL** Collaboration, G. Alexander *et al.*, “ Σ^+ , Σ^0 and Σ^- hyperon production in hadronic Z^0 decays”, *Z. Phys. C* **73** (1997) 587–600.
- [6] **L3** Collaboration, M. Acciarri *et al.*, “Inclusive Σ^+ and Σ^0 production in hadronic Z decays”, *Phys. Lett. B* **479** (2000) 79–88.
- [7] **ALICE** Collaboration, S. Acharya *et al.*, “Production of light-flavor hadrons in pp collisions at $\sqrt{s} = 7$ and $\sqrt{s} = 13$ TeV”, *Eur. Phys. J. C* **81** (2021) 256.
- [8] **ATLAS** Collaboration, G. Aad *et al.*, “ K_S^0 and Λ production in pp interactions at $\sqrt{s} = 0.9$ and 7 TeV measured with the ATLAS detector at the LHC”, *Phys. Rev. D* **85** (2012) 012001.
- [9] **Particle Data Group** Collaboration, R. L. Workman *et al.*, “Review of Particle Physics”, *PTEP* **2022** (2022) 083C01.

-
- [10] **ALICE** Collaboration, J. Adam *et al.*, “Enhanced production of multi-strange hadrons in high-multiplicity proton-proton collisions”, *Nature Phys.* **13** (2017) 535–539.
 - [11] M. A. Lisa, S. Pratt, R. Soltz, and U. Wiedemann, “Femtoscopy in Relativistic Heavy Ion Collisions: Two Decades of Progress”, *Ann. Rev. Nucl. Part. Sci.* **55** (2005) 357–402.
 - [12] H. Djapo, B.-J. Schaefer, and J. Wambach, “Appearance of hyperons in neutron stars”, *Phys. Rev. C* **81** (2010) 035803.
 - [13] J. Schaffner-Bielich, “Strangeness in Compact Stars”, *Nucl. Phys. A* **835** (2010) 279–286.
 - [14] I. Vidana, V. M. Sarti, J. Haidenbauer, D. L. Mihaylov, and L. Fabbietti, “Neutron Star Properties and Femtoscopic Constraints”, *Eur. Phys. J. A* **61** (2025) 59.
 - [15] **ALICE** Collaboration, S. Acharya *et al.*, “p-p, p- Λ , and Λ - Λ correlations studied via femtoscopy in pp reactions at $\sqrt{s} = 7$ TeV”, *Phys. Rev. C* **99** (2019) 024001.
 - [16] D. L. Mihaylov, J. Haidenbauer, and V. M. Sarti, “Constraining the p Λ interaction from a combined analysis of scattering data and correlation functions”, *Phys. Lett. B* **850** (2024) 138550.
 - [17] O. Hashimoto and H. Tamura, “Spectroscopy of Λ hypernuclei”, *Prog. Part. Nucl. Phys.* **57** (2006) 564–653.
 - [18] D. Lonardoni, A. Lovato, S. Gandolfi, and F. Pederiva, “Hyperon Puzzle: Hints from Quantum Monte Carlo Calculations”, *Phys. Rev. Lett.* **114** (2015) 092301.
 - [19] D. Gerstung, N. Kaiser, and W. Weise, “Hyperon–nucleon three-body forces and strangeness in neutron stars”, *Eur. Phys. J. A* **56** (2020) 175.
 - [20] **J-PARC E40** Collaboration, T. Nanamura *et al.*, “Measurement of differential cross sections for Σ^+p elastic scattering in the momentum range 0.44–0.80 GeV/ c ”, *PTEP* **2022** (2022) 093D01.

-
- [21] J. Haidenbauer, U.-G. Meißner, and S. Petschauer, “Do $\Xi\Xi$ bound states exist?”, *Eur. Phys. J. A* **51** (2015) 17.
- [22] A. Mathis, “First Measurement of the Proton- Σ^0 Interaction via the Femtoscopy Method”, *Doctoral thesis, Technische Universität München* (2020).
- [23] **ALICE** Collaboration, S. Acharya *et al.*, “Investigation of the p- Σ^0 interaction via femtoscopy in pp collisions”, *Phys. Lett. B* **805** (2020) 135419.
- [24] E. Rutherford, “The scattering of α and β particles by matter and the structure of the atom”, *Phil. Mag. Ser. 6* **21** (1911) 669–688.
- [25] N. Bohr, “On the constitution of atoms and molecules”, *Phil. Mag. Ser. 6* **26** (1913) 1–24.
- [26] J. Ballam, V. L. Fitch, S. B. Treiman, R. R. Rau, K. Huang, and T. Fulton, “Proceedings, 6th Annual Conference on High Energy Nuclear Physics: Rochester, New York, USA, April 3-7, 1956”, Interscience (1956).
- [27] M. Gell-Mann, “A schematic model of baryons and mesons”, *Phys. Lett.* **8** (1964) 214–215.
- [28] G. Zweig, “An SU(3) model for strong interaction symmetry and its breaking. Version 2” in “Developments in the Quark Theory of Hadrons”, vol. 1, (1964) 22–101.
- [29] M. Gell-Mann, “The Eightfold Way: A Theory of strong interaction symmetry”, (1961).
- [30] E. Wigner, “On the Consequences of the Symmetry of the Nuclear Hamiltonian on the Spectroscopy of Nuclei”, *Phys. Rev.* **51** (1937) 106–119.
- [31] D. Griffiths, “Introduction to elementary particles”, *Wiley-VCH* (2008).
- [32] Cush, “Standard model of elementary particles”, *Wikimedia Commons* (2024). Accessed last in February 2025.

-
- [33] G. Jaeger, “Exchange Forces in Particle Physics”, *Found. Phys.* **51** (2021) 13.
- [34] A. Einstein, “Die Grundlage der allgemeinen Relativitätstheorie”, *Annalen Phys.* **49** (1916) 769–822.
- [35] P. W. Higgs, “Broken Symmetries and the Masses of Gauge Bosons”, *Phys. Rev. Lett.* **13** (1964) 508–509.
- [36] M. Y. Han and Y. Nambu, “Three-Triplet Model with Double SU(3) Symmetry”, *Phys. Rev.* **139** (1965) B1006–B1010.
- [37] W. A. Bardeen, H. Fritzsch, and M. Gell-Mann, “Light-Cone Current Algebra, π^0 Decay, and e^+e^- Annihilation” in “Topical Meeting on the Outlook for Broken Conformal Symmetry in Elementary Particle Physics” (1972), [arXiv:hep-ph/0211388](https://arxiv.org/abs/hep-ph/0211388).
- [38] K. Geiger, “Effective field theory approach to parton-hadron conversion in high energy QCD processes”, *Phys. Rev. D* **51** (1995) 3669–3687.
- [39] F. Gross *et al.*, “50 Years of quantum chromodynamics”, *Eur. Phys. J. C* **83** (2023) 1125.
- [40] J. Campbell, J. Huston, and F. Krauss, “The Black Book of Quantum Chromodynamics: a Primer for the LHC Era”, *Oxford University Press* (2018).
- [41] C.-N. Yang and R. L. Mills, “Conservation of Isotopic Spin and Isotopic Gauge Invariance”, *Phys. Rev.* **96** (1954) 191–195.
- [42] **CMS** Collaboration, “Measurement of azimuthal correlations among jets and determination of the strong coupling in pp collisions at $\sqrt{s} = 13$ TeV”, *CERN* (2023), <https://cds.cern.ch/record/2868568>.
- [43] D. E. Soper, “BASICS OF QCD PERTURBATION THEORY” in “Flavor Physics for the Millennium”, *World Scientific* (2001) 267–316.
- [44] R. P. Feynman, “Space-Time Approach to Quantum Electrodynamics”, *Phys. Rev.* **76** (1949) 769–789.

-
- [45] H. Georgi, “Effective Field Theory”, *Ann. Rev. Nucl. Part. Sci.* **43** (1993) 209–252.
 - [46] E. Epelbaum, H.-W. Hammer, and U.-G. Meissner, “Modern theory of nuclear forces”, *Rev. Mod. Phys.* **81** (2009) 1773–1825.
 - [47] T. Hatsuda, “Lattice quantum chromodynamics and baryon-baryon interactions”, *Front. Phys. (Beijing)* **13** (2018) 132105.
 - [48] K. Nagata, “Finite-density lattice QCD and sign problem: Current status and open problems”, *Prog. Part. Nucl. Phys.* **127** (2022) 103991.
 - [49] L. Van Hove, “Theoretical prediction of a new state of matter, the ‘Quark - Gluon Plasma’ (also called ‘Quark Matter’)” in “17th International Symposium on Multiparticle Dynamics” (1986) 801–818.
 - [50] H. Satz, “The Quark-Gluon Plasma: A Short Introduction”, *Nucl. Phys. A* **862-863** (2011) 4–12.
 - [51] J. Kapusta, J. Kapusta, B. Müller, and J. Rafelski, “Quark-Gluon Plasma: Theoretical Foundations: An Annotated Reprint Collection”. *Elsevier Science* (2003).
 - [52] **ALICE** Collaboration, S. Acharya *et al.*, “The ALICE experiment: a journey through QCD”, *Eur. Phys. J. C* **84** (2024) 813.
 - [53] J. Rafelski, “Melting hadrons, boiling quarks”, *Eur. Phys. J. A* **51** (2015) 114.
 - [54] P. Braun-Munzinger and J. Wambach, “Colloquium: Phase diagram of strongly interacting matter”, *Rev. Mod. Phys.* **81** (2009) 1031–1050.
 - [55] A. Bzdak, S. Esumi, V. Koch, J. Liao, M. Stephanov, and N. Xu, “Mapping the phases of quantum chromodynamics with beam energy scan”, *Phys. Rept.* **853** (2020) 1–87.
 - [56] Y. Fujimoto, K. Fukushima, K. Hotokezaka, and K. Kyutoku, “Gravitational Wave Signal for Quark Matter with Realistic Phase Transition”, *Phys. Rev. Lett.* **130** no. 9 (2023) 091404.

-
- [57] J. N. Guenther, “Overview of the QCD phase diagram: Recent progress from the lattice”, *Eur. Phys. J. A* **57** (2021) 136.
- [58] **HotQCD** Collaboration, A. Bazavov *et al.*, “Chiral crossover in QCD at zero and non-zero chemical potentials”, *Phys. Lett. B* **795** (2019) 15–21.
- [59] J. Chen *et al.*, “Properties of the QCD matter: review of selected results from the relativistic heavy ion collider beam energy scan (RHIC BES) program”, *Nucl. Sci. Tech.* **35** (2024) 214.
- [60] M. Bluhm *et al.*, “Dynamics of critical fluctuations: Theory – phenomenology – heavy-ion collisions”, *Nucl. Phys. A* **1003** (2020) 122016.
- [61] **STAR** Collaboration, T. Nonaka, “Conserved Charge Fluctuations from RHIC BES and FXT”, *Universe* **10** (2024) 49.
- [62] C. Bierlich *et al.*, “A comprehensive guide to the physics and usage of PYTHIA 8.3”, *SciPost Phys. Codeb.* **2022** (2022) 8.
- [63] T. Pierog, I. Karpenko, J. M. Katzy, E. Yatsenko, and K. Werner, “EPOS LHC: Test of collective hadronization with data measured at the CERN Large Hadron Collider”, *Phys. Rev. C* **92** (2015) 034906.
- [64] C. Bierlich and J. R. Christiansen, “Effects of color reconnection on hadron flavor observables”, *Phys. Rev. D* **92** (2015) 094010.
- [65] M. Gyulassy, I. Vitev, X.-N. Wang, and B.-W. Zhang, “Jet Quenching and Radiative Energy Loss in Dense Nuclear Matter”, [arXiv:nuc1-th/0302077](https://arxiv.org/abs/nuc1-th/0302077).
- [66] H. Song, S. A. Bass, U. Heinz, T. Hirano, and C. Shen, “200 AGeV Au+Au Collisions Serve a Nearly Perfect Quark-Gluon Liquid”, *Phys. Rev. Lett.* **106** (2011) 192301. [Erratum: *Phys. Rev. Lett.* **109** (2012) 139904].
- [67] P. Koch, B. Muller, and J. Rafelski, “Strangeness in relativistic heavy ion collisions”, *Phys. Rept.* **142** (1986) 167–262.

-
- [68] D. Molnar and S. A. Voloshin, “Elliptic Flow at Large Transverse Momenta from Quark Coalescence”, *Phys. Rev. Lett.* **91** (2003) 092301.
 - [69] V. Greco, C. M. Ko, and P. Levai, “Partonic coalescence in relativistic heavy ion collisions”, *Phys. Rev. C* **68** (2003) 034904.
 - [70] **ALICE** Collaboration, S. Acharya *et al.*, “Observation of partonic flow in proton-proton and proton-nucleus collisions”, [arXiv:2411.09323](#).
 - [71] **ALICE** Collaboration, S. Acharya *et al.*, “Transverse momentum spectra and nuclear modification factors of charged particles in pp, p-Pb and Pb-Pb collisions at the LHC”, *JHEP* **11** (2018) 013.
 - [72] W. Greiner, L. Neise, and H. Stöcker, “Thermodynamics and Statistical Mechanics”, Classical Theoretical Physics, *Springer* (1995).
 - [73] J. W. Gibbs, “Elementary Principles in Statistical Mechanics”, *Charles Scribner’s Sons* (1902).
 - [74] R. Hagedorn, “Statistical thermodynamics of strong interactions at high-energies”, *Nuovo Cim. Suppl.* **3** (1965) 147–186.
 - [75] F. Becattini and G. Passaleva, “Statistical hadronization model and transverse momentum spectra of hadrons in high energy collisions”, *Eur. Phys. J. C* **23** (2002) 551–583.
 - [76] A. Andronic, P. Braun-Munzinger, K. Redlich, and J. Stachel, “Decoding the phase structure of QCD via particle production at high energy”, *Nature* **561** (2018) 321–330.
 - [77] A. Andronic, P. Braun-Munzinger, J. Stachel, and H. Stocker, “Production of light nuclei, hypernuclei and their antiparticles in relativistic nuclear collisions”, *Phys. Lett. B* **697** (2011) 203–207.
 - [78] **ALICE** Collaboration, S. Acharya *et al.*, “Production of ^4He and $^4\overline{\text{He}}$ in Pb-Pb collisions at $\sqrt{s_{\text{NN}}} = 2.76$ TeV at the LHC”, *Nucl. Phys. A* **971** (2018) 1–20.
 - [79] **ALICE** Collaboration, S. Acharya *et al.*, “Multiplicity dependence of charged-particle production in pp, p-Pb, Xe-Xe and Pb-Pb collisions at the LHC”, *Phys. Lett. B* **845** (2023) 138110.

-
- [80] V. Vovchenko, B. Dönigus, and H. Stoecker, “Canonical statistical model analysis of p-p, p-Pb, and Pb-Pb collisions at energies available at the CERN Large Hadron Collider”, *Phys. Rev. C* **100** (2019) 054906.
- [81] V. Vovchenko, B. Dönigus, and H. Stoecker, “Multiplicity dependence of light nuclei production at LHC energies in the canonical statistical model”, *Phys. Lett. B* **785** (2018) 171–174.
- [82] Q. Wang, P.-P. Yang, and F.-H. Liu, “Comparing a few distributions of transverse momenta in high energy collisions”, *Results Phys.* **12** (2019) 259–267.
- [83] J. Cleymans and D. Worku, “Relativistic thermodynamics: Transverse momentum distributions in high-energy physics”, *Eur. Phys. J. A* **48** (2012) 160.
- [84] E. Schnedermann, J. Sollfrank, and U. W. Heinz, “Thermal phenomenology of hadrons from 200 AGeV S+S collisions”, *Phys. Rev. C* **48** (1993) 2462–2475.
- [85] E. Schnedermann and U. W. Heinz, “Hydrodynamical assessment of 200 AGeV collisions”, *Phys. Rev. C* **50** (1994) 1675–1683.
- [86] C. Tsallis, “Possible generalization of Boltzmann-Gibbs statistics”, *J. Statist. Phys.* **52** (1988) 479–487.
- [87] **STAR** Collaboration, B. I. Abelev *et al.*, “Strange particle production in p+p collisions at $\sqrt{s} = 200$ GeV”, *Phys. Rev. C* **75** (2007) 064901.
- [88] **PHENIX** Collaboration, A. Adare *et al.*, “Identified charged hadron production in $p + p$ collisions at $\sqrt{s} = 200$ and 62.4 GeV”, *Phys. Rev. C* **83** (2011) 064903.
- [89] **ALICE** Collaboration, K. Aamodt *et al.*, “Production of pions, kaons and protons in pp collisions at $\sqrt{s} = 900$ GeV with ALICE at the LHC”, *Eur. Phys. J. C* **71** (2011) 1655.
- [90] **CMS** Collaboration, V. Khachatryan *et al.*, “Strange particle production in pp collisions at $\sqrt{s} = 0.9$ and 7 TeV”, *JHEP* **05** (2011) 064.

-
- [91] J. Cleymans and D. Worku, “The Tsallis distribution in proton-proton collisions at $\sqrt{s} = 0.9$ TeV at the LHC”, *J. Phys. G* **39** (2012) 025006.
- [92] D. Prato and C. Tsallis, “Nonextensive foundation of Lévy distributions”, *Phys. Rev. E* **60** (1999) 2398.
- [93] Z. Tang, Y. Xu, L. Ruan, G. van Buren, F. Wang, and Z. Xu, “Spectra and radial flow at relativistic heavy ion collisions with Tsallis statistics in a blast-wave description”, *Phys. Rev. C* **79** (2009) 051901.
- [94] N. Metropolis and S. Ulam, “The Monte Carlo Method”, *J. Am. Statist. Assoc.* **44** (1949) 335–341.
- [95] T. Sjostrand, S. Mrenna, and P. Z. Skands, “PYTHIA 6.4 physics and manual”, *JHEP* **05** (2006) 026.
- [96] K. Werner, “Revealing a deep connection between factorization and saturation: New insight into modeling high-energy proton-proton and nucleus-nucleus scattering in the EPOS4 framework”, *Phys. Rev. C* **108** (2023) 064903.
- [97] K. Werner and B. Guiot, “Perturbative QCD concerning light and heavy flavor in the EPOS4 framework”, *Phys. Rev. C* **108** (2023) 034904.
- [98] K. Werner, “Parallel scattering, saturation, and generalized Abramovskii-Gribov-Kancheli (AGK) theorem in the EPOS4 framework, with applications for heavy-ion collisions at $\sqrt{s_{NN}}$ of 5.02 TeV and 200 GeV”, *Phys. Rev. C* **109** (2024) 034918.
- [99] K. Werner, “Core-corona procedure and microcanonical hadronization to understand strangeness enhancement in proton-proton and heavy ion collisions in the EPOS4 framework”, *Phys. Rev. C* **109** (2024) 014910.
- [100] D. E. Soper, “Parton distribution functions”, *Nucl. Phys. B Proc. Suppl.* **53** (1997) 69–80.
- [101] B. Andersson, “*The Lund Model*”, Cambridge Monographs on Particle Physics, Nuclear Physics and Cosmology, vol. 7, *Cambridge University Press* (2023).

-
- [102] B. R. Webber, “A QCD model for jet fragmentation including soft gluon interference”, *Nucl. Phys. B* **238** (1984) 492–528.
- [103] B. Andersson, G. Gustafson, and T. Sjostrand, “Baryon Production in Jet Fragmentation and Υ -Decay”, *Phys. Scripta* **32** (1985) 574.
- [104] P. Kotko, L. Motyka, and A. Stasto, “Color reconnection effects in J/ψ hadroproduction”, *Phys. Lett. B* **844** (2023) 138104.
- [105] R. Kleiss, W. J. Stirling, and S. D. Ellis, “A new Monte Carlo treatment of multiparticle phase space at high energies”, *Comput. Phys. Commun.* **40** (1986) 359.
- [106] R. J. Oakes, “Baryon-Baryon Interactions and the Eightfold Way”, *Phys. Rev.* **131** (1963) 2239–2241.
- [107] P. D. DeSouza, G. A. Snow, and S. Meshkov, “S-Wave Hyperon-Nucleon Interactions and SU_3 Symmetry”, *Phys. Rev.* **135** (1964) B565–B567.
- [108] **NPLQCD** Collaboration, M. Illa *et al.*, “Low-energy scattering and effective interactions of two baryons at $m_\pi \sim 450$ MeV from lattice quantum chromodynamics”, *Phys. Rev. D* **103** no. 5 (2021) 054508.
- [109] H. Yukawa, “On the Interaction of Elementary Particles. I”, *Proc. Phys. Math. Soc. Jap.* **17** (1935) 48–57.
- [110] J. Haidenbauer and U.-G. Meissner, “Jülich hyperon-nucleon model revisited”, *Phys. Rev. C* **72** (2005) 044005.
- [111] T. A. Rijken, V. G. J. Stoks, and Y. Yamamoto, “Soft core hyperon-nucleon potentials”, *Phys. Rev. C* **59** (1999) 21–40.
- [112] T. A. Rijken, M. M. Nagels, and Y. Yamamoto, “Baryon-Baryon Interactions: Nijmegen Extended-Soft-Core Models”, *Prog. Theor. Phys. Suppl.* **185** (2010) 14–71.
- [113] M. M. Nagels, T. A. Rijken, and Y. Yamamoto, “Extended-soft-core baryon-baryon model ESC16. II. Hyperon-nucleon interactions”, *Phys. Rev. C* **99** (2019) 044003.

-
- [114] Y. Fujiwara, C. Nakamoto, and Y. Suzuki, “Unified Description of NN and YN Interactions in a Quark Model with Effective Meson-Exchange Potentials”, *Phys. Rev. Lett.* **76** (1996) 2242–2245.
- [115] Y. Fujiwara, T. Fujita, M. Kohno, C. Nakamoto, and Y. Suzuki, “Resonating-group study of baryon-baryon interactions for the complete baryon octet: NN interaction”, *Phys. Rev. C* **65** (2001) 014002.
- [116] Y. Fujiwara, Y. Suzuki, and C. Nakamoto, “Baryon-baryon interactions in the SU(6) quark model and their applications to light nuclear systems”, *Prog. Part. Nucl. Phys.* **58** (2007) 439–520.
- [117] S. Weinberg, “Phenomenological Lagrangians”, *Physica A* **96** no. 1-2 (1979) 327–340.
- [118] S. Weinberg, “Nuclear forces from chiral lagrangians”, *Phys. Lett. B* **251** (1990) 288–292.
- [119] S. Petschauer, J. Haidenbauer, N. Kaiser, U.-G. Meißner, and W. Weise, “Hyperon-Nuclear Interactions From SU(3) Chiral Effective Field Theory”, *Front. in Phys.* **8** (2020) 12.
- [120] J. Haidenbauer, S. Petschauer, N. Kaiser, U. G. Meissner, A. Nogga, and W. Weise, “Hyperon-nucleon interaction at next-to-leading order in chiral effective field theory”, *Nucl. Phys. A* **915** (2013) 24–58.
- [121] J. Haidenbauer, U.-G. Meißner, A. Nogga, and H. Le, “Hyperon–nucleon interaction in chiral effective field theory at next-to-next-to-leading order”, *Eur. Phys. J. A* **59** (2023) 63.
- [122] J. Haidenbauer, U. G. Meißner, and A. Nogga, “Hyperon–nucleon interaction within chiral effective field theory revisited”, *Eur. Phys. J. A* **56** (2020) 91.
- [123] J. Haidenbauer and U.-G. Meißner, “Exploring the Σ^+p interaction by measurements of the correlation function”, *Phys. Lett. B* **829** (2022) 137074.

-
- [124] P. Reinert, H. Krebs, and E. Epelbaum, “Semilocal momentum-space regularized chiral two-nucleon potentials up to fifth order”, *Eur. Phys. J. A* **54** (2018) 86.
- [125] “Personal communication with Johann Haidenbauer”, (2025).
- [126] **NPLQCD** Collaboration, S. R. Beane, P. F. Bedaque, T. C. Luu, K. Orginos, E. Pallante, A. Parreno, and M. J. Savage, “Hyperon-nucleon scattering from fully-dynamical lattice QCD”, *Nucl. Phys. A* **794** (2007) 62–72.
- [127] **HAL QCD** Collaboration, T. Inoue, S. Aoki, T. Doi, T. Hatsuda, Y. Ikeda, N. Ishii, K. Murano, H. Nemura, and K. Sasaki, “Two-baryon potentials and H-dibaryon from 3-flavor lattice QCD simulations”, *Nucl. Phys. A* **881** (2012) 28–43.
- [128] **KEK-PS E-251** Collaboration, J. K. Ahn *et al.*, “ Σ^+p elastic scattering in the region of $300 \leq p_\Sigma \leq 600$ MeV/ c with a scintillating fiber target”, *Nucl. Phys. A* **648** (1999) 263–279.
- [129] **KEK-PS E289** Collaboration, J. K. Ahn *et al.*, “ Σ^+p elastic scattering cross sections in the region of $350 \leq p_{\Sigma^+} \leq 750$ MeV/ c with a scintillating fiber active target”, *Nucl. Phys. A* **761** (2005) 41–66.
- [130] M. M. Nagels, T. A. Rijken, and J. J. De Swart, “A potential model for hyperon-nucleon scattering”, *Annals Phys.* **79** (1973) 338–385.
- [131] V. G. J. Stoks and T. A. Rijken, “Soft-core baryon-baryon potentials for the complete baryon octet”, *Phys. Rev. C* **59** (1999) 3009–3020.
- [132] H. A. Bethe, “Theory of the Effective Range in Nuclear Scattering”, *Phys. Rev.* **76** (1949) 38–50.
- [133] W. Bruckner, B. Granz, D. Ingham, K. Kilian, U. Lynen, J. Niewisch, B. Pietrzyk, B. Povh, H. G. Ritter, and H. Schroder, “Strangeness exchange reaction on nuclei”, *Phys. Lett. B* **62** (1976) 481–484.
- [134] H. Clement, “On the history of dibaryons and their final observation”, *Prog. Part. Nucl. Phys.* **93** (2017) 195.

-
- [135] B. Dönigus, “Selected highlights of the production of light (anti-)(hyper-)nuclei in ultra-relativistic heavy-ion collisions”, *Eur. Phys. J. A* **56** (2020) 280.
 - [136] D. J. Millener, C. B. Dover, and A. Gal, “ Λ -nucleus single-particle potentials”, *Phys. Rev. C* **38** (1988) 2700–2708.
 - [137] A. Gal, E. V. Hungerford, and D. J. Millener, “Strangeness in nuclear physics”, *Rev. Mod. Phys.* **88** (2016) 035004.
 - [138] A. Gal and C. B. Dover, “Narrow Σ -Hypernuclear States”, *Phys. Rev. Lett.* **44** (1980) 379. [Erratum: *Phys. Rev. Lett.* **44** (1980) 962].
 - [139] R. S. Hayano, T. Ishikawa, M. Iwasaki, H. Ota, E. Takada, H. Tamura, A. Sakaguchi, M. Aoki, and T. Yamazaki, “Evidence for a bound state of the $^4_\Sigma\text{He}$ hypernucleus”, *Phys. Lett. B* **231** (1989) 355–358.
 - [140] T. Nagae *et al.*, “Observation of a $^4_\Sigma\text{He}$ Bound State in the $^4\text{He}(\text{K},\pi^-)$ Reaction at 600 MeV/c”, *Phys. Rev. Lett.* **80** (1998) 1605–1609.
 - [141] T. Harada, Y. Akaishi, S. Shinmura, and H. Tanaka, “Structure of the $^4_\Sigma\text{He}$ hypernuclear bound state”, *Nucl. Phys. A* **507** (1990) 715–730.
 - [142] J. Dabrowski, “Isospin dependence of the single-particle potential of the Σ hyperon in nuclear matter”, *Phys. Rev. C* **60** (1999) 025205.
 - [143] H. Noumi *et al.*, “Sigma-Nucleus Potential in $A = 28$ ”, *Phys. Rev. Lett.* **89** (2002) 072301. [Erratum: *Phys. Rev. Lett.* **90** (2003) 049902].
 - [144] G. Backenstoss, T. Bunaciu, S. Charalambus, J. Egger, H. Koch, A. Bamberger, U. Lynen, H. G. Ritter, and H. Schmitt, “Observations of Σ hyperonic atoms”, *Phys. Lett. B* **33** (1970) 230–232.
 - [145] C. J. Batty, S. F. Biagi, M. Blecher, S. D. Hoath, R. A. J. Riddle, B. L. Roberts, J. D. Davies, G. J. Pyle, G. T. A. Squier, and D. M. Asbury, “Measurement of strong interaction effects in Σ atoms”, *Phys. Lett. B* **74** (1978) 27–30.
 - [146] C. J. Batty, E. Friedman, and A. Gal, “Strong interaction physics from hadronic atoms”, *Phys. Rept.* **287** (1997) 385–445.

-
- [147] R. J. Powers *et al.*, “Strong-interaction effect measurements in sigma hyperonic atoms of W and Pb”, *Phys. Rev. C* **47** (1993) 1263–1273.
- [148] E. Friedman and A. Gal, “In-medium nuclear interactions of low-energy hadrons”, *Phys. Rept.* **452** (2007) 89–153.
- [149] Theoretical High Energy Physics Group of the Radboud University Nijmegen, “NN-OnLine”, <https://nn-online.org/>. Accessed last in February 2025.
- [150] W. J. Briscoe, M. Döring, H. Haberzettl, I. I. Strakovsky, and R. L. Workman, “Scattering analysis interactive dial-in (SAID) data base”, https://gwdac.phys.gwu.edu/analysis/nn_analysis.html. Accessed last in February 2025.
- [151] G. Alexander, U. Karshon, A. Shapira, G. Yekutieli, R. Engelmann, H. Filthuth, and W. Lughofer, “Study of the Λ -N System in Low-Energy Λ -p Elastic Scattering”, *Phys. Rev.* **173** (1968) 1452–1460.
- [152] B. Sechi-Zorn, B. Kehoe, J. Twitty, and R. A. Burnstein, “Low-Energy Λ -Proton Elastic Scattering”, *Phys. Rev.* **175** (1968) 1735–1740.
- [153] J. A. Kadyk, G. Alexander, J. H. Chan, P. Gaposchkin, and G. H. Trilling, “ Λ p interactions in momentum range 300 to 1500 MeV/ c ”, *Nucl. Phys. B* **27** (1971) 13–22.
- [154] H. A. Rubin and R. A. Burnstein, “Low-Energy (Σ^+, p) and (Σ^-, p) Elastic Scattering”, *Phys. Rev.* **159** (1967) 1149–1156.
- [155] F. Eisele, H. Filthuth, W. Foehlich, V. Hepp, and G. Zech, “Elastic $\Sigma^\pm p$ scattering at low energies”, *Phys. Lett. B* **37** (1971) 204–206.
- [156] D. Logoteta, “Hyperons in Neutron Stars”, *Universe* **7** (2021) 408.
- [157] D. D. Ivanenko and D. F. Kurdgelaidze, “Hypothesis concerning quark stars”, *Astrophysics* **1** (1965) 251–252.
- [158] M. G. Alford, A. Schmitt, K. Rajagopal, and T. Schäfer, “Color superconductivity in dense quark matter”, *Rev. Mod. Phys.* **80** (2008) 1455–1515.

-
- [159] E. R. Most, A. Motornenko, J. Steinheimer, V. Dexheimer, M. Hanauske, L. Rezzolla, and H. Stoecker, “Probing neutron-star matter in the lab: Similarities and differences between binary mergers and heavy-ion collisions”, *Phys. Rev. D* **107** (2023) 043034.
 - [160] **LIGO Scientific, Virgo** Collaboration, B. P. Abbott *et al.*, “GW170817: Observation of Gravitational Waves from a Binary Neutron Star Inspiral”, *Phys. Rev. Lett.* **119** (2017) 161101.
 - [161] J. Schaffner-Bielich, “Compact Star Physics”, *Cambridge University Press* (2020).
 - [162] S. Chandrasekhar, “The Maximum Mass of Ideal White Dwarfs”, *Astrophys. J.* **74** (1931) 81–82.
 - [163] R. C. Tolman, “Static Solutions of Einstein’s Field Equations for Spheres of Fluid”, *Phys. Rev.* **55** (1939) 364–373.
 - [164] J. R. Oppenheimer and G. M. Volkoff, “On Massive Neutron Cores”, *Phys. Rev.* **55** (1939) 374–381.
 - [165] J. Heyl *et al.*, “Exploring the physics of neutron stars with high-resolution, high-throughput X-ray spectroscopy”, [arXiv:1903.06777](https://arxiv.org/abs/1903.06777).
 - [166] N. Andersson, “A Gravitational-Wave Perspective on Neutron-Star Seismology”, *Universe* **7** (2021) 97.
 - [167] P. Haensel, A. Y. Potekhin, and D. G. Yakovlev, “Neutron Stars 1: Equation of State and Structure”, vol. 326, *Springer* (2007).
 - [168] V. Kalogera and G. Baym, “The Maximum Mass of a Neutron Star”, *Astrophys. J. Lett.* **470** (1996) L61–L64.
 - [169] R. W. Romani, D. Kandel, A. V. Filippenko, T. G. Brink, and W. Zheng, “PSR J0952–0607: The Fastest and Heaviest Known Galactic Neutron Star”, *Astrophys. J. Lett.* **934** (2022) L17.
 - [170] O. Ivanytskyi, D. Blaschke, T. Fischer, and A. Bauswein, “Early deconfinement of asymptotically conformal color-superconducting quark matter in neutron stars”, *EPJ Web Conf.* **274** (2022) 07010.

-
- [171] **ALICE** Collaboration, S. Acharya *et al.*, “Towards the understanding of the genuine three-body interaction for p–p–p and p–p– Λ ”, *Eur. Phys. J. A* **59** (2023) 145.
- [172] J. Haidenbauer, U. G. Meißner, N. Kaiser, and W. Weise, “Lambda-nuclear interactions and hyperon puzzle in neutron stars”, *Eur. Phys. J. A* **53** (2017) 121.
- [173] L. Fabbietti, V. Mantovani Sarti, and O. Vazquez Doce, “Study of the Strong Interaction Among Hadrons with Correlations at the LHC”, *Ann. Rev. Nucl. Part. Sci.* **71** (2021) 377–402.
- [174] R. Hanbury Brown and R. Q. Twiss, “A new type of interferometer for use in radio astronomy”, *Phil. Mag. Ser. 7* **45** (1954) 663–682.
- [175] R. Hanbury Brown and R. Q. Twiss, “A Test of a New Type of Stellar Interferometer on Sirius”, *Nature* **178** (1956) 1046–1048.
- [176] G. Baym, “The Physics of Hanbury Brown-Twiss intensity interferometry: From stars to nuclear collisions”, *Acta Phys. Polon. B* **29** (1998) 1839–1884.
- [177] U. W. Heinz and B. V. Jacak, “Two-particle correlations in relativistic heavy-ion collisions”, *Ann. Rev. Nucl. Part. Sci.* **49** (1999) 529–579.
- [178] G. Goldhaber, S. Goldhaber, W.-Y. Lee, and A. Pais, “Influence of Bose-Einstein Statistics on the Antiproton-Proton Annihilation Process”, *Phys. Rev.* **120** (1960) 300–312.
- [179] **STAR** Collaboration, J. Adams *et al.*, “Proton- Λ correlations in central Au+Au collisions at $\sqrt{s} = 200$ GeV”, *Phys. Rev. C* **74** (2006) 064906.
- [180] **STAR** Collaboration, L. Adamczyk *et al.*, “ $\Lambda\Lambda$ Correlation Function in Au+Au Collisions at $\sqrt{s_{NN}} = 200$ GeV”, *Phys. Rev. Lett.* **114** (2015) 022301.
- [181] R. L. Jaffe, “Perhaps a Stable Dihyperon”, *Phys. Rev. Lett.* **38** (1977) 195–198. [Erratum: *Phys. Rev. Lett.* **38** (1977) 617].

-
- [182] **ALICE** Collaboration, S. Acharya *et al.*, “Search for a common baryon source in high-multiplicity pp collisions at the LHC”, *Phys. Lett. B* **811** (2020) 135849.
- [183] **ALICE** Collaboration, S. Acharya *et al.*, “Common femtoscopic hadron-emission source in pp collisions at the LHC”, *Eur. Phys. J. C* **85** (2025) 198.
- [184] N. Bock, “Femtосcopy and energy-momentum conservation effects in proton-proton collisions at 900 GeV in ALICE”, *J. Phys. Conf. Ser.* **270** (2011) 012022.
- [185] S. Pratt, “Pion interferometry of quark-gluon plasma”, *Phys. Rev. D* **33** (1986) 1314–1327.
- [186] A. M. Badalian, L. P. Kok, M. I. Polikarpov, and Y. A. Simonov, “Resonances in coupled channels in nuclear and particle physics”, *Phys. Rept.* **82** (1982) 31–177.
- [187] R. Lednicky, “Finite-size effects on two-particle production in continuous and discrete spectrum”, *Phys. Part. Nucl.* **40** (2009) 307–352.
- [188] D. L. Mihaylov, “Analysis techniques for femtосcopy and correlation studies in small collision systems and their applications to the investigation of p- Λ and Λ - Λ interactions with ALICE”, *Doctoral thesis, Technische Universität München* (2021).
- [189] A. N. Makhlin and Y. M. Sinyukov, “The hydrodynamics of hadron matter under pion interferometric microscope”, *Z. Phys. C* **39** (1988) 69.
- [190] R. Lednicky and V. L. Lyuboshits, “Final State Interaction Effect on Pairing Correlations Between Particles with Small Relative Momenta”, *Yad. Fiz.* **35** (1981) 1316–1330.
- [191] **ALICE** Collaboration, S. Acharya *et al.*, “Investigating the p- π^\pm and p-p- π^\pm dynamics with femtосcopy in pp collisions at $\sqrt{s} = 13$ TeV”, [arXiv:2502.20200](https://arxiv.org/abs/2502.20200).

-
- [192] D. L. Mihaylov, V. Mantovani Sarti, O. W. Arnold, L. Fabbietti, B. Hohlweger, and A. M. Mathis, “A femtosopic correlation analysis tool using the Schrödinger equation (CATS)”, *Eur. Phys. J. C* **78** (2018) 394.
- [193] R. Lednicky and M. I. Podgoretsky, “The Interference of Identical Particles Emitted by Sources of Different Sizes”, *Sov. J. Nucl. Phys.* **30** (1979) 432.
- [194] L. D. Landau and E. M. Lifshits, “Quantum Mechanics: Non-Relativistic Theory”, *Course of Theoretical Physics*, vol. 3, *Butterworth-Heinemann* (1991).
- [195] D. J. Griffiths and D. F. Schroeter, “Introduction to Quantum Mechanics”, vol. 3, *Cambridge University Press* (2018).
- [196] J. D. Jackson and J. M. Blatt, “The Interpretation of Low Energy Proton-Proton Scattering”, *Rev. Mod. Phys.* **22** (1950) 77–118.
- [197] M. Gmitro, J. Kvasil, R. Lednicky, and V. L. Lyuboshits, “On the sensitivity of nucleon-nucleon correlations to the form of short-range potential”, *Czech. J. Phys. B* **36** (1986) 1281.
- [198] G. Gamow, “Zur Quantentheorie des Atomkernes”, *Z. Phys.* **51** (1928) 204–212.
- [199] M. Abramowitz and I. Stegun, “Handbook of Mathematical Functions: With Formulas, Graphs, and Mathematical Tables”, Applied mathematics series, *Dover Publications* (1965).
- [200] **WA97** Collaboration, F. Antinori *et al.*, “Centrality dependence of the expansion dynamics in Pb-Pb collisions at 158 AGeV/c”, *J. Phys. G* **27** (2001) 2325–2344.
- [201] M. Galassi *et al.*, “GNU Scientific Library: Reference Manual”, *Network Theory* (2009).
- [202] A. Messiah, “Quantum Mechanics”, No. 1 in Quantum Mechanics, *North-Holland Publishing Company* (1961).

-
- [203] F. M. S. Lima, “Lecture notes on Legendre polynomials: their origin and main properties”, [arXiv:2210.10942](#).
- [204] J. Haidenbauer, G. Krein, and T. C. Peixoto, “Femtoscopic correlations and the $\Lambda_c N$ interaction”, *Eur. Phys. J. A* **56** (2020) 184.
- [205] A. Ohnishi, K. Morita, K. Miyahara, and T. Hyodo, “Hadron–hadron correlation and interaction from heavy–ion collisions”, *Nucl. Phys. A* **954** (2016) 294–307.
- [206] K. Morita, A. Ohnishi, F. Etminan, and T. Hatsuda, “Probing multistrange dibaryons with proton-omega correlations in high-energy heavy ion collisions”, *Phys. Rev. C* **94** (2016) 031901. [Erratum: *Phys. Rev. C* **100** (2019) 069902].
- [207] E. Schrödinger, “Quantisierung als Eigenwertproblem”, *Annalen Phys.* **384** (1926) 361–376.
- [208] B. A. Lippmann and J. Schwinger, “Variational Principles for Scattering Processes. I”, *Phys. Rev.* **79** (1950) 469–480.
- [209] R. V. Reid, Jr., “Local phenomenological nucleon-nucleon potentials”, *Annals Phys.* **50** (1968) 411–448.
- [210] Y. Kamiya, T. Hyodo, and A. Ohnishi, “Femtoscopic study on DD^* and $D\bar{D}^*$ interactions for T_{cc} and $X(3872)$ ”, *Eur. Phys. J. A* **58** (2022) 131.
- [211] K. Morita, T. Furumoto, and A. Ohnishi, “ $\Lambda\Lambda$ interaction from relativistic heavy-ion collisions”, *Phys. Rev. C* **91** (2015) 024916.
- [212] E. Lopienska, “The CERN accelerator complex.”, CERN (2022). <https://cds.cern.ch/images/CERN-GRAPHICS-2022-001-1>. Accessed last in February 2025.
- [213] L. Evans and P. Bryant, “LHC Machine”, *JINST* **3** (2008) S08001.
- [214] R. Assmann, M. Lamont, and S. Myers, “A brief history of the LEP collider”, *Nucl. Phys. B Proc. Suppl.* **109** (2002) 17–31.

-
- [215] J. Wenninger, “Machine Protection and Operation for LHC” in “2014 Joint International Accelerator School: Beam Loss and Accelerator Protection” (2016) 377–401, [arXiv:1608.03113](#).
- [216] **ALICE** Collaboration, K. Aamodt *et al.*, “The ALICE experiment at the CERN LHC”, *JINST* **3** (2008) S08002.
- [217] **ALICE** Collaboration, P. Cortese *et al.*, “ALICE: Physics Performance Report, Volume I”, *J. Phys. G* **30** (2004) 1517–1763.
- [218] **ALICE** Collaboration, B. Alessandro *et al.*, “ALICE: Physics Performance Report, Volume II”, *J. Phys. G* **32** (2006) 1295.
- [219] **L3** Collaboration, B. Adeva *et al.*, “The Construction of the L3 Experiment”, *Nucl. Instrum. Meth. A* **289** (1990) 35–102.
- [220] **ALICE** Collaboration, “3D ALICE schematic RUN 2”, 2017. <https://alice-figure.web.cern.ch/node/11219>. Accessed last in February 2025.
- [221] **ALICE** Collaboration, K. Aamodt *et al.*, “Alignment of the ALICE Inner Tracking System with cosmic-ray tracks”, *JINST* **5** (2010) P03003.
- [222] **ALICE** Collaboration, G. Dellacasa *et al.*, “ALICE technical design report of the inner tracking system (ITS)”, *CERN-LHCC-99-12* (1999).
- [223] **ALICE** Collaboration, B. B. Abelev *et al.*, “Performance of the ALICE Experiment at the CERN LHC”, *Int. J. Mod. Phys. A* **29** (2014) 1430044.
- [224] J. Wiechula, “Inbetriebnahme und Kalibrierung der ALICE-TPC”, *Doctoral thesis, Goethe Universität Frankfurt am Main* (2008), <https://cds.cern.ch/record/1295506>.
- [225] **ALICE** Collaboration, J. Alme *et al.*, “The ALICE TPC, a large 3-dimensional tracking device with fast readout for ultra-high multiplicity events”, *Nucl. Instrum. Meth. A* **622** (2010) 316–367.
- [226] F. Sauli, “GEM: A new concept for electron amplification in gas detectors”, *Nucl. Instrum. Meth. A* **386** (1997) 531–534.

-
- [227] **ALICE** Collaboration, C. Lippmann, “Upgrade of the ALICE Time Projection Chamber”, *CERN-LHCC-2013-020 / ALICE-TDR-016* (2013).
- [228] **ALICE** Collaboration, “First results of the ALICE detector performance in pp collisions at 13 TeV”, *ALICE-PUBLIC-2015-004* (2015).
- [229] **ALICE** Collaboration, G. Dellacasa *et al.*, “ALICE Time-Of-Flight system (TOF) : Technical Design Report”, *CERN-LHCC-2000-012* (2000).
- [230] **ALICE** Collaboration, “The ALICE figure repository”, <https://alice-figure.web.cern.ch/>. Accessed last in February 2025.
- [231] **ALICE** Collaboration, G. Dellacasa *et al.*, “ALICE Photon Spectrometer (PHOS) : Technical Design Report”, *CERN-LHCC-99-004* (1999).
- [232] **ALICE** Collaboration, P. Cortese *et al.*, “ALICE Electromagnetic Calorimeter Technical Design Report”, *CERN-LHCC-2008-014 / CERN-ALICE-TDR-014* (2008).
- [233] **ALICE** Collaboration, J. Allen *et al.*, “ALICE DCal: An Addendum to the EMCal Technical Design Report Di-Jet and Hadron-Jet correlation measurements in ALICE”, *CERN-LHCC-2010-011 / ALICE-TDR-14-add-1* (2010).
- [234] **ALICE** Collaboration, P. Cortese *et al.*, “ALICE forward detectors: FMD, TO and VO : Technical Design Report”, *CERN-LHCC-2004-025* (2004).
- [235] S. van der Meer, “Calibration of the effective beam height in the ISR”, *CERN-ISR-PO-68-31* (1968).
- [236] **ALICE** Collaboration, S. Acharya *et al.*, “ALICE upgrades during the LHC Long Shutdown 2”, *JINST* **19** no. 05 (2024) P05062.
- [237] M. Ivanov, I. Belikov, P. Hristov, and K. Safarik, “Track reconstruction in high density environment”, *Nucl. Instrum. Meth. A* **566** (2006) 70–74.

-
- [238] **ALICE** Collaboration, “AliRoot: ALICE Software Framework”, <https://github.com/alisw/AliRoot>. Accessed last in February 2025.
- [239] R. E. Kalman, “A New Approach to Linear Filtering and Prediction Problems”, *J. Fluids Eng.* **82** (1960) 35–45.
- [240] **ALICE** Collaboration, P. Cortese, F. Carminati, C. W. Fabjan, L. Riccati, and H. de Groot, “ALICE computing: Technical Design Report”, *CERN* (2005), <https://cds.cern.ch/record/832753>.
- [241] **ALICE** Collaboration, K. Aamodt *et al.*, “Strange particle production in proton-proton collisions at $\sqrt{s} = 0.9$ TeV with ALICE at the LHC”, *Eur. Phys. J. C* **71** (2011) 1594.
- [242] **ALICE** Collaboration, S. Acharya *et al.*, “Multiplicity dependence of (multi-)strange hadron production in proton-proton collisions at $\sqrt{s} = 13$ TeV”, *Eur. Phys. J. C* **80** (2020) 167.
- [243] “Personal communication with Marian Ivanov”, (2024).
- [244] **ALICE** Collaboration, “AliPhysics: ALICE Analysis Repository”, <https://github.com/alisw/AliPhysics>. Accessed last in February 2025.
- [245] R. Brun and F. Rademakers, “ROOT - An Object Oriented Data Analysis Framework” in “Proceedings AIHENP’96 Workshop, Lausanne, Sep. 1996”, *Phys. Res. A* **389** (1997) 81-86.
- [246] “ROOT manual”, <https://root.cern/manual/>. Accessed last in February 2025.
- [247] I. Kisel, I. Kulakov, and M. Zyzak, “Standalone First Level Event Selection Package for the CBM Experiment”, *IEEE Transactions on Nuclear Science* **60** (2013) 3703–3708.
- [248] L. Barioglio, F. Catalano, M. Concas, P. Fecchio, F. Grosa, F. Mazzaschi, and M. Puccio, “Hipe4ML”, Zenodo (2022).
- [249] T. Akiba, S. Sano, T. Yanase, T. Ohta, and M. Koyama, “Optuna: A Next-generation Hyperparameter Optimization Framework”, Association for Computing Machinery, KDD ’19 (2019) 2623–2631.

-
- [250] T. Chen and C. Guestrin, “XGBoost: A Scalable Tree Boosting System”, [arXiv:1603.02754](https://arxiv.org/abs/1603.02754).
- [251] **GEANT4** Collaboration, S. Agostinelli *et al.*, “GEANT4—a simulation toolkit”, *Nucl. Instrum. Meth. A* **506** (2003) 250–303.
- [252] J. Allison *et al.*, “GEANT4 developments and applications”, *IEEE Trans. Nucl. Sci.* **53** (2006) 270.
- [253] J. Allison *et al.*, “Recent developments in GEANT4”, *Nucl. Instrum. Meth. A* **835** (2016) 186–225.
- [254] S. L. Lauritzen, “Time Series Analysis in 1880: A Discussion of Contributions made by T.N. Thiele”, *International Statistical Review* **49** (1981) 319–331.
- [255] L. McGee, “Discovery of the Kalman Filter as a Practical Tool for Aerospace and Industry”, *National Aeronautics and Space Administration* (1985).
- [256] R. Fruhwirth, “Application of Kalman filtering to track and vertex fitting”, *Nucl. Instrum. Meth. A* **262** (1987) 444–450.
- [257] **CBM** Collaboration, P. Senger, “Probing dense QCD matter in the laboratory—The CBM experiment at FAIR”, *Phys. Scripta* **95** (2020) 074003.
- [258] **ALICE** Collaboration, S. Acharya *et al.*, “Measurement of beauty-quark production in pp collisions at $\sqrt{s} = 13$ TeV via non-prompt D mesons”, *JHEP* **10** (2024) 110.
- [259] **ALICE** Collaboration, D. Adamova *et al.*, “Production of $\Sigma(1385)^\pm$ and $\Xi(1530)^0$ in p-Pb collisions at $\sqrt{s_{NN}} = 5.02$ TeV”, *Eur. Phys. J. C* **77** (2017) 389.
- [260] **ALICE** Collaboration, L. K. Graczykowski, M. Jakubowska, K. R. Deja, and M. Kabus, “Using machine learning for particle identification in ALICE”, *JINST* **17** (2022) C07016.

-
- [261] **ATLAS, LHCb** Collaboration, S. Schramm, “Machine learning at CERN: ATLAS, LHCb, and more”, *PoS ICHEP2018* (2019) 158.
- [262] S. Mondal and L. Mastrolorenzo, “Machine learning in high energy physics: a review of heavy-flavor jet tagging at the LHC”, *Eur. Phys. J. ST* **233** (2024) 2657–2686.
- [263] C. Sammut and G. Webb, “Encyclopedia of Machine Learning and Data Mining”, *Springer* (2017).
- [264] G. James, D. Witten, T. Hastie, R. Tibshirani, and J. Taylor, “An Introduction to Statistical Learning”, *Springer Texts in Statistics* (2023).
- [265] “XGBoost Documentation”,
<https://xgboost.readthedocs.io/en/stable/>. Accessed last in February 2025.
- [266] J. Bergstra, R. Bardenet, Y. Bengio, and B. Kégl, “Algorithms for hyper-parameter optimization” in “Proceedings of the 24th International Conference on Neural Information Processing Systems”, *Curran Associates Inc., NIPS’11* (2011) 2546–2554.
- [267] W.-Y. Loh, “Fifty Years of Classification and Regression Trees”, *International Statistical Review* **82** (2014) 329–348.
- [268] J. H. Friedman, “Greedy function approximation: A gradient boosting machine.”, *Annals Statist.* **29** (2001) 1189–1232.
- [269] J. H. Friedman, “Stochastic gradient boosting”, *Comput. Stat. Data Anal.* **38** (2002) 367–378.
- [270] L. S. Shapley, “Notes on the N-Person Game – II: The Value of an N-Person Game”, *RAND Corporation* (1951).
- [271] S. M. Lundberg and S.-I. Lee, “A unified approach to interpreting model predictions” in “Advances in Neural Information Processing Systems **30**”, *Curran Associates Inc., NIPS’17* (2017) 4765–4774.
- [272] A. Ghosh, B. Nachman, and D. Whiteson, “Uncertainty-aware machine learning for high energy physics”, *Phys. Rev. D* **104** no. 5 (2021) 056026.

-
- [273] **ALICE** Collaboration, S. Acharya *et al.*, “ π^0 and η meson production in proton-proton collisions at $\sqrt{s} = 8$ TeV”, *Eur. Phys. J. C* **78** (2018) 263.
- [274] S. Merkel, “Messung der Produktion von Σ^+ und $\bar{\Sigma}^-$ in pp-Kollisionen bei $\sqrt{s} = 13$ TeV mit dem ALICE-Experiment”, Master thesis, Goethe-Universität Frankfurt am Main (2021).
- [275] J. Podolanski and Rafael Armenteros, “III. Analysis of V-events”, *Philosophical Magazine Series 1* **45** (1954) 13–30.
- [276] **ALICE** Collaboration, S. Acharya *et al.*, “Performance of the ALICE Electromagnetic Calorimeter”, *JINST* **18** (2023) P08007.
- [277] P. Skands, S. Carrazza, and J. Rojo, “Tuning PYTHIA 8.1: the Monash 2013 tune”, *Eur. Phys. J. C* **74** (2014) 3024.
- [278] D. Drijard, H. G. Fischer, and T. Nakada, “Study of event mixing and its application to the extraction of resonance signals”, *Nucl. Instrum. Meth. A* **225** (1984) 367.
- [279] B. Efron, “Bootstrap Methods: Another Look at the Jackknife”, *Annals Statist.* **7** (1979) 1–26.
- [280] V. Vovchenko and H. Stoecker, “Thermal-FIST: A package for heavy-ion collisions and hadronic equation of state”, *Comput. Phys. Commun.* **244** (2019) 295–310.
- [281] **ALICE** Collaboration, S. Acharya *et al.*, “Data-driven precision determination of the material budget in ALICE”, *JINST* **18** (2023) P11032.
- [282] **ALICE** Collaboration, S. Acharya *et al.*, “Multiplicity dependence of π , K, and p production in pp collisions at $\sqrt{s} = 13$ TeV”, *Eur. Phys. J. C* **80** (2020) 693.
- [283] R. Barlow, “Systematic Errors: facts and fictions” in “Conference on Advanced Statistical Techniques in Particle Physics” (2002) 134–144, [arXiv:hep-ex/0207026](https://arxiv.org/abs/hep-ex/0207026).
- [284] “Personal communication with Benjamin Dönigus”, (2024).

-
- [285] ALICE Collaboration, “Multiplicity dependence of (multi-)strange hadron production in proton-proton collisions at $\sqrt{s} = 13$ TeV”, *HEPData collection* (2021).
- [286] P. Z. Skands, “Tuning Monte Carlo generators: The Perugia tunes”, *Phys. Rev. D* **82** (2010) 074018.
- [287] P. Kisel, I. Kisel, P. Senger, I. Vassiliev, and M. Zyzak, “Strange Particle Reconstruction by the Missing Mass Method”, *EPJ Web Conf.* **173** (2018) 04009.
- [288] **ALICE** Collaboration, I. Abualrob *et al.*, “ $\bar{\Sigma}^{\pm}$ production in pp and p-Pb collisions at $\sqrt{s_{NN}} = 5.02$ TeV with ALICE”, [arXiv:2507.13183](#).
- [289] **ALICE** Collaboration, F. Reidt, “Upgrade of the ALICE ITS detector”, *Nucl. Instrum. Meth. A* **1032** (2022) 166632.
- [290] F.-Q. Wang, “Residual correlation in two-proton interferometry from Λ -proton strong interactions”, *Phys. Rev. C* **60** (1999) 067901.
- [291] A. Kisiel, H. Zbroszczyk, and M. Szymański, “Extracting baryon-antibaryon strong interaction potentials from $p\bar{\Lambda}$ femtoscopic correlation functions”, *Phys. Rev. C* **89** (2014) 054916.
- [292] **ALICE** Collaboration, S. Acharya *et al.*, “Multiplicity dependence of (multi-)strange hadron production in proton-proton collisions at $\sqrt{s} = 13$ TeV”, *Eur. Phys. J. C* **80** (2020) 167.
- [293] ALICE Collaboration, “Multiplicity dependence of π , K, and p production in pp collisions at $\sqrt{s} = 13$ TeV”, *HEPData collection* (2020).
- [294] J. L. Nagle and W. A. Zajc, “Small System Collectivity in Relativistic Hadronic and Nuclear Collisions”, *Ann. Rev. Nucl. Part. Sci.* **68** (2018) 211–235.
- [295] **ALICE** Collaboration, S. Acharya *et al.*, “Multiplicity and event-scale dependent flow and jet fragmentation in pp collisions at $\sqrt{s} = 13$ TeV and in p-Pb collisions at $\sqrt{s_{NN}} = 5.02$ TeV”, *JHEP* **03** (2024) 092.

-
- [296] **ALICE** Collaboration, S. Acharya *et al.*, “Investigating the role of strangeness in baryon–antibaryon annihilation at the LHC”, *Phys. Lett. B* **829** (2022) 137060.
- [297] **ALICE** Collaboration, K. Aamodt *et al.*, “Femtoscopy of pp collisions at $\sqrt{s} = 0.9$ and 7 TeV at the LHC with two-pion Bose-Einstein correlations”, *Phys. Rev. D* **84** (2011) 112004.
- [298] “Personal communication with Maximilian Korwieser”, (2024).
- [299] “Personal communication with Yuki Kamiya”, (2025).
- [300] M. Göbel and A. Kievsky, “Nucleon-nucleon correlation functions from different interactions in comparison”, [arXiv:2505.13433](#).
- [301] H. Polinder, J. Haidenbauer, and U.-G. Meissner, “Hyperon-nucleon interactions—a chiral effective field theory approach”, *Nucl. Phys. A* **779** (2006) 244–266.
- [302] Q. N. Usmani and A. R. Bodmer, “ Λ single particle energies”, *Phys. Rev. C* **60** (1999) 055215.
- [303] **ALICE** Collaboration, S. Acharya *et al.*, “Study of the Λ - Λ interaction with femtoscopy correlations in pp and p -Pb collisions at the LHC”, *Phys. Lett. B* **797** (2019) 134822.



Publiziert unter der Creative Commons-Lizenz Namensnennung - Nicht kommerziell - Keine Bearbeitungen
(CC BY-NC-ND) 4.0 International.

Published under a Creative Commons Attribution-NonCommercial-NoDerivatives (CC BY-NC-ND) 4.0
International License.

<https://creativecommons.org/licenses/by-nc-nd/4.0/>